SEISMIC DESIGN OF TIMBER STEEL HYBRID HIGH-RISE BUILDINGS

by

Xiaoyue Zhang

B.A.Sc., Chongqing University, China, 2009

M.A.Sc., Tongji University, China, 2012

A THESIS SUBMITTED IN PARTIAL FULFILLMENT OF

THE REQUIREMENTS FOR THE DEGREE OF

DOCTOR OF PHILOSOPHY

in

THE FACULTY OF GRADUATE AND POSTDOCTORAL STUDIES

(Forestry)

THE UNIVERSITY OF BRITISH COLUMBIA

(Vancouver)

June 2017

Abstract

Timber-steel hybrid systems utilize timber as main construction material, but also take advantage of the ductility and stiffness that steel provides. For a novel hybrid system to gain recognition, experimental data must be supported by numerical analysis to predict its structural performance. “Finding the Forest Through the Trees” (FFTT) is one proposal for a timber-steel hybrid system using mass-timber panels as shear walls and floor slabs connected with steel header beams.

This thesis presents research to evaluate the seismic performance of the FFTT hybrid system using experimental methods, numerical modeling, and reliability analysis. The FFTT system was investigated on two levels: i) component design, and ii) system design. On the component level, the strength, stiffness, ductility, and failure mechanisms of the two key connections were evaluated experimentally. CLT (Cross Laminated Timber) wall to steel beam connection tests results demonstrated that appropriate connection layouts can lead to the desired failure mechanism while avoiding crushing of the mass-timber panels. For the hold-down connection, a modified HSK (Holz-Stahl-Komposit) assembly with high force and stiffness capacity together with ductile behaviour was proposed. On the system level, the seismic response of the FFTT system with different ductility values was investigated using nonlinear 2D and 3D models subjected to a number of ground motion acceleration records. The seismic reliability with various uncertainties was analysed in order to investigate the FFTT system from a performance based approach. Based on the results, an appropriate seismic force reduction factor specific to the FFTT system was proposed. Finally, a feasibility study confirmed the possibility of the practical application of this system. This thesis can serve as a precursor for developing design guidelines for tall wood-hybrid building systems in seismic regions.

Lay Summary

The main objective of this research is to investigate how the FFTT system, as an example of a timber-steel hybrid system, can meet the relevant structural design criteria for seismic loading at the component and system level.

The results of the experimental investigation for the wall-beam connection provides design guidance for the key connection of the FFTT system; The modified HSK hold-down provides a solution to one of the key structural challenges of tall and light structures; The R_d factor estimation provides important guidance for the practical design, and ultimately, the application, of the FFTT system; The seismic reliability analyses compared two response surface methods which includes stepwise ANOVA and GA method, together with Second Order Reliability Method to estimate the structural reliability considering a wide range of random variables; The feasibility investigation confirmed the possibility of this type of structure.

Preface

Chapter 3 was co-authored by Mr. Md Riasat Azim, Ms. Pooja Bhat, Dr. Marjan Popovski and Dr. Thomas Tannert. Md Riasat Azim and Pooja Bhat were responsible for designing and conducting the experimental tests. Xiaoyue Zhang was responsible for analyzing the results and preparing the manuscript. Dr. Marjan Popovski and Dr. Thomas Tannert offered advice during the design and analysis of the research and the manuscript.

Chapter 4 was co-authored by Dr. Marjan Popovski and Dr. Thomas Tannert. Xiaoyue Zhang was responsible for designing the research program, performing the experimental tests, analyzing the results and preparing the manuscript. Dr. Marjan Popovski and Dr. Thomas Tannert contributed to the experimental design and analysis, and the preparation of the manuscript.

Chapter 5 was co-authored by Mr. Michael Fairhurst and Dr. Thomas Tannert. Xiaoyue Zhang was responsible for designing the study, the numerical model and preparing the manuscript. Michael Fairhurst contributed to the numerical modeling and preparing the manuscript. Dr. Thomas Tannert provided guidance throughout the study.

Chapter 6 was co-authored by Mr. Md Shahnewaz and Dr. Thomas Tannert. Xiaoyue Zhang was responsible for designing the research program, numerical modeling, data analysis, and preparing the manuscript. Md Shahnewaz contributed with performing the Genetic Algorithm analyses. Dr. Thomas Tannert provided guidance throughout the study.

Table of Contents

List of Tables

List of Figures

Acknowledgements

This research was supported by MITCAS Canada through an Accelerate project with FPInnovations and a Doctoral Scholarship from the China Scholarship Council.

I would like to express my enduring gratitude to my research supervisor, Dr. Thomas Tannert for his academic guidance. Without his help, I would not have been able to accomplish my Ph.D. degree. His advice, encouragement, and patience through the past five years have helped me to develop research skills in timber engineering.

I owe particular thanks to Dr. Marjan Popovski from FPInnovations for his kind help and valuable suggestions. He was always available for sharing his knowledge and discussion, enlarging my vision of science and providing coherent answers to my endless questions.

Thanks to Dr. Frank Lam, his questions taught me to think more deeply, and he inspired me to continue my work in this field. Also I would like to thank Dr. Asif Iqbal and Dr. Leander Bathon for providing useful suggestions and advice. Thanks to TiComTec and Purbond AG for providing HSK connectors and Polyurethane adhesive for the experimental tests. I owe my thanks to Eric Karsh from Equilibrium Consulting for his time and advice on the FFTT system.

I offer my gratitude to the faculty, staff, and friends at the UBC. In particular Pooja and Riasat for the hard work on the connection experimental test, Michael for the help and suggestions on 3D modeling, and Shahnewaz for the genetic algorithm analysis.

Special thanks are owed to my husband and my parents, whose have supported me throughout my years of education.

Chapter 1: Introduction

1.1 Overview

Wood is one of the most significant and attractive building materials due to its renewability and its lower environmental impact compared to steel and concrete. Throughout the early 20th century, a multitude of mid-rise timber structures were constructed in Canada and the US. Building tall structures with wood is not a new phenomenon – timber pagodas built hundreds of years ago in China and Japan are still standing today despite exposure to seismic events, strong winds, and high-moisture environments (Lam et al., 2008; Takei et al., 1997). The history of fire losses in timber buildings resulted in area and height restrictions being placed on buildings of combustible construction in the 20th century (Buchanan et al., 2014). According to the 2010 National Building Code of Canada (NBCC) (NRC, 2010), the height of wood light frame construction is limited to 4 storeys for residential buildings.

With the rapidly increasing human population and the corresponding pressures on land resources, it has been argued that it is a matter of urgency to find a way to expand the possibilities of using wood as an efficient solution for large-scale tall buildings (Green and Karsh, 2012). Currently, regulations are changing: the British Columbia Building Code (BCBC, 2012) allows 6 storeys light-frame wood construction up to a maximum building height (measured between grade and the floor level of the top storey) of 18 meters due to advances in fire separation/fire-stopping system testing and technology.

In addition, the production of mass-timber panels significantly increased the feasibility for timber products in the construction sector. The three main mass-timber panel products in the current marketplace are Cross-Laminated-Timber (CLT), Laminated Strand Lumber (LSL) and Laminated

Veneer Lumber (LVL). These mass-timber panels provide a more sustainable building material compared to concrete or steel, with reliable structural properties and push the feasible height of timber structures into the high-rise building range (more than 8 storeys). Although wood is a combustible material, mass-timber structures have been recognized to perform well in fire as there is a sufficient mass of wood that allows a char layer to form (incomplete combustion), which in turn helps to insulate the remaining wood from heat penetration (Gagnon and Pirvu, 2011).

Recent efforts within the design and construction community have aimed to expand the height and area limits for timber buildings to develop taller and lager wood structures. Many recent studies (e.g., Ceccotti et al., 2010; Popovski et al., 2010; Gagnon and Pirvu, 2011; Fragiacomo et al., 2011; Pei et al., 2013a; Gavric et al., 2014) have confirmed good structural performance of mass-timber structures and adequate seismic performance when using ductile connectors. Currently, the most accepted method for timber high-rises is the use of timber-based hybrid structural systems. Hybrid systems combine the advantages of two or more materials and can overcome the limitations of light-frame wood construction.

Hybrid timber-steel structures have been identified as one option for timber high-rises. This type of structure utilizes mass-timber as the main construction material while taking advantage of the ductility that steel provides. One such system is the so-called “Finding the Forest Through the Trees” (FFTT) system (Green and Karsh, 2012), which is a mass-timber vertical system with embedded steel beam sections that provide ductility under significant lateral loading. This system is discussed in detail in Chapter 2.

1.2 Motivation

Mass-timber buildings are changing the scale of what is possible to be built in wood around the world due to their inherent fire resistance and environmental benefits. Mass timber-steel hybrid structures are considered a promising solution for high-rise wood-based buildings. However, the current building codes in North America focus on the light frame structures, providing some design guidelines for the mass-timber structures, but none specifically for timber-based hybrid buildings. Therefore, experimental data must be gathered and supported by computational modeling and analysis to predict the structural behavior of timber-steel hybrid systems in order to prove their viability as safe structural systems. For the FFTT system (Green and Karsh, 2012), as an example of novel timber-steel hybrid structure, both component and system level testing are required, along with detailed finite element analyses (FEA) to optimize the structural details.

1.3 Objective

The main objective of this Ph.D. research is to investigate how the FFTT system, as an example of a timber-steel hybrid system, can meet the relevant structural design criteria for seismic loading at the component and system level. As a secondary objective, a hold-down solution that allows the desired strong column/weak beam failure mechanism is investigated. The goal of this research is providing appropriate information to increase the acceptance and use of this novel mass-timber steel hybrid high-rise structural concept.

1.4 Organization of thesis

To provide structural design guidance for novel hybrid systems, such as the FFTT system, the first step is to obtain the required information from component and system testing. The system information comes from the Tall Wood report (Green and Karsh, 2012) which proposed the FFTT

system. The information related to component material properties, such as force-deformation behaviour and nonlinear response is provided from experiments and FEA. In order to explore the possibility of the construction of mid-rise and high-rise structures using the FFTT system, specifically considering its structural behaviour under seismic loads, this research includes two main stages:

i) Component design

- Design and experimental tests of CLT wall-steel beam connections
- Design and experimental tests of modified Holz-Stahl-Komposit-System (HSK) hold-down connections

ii) System design

- Estimation of NBCC Seismic design (R_o, R_d) Factors for the FFTT system
- Analyses of seismic reliability

This thesis is presented in manuscript-based format. Chapter 2 gives a literature review and provides the information to develop sufficient understanding of the field of study. Chapter 3 and Chapter 4 elaborate on the novel timber-steel hybrid system from component level which include the design and experimental investigation on wall-beam connections and high capacity hold-down connections, respectively. Chapter 5 discusses the ductility estimation of the novel FFTT mass-timber steel hybrid structure on the system level; Chapter 6 investigates the seismic reliability of the structure; Chapter 7 presents a feasibility study; and Chapter 8 contains a discussion of the results of this research and proposes new ideas related to the future research.

Chapter 2: Literature Review

2.1 Tall wood buildings

2.1.1 Ancient examples from Asia

As one of the oldest building materials, wood has a long history of utilization in tall structures; tall wood structures have existed for hundreds of years in China and Japan. An example is the Yingxian Pagoda, a 9 storey, 67.4 m tall pagoda located in the Shanxi province of Northern China (Lam et al., 2008), shown in Figure 2.1a. Constructed in 1056 AD, it is one of the world's oldest existing tall timber buildings. Built on a 4 m stone platform foundation, the structure consists entirely of wood. An exterior and interior circular arrangement of timber columns support the five visible storeys and four additional floors hidden within, shown in Figure 2.1b. The pagoda has survived over 900 years of wind and seismic activity, including seven strong earthquakes, with minimal damage. The United Nations Educational, Scientific and Cultural Organization (UNESCO) describes it as "a miracle in the history of Chinese architecture" (Gerard, 2014).

a)  b) 

Figure 2.1 Yingxian Wooden Pagoda, China: a) The overview of the pagoda; b) the beam and column design detail (Wikimedia)

Hōryū-ji, a 5 storey wooden pagoda in Nara, Japan that is 32.5 m high, is another example, illustrated in Figure 2.2. As a Buddhist temple, built around 711 AD, Hōryū-jiis widely acknowledged to be one of the oldest wooden buildings existing in the world. In 1993, Hōryū-ji was inscribed together with Hokki-ji as a UNESCO World Heritage Site (Takei et al., 1997).

Figure 2.2 Horyuji Temple, Japan (Wikimedia)

2.1.2 Ancient examples from Europe

Europe has a long history of construction of tall wood buildings. The wooden Church of Urnes (the Stavkirke, or "Stave Church") was built during the 12th and 13th centuries, and still stands in its original location (Bugge, 1953), shown in Figure 2.3a. The Stave Church is an outstanding example of traditional Scandinavian wooden architecture. It brings together traces of Celtic art, Viking traditions and Romanesque spatial structures (Fazio et al., 2003). The inside view of the church is illustrated as shown in Figure 2.3b. The Urnes Stave Church was declared a World Heritage Site in 1979, and according to UNESCO: "The Stave Church constitutes one of the most elaborate and technologically advanced types of wooden construction that existed in North-Western Europe during the middle ages."

a) 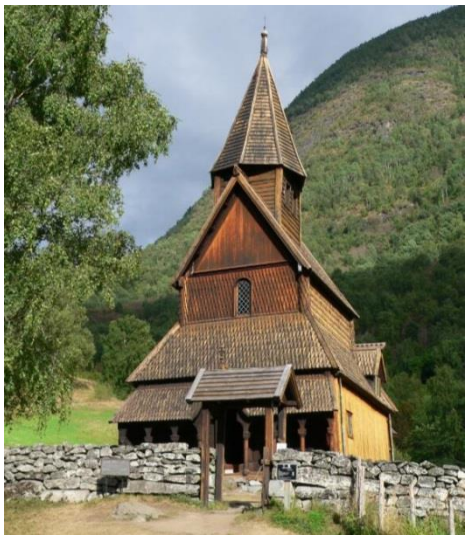 b) 

Figure 2.3 Urnes Stave Church, Norway (Fazio et al., 2003): a) The front view of the church; b) inside view of the church (Wikimedia)

Another tall wooden building, the Barsana Monastery, located in the Maramures Region of Northern Transylvania, has been standing at 56 m tall since 1720 and is the tallest wooden building in Europe (Karacabeyli and Lum, 2014).

2.1.3 Examples from Australia and Canada

Furthermore, several countries around the world, including Australia and Canada, have a history of constructing tall wood buildings. Constructed in 1923 in Brisbane, Australia, the Perry House is one of the oldest and tallest timber structures in Australia (Holland, 2001). The Perry House is a seven-story, 37.2 m, timber structure composed of a heavy timber interior and brick facade. Originally built for retail operations, it was recently converted into a boutique hotel.

Tall wood buildings were built across Canada until the 1940s with un-reinforced brick/mortar used for exterior walls and heavy timber support beams and posts in the interior (commonly known as brick-and-beam construction). The six-storey Leckie Building (Koo, 2013), shown in Figure 2.4a,

was constructed in 1908 in Vancouver, Canada. The use of brick-and-beam construction allowed a large, open floor plan that was used for office and industrial functions. The building went through seismic renovations in the early 1990s and currently houses offices, shops, and restaurants. Another example is "The Landing", as shown in Figure 2.4b, which was constructed in 1905 in Vancouver's Gastown as a large warehouse. It is one of the largest brick-and-beam buildings in Canada with a floor space of 16,000 m^2 (Koo, 2013). It is 9 storeys tall and was retrofitted in 1987 to meet modern building code requirements.

a)  b) 

Figure 2.4 Old tall wood buildings in Canada: a) Leckie Building; b) The Landing (Koo, 2013)

Although wood is the most common construction material in North America, it is typically perceived as weaker and more susceptible to fire than alternatives like steel and concrete. These fears have been codified over the past century by means of restrictive limits on the height and area of timber buildings (Green and Karsh, 2012).

2.1.4 Height restrictions of wood buildings

Wood is a combustible material; for this reason, light-frame wood construction normally requires membrane type protection, such as gypsum board. Mass-timber designs, on the other hand, have

been recognized to perform well in fire according to North-American and International standards (Gagnon and Pirvu, 2011). Mass-timber can rely on the solid nature of the wood panels to provide an inherent fire-resistance to the structure. Figure 2.5 shows the wood frame structure height regulation in British Columbia. Currently timber construction is allowed up to six storeys in almost every province and in 2015 NBCC. By using the mass-timber panels, however, the structural height could be increased further.

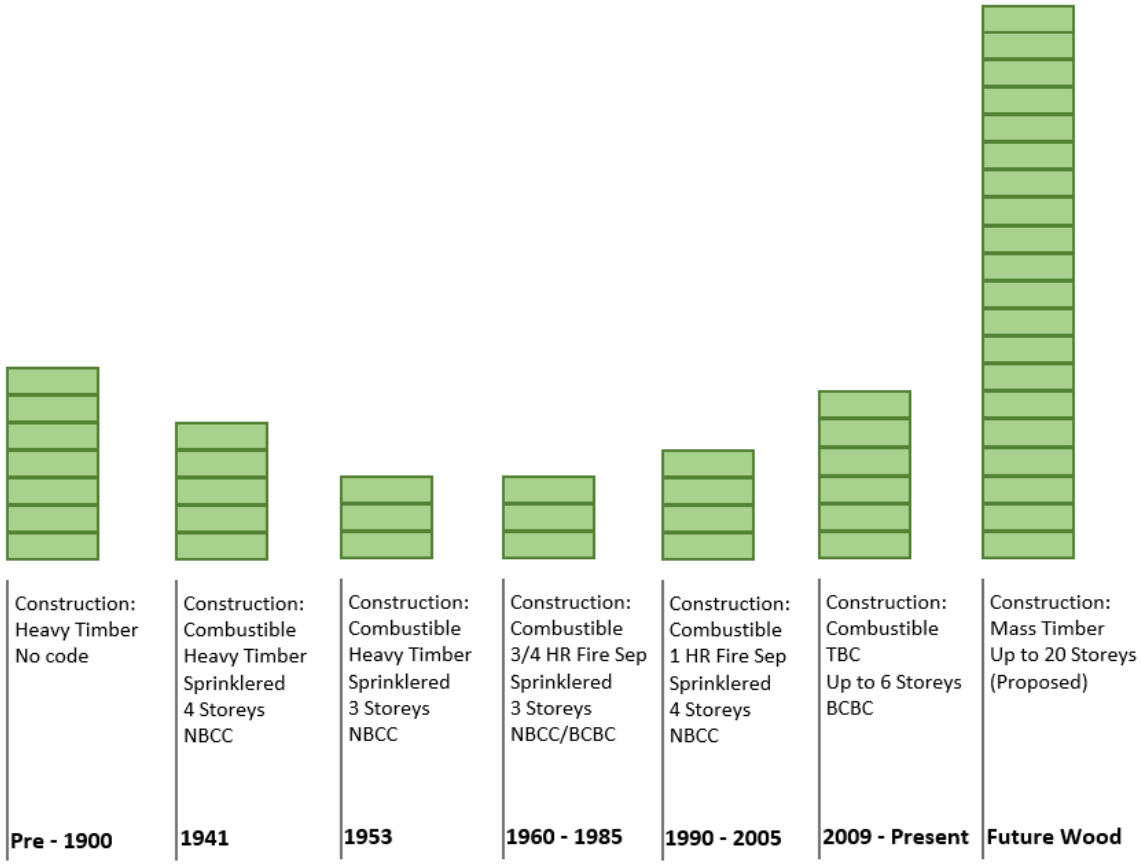

Figure 2.5 Wood frame structure height by regulation in British Columbia (Green and Karsh, 2012)

2.1.5 Tall wood renaissance

Recently, wood construction has experienced a renaissance. With construction professionals and designers seeking lower carbon footprint building alternatives and renewable materials, there is a

growing interest in expanding the tall wood building sector worldwide. Building professionals and government officials alike have been drawn to its sustainability features: timber stores carbon dioxide, is renewable, and prevents pollution typically generated during the extraction and manufacturing of steel and concrete. Timber also offers unique design possibilities and architectural appeal. However, fears about fire safety and structural performance have continued to limit its use in tall wood buildings.

To counteract these fears, a considerable amount of research in Europe, Canada, and New Zealand has begun to convince the public that wood can be as a safe alternative to steel and concrete for building construction. Building taller with wood is not only achievable, it's already underway with advanced construction technologies and modern mass-timber products (see section 2.2.4). Height limits for wooden structures have been relaxed in some regions of the world, while others have introduced options for performance-based design solutions. Currently, proposals for timber structures up to 30 storeys high have been made in Norway, Austria, and Canada (Gerard, 2014).

In the past 10 years over 28 wood buildings, 7 storeys and taller, have been constructed around the world, demonstrating the safety and performance of these buildings and the innovative wood products used to construct them. In 2006, the Swedish city of Växjö declared its intention to promote the use of timber in construction, beginning with the development of an area called Valle Broar (Serrano, 2009). The first project to be completed as part of this initiative is an 8 storey, 134-apartment structure comprising seven timber floors, as shown in Figure 2.6. The design uses glulam members and prefabricated solid wood frame construction for structural wall and floor supports. It also includes instruments to measure deformation and track the vertical displacement of the structure over time. More than a year and a half after construction, sensors indicated that the building had moved by only 20 mm, which calmed displacement fears (Serrano, 2009).

Figure 2.6 Valle Broar, Växjö (Google Image)

In London, England, the 9 storey Stadthaus Murray Groove building (shown in Figure 2.7) was erected in 2009 as the world's tallest contemporary timber residential building at its time of completion. It was designed by Waugh Thistleton Architects and is considered as the pioneer of timber residential tower buildings. This residential apartment complex consists of a reinforced concrete ground level topped by 8 storeys constructed from CLT. It is shaped like a cellular structure using timber load bearing walls where all components are made of wood, including stair and elevator cores. CLT was selected due to its strength, high-quality, and rapid erection time due to the use of prefabricated building elements. The prefabricated system allowed a team of four carpenters to build the superstructure in less than four weeks (KLH, 2015).

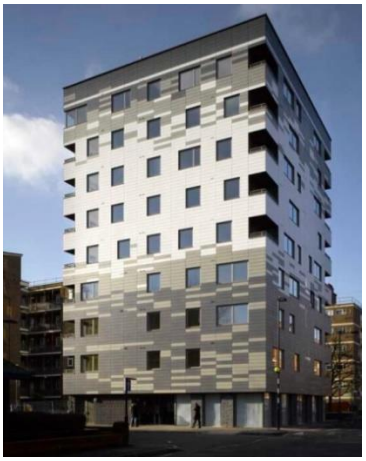

Figure 2.7 Stadthaus, London (Waugh Thistleton Architects)

The Bridport House, shown in Figure 2.8, finished in 2011, is the UK's first building constructed entirely from CLT. The 8 storey residential structure, designed by Karakusevic Carson, consists of prefabricated CLT panels topped by a concrete slab (for acoustic purposes). As an eight-floor multi-storey residential building, it was designed to provide 41 residential units (Birch, 2011). The decision to use CLT rather than steel or concrete stemmed from weight concerns due to the presence of a storm relief sewer under the site. This also reduced foundation demands, as the use of CLT resulted in a lighter building. The panels were edge-glued to make connection locations more air- and water-tight, improving acoustic and fire performance. Prefabricated panelized construction resulted in a construction time of 10 weeks, less than half the estimated time for a similar concrete structure (Gerard, 2014).

Figure 2.8 Bridport House, UK (peterbrett.com)

The Forté Building, a 10 storey wooden apartment building in Melbourne, Australia, built in 2013, is shown in Figure 2.9a. At its time of completion it was the tallest building made of wood in the world and Australia's first residential timber tall building (Wood Solutions Design and Build, 2013). The primary structure is made of 759 prefabricated CLT panels (485 tons). Concrete floor slabs were used for fire separation and acoustic performance. Fire testing during the design phase demonstrated that CLT panels would provide sufficient fire resistance. Despite this, the design

team added gypsum to many wall and ceiling elements for additional non-combustible protection. The project team reported significantly faster, safer, and higher-precision construction with the prefabricated system than typically achieved with traditional materials and its sustainable attributes were brought forward in the marketing strategy used to promote the project (Land Lease, 2015; Gerard, 2014). Figure 2.9b illustrates the construction of the building.

a)  b) 

Figure 2.9 Forté Building, Australia: a) Overview; b) Construction (victoriaharbour.com.au)

The Italian Via Cenni, the first CLT project in an earthquake-prone area, was completed in 2013. The social housing project comprises four 27 m high, 9 storey wooden towers and is presented as a showcase for social housing using multi-storey timber construction. The design includes large nailed web plates and self-tapping screws to facilitate continuous load transfer between structural elements. Similar to the previous examples, a gypsum board protective covering was used despite sufficient inherent fire resistance of the CLT structural panels (Storaenso, 2015).

Another tall wood building, the Treet, shown in Figure 2.10, is located in Bergen, Norway. This 14 storey project, started in 2014 and completed by the end of 2015, was the tallest timber-framed building in the world at its time of completion. All main load-bearing elements are made of wood.

Glulam is used for the trusses, while CLT is used for the elevator shafts, staircases, and internal walls (Abrahamsen and Malo, 2014).

Figure 2.10 Treet, Norway (thechronicleherald.ca)

Canada is well-placed at a time of growth in the timber engineering sector as a country with vast forestry resources and world-class engineers, architects, wood suppliers, and builders. As a consequence, in the last ten years, a series of tall wood buildings have been constructed. The Fondaction Québec Building which utilizes glulam (completed in 2008) and the District 03 building which uses CLT (completed in 2013) are both examples of six storey buildings erected in Quebec with wood (CECOBOIS, 2013; Beaucher, 2015). In 2014, the Wood Innovation & Design Centre (WIDC) was completed in Prince George, BC, shown in Figure 2.11. At 29.5 m high, the WIDC is currently the tallest contemporary wood building in North America.

The recent erection of tall wood buildings demonstrates the rapid growth of knowledge and expertise in high-rise timber construction in the world. The reduced carbon footprint and embodied operational energy performance of these buildings is appealing to communities that are committed to sustainable development and climate change mitigation.

Figure 2.11 Wood Innovation & Design Centre (forum.skyscraperpage.com)

2.1.6 Timber-hybridization

As demonstrated in Section 2.1.5, many tall wood buildings have been constructed in the last few years. Aside from the renewability and the reduced environmental impact, another advantage of wood material is its high strength to weight ratio compared to steel and concrete. This characteristic can result in lighter structures and lower forces during ground excitation. However, there are not many pure wood high-rise structures due to some of the challenges associated with wood construction. The most prominent from a structural, or more specifically seismic, perspective is its brittle nature when loaded in tension or shear. Under these loading types, timber will break in a non-ductile manner, which is not ideal as it does not dissipate much energy and could lead to a brittle, catastrophic failure of the structure. Due to their lack of ductility in seismic design, lack of weight against overturning forces induced by wind or earthquakes, and possibly lack of stiffness in wind design, a variety of proposed mid- and high-rise timber buildings are forced to consider wood-based hybrid solutions.

Almost all timber structures, to some extent, are hybrid structures since connections are made using steel and foundations are usually concrete. However, true hybridization is the process of combining two or more materials to form a system which makes use of the strength of each

material and overcomes their weaknesses. Hybridization can be classified as component level and system level hybridization. Component level hybridization exists when two different materials are combined together to act as a single structural unit. Common examples for this hybridization level include reinforced concrete, bridge decks, hybrid slab/diaphragms, hybrid beams and columns. System level hybridization refers to different materials combined together at the structural level to share the loads acting on them. Examples include vertical mixed systems where the first few storeys are built from a material different than that of the upper storeys; steel frames with timber floors; hybrid roof trusses where timber is used for the top member of the truss and steel as the bottom chord; hybrid frames where wood and steel share both gravity and lateral loads (Khorasani, 2011); and wood infill walls in steel frames (Dickof, 2013).

In Canada, and most other countries around the world, building codes have height and area limitations on wood construction due to fire safety considerations. These limitations in building codes can be overcome if wood is used in combination with non-combustible materials (Cheung, 2000). Therefore, tall structures often utilize either component or system level hybridization.

2.1.7 Examples of wood hybrid structures

Scotia Place (Moore, 2000), a 12 storey studio apartment building in Auckland, New Zealand that was built in 2000, is an example of a hybrid concrete-timber-steel structure (Figure 2.12a). The building is supported with a concrete basement, utilizes a concrete transfer slab at the ground level, and the structural steel superstructure is combined with timber diaphragms. The Kanazawa M Building, shown in Figure 2.12b, constructed in 2005 in Kanazawa, Japan, provides examples of both system and component hybridization. It is a 5 storey building with four timber-steel composite levels supported by a reinforced concrete first floor. The building system comprises steel-timber

composite frames, concrete floor and roof slabs, plywood walls, and steel frame stairs (Koshihara et al., 2005).

a)  b) 

Figure 2.12 Timber-based hybrid building examples: a) Scotia Place (Moore, 2000); b) Kanazawa M Building (Koshihara et al., 2005)

H8, shown in Figure 2.13, designed by Schankula Architekten and constructed in Bad Aibling, Germany, in 2011, is an eight-storey building comprised of CLT floors and walls with a concrete core. The prefabricated CLT panels are covered in gypsum board to provide additional fire protection. The panelized system permitted a construction assembly time of approximately 16 working days, or one storey every two days (Gerard, 2014).

Figure 2.13 H8, Germany (binderholz.com)

Located in Carinthia, Austria, the Pyramidekogel Tower (Lackner and Vodicka, 2013), shown in Figure 2.14, was built in 2013. This observation tower spirals almost 100 m into the air, making it the world's highest wooden observation tower. The tower extends over ten levels with two platforms. Curved glulam columns, with maximum individual length of 27 m, provide vertical and lateral support. The columns are support in their weak direction by HSS steel rectangular tubes forming elliptical steel rings and diagonal struts (Hausegger, 2013; Pyramidenkogel, 2013; Karacabeyli and Lum, 2014).

Figure 2.14 Pyramidenkogel lookout tower, Austria (Pyramidenkogel 2013)

In Austria, the Lifecycle Tower One (Professner and Mathis, 2012), erected in 2012, was the world's first building from Cree (Cree, 2010), an Austrian construction company. The project started as an Arup feasibility design for a 20 storey heavy timber building, and resulted in the construction of an 8 storey office building, shown in Figure 2.15. Its first floor is made of concrete while the seven floors above utilize wood and concrete in a hybrid system (BUESBB, 2013). The LifeCycle Tower One was the world's first wood-based hybrid modular buildings that achieved a passive house standard (Zangerl and Tahan, 2013). Passive house is the world's leading standard in low energy buildings (Audenaertet al., 2008; Badescu and Sicre, 2003).

Figure 2.15 Lifecycle Tower One, Austria (engineering.com)

The UBC Earth Sciences Building (Canadian Wood Council, 2012), shown in Figure 2.16a, completed in 2012, with a timber academic wing and a concrete laboratory wing, is another example of a mass-timber and concrete hybrid application. The photo in Figure 2.16b shows the flying staircase which uses HSK connections to provide a high force capacity and stiffness.

a) 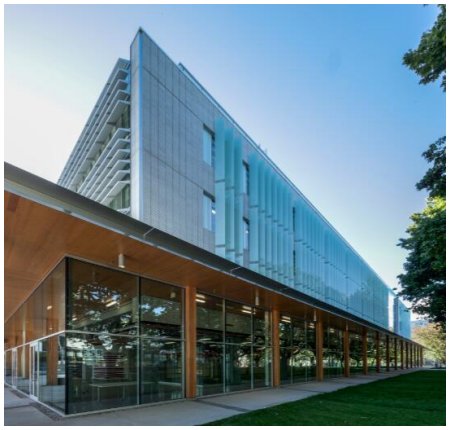 b) 

Figure 2.16 UBC Earth Sciences Building: a) Overview; b) flying staircase

Origine, a major 13 storey residential project in Quebec City's Pointe-aux-Lièvres eco-district, will consist of a 12-floor solid wood structure on a concrete podium and will measure 40.9m in height, as shown in Figure 2.17. This building is to be constructed of mostly CLT with a concrete podium on the top. The work began in 2015 (Origine Écocondos, 2015; Gosselin et al., 2015).

Figure 2.17 Origine, Quebec City,Canada (condosorigine.com)

Currently, the tallest contemporary hybrid wood building is UBC's Brock Commons Building (UBC News, 2016), as shown in Figure 2.18. The 18 storey (53 m) mass wood structure and facade was completed four months ahead of schedule, showcasing the advantages of building with wood. Brock Commons is the first mass wood, steel and concrete hybrid project taller than 14 storeys in the world. The building has a concrete podium and two concrete cores, with 17 storeys of CLT floors supported on glulam columns. The cladding for the facade is made with 70 percent wood fibre (Poirier et al., 2016).

Figure 2.18 UBC's Brock Commons Buildings, Canada (UBC News 2016)

Aside from the previously listed completed projects, different conceptual designs using the hybridization concept have been proposed for tall-wood buildings up to 30 storeys. Two studies that exemplify this are "The Case for Tall Wood Buildings" which propose the FFTT system (Green and Karsh, 2012), as introduced in Section 2.4, and the wood-concrete hybrids developed by SOM (SOM, 2013), as shown in Figure 2.19a.

a) b)

Figure 2.19 SOM Timber Tower: a) SOM's prototype 42 storeys building; b) Concrete joint frame system (SOM 2013)

The goal of the SOM Timber Tower Research Project was to develop a structural system for tall buildings using mass-timber as the main structural material and minimizing the embodied carbon footprint of the building. The research was applied to a prototypical building based on an existing concrete benchmark building: the Dewitt-Chestnut Apartments, a 120 m, 42 storey building in Chicago designed by SOM and built in 1965. An innovative "Concrete Jointed Timber Frame", as shown in Figure 2.19b, is proposed to resist the overturning and lateral forces induced by significant wind loading. This system relies primarily on mass-timber for the main structural elements, with supplementary reinforced concrete at the connecting joints. This system plays to

the strengths of both materials. The result is an efficient structure that could compete with reinforced concrete and steel while reducing the carbon footprint by up to 75% (SOM, 2013). Although this design is in its proposal phase, SOM believes that the mass timber-concrete timber skyscraper is technically feasible from the standpoint of structural engineering, architecture, interior layouts, and building services. However before it is built, additional research and physical testing is necessary to verify the performance of the structural system (SOM, 2013).

2.2 Steel and timber as structural materials

Timber-steel hybrid structures are a good option for timber-based high-rise buildings. Before considering a new type of construction, it is essential for engineers to understand the mechanical properties of the materials chosen for the design because the structural response of buildings is influenced by the nature and behaviour of their constituent construction materials.

2.2.1 Steel as a structural material

As a homogeneous and isotropic material, steel exhibits properties that make it one of the most versatile structural materials. It has high tensile and compression strengths together with high stiffness, uniformity, and high ductility. These properties make it the material of choice for numerous structures such as bridges, high rise buildings, and towers. Table 2.1 lists the approximate material properties for structural steel and timber (Spruce-Pine-Fir).

Table 2.1 Material properties of steel and timber (CSA S-16, 2009; CSA 086, 2010)

Material	Density (kg/m^3)	Elastic Modulus (MPa)	Compressive Strength (MPa)	Tensile Strength (MPa)	Poisson Ratio
Steel	7800	200000	400 ~1000	400 ~ 1000	0.3 ~ 0.31
S-P-F SS/No.1/No.2	350 ~ 420	6500 ~ 10500	Parallel 9.0 ~ 14.5 Perpendicular 5.3	Parallel 4.9 ~ 8.6 Perpendicular 0.5	0.2 ~ 0.21

Steel generally exhibits a linear stress-strain relationship up to a well-defined yield point as shown in Figure 2.20a. The linear portion of the curve is the elastic region and the slope is defined by the modulus of elasticity. As deformation continues, the material yields and loses stiffness. The stress increases due to strain hardening until ultimate strength. The post-yielding, strain hardening and necking regions can be very large (Kulak and Grondin, 2011). An example of the hysteresis loop for a flexible steel plate, as shown in Figure 2.20b, confirms the high ductility. The round and full loop shape results in good energy dissipation of steel as it does not buckle, distort, rotate, clink, warp or splinter. Steel also can be rolled or cut into a variety of sizes and shapes without changing its composition or physical properties through structural steel fabrication. Because of these advantages, among others, steel has become a predominant material in the construction industry to develop new and innovative structural solutions (Assakkaf, 2002).

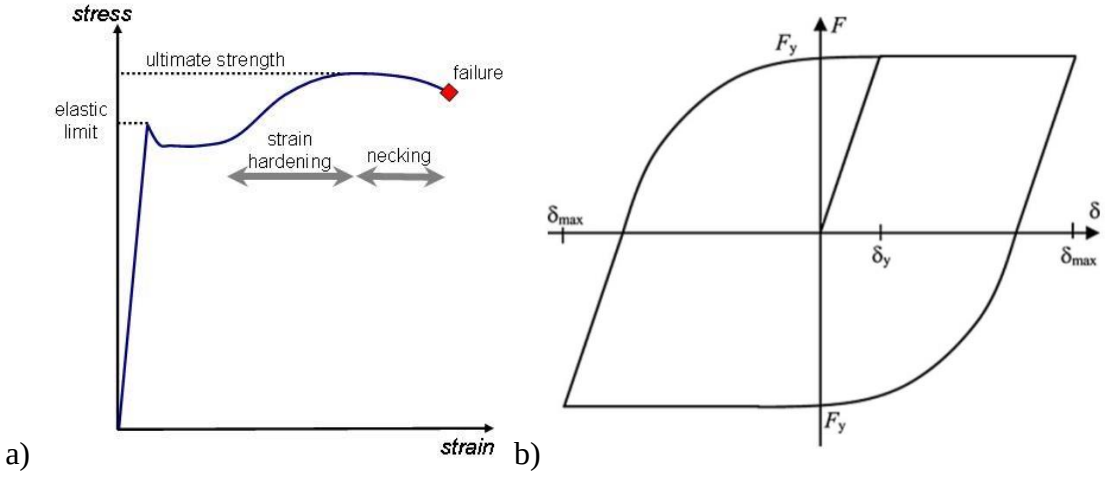

Figure 2.20 a) Stress-Strain curve for mild steel; b) Hysteresis loop of steel (López-Almansa et al., 2014)

Although steel has many advantages as structural material, it also has disadvantages. Whereas reinforced concrete and glulam columns are generally sturdy due to their large cross section (Assakkaf, 2002). When subjected to cyclic loading, the strength of structural steel member reduces because of fatigue which may result in the loss of its ductility (Campbell, 2008). Moreover,

steel structures are susceptible to corrosion when exposed to air, water, and humidity; hence, they must be painted periodically (Miodek, 2002). Also, steel strength is reduced tremendously at high temperatures as in the case of fires, therefore, steel structures require high maintenance and fireproofing costs (Buchanan, 2001).

2.2.2 Timber as structural material

Wood is an anisotropic material and the properties of timber are very variable. Timber has unique and independent mechanical properties in the directions of three mutually perpendicular axes: longitudinal (parallel to the grain), radial (normal to the growth rings/perpendicular to the grain in the radial direction), and tangential (perpendicular to the grain but tangent to the growth rings; Kretschmann, 2010). Also, wood is a hygroscopic material; it gains and loses moisture depending on the environmental conditions to which it is exposed (Wood Design Manual, 2010). The loss and gain moisture affects dimensional stability and strength, and the presence of water in combination with other conditions can cause decay. Therefore, the strength properties of timber products are retrieved by engineers based on the grading specified by CSA 086 (2014).

For the non-linear behaviour parallel and perp. to grain, Grosse (2005) proposed a five stage nonlinear material model for timber incorporating degradation as shown in Figure 2.21. Stage I represents linear elastic response; stage II occurs above proportional limit compressive strength of timber; in stage III, the compressive strength is controlled by localized buckling of fibers. Microscopically recognizable kinks form at this stage, which is termed as “transient kinking”. Stage IV is considered as “Steady State Kinking”; and finally, stage V shows a very large compressive deformation stage characterized by large amounts of hardening. For compression perpendicular to grain, the failure mode is described as ductile. Failure is originated by kinking of

the cell walls parallel to the load. In the case of radial loading a slight strength-drop is observed after reaching the maximum load.

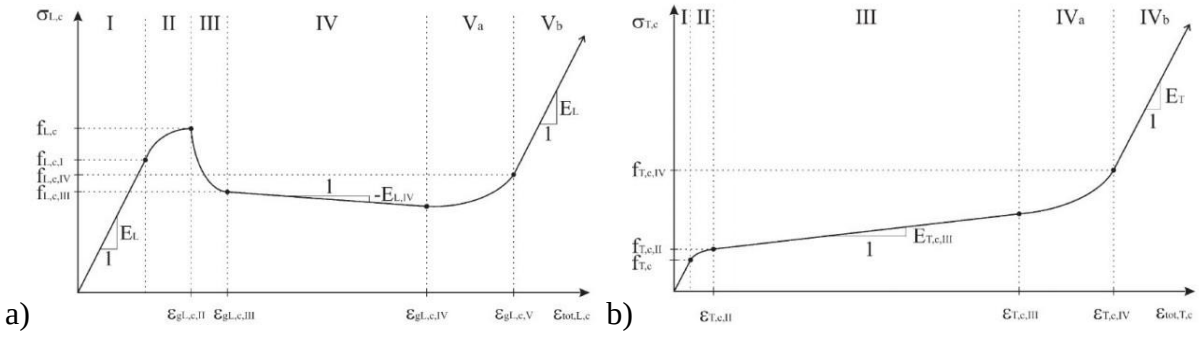

Figure 2.21 Nonlinear material model of timber in compression: a) Parallel to grain; b) Perpendicular to grain (Grosse, 2005)

Amongst construction materials, wood stands out as a unique and versatile product. Its aesthetic appeal, tensile strength, insulation qualities, and ease of fabrication enable it for use in an extensive array of construction applications. Wood possesses several benefits that make it an excellent candidate for use in a wide variety of construction projects. One such benefit is the low heat conductivity (Hungarian Midleks, 2016) which allows wood to be used in various insulation applications. Wood also provides highly sought after acoustic properties and is the material of choice for the construction of structures where proper acoustics is important, such as concert halls. Wood is resistant to electrical currents, making it an optimal material for electrical insulation. Wood also provides high bending and tensile strength to weight ratios.

2.2.3 Glued laminated timber

Glued laminated timber, also called glulam, is an engineered wood product comprised of layers of dimensional lumber bonded together with durable, moisture-resistant structural adhesives. These laminations are stacked and glued in a straight form for columns or beams (Figure 2.22a), as well

as curved or arched shapes (Figure 2.22b). Being an engineered product, members are manufactured in accordance with the guidelines outlined by CSA O177 (CSA O177, 2015). Glulam overcomes some drawbacks of sawn timber. Because of their composition, large glulam members can be manufactured from a variety of smaller trees harvested from second- and third-growth forests and plantations (APA, 2010). Glulam provides the strength and versatility of large wood members without relying on the old growth-dependent solid-sawn timbers. Additionally, laminating is an effective way of using high strength lumber of limited dimension to manufacture large structural members in many shapes and sizes. Also glulam members typically have more consistent and reliable structural properties compared with sawn lumber.

a)  b) 

Figure 2.22 a) Glulam column (UBC Forestry department: forestry.ubc.ca); b) Glulam arch (Sheffield Winter Garden: Wikipedia)

2.2.4 Mass timber

Mass-timber is characterized by the use of large solid wood panels for wall, floor, and roof construction. The three main mass-timber products in the current marketplace are CLT, LSL and LVL. As fire safety is one important limitation to the height of current light-frame wood construction, the production of mass-timber panels can significantly increase the share of timber

products in the construction market. Aside from the desired performance in fire, there are many distinct advantages for mass-timber construction compared to conventional cast-in-place concrete building construction. Wood stores carbon -the most effective tool for carbon removal from the atmosphere is a tree, and trees are renewable. Construction costs compete on labor savings. Building with off-site prefabricated mass-timber components is faster, safer and more precise. Also damage remediation in timber buildings is simpler.

2.2.5 Cross laminated timber

CLT products, examples shown in Figure 2.23a, were developed in Germany and Austria in the early 1990's as an alternative to masonry and concrete construction, and have gained popularity in both residential and non-residential applications in Europe and North America (Gagnon and Pirvu, 2011). CLT panels are mass-timber plates made from smaller framing lumber laminated crosswise on their wide faces. North American CLT is typically produced as three-, five-, seven-, and nine-layer panels (Figure 2.23b) of 2×6 lumber depending on the structural requirements and can be used as shearwalls, flooring and roofing. CLT production process consists of four main steps: 1) cross cutting of logs; 2) trimming and grading of lamella and cutting out flawed sections ; 3) finger jointing of lamella; 4) face gluing (Gagnon and Pirvu, 2011). Because of this process, CLT contains few defects and is a nearly homogeneous material.

a)  b) 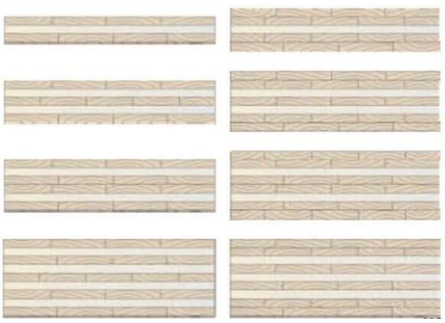

Figure 2.23 CLT: a) CLT panels; b) CLT panel cross-sections (Mohammad et al., 2012)

There are many advantages when using CLT as walls and floor panels. The cross-laminating process creates improved dimensional stability in the product which allows for prefabrication of wide and long panels. Additionally, high in-plane and out-of-plane strength and stiffness properties in both directions can be provided for panels allowing for a two-way action capability similar to a reinforced concrete slab. The cross lamination in CLT also considerably increases the splitting resistance for certain types of connection systems (Mohammad et al., 2012).

However, CLT also has its drawbacks. For CLT with crosswise board layups, rolling shear stresses, which are defined as the shear stress in a radial-tangential plane perpendicular to the grain direction, may be induced in the cross layers under certain loading scenarios. For example, when a CLT floor is supported by columns, high concentrated loads may cause shear around the supporting area or high bending loads on short-span floors or beams. The rolling shear strength of wood is fairly low, e.g. in Eurocode 5 (CEN, 2004), a characteristic rolling shear strength value of 1.0 MPa is used independent of strength class. Therefore, it is important to understand the rolling shear strength properties of CLT products subjected to heavy and highly concentrated out-of-plane loads (Li et al., 2014).

Various tests have been conducted to investigate the structural performance CLT shear walls. One of the most comprehensive studies to quantify the seismic behaviour of low- and mid-rise CLT construction was the SOFIE project (Gagnon and Pirvu, 2011), which included tests on connections and in-plane cyclic tests on CLT walls with different connection layouts and openings. The results confirmed that the connection layout and design has a strong influence on the overall system behaviour, because the CLT panels are very rigid and almost all energy under cyclic loading was dissipated by the connections (Ceccotti et al., 2006).

Another series of monotonic and cyclic tests on CLT walls with different wall configurations and connections were performed at FPInnovations , see Figure 2.24a. The tests confirmed that CLT wall panels behaved as rigid bodies and that the lateral deformation and system ductility of CLT assemblies are greatly influenced by the base connectors (Popovski et al. 2010), see Figure 2.24b.

a)  b) 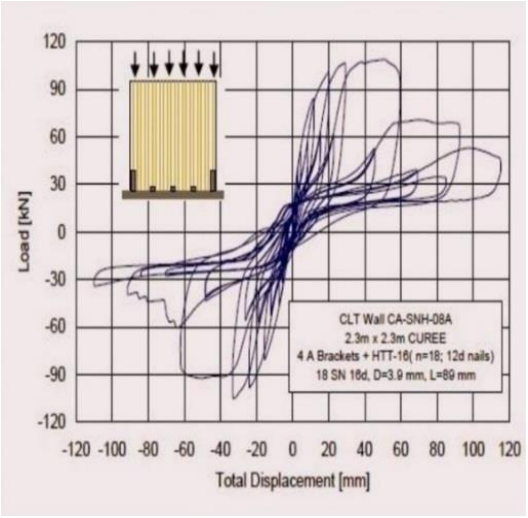

Figure 2.24 Seismic behavior of CLT panel: a) Test specimen; b) Hysteresis loop (Popovski et al., 2010)

2.3 Design of lateral load resisting systems

2.3.1 Background

Both wind -and earthquakes create lateral loads on buildings. Earthquakes can occur anywhere; however, the likelihood of earthquakes strong enough to threaten buildings is especially high in certain geographic areas. Earthquakes cannot be prevented, but sound design and construction based on research and compliance with building code requirements can reduce their effects (AWC, 2015). In high seismic hazard areas, the seismic design of buildings becomes an important consideration.

For wood buildings, because of the material's inherent lightweight properties compared to other construction materials, the inertial seismic forces, which are proportional to weight, are reduced. Another core of seismic design is to allow inelastic action in pre-defined ductile zones to provide a mechanism for dissipating energy within the structural system. As wood is a brittle material when loaded in tension or shear parallel to grain, these ductile zones in wood structures are usually steel connections, though configurations may vary greatly. For light wood frame buildings, the multiple nailed connections in framing members, shear walls and diaphragms exhibit ductile behavior (the ability to yield and displace without sudden brittle fracture; AWC, 2015), and these connections are considered energy dissipation devices.

Selecting a structural typology that is suitable to the building's intended use is essential. Generally speaking, there are four different strategies to provide Lateral Load Resisting Systems (LLRS) for wood buildings: i) the use of the vertical circulation core(s); ii) perimeter walls; iii) interior shear walls, trusses, moment frames, diagonal bracing, and iv) a combination of these (Karacabeyli and Lum, 2014).

2.3.2 Force-based design approach

To design the LLRS of structures, two main approaches exist: i) Forced Based Design Approach (FBDA) and ii) Displacement Based Design Approach (DBDA). DBDA was developed to achieve, rather than be bounded by, displacement limits that could be strain-based or drift based (Priestley, 1993). However, current seismic design in the North America, and in most of the world, is carried out in accordance with FBDA. In the FBDA, elastic forces are determined, based on initial elastic estimate of building period together with a design acceleration spectrum for 5 percent damping (Park, 1996), sometimes the effective damping can be reduced when expecting less energy, i.e, for

serviceability checks. Design force levels are reduced from the elastic level by dividing the code-specified force-reduction factors. In the International Building Code (IBC, 2012) and FEMA P-695 (FEMA, 2009), the response modification factor is defined as R, while in the NBCC (NRC, 2015), there are two force modification factors: R_d related to ductility and R_o related to overstrength.

The ductility factor reflects the reduction in force seen in a structure responding inelastically compared to the equivalent elastic structure, and is a function of the ductility, or ability of the system to deform beyond yielding. The overstrength factor represents the reserve strength within the system which comes from factors such as member oversizing in design and strain hardening in the materials. Displacements are checked at the end of the design process, based on assumed relationship between elastic and inelastic displacement. If it is found that the displacement excessed the code drift limit, or material strain limits, then the building stiffness may be adjusted and new design force levels are established (Priestley, 2002).

2.3.3 Seismic performance factor quantification

One of the key steps in the seismic design is the determination of force modification factors for the structural system. In NBCC 2010 (NRC, 2010), values for seismic performance factors according to the LLRS are presented in Table 4.1.8.9. The most commonly used LLRSs in steel are moment frames and braced frames; the most commonly used wood-based system is light-frame wood construction, comprised of sawn lumber members sheathed with wood-based panels , and nailed connections. Wood frame shear walls are usually designed to provide ductility through the yielding of panel-to-sheathing connections. Steel frames can be designed to provide different

levels of ductility: D (ductile), MD (moderate ductility), LD (limited ductility) and CC (conventional construction) systems are all considered in the NBCC (NRC, 2010).

NBCC 2010 (NRC 2010) defines the system overstrength, R_o, as a combination of factors:

Eq.2.1

$$R_o = R_{size} R_{\varphi} R_y R_{sh} R_{mech}$$

Where R_{size} is the overstrength arising from restricted choices for sizes of members and elements and rounding of sizes; R_{φ} is a factor accounting for the difference between nominal and factored resistances, equal to $1/\varphi$, where φ is the material resistance factor; R_y is the ratio of "actual" yield strength to minimum specified yield strength; R_{sh} is the overstrength due to the development of strain hardening; and R_{mech} is the overstrength arising from mobilizing the full capacity of the structure such that a collapse mechanism is formed. R_{size}, R_{φ}, R_y, R_{sh} and R_{mech} are usually derived statistically considering the difference between the design and the actual construction.

Currently, there are no specific procedures in Canada that deal with development of R_d factors for new systems. Rather, procedures developed in the US are suggested for the development of potential R_d factors such as the FEMA P-695 or FEMA P-795 procedures. FEMA P-695 (FEMA, 2009) provides a consistent method for evaluating the building system performance and the seismic response parameters (R, C_d, Ω_o) used in ASCE 7-10 (ASCE7-10, 2010), so that the analyzed structural system meets the desired safety margin against collapse. The methodology directly accounts for the potential variations in structural configuration of buildings, ground motions, and the quality of the available test results for the behavior characteristics of the structural elements by using the incremental dynamic analysis. The primary application of the procedure is for the seismic evaluation of new structural systems, so that they have equivalent margin against

collapse for the maximum considered earthquake (Karacabeyli and Lum, 2014). The drawbacks of the FEMA P695 (FEMA, 2009) procedure are that it is very complex, very time consuming and computationally extensive.

FEMA P-795 (FEMA, 2011) provides a Component Equivalency Methodology to evaluate the seismic performance equivalency of structural elements, connections, or sub-assemblies whose inelastic response controls the collapse performance of a seismic-force-resisting system (SFRS). The statistically based procedure is applied to developing, evaluating and comparing test data on new components that are proposed as substitutes for code-approved SFRSs, and it is derived from the general methodology contained in in FEMA P-695 (FEMA, 2009).

Aside from the two FEMA procedures, designers can also use a preliminary procedure proposed by Pei et al. (2013a), to calibrate the force modification factors for new wood-based structural systems. The procedure assumes that the inter-storey drift is the main parameter that directly relates to structural damage and the appropriate factor is chosen based on the accepted probability of exceeding a defined maximum drift limit related to collapse prevention.

2.4 Seismic reliability analysis

Reliability analyses form the basis of "Performance-Based Design" (FEMA, 1997; FEMA, 2006) and allow the structures to be designed to meet certain target performance objective. Seismic reliability analyses should consider uncertainties to provide a comprehensive safety assessment of a structure such as ground motions characteristics (peak ground accelerations, frequency contents, duration of shaking), structural weight (dead loads and live loads), material properties (strength and stiffness), and connection properties (strength, stiffness, ductility) amongst others (Haukaas, 2008). In reliability analyses, uncertainty can be characterized as either aleatory (natural

randomness that cannot be reduced) or epistemic (lack of knowledge that can be reduced) (Kiureghian and Ditlevsen, 2009).

The evaluation of seismic structural reliability has focused on reinforced concrete and steel structures. Dymiotis et al. (1999) conducted structural modeling and probabilistic assessment of reinforced concrete (RC) frames subjected to seismic loading; Yun et al. (2002) presented a performance prediction and evaluation procedure for the steel moment frames based on nonlinear dynamics and reliability theory; Papadrakakis et al. (2004) proposed a robust and efficient methodology for performing reliability-based structural optimum design of steel frames under seismic loading; Lin et al. (2010) evaluated the seismic reliability of eccentrically braced frame (EBF) and buckling-restrained braced frame (BRBF) systems in comparison with that of moment-resisting frame (MRF) systems. Khatibinia et al. (2013) introduced an efficient metamodeling framework in conjunction with the Monte-Carlo Simulation (MCS) is to reduce the computational cost in seismic reliability assessment of existing RC structures.

Most studies on seismic reliability of timber structures and have focused on low-rise light-frame systems. Filiatrault and Folz (2002) discus the application of performance-based seismic design to wood framed buildings through a direct-displacement methodology. Rosowsky (2002) developed a risk-based procedure for performance-based design of wooden shear walls. Rosowsky and Ellingwood (2002) provided an overview of performance-based design models and tools, and suggested a methodology for assessing the response of light-frame residential construction exposed to various levels of natural and man-made hazards. Van de Lindt and Walz (2003) developed a hysteretic response model for wood shear walls based on experimental data for ten single panel walls. Kim and Rosowsky (2005) applied fragility techniques to light-frame structures treating the shear walls as isolated subassemblies. Nonlinear dynamic time-history analyses were

used to predict the performance of the shear walls considering a suite of suitably scaled ground motions to represent the seismic hazard. Van de Lindt (2005) developed a damage-based seismic reliability model for a symmetric one-story light-frame wood building. It provided the basic methodology to calibrate a seismic damage model and compute the structural reliability using a damage-based limit state function. Subsequently, van de Lindt et al. (2008) presented the basic concept of applying system identification logic for Performance-based Seismic Design (PBSD) of wood frame structures. Wang et al. (2010) extended the direct displacement design (DDD) procedure to mid-rise wood-frame structures and developed a set of factors for the procedure to meet specified performance levels with certain target probabilities. Yin and Li (2011) considered two separate models for the earthquake loading, using a Poisson process for occurrence and Type II distribution for intensity, and a filtered Poisson process for snow loads that increased the load in each event.

A non-linear seismic reliability analysis was presented by Li et al. (2011a; b) to evaluate the performance reliability of two and three post-and-beam timber buildings under seismic excitation. Damage to the building through a set of ground motions was quantified by the peak inter-storey drift. Response surfaces were generated using the ground motion characteristics (peak ground acceleration, structural mass, and shear wall characteristics) and used to perform the FORM and IS analyses to calculate the structural system reliability. For tall wood buildings, however, little is known about their seismic reliability.

2.5 The “FFTT” system

2.5.1 Background

Hybrid timber-steel structures have been identified as a good option for timber high-rises. Steel elements can be designed to provide ductility, high tensile capacity, and stiffness, while timber can be easily fabricated into all kinds of shapes and sizes to fit practically any construction need and is used for providing building enclosure (Khorasani, 2011). Using timber reduces the environmental impact and low carbon footprint by reducing greenhouse gas emissions. The reduced building weight leads to reduced transportation costs. Timber-steel hybrid vertical and lateral elements can increase load carrying capacities without increasing cross sections (Stiemer, 2012; Khorasani, 2011), an example is steel-frame wood-infill systems (Dickof et al., 2012).

Timber-steel hybrid systems combine the advantages of wood and steel properties. Steel excels in tension and timber behaves well in compression. As mentioned in Sections 2.1 and 2.2, using wood as the main construction can reduce the embodied energy and carbon footprint of buildings and solid wood systems exhibit higher strength and stiffness and superior dimensional stability compared to traditional sawn lumber systems. Timber construction, due to the low weight of the material, results in lower gravity and seismic loads compared to reinforced concrete construction. The potential savings in foundation costs are expected to be significant, particularly in poor soil conditions. Steel elements provide the necessary ductility and tensile capacity in hybrid structural systems and may include traditional braced frames or moment frames, or more innovative steel systems including steel plate shear walls, buckling restrained braces, or link beams. Using steel-timber hybridization also allows for more efficient construction sequencing than cast-in-place concrete (Karacabeyli and Lum, 2014).

2.5.2 The "FFTT" concept

One conceptual design for a timber-steel hybrid system has been proposed by Michael Green and Eric Karsh; the system is labeled "FFTT" (Green and Karsh, 2012). FFTT is a unique tilt-up system that effectively balloon-frames mass-timber panels, and is proposed for buildings ranging from 10 to 30 storeys. The FFTT system consists of a solid-wood central elevator and stair core and wood floor slabs with perimeter wood moment frames or interior wood shear walls. Standard reinforced concrete is envisioned for basements and foundations, but concrete is not structurally necessary elsewhere in the building. A rendering of a 20 storey FFTT building is presented in Figure 2.25a, while Figure 2.25b shows an inside view of the FFTT system.

The proposed system is based on the "strong column/weak beam" structural concept which means that the beams and horizontal elements of the structure should break before the gravity-resisting columns. This helps the structure dissipate seismic energy without the total collapse. According to this design concept, the FFTT system consists of balloon-type mass-timber walls that run along the height of the building, that act as the vertical and the lateral load resisting system. Beam elements made of steel sections are bolted to the wall panels and act as the ductile weak link of the system, as shown in Figure 2.26.

a)  b) 

Figure 2.25 a) 20 Storey FFTT Rendering; b) Inside view of the FFTT system (Green and Karsh, 2012)

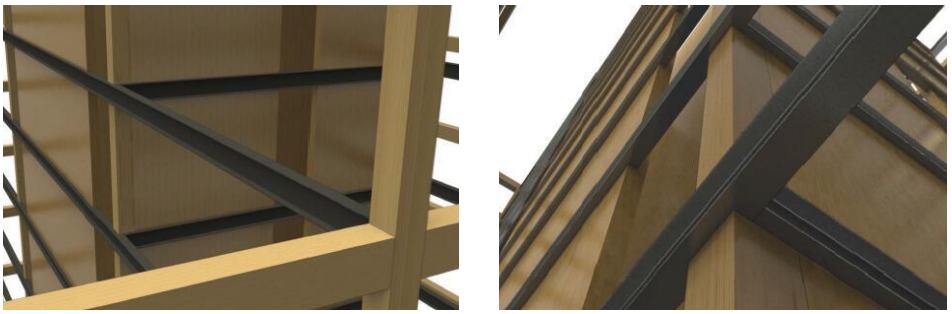

Figure 2.26 Solid panel core and intersecting ductile steel link beams (Green and Karsh, 2012)

The FFTT system dissipates seismic energy by providing plastic hinges in the interconnecting steel beams, thus allowing control over the level of seismic forces during a severe seismic event. This mechanism also protects the timber elements, much like a fuse that limits the level of power that runs through an electrical system. In the FFTT system, to transfer the horizontal loading to the foundation and to achieve the strong-column/weak-beam failure mechanism, shear wall and moment frame systems are proposed as the primary Lateral Load Resisting Systems (LLRS), Figure 2.27 shows three different LLRSs in FFTT system which includes a mass-timber panel core

(Figure 2.27a), perimeter shear and load bearing walls (Figure 2.27b) and interior shear and load bearing walls (Figure 2.27c).

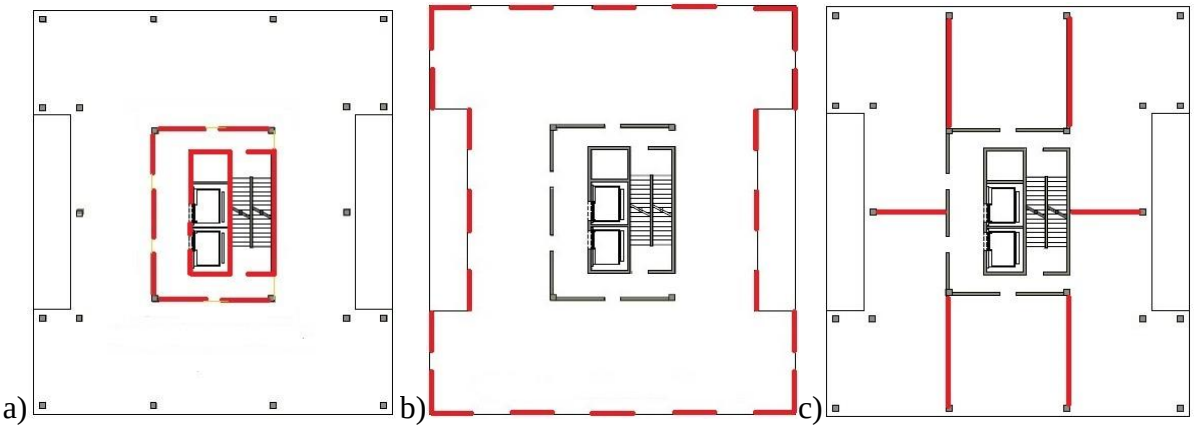

Figure 2.27 LLRS for FFTT system: a) Mass-timber panel core; b) Perimeter shear and load bearing walls; c) Interior shear and load bearing walls

Being used individually or in combination, these three LLRSs can be used to create four different structural options in FFTT system which are adaptable for use in residential and office buildings and provide different maximum structural heights.

In Option 1, proposed for up to 12 storeys, wood core walls and glulam perimeter columns are deployed as structure (Figure 2.28a). The interior walls are required to have a load bearing function, resulting in flexibility of floor plan layout. The absence of exterior load bearing walls allows for flexibility in the façade design of its. Additionally, interior modifications for future changes are easily made. Option 1 is deemed competitive in terms of use and planning to its concrete benchmark.

In Option 2, in addition to the structural wood core walls and glulam perimeter columns, interior structural walls are introduced for building heights up to 20 storeys (Figure 2.28b). This option also allows for flexibility in the façade design because of the absence of exterior structural walls.

In terms of interior planning, the introduction of interior load bearing walls diminishes some flexibility in floor plan layout and future changes.

Option 3 is similar to Option 2, with a maximum achievable building height of 20 storeys. This is accomplished by utilizing structural wood core walls and introducing exterior structural wood walls. Here, the exterior structural walls have replaced the interior structural walls and perimeter glulam columns in Option 2 (Figure 2.28c).

Finally, Option 4 pushes the maximum building height to 30 storeys. To do so, it utilizes structural core walls, structural interior walls and structural exterior walls (Figure 2.28d). As a result, it offers the least flexibility. As a result, this option is limited in its flexibility and use (Green and Karsh, 2012).

The FFTT system is an example of a novel timber-steel hybrid structural system. The following chapters investigate the FFTT system in detail at the component and structural level.

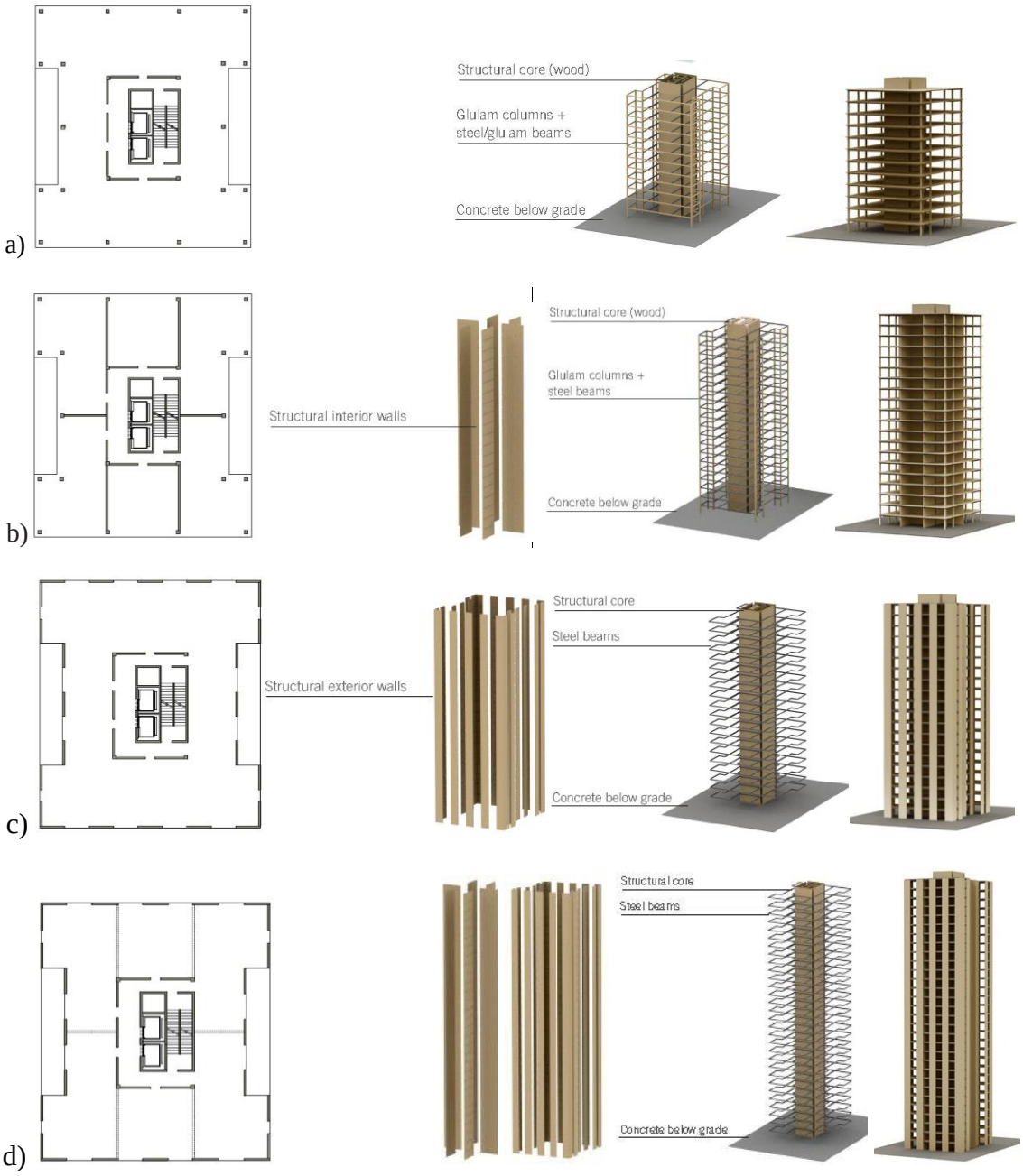

Figure 2.28 Four design option for FFTT system: a) Option 1(up to 12 storeys); b) Option 2 (up to 20 storeys); c) Option 3 (up to 20 storeys); d) Option 4 (up to 30 storeys) (Green and Karsh, 2012)

Chapter 3: Wall-beam Connection Design[1]

3.1 Introduction

As an innovative mass-timber steel hybrid system, the proposed FFTT system has a unique energy dissipation strategy compared to traditional light-frame wood buildings. Using the inherent vertical strength of solid mass-timber panel construction, the FFTT approach is to achieve "strong column/weak beam" mechanism comprising shear walls and moment frames with good ductility and sufficient strength and stiffness to resist all required loading conditions (Green and Karsh, 2012). Figure 3.1 illustrates the strong column/weak beam concept for the FFTT system.

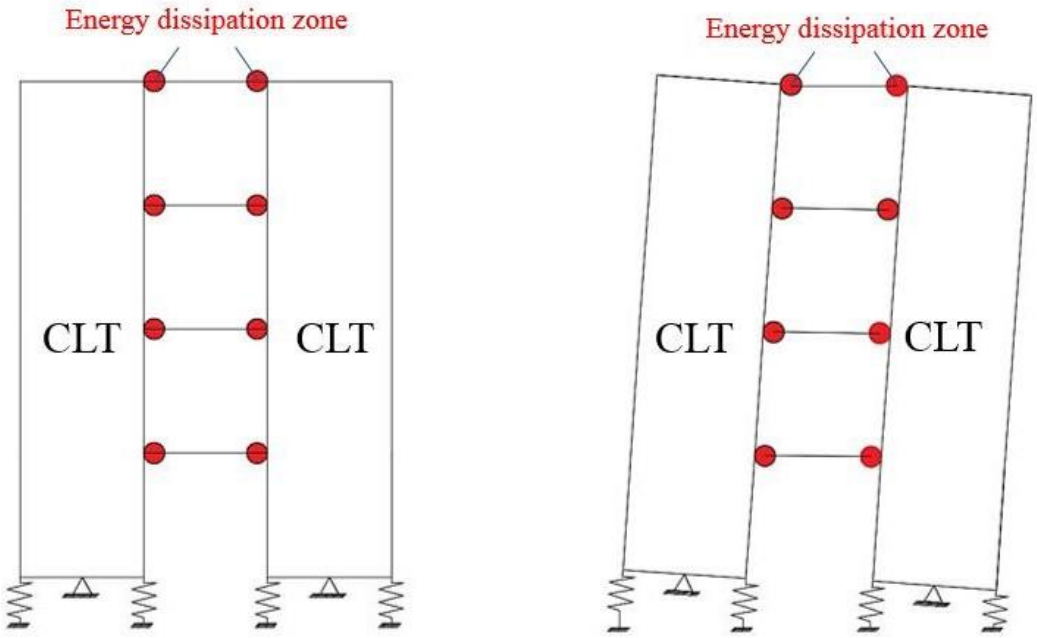

Figure 3.1 The strong column/ weak beam concept for FFTT system

[1] A version of this chapter is accepted for publication in Canadian Journal of Civil Engineering. Zhang X., Azim R., Bhat P., Popovski M. and Tannert T. (2016). Seismic performance of embedded steel beam connection in cross-laminated timber panels for tall-wood hybrid system.

The “strong columns”, in this instance, are large CLT or LSL/LVL panels. The panels are linked together by "weak", but ductile, structural steel beams, for instance, wide flange beams which are proportioned to develop plastic hinges at or near design load levels (as per the principles of capacity design), while providing the required stiffness. These steel beams are embedded into the wall panels, tie the wall panels together, and provide the system with ductility.

Figure 3.2 shows the concept of the mass-timber panel-steel beam interface. According to the Tall Wood report (Green and Karsh, 2012), the steel beams can be designed to have reduced cross-section near the end of the beam, such that the desired hinge locations can be achieved while the majority of the beam stiffness is retained.

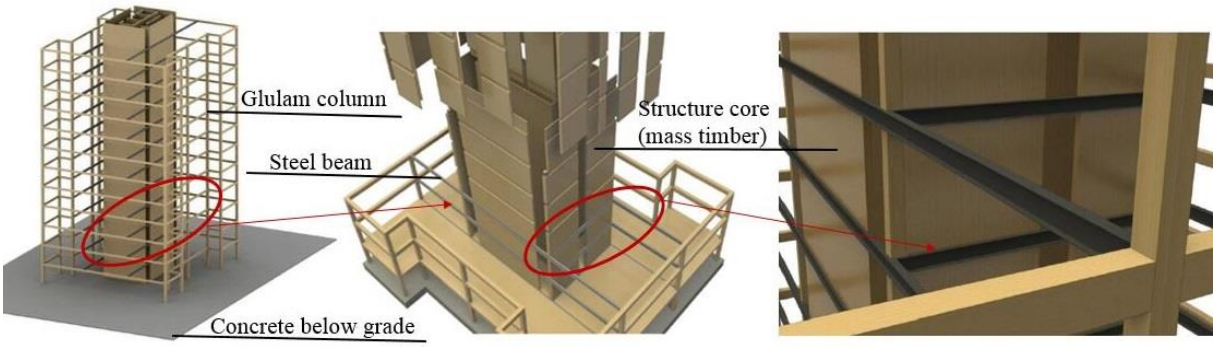

Figure 3.2 The concept of mass-timber panel-steel beam interface

3.2 Objective

As the energy dissipation zones are located at the mass-timber wall-steel beam interfaces, it is essential to understand the cyclic behavior of these connections. In this case, the objective of the research, based on two thesis projects (Bhat, 2013; Azim, 2014; Bhat et al., 2014), is to determine an appropriate layout for the CLT wall-steel hybrid connection and investigate the dynamic behavior together with the energy dissipation of this core connection. To achieve this objective, different layouts were tested under quasi-static monotonic and reversed cyclic loading.

3.3 Description of the connection assemblies

Tests of the FFTT CLT wall-steel beam connection were conducted by Bhat (2013) and Azim (2014) in Structural Laboratory of FPInnovations, Vancouver, to validate the hypothesis of the strong-column/weak-beam failure mechanism of the FFTT system. Also, energy dissipation under cyclic loading was investigated.

Table 3.1: Test configurations

Series	Steel profile	e_l (mm)	e_d (mm)	Reduced Cross Section	Distance between bearing plates (mm)
S1	W 150 (Class II)	900	50	None	No bearing plates
S2	W 150 (Class II)	900	100	None	No bearing plates
S3	W 150 (Class II)	900	100	Yes	No bearing plates
S4	HSS 100	600	50	None	No bearing plates
S5	HSS 100	600/300 [1]	50	None	No bearing plates
S6	W 100 (Class I)	500	100	None	350
S7	W 100 (Class I)	900	85	None	665

Note: [1]) Two different e_1 were investigated: e_1*=600 mm and* e_1*=300 mm*

The test specimens consisted of 7-ply CLT panels, 3,000 mm long, 900 mm wide, and 239 mm thick, with different layouts of the embedded steel beams. Seven test series with different embedment lengths (e_l) and embedment depths (e_d) of the steel beams were designed as summarized in Table 3.1. The embedment length is measured inside the CLT panel in the direction of the steel beam, while the embedment depth is the distance the steel cross section penetrates into the edge thickness of the CLT panel. Figure 3.3 illustrates the schematic form and Figure 3.4 shows a photograph of all the test specimens.

Series S1 and S2 utilized W150×14 Class II wide-flange steel beams, with an embedment depth of 50 mm for S1, as shown in Figure 3.4a, and 100 mm for S2, as shown in Figure 3.4b. For Series S3, the flange width of the Class II steel beam was reduced to 89 mm, resulting in a 16% reduction

in cross sectional area to induce yielding at a lower load level, see Figure 3.4c). Series S4 (Figure 3.4d) and S5 (Figure 3.4e) used HSS (100×50×3.175) steel beams with different embedment lengths (600 mm and 300 mm). Series S6 (Figure 3.4f) and S7 (Figure 3.4g) also utilized wide-flange steel beams, as with S1 and S2, but in this case beams with Class I bending section type were selected (W100×19). Furthermore, steel bearing plates and internal stiffeners (ASTM A992 flat steel 150×100×6.25 mm and 87×50×6.25 mm, respectively) were used in Series S6 and S7 to specify the internal lever arm in the CLT panels and avoid premature buckling of the profile. The installment details of the steel bearing plates and internal stiffeners is shown in Figure 3.4h. Configuration S6 had an embedment length of 500 mm inside CLT panel and an embedment depth of 85 mm. Configuration S7 had a 900 mm embedment length with an embedment depth of 100 mm.

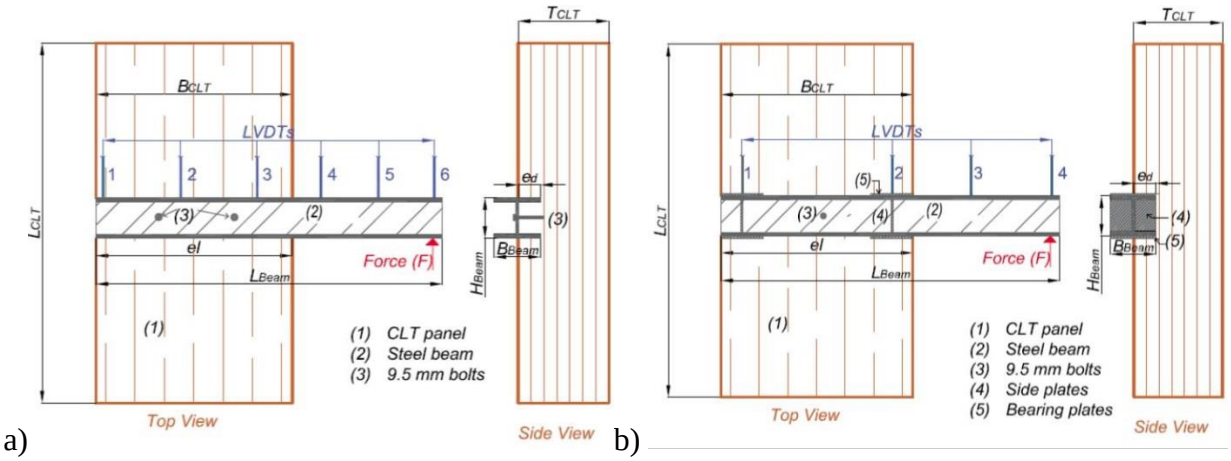

Figure 3.3 Test setup for CLT wall-steel beam connection: a) schematic form for Series S1-S5; b) schematic form for Series S6-S7

a) 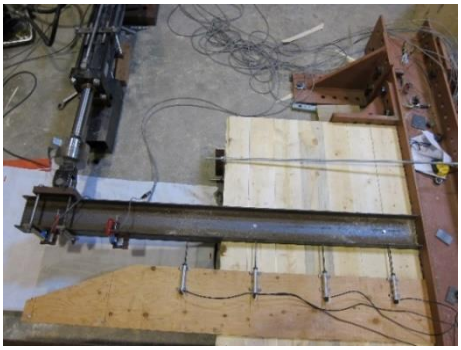 b) 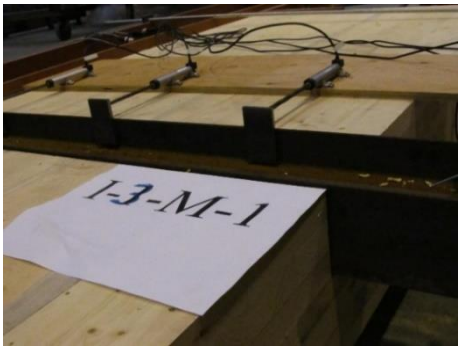

c) 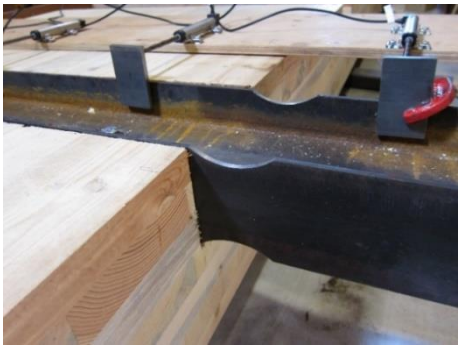 d) 

e) 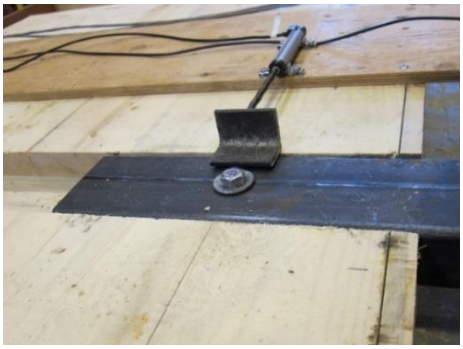 f) 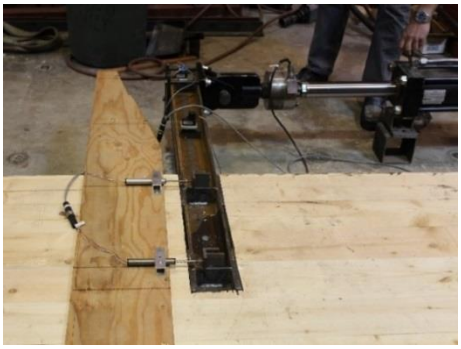

g)  h) 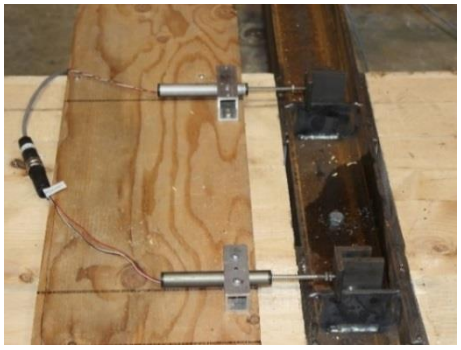

Figure 3.4 Photographs for test series: a) test setup for S1; b) test setup for S2; c) test setup for S3; d) test setup for S4; e) test setup for S5; f) test setup for S6; g) test setup for S7; h) installment detail of the steel bearing plates and internal stiffeners for S6 and S7

The main parameters of the specimens of each test series are summarized in Table 3.1. The beams were placed into pre-cut slots in the CLT panels and held in place using two 9.5 mm lag bolts in pre-drilled holes. Three specimens per test series were produced and subsequently tested.

3.4 Materials

The CLT samples were cut from a commercial product, CrossLam™ SLT3, which meets the requirements of the CLT manufacturing standard ANSI/APA PRG 320 (ANSI/APA, 2011). The CLT panel was produced from SPF (Spruce-Pine-Fir) grades No.1 and No.2 with the two outer layers being 32 mm thick and the five inner layers 35 mm thick each, for a total thickness of 239 mm. The average apparent density of the specimens, calculated based on weight and volume, was 430 kg/m^3. The average moisture content of the specimens measured by moisture meter was 9.4%. The design material properties listed by the manufacturer of the CLT product (Structurlam) used in the project are summarized in Table 3.2 (Bhat, 2013).

For Series S1, S2, S3, S6 and S7, wide-flange steel profiles of ASTM A992 mild-steel with a yield strength of 350 MPa were used. For Series S4 and S5, HSS profiles of ASTM A500 Grade B steel with a yield strength of 300 MPa and a modulus of elasticity of 210 GPa were used.

Table 3.2 CLT properties (Structurlam, 2012)

Properties	Strength (Mpa)
Compressive Strength ($f_{c,0}$)	11.5
Tensile Strength ($f_{t,0}$)	5.5
Bending Strength ($f_{b,0}$ and $f_{b,90}$)	11.8
Shear Strength ($f_{v,0}$ and $f_{v,90}$)	1.5
Rolling Shear Strength (f_{rv})	0.5
Modulus of Elasticity (E_0 and E_{90})	9500

3.5 Methods

The CLT panels were placed horizontally and were bolted to the test floor at both ends to restrain them from translation, rotation or uplift. The load was applied by means of a hydraulic actuator at the end of the projecting steel beam at a distance of 762 mm from the edge of the CLT panel. For test Series S1-S5, six Linear Variable Differential Transformers (LVDT) (labelled 1 to 6) along the steel beam were mounted to measure the relative horizontal displacement between beam and panel, see Figure 3.3a. For Series S6 and S7, four LVDTs were attached to the embedded beam with the first LVDT placed 152.4 mm from the edge of the panel and two LVDTs inside the CLT panel located at the centre of the bearing plates, see Figure 3.3b. The LVDTs placed on the cantilever portion were located 350 mm and 700 mm away from the beam-wall interface.

Both static and cyclic test were conducted using displacement control. In the quasi-static test, a monotonic load was applied at a constant rate of 12.7 mm/minute. This displacement rate created a beam rotation rate of 0.9 ^{0}/min and resulted in a test duration of approximately ten minutes. The loading for the tests was continued until the applied load dropped to 80% of the peak observed load. The applied load and the relative displacements were recorded during testing. In the reversed cyclic loading, the tests followed the CUREE loading protocol according to ASTM E2126-09 method C (ASTM, 2009) with the target displacement chosen as the displacement at peak load from the monotonic test. The loading history starts with six initiation cycles at small amplitudes (5% of the target displacement). Further, each phase of the loading history consists of a primary cycle with amplitude expressed as a fraction (percentage) of the reference deformation and subsequent trailing cycles with amplitudes of 75% of the primary one until test specimens fail. This loading protocol is illustrated as Figure 3.5.

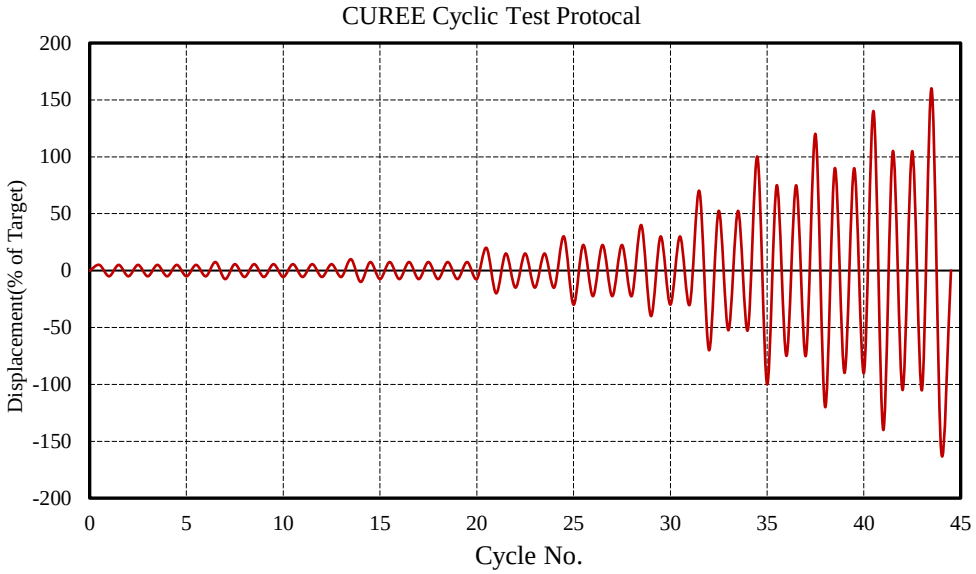

Figure 3.5 CUREE Method C loading protocol (ASTM, 2009)

Two replicates for each series were tested under quasi-static monotonic loading, while a third specimen was tested under reversed cyclic loading. From the recorded applied load (F) and the displacement of the beam (d), the applied moment and the resulting beam rotation were obtained according to Eq. 3.1 where (L) is the length of the beam:

Eq. 3.1

$$M = F \times L; \qquad R = D / L$$

The yield moment (M_Y) and rotation at yield (R_Y), the maximum moment (M_M) together with its corresponding rotation (R_M), as well as the rotation at failure (R_U) when the load dropped to 80% of maximum yielding moment, were determined. The connection stiffness, k, was computed for the loading range of 10% to 40%, as shown in Eq. 3.2:

Eq. 3.2

$$k = \frac{0.4\,M_M - 0.1M_M}{0.4\,R_M - 0.1R_M}$$

The connection ductility, μ, was calculated as the ratio between the rotation at capacity and the yield rotation from the load-displacement curves, as presented in Eq. 3.3:

Eq. 3.3
$$\mu = \frac{R_U}{R_Y}$$

In the reversed cyclic tests, the yield point moment and rotation (M_Y and R_Y) were determined by developing an idealized Equivalent Energy Elastic-Plastic (EEEP) curve based on the first cyclic envelope, following the procedure (Eq.3.4) outlined in ASTM E2126-09 (2009):

Eq. 3.4
$$M_Y = \left(R_u - \sqrt{R_u^2 - \frac{2A}{k}} \right) k$$

Where A is the area under the curve from zero to the ultimate load, and k is the elastic stiffness.

The hysteretic energy dissipated by a system or connection undergoing quasi-static or dynamic loading represents a performance measure when subjected to seismic loads (Karacabeyli and Popovski, 2003). Since there is a positive correlation between the dissipated hysteretic energy and the inelastic deformation demands, stable hysteretic loops with large energy dissipative capacity at the connection level provide a better performance of the system. This is often observed during cyclic tests, where if two systems with similar strength are tested under the same cyclic loading protocol, the one with the higher energy absorption, i.e., "fuller" hysteresis loops, exhibits superior performance. Thus, dissipated energy is a term that has become synonymous to performance. Herein, the total cumulative dissipated energy in the reversed cyclic tests (E) is calculated according to Eq.3.5:

Eq. 3.5

$$E = \sum_{i=1}^{n} A_i$$

Where (A_i) presents the area within the hysteresis loop under each load cycle.

3.6 Results and discussion of monotonic tests

The moment-rotation curves of the steel beams for each test specimen are shown in Figure 3.6. The plots are based on the rotations obtained from LVDT-6 (S1-S5) and LVDT-4 (S6-S7) placed at the cantilever end of the beam. The results are also summarized in Table 3.3. Figure 3.6 illustrates the differences in behaviour between the series which can be grouped into three categories: S1-S2-S3, S4-S5, and S6-S7.

Table 3.3 Summary of monotonic test results

Series	$M_{Y,a}$ [kNm]	$M_{M,a}$ [kNm]	M_Y [kNm]	M_M [kNm]	R_Y [^{0}]	R_M [^{0}]	R_U [^{0}]	k [kNm/^{0}]	μ [-]
S1	31.6	34.6	29.9	33.4	1.5	2.1	3.9	18.2	2.6
S2			31.9	34.4	1.5	2.1	3.9	20.5	2.7
S3			33.4	34.2	1.8	2.0	4.6	16.4	2.6
S4	8.1	12.2	13.1 [1)]	14.1	2.6 [1)]	4.4	9.1	6.9	3.5
S5			13.0 [1)]	14.4	3.4 [1)]	6.1	13.3	5.4	3.9
S6	32.9	37.5	36.9	46.7	1.5	4.5	4.5	31.2	3.1
S7			33.8	40.3	1.8	13.7	14.0	21.7	7.7

Note: [1)] No clearly defined yield point observed in tests

Series S1, S2 and S3, which utilized wide flange steel beams, all exhibited similar stiffness, yield points, and ductility, irrespective of the variations in beam embedment. The different embedment lengths, however, led to differences in failure modes as illustrated in the photos in Figure 3.7.

Connection assemblies with fully embedded beams performed better compared to those with partial embedment. The beam yielding occurred at the panel-beam interface at the exposed side of the top (tension) flange, while the in-plane movement of the beam caused negligible wood crushing at the interface. In case of assembly S1, the tendency of the beam to deform out of the loading plane beyond yielding resulted in the pull-out of wood material below the embedded portion of the beam near the wall-beam interface (Figure 3.7a). In the case of S2, not much wood pull-out occurred beneath the embedded beam, however a crack in the layer below the embedded beam was observed (Figure 3.7b). The yielding of the beam led the cantilever end to lift up near the interface (Figure 3.7c) but no wood crushing in the panel or at the interface was observed. Assembly S3 (reduced cross section) showed an increase in yield and ultimate rotation. Beam yielding occurred at the point of cross-section reduction at the exposed side of the top flange (Figure 3.7d). Overall, the differences between Series S1-S3 were relatively small. Post-yielding, the stiffness quickly degraded and changes in the embedment depth did not have any effect. With an average ductility of 2.6, the wide flange beams in Series S1-S3 do not facilitate ductile behaviour.

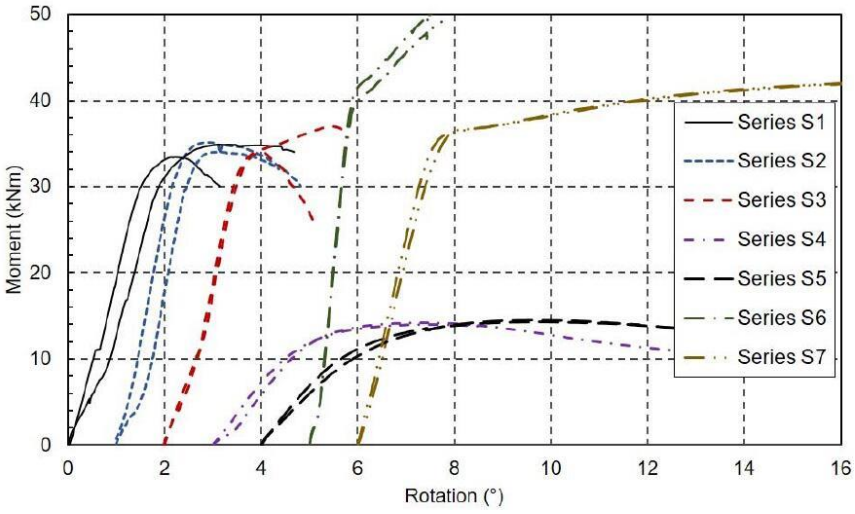

Figure 3.6 Force-displacement curve for all the test series under monotonic loading

Series S4 and S5 utilized hollow section steel beams with different embedment lengths and exhibited different behaviour compared to the other series. Yield moment, ultimate moment and stiffnesses of these two series were significantly lower. Beam yielding of the HSS sections occurred at the beam-wall interface at a bending moment of that was only 40% of that of the assemblies with wide flange steel beams. The stiffness was also significantly reduced; ductility, however, was higher for the assemblies in Series S4-S5. The connection assemblies were able to retain the load carrying capacity long after yielding and displayed a flat post-yield curve. The maximum rotations increased more than three times compared to the wide flange I-sections. Due to the uniform bearing on the CLT panel, yielding occurred symmetrically on both faces (Figure 3.7e). Neither beam uplift nor withdrawal of lag bolts was observed. However, wood crushing of up to 10 mm was recorded at the interface in the layer with grain orientation perpendicular to the load (Figure 3.7f).

Assemblies in Series S6 and S7 utilized small cross section wide flange steel beams with additional steel bearing plates. The obtained yield moment, ultimate moment, stiffness and ductility for these assemblies were higher compared to the other test series. Both S6 and S7 series exhibited well defined yield points (Figure 3.7h) at similar bending moments. The ultimate moment and stiffness for S6 was slightly higher than that for S7. As can be seen from Figure 3.6, the S7 configuration could also undergo larger rotations than S6 leading to increased ductility. In both cases, the deformations inside the CLT panel were small (around 2 mm). However, the S6 series exhibited rolling shear failure in the CLT panel because the flanges penetrated into the fourth layer of the CLT panel oriented perpendicular to the grain, see Figure 3.7g. The partial embedment in Series S7 helped to avoid this undesirable failure mode and led to a significant increase in ductility.

a)  b) 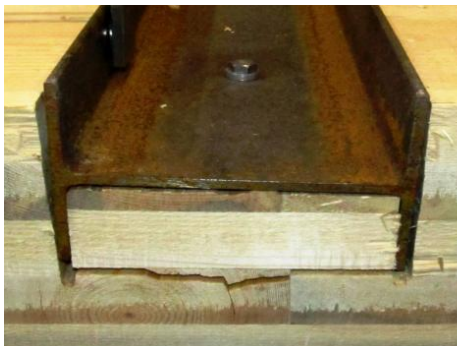

c)  d) 

e)  f) 

g)  h) 

Figure 3.7 Failure modes after test: a) S1 pull out of wood; b) S2 timber cracking; c) S2 beam uplift; d) S3 bucking of the steel beam; e) S4 yielding of the steel beam; f) S5 yielding and crushing; g) S6 steel beam yielding and rolling shear ; h) S7 steel beam yielding

Table 3.3 includes a comparison between the experimentally observed yield and maximum moments and the calculated yield and maximum moments, considering full plastic cross sections. While for the Class II cross section of Series S1-S3, both the yield and the plastic moment are in very close agreement with the expectations, some discrepancies in the connections with HSS were observed. The moment-rotation curves of the HSS section in Series S4-S5 did not exhibit a clear yield point but a slow deviation from linearity; the experimentally determined maximum moment, however, was relatively close to the theoretical plastic moment. For Series S6-S7, clearly defined yield points were observed and the experimental and theoretical yield moment were in good agreement. The plastic moment, however, was significantly lower than the experimentally obtained maximum moment, which can be explained by the fact that buckling was prevented by adding steel plates.

3.7 Results and discussion of reversed cyclic tests

The moment-rotation curves obtained from the cyclic tests are illustrated in Figure 3.8; the results obtained from the positive and negative first cycle envelope curves are summarized in Table 3.4. The failure modes were similar to those observed in the monotonic tests (Figure 3.7).

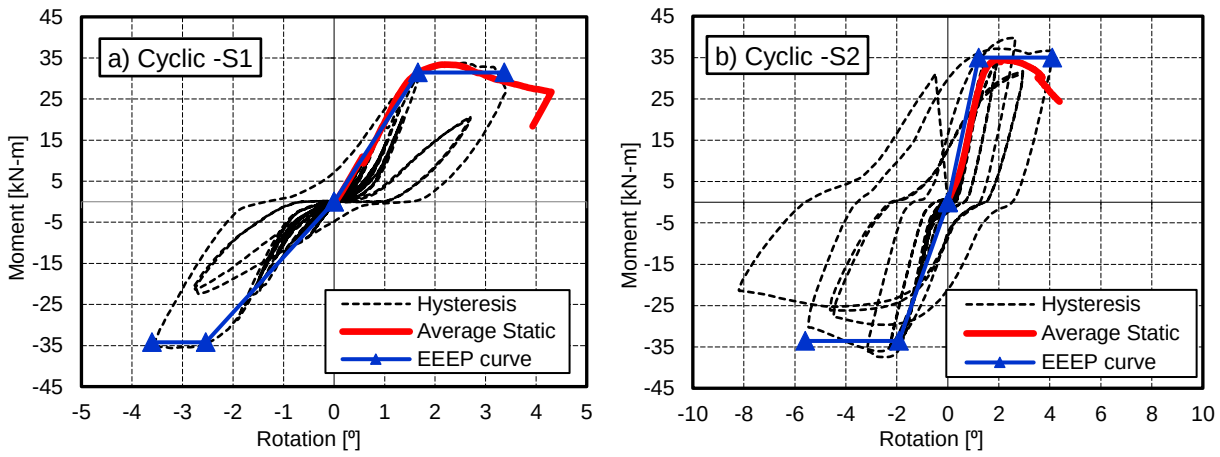

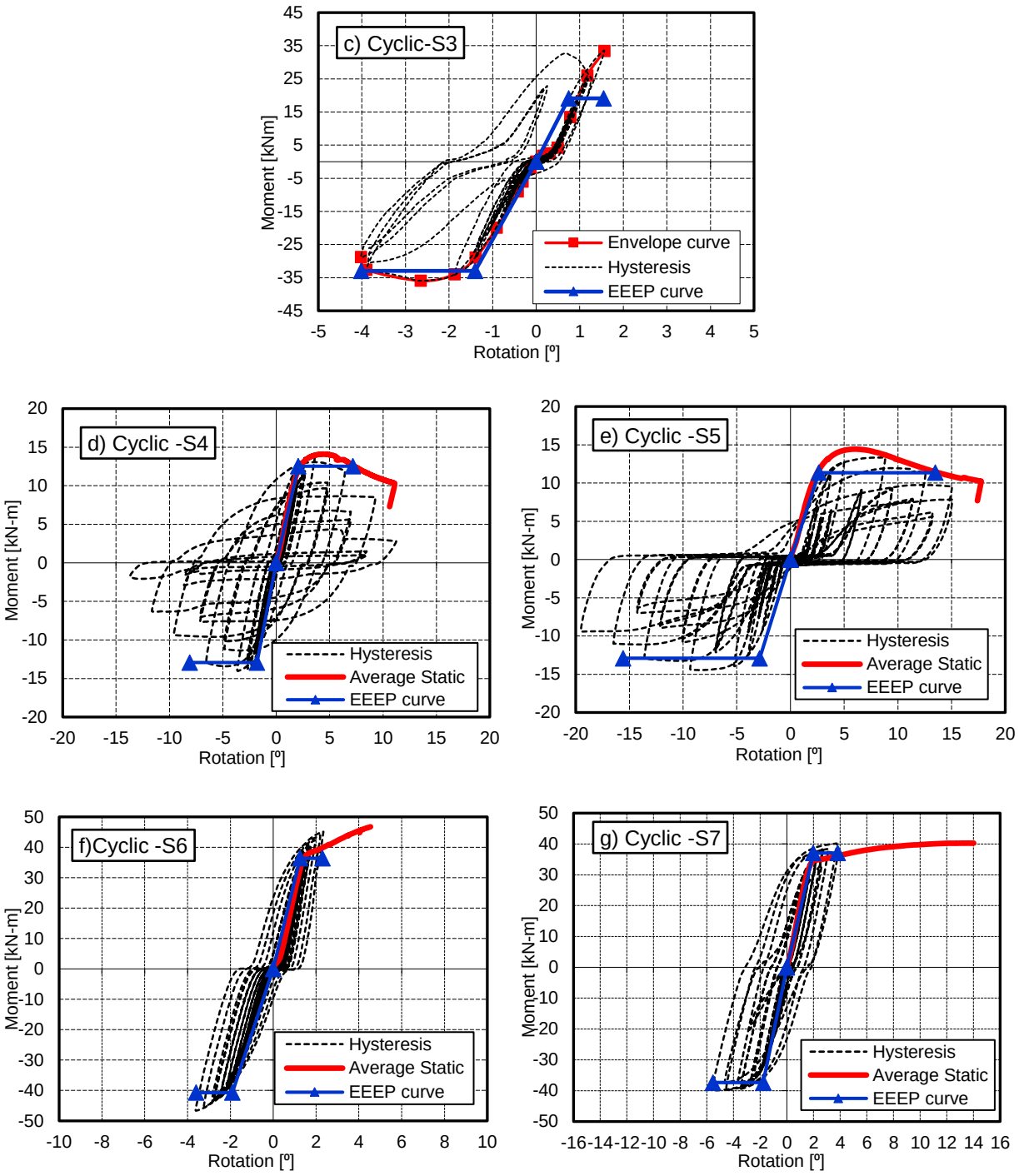

Figure 3.8 Moment-rotation curve from reversed cyclic test: hysteresis loop for a) S1; b) S2; c S3; d) S4; e) S5; f) S6; g) S7

Table 3.4 Summary of reversed cyclic test results

	M_Y [kNm]	M_M [kNm]	R_Y [^{0}]	R_M [^{0}]	R_U [^{0}]	k [kNm/^{0}]	μ [-]	E [kNm^0]
S1	31.5	33.8	1.7	2.6	3.4	19.0	2.0	219
	-34.2	-35.6	-2.5	-3.2	-3.6	-15.0	-1.4	
S2	35.0	39.9	1.2	2.6	4.1	29.0	3.4	1091
	-33.6	-37.1	-1.9	-2.4	-5.6	-17.5	-2.9	
S3	-	33.2	0.7	1.6	1.6	25.7	2.1	255
	-33.0	-36.1	-1.4	-2.6	-4.0	-23.5	-2.9	
S4	12.5	13.7	2.1	3.6	7.2	6.1	3.5	1211
	-12.9	-13.9	-1.8	-3.6	-8.1	-7.2	-4.5	
S5	11.4	13.3	2.7	8.5	13.5	4.3	5.1	1609
	-12.9	-14.5	-2.9	-9.0	-15.6	-4.5	-5.5	
S6	36.4	45.1	1.3	2.3	2.3	21.4	1.8	746
	-40.7	-46.7	-1.9	-3.6	-3.6	-21.4	-1.9	
S7	37.1	40.2	1.9	3.7	3.8	18.7	2.1	1386
	-37.4	-40.5	-1.8	-5.4	-5.6	-21.1	-3.1	

Note: - minus sign indicates values for negative side of the hysteresis loop

The moment capacity and stiffness of the embedded steel beam connection for all seven test series followed a similar trend as observed in the monotonic tests. While capacity, stiffness and ductility were similar for assemblies of Series S1-S3, the dissipated energy in Series S2 was significantly (four times) higher than that for Series S1 and S3. This suggests that reduction of the embedment depth (S1) or reduction in the beam cross section (S3), leads to less-desirable performance. The behaviour under cyclic loading confirmed that the beam plastification is the most important factor contributing towards the ductility of the assembly. The CLT panels behaved as rigid members and resisted in-plane deformation under the beam bearing, dissipating little energy. Series S1 underwent the fewest cycles before failure occurred as the pull-out of the embedded portion of the beam. Loading was continued only until 70% of the target displacement since the lag bolts began withdrawing before the onset of beam yielding. The yield and maximum moments were similar

between positive and negative sides but the stiffness and ductility on the positive side were slightly higher. Significant wood pull-out was observed in Series S2. The cyclic load was continued until achieving 100% of target displacement. Since the actuator was not anchored, significant uplift and yielding out of plane was observed at the cantilever end of the beam. The cyclic loading for Series S3 was continued until achieving 100% of target displacement. The stiffness is the highest among S1-S3, but the ductility is similar to Series S1. The embedded end of the beam was properly held in place. The eccentricity due to the non-symmetric beam yielding in assemblies S2 and S3 resulted in out-of-plane buckling and decreased the in-plane deformation capacity of the system.

Series S4 and S5 were tested with a smaller HSS section, and hence, exhibited lower yield and ultimate moments. These sections, however, do provide significantly higher ductility and showed no decrease in ductility when comparing their cyclic tests to their monotonic tests. Furthermore, the large deformation capacity of these beams also increased their energy dissipation capacity. The hysteresis loops were large, implying a connection with adequate energy dissipation capacity for the desired seismic application. The hysteretic behaviour of the beam in the embedded portion was linear and the nonlinearity in the system was provided by yielding at the beam-CLT interface and in-plane deformation of the cantilever portion of the beam. Series S5, which utilized beams with reduced embedment length, did not lead to any differences in yield and ultimate moment. However, the reduced embedment length led to wood crushing and subsequent pinching in the hysteresis loops.

Series S6 and S7 reached higher moment capacities and stiffnesses because of the use of the Class I W sections along with steel bearing plates and side plates. These Class I W sections were able to achieve full plasticity and were able to maintain their plastic moments over larger rotations. For Series S6, the cyclic loading was continued until achieving 150% of target displacement. The

failure mode in this case consisted of rolling shear in the fourth laminate of the CLT panel along with crushing of wood. This undesirable failure mechanism was caused by the larger loads that the beams transferred before buckling and was avoided in Series S7 by adding steel bearing plates. The larger lever arm produced by the longer embedment and the fact that the steel beam did not end close to the weak CLT cross layer facilitated this behaviour. The load for Series S7 was continued until 160% of target displacement and the assembly behaviour was more ductile, with typical steel hysteresis loops, implying that the connection is able to provide adequate performance for seismic applications. While the capacity and the stiffness were purely driven by the beam cross section and were very similar between Series S6 and S7, the partial embedment used in Series S7 lead to higher ductility and energy dissipation.

3.8 Summary

This Chapter presented experiments conducted on steel-wood connections which are the main energy dissipating component of the novel FFTT steel-timber hybrid system. Full-size 7-ply CLT panels with embedded steel beams were tested under quasi-static monotonic and reversed cyclic loading to investigate the effects of the chosen beam profile (wide flange W and hollow rectangular sections), and beam embedment length and depth (partial and full embedment). From the results presented in this chapter the following main conclusions can be drawn:

1) The connection assemblies comprising embedded steel beams were able to obtain the desired ductile beam failure mechanism at the CLT wall-beam interface;

2) The type of steel section had a significant impact on performance of the assemblies; wide flange W sections achieved much higher moment capacity than HSS sections. HSS sections, however, provided much higher ductility and were not prone to out-of-plane buckling;

3) The use of Class I wide flange cross sections, in addition to steel bearing plates, provided the best performance of any tested wide flange steel bam assembly. In this case, high capacity and stiffness were achieved along with a moderate ductility;

4) The embedment depth of the steel beam was also an important factor that influenced the behaviour of the assemblies. To avoid local rolling shear failure in the CLT, the edge of the steel beam should not end in a perpendicular CLT layer. The tested assemblies with smaller embedment depths combined with full embedment lengths exhibited superior performance to those with larger embedment depth, but reduced embedment length; and

5) The connection performance in the cyclic tests was similar in terms of yield and maximum moment and stiffness to that obtained during the static tests. Most of the energy was dissipated as a result of the deformation of the cantilever portion of the embedded steel beam. The ductility obtained during the cyclic tests, however, was lower than that obtained during the static tests.

To summarize, the CLT wall to steel beam connection tests demonstrated that appropriate connection layouts can lead to the desired failure mechanism while avoiding excessive crushing of the mass-timber panels. The tests also confirmed the feasibility of the energy dissipation strategy in the concept design of the FFTT timber-steel hybrid system. HSS steel beam sections were shown able to provide the desired hysteretic behaviour with the highest ductility, which is essential in the seismic design of timber-based hybrid structures. While the wide flange steel beams with steel bearing plates also can provide relatively high ductility and high strength.

Chapter 4: High Capacity Hold-down Design[2]

4.1 Introduction

To provide resistance against the overturning moment induced by lateral wind or seismic loads, anchors or "hold-downs" are installed to transfer vertical forces to the foundation in timber structures. Compared to steel and concrete, timber is a light material, leading to possible reduction in foundation costs, and lower lateral seismic forces. But the low self-weight of timber structures provides less inherent resistance against overturning forces and can cause stability problems. As a consequence, one challenge with constructing tall wood buildings is to anchor the large uplifting forces from lateral loads. The overturning resistance for tall timber structures needs to be addressed, either by reducing the uplift forces or by developing hold-down solutions.

Different types of anchorage systems are currently available for wood construction. For one- and two-storey wood structures, the conventional solution is straps, or hold-downs, that emerge from the foundation and are nailed to shear walls, as shown in Figure 4.1a. Others options include foundation bolts or threaded rods. Usually, the maximum capacity of traditional hold-downs is around 50 kN. With the growth in multi-storey wood-framed structures, rod systems have become an increasingly popular solution for these larger structures. Figure 4.1b shows a Simpson Strong-Tie® Strong-Rod™ system (Simpson Strong Tie Ltd., 2015) which can transfer loads of up to 120 kN, while maintaining reasonable costs on materials and labor. Instead of using metal brackets,

[2] A version of this chapter has been submitted to Construction and Building Material. Zhang, X., Tannert, T. and Popovski M. (2016). High-capacity Hold-down for Tall Timber Buildings. (Under Review)

continuous tie-down systems consist of rods, coupler nuts, bearing plates and shrinkage-compensation devices that create a continuous load path to the foundation.

Figure 4.1 Hold-downs for timber structures: a) Traditional option; b) Strong-Rod™ (Simpson Strong-Tie Ltd.); c) Tube connector (Schneider et al., 2014)

The uplift forces will be much larger for high-rises buildings, and these hold-downs will not be able resist them. Consequently, high-capacity hold-down solutions that maintain structural integrity need to be developed. A novel round tube connector was proposed by Schneider (Schneider, 2015; Schneider et al., 2014), as shown in Figure 4.1c. This connector consists of hollow steel tubes placed inside mass-timber panels. Quasi-static monotonic and reversed cyclic testing demonstrated that this novel connection prevents damage to the wood, has high initial stiffness, and provides a high level of ductility.

4.2 HSK-System

Another potential option is the Holz-Stahl-Komposit-System (HSK-System)™, which is based on adhesively bonded perforated steel plates. The geometric parameters of the perforated steel plate are shown Figure 4.2a. The holes in the plate are filled by the adhesive after inserting it into the

wood, forming so-called “Adhesive Dowels” (AD). The “bond capacity” is based on the sum of the individual adhesive dowel capacities. The Steel Links (SL) between the plate holes determine the plate capacity. The capacity of an HSK connection is governed by the minimum of: i) the steel plate, ii) the adhesive bond, and iii) the wood capacity. Previous research showed that the connection is stiff, ductile and can be designed to produce a ductile steel failure mode under static as well as fatigue loading (Bathon et al., 2014).

a) 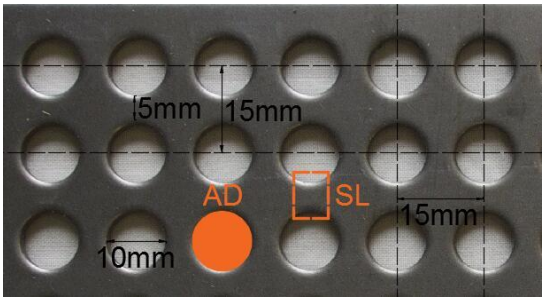

b) 

Figure 4.2 HSK connection: a) Geometry of perforated steel plate; b) Conventional HSK hold-down

Figure 4.2b shows the conventional HSK hold-down design. The perforated steel plates are welded to reduced section steel side plates which provide a ductile fuse for capacity design. The most famous application of the HSK plates is in the 5 storey free-floating cantilevered solid timber staircase of the Earth and Ocean Science Centre in UBC, Vancouver (Karsh and Gafner, 2012). The connector has also been utilized in tall building projects such as the Wood Innovation Design Centre in Prince George, which is currently North America’s tallest contemporary pure wood building (Poirier et al., 2016). Another application of the HSK system was in a wooden wind mill tower with a total height of 100 m (Harms et al., 2012).

4.3 Objective

For timber-based high-rise structures, hold-downs must be strong and stiff enough to resist the large uplifting forces, but also provide ductility for energy dissipation. The HSK hold-down provides high stiffness and strength, but so far has only been applied in tall wood structures located in low seismic areas, partially due to the lack of research under reversed cyclic loading, a situation where the reduced section steel side plates could potentially buckle. The objective of this chapter is to design a modified HSK hold-down. To achieve this objective, material and component level tests, as well as mid-scale and full-scale hold-down tests were conducted under quasi-static monotonic and reversed cyclic loading conditions.

4.4 Hold-down using modified HSK system

The HSK system is modified by attaching the perforated plates to a steel profile which does not have a reduced section, as illustrated in Figure 4.3c. The yielding fuse is provided by a section of plate where duct-tape is used to cover rows of holes in the perforated steel plate, as shown in Figure 4.3a, such that in these rows no adhesive bond can form, shown in Figure 4.3b. This modification allows for a yield mechanism to develop inside the connection assembly which will be restrained from buckling.

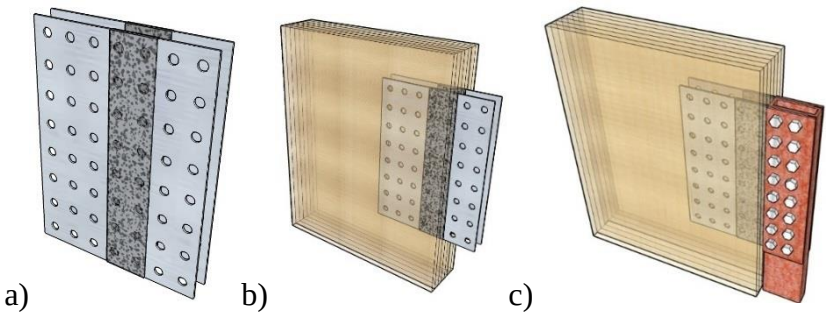

Figure 4.3 Modified HSK hold-down: a) Use of Duct Tape; b) Inserted into CLT panel; c) Complete system

4.5 Materials

The perforated steel plates have a uniform pattern, with hole diameters of 10 mm, length of the steel links between holes of 5 mm, and plate thickness of 2.55 mm, as illustrated in Figure 4.2a. The steel grade was S275 with specified yield stress of 275 N/mm^2 (BS EN 10025). Two of the test series: Series 1-3a and Series 1-4, were fabricated using Douglas-Fir (*Pseudotsuga menziesii*) 20f-E grade glulam; the rest of specimens were fabricated using 3-ply CLT panels, grade V2M1. The CLT panels (3-ply, 5-ply, and 7-ply) were supplied by Structurlam Products Ltd. and fabricated according to ANSI/APA PRG 320-2012 (APA, 2012), as shown in Figure 4.4a. The wood species was Spruce-Pine-Fir (SPF) No.1/No. 2, with a density of approximately 450 kg/m^3. The moisture content of the wood products was determined by means of handheld electric resistance meters and resulted in an average value of 10% (+/-2%). 3M® Scotch Cloth 220 duct tape (Figure 4.4b) was selected to cover part of the perforated steel plates. 6 mm thickness Polyethylene Vapor Barrier sheets (plastic sheet), which meet the Canadian Standard (CAN/CGSB-51.34-M86, 1996) were applied between the wood panels to reduce the friction, as shown in Figure 4.4c. The applied adhesive was CR-421 by Purbond® (two-component polyurethane-PUR), commonly used for on-site applications, with a viscosity of 4,000 cps, an open work time of 10-20 min and an expected shear strength when bonded to wood of around 3.6~7.8 MPa (Gonzales et al., 2016).

a)  b)  c) 

Figure 4.4 Required materials: a) CLT panel; b) Duct tape; c) Plastic sheet

4.6 Material level tests

4.6.1 Overview

Before testing the modified hold-down, the HSK basic structural characteristics were validated based on four different test series: 1) tension tests of the perforated steel plates to determine their yield and maximum strength (Series 1-1); 2) half cycle reversed tests on perforated steel plates to determine their ductility and energy dissipation (Series 1-2); 3) tests to determine the strength of the adhesive bond (Series 1-3); and 4) tests to confirm the connector properties (Series 1-4).

4.6.2 Methods

For Series 1-1 and 1-2, the steel plates were clamped into the test machine, as shown in Figure 4.5a. The displacement controlled load was applied at 2 mm/min, and the applied force and displacement were recorded until the test specimens failed. For Series 1-2, 80% of the maximum displacement from the monotonic test was used as the target displacement and a half cycle CUREE loading protocol (ASTM E2126-09, 2009), as shown in Figure 4.5b, with 2mm/min, was used. All tests were carried out in the Material Laboratory at the University of British Columbia Vancouver (UBC) utilizing a INSTRON® material testing machine (250 kN capacity).

a)  b) 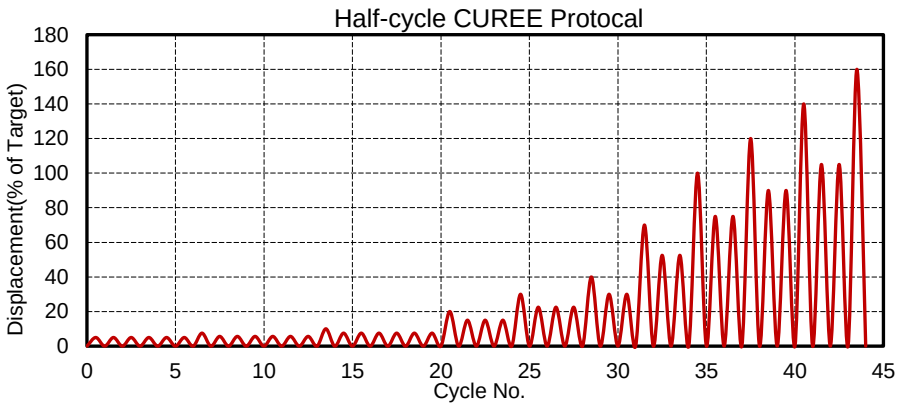

Figure 4.5 a) Test setup; b) Half-cycle CUREE loading protocol

The preparation of specimens for Series 1-3 and 1-4 consisted of three steps: 1) cutting a slot into the timber specimen with a length equivalent to the HSK plate length; 2) gluing the steel plate into the slot; and 3) curing of the test specimen. For Series 1-3a-c, the depth of the slot was cut to 32.5mm in order to embed two lines of three rows of holes for a total of 6 adhesive dowels, as shown in Figure 4.6a. Glulam wood panels were used in Series 1-3a; the HSK plates in Series 1-3b and Series 1-3c were inserted into a perpendicular and parallel layer of the CLT panel, respectively. For Series 1-3d, the slot was cut to 47.5 mm in order to embed three lines of three rows of holes for a total of 9 adhesive dowels and the HSK plate was inserted into a perpendicular layer of the CLT panel, as shown in Figure 4.6b. For Series 1-4, the slot in the glulam beam was cut to 77.5 mm to embed five lines of three rows of holes for a total of 15 adhesive dowels, as shown in Figure 4.6c. Figure 4.6d shows the setup for the material level tests and Table 4.1 summaries the series parameters.

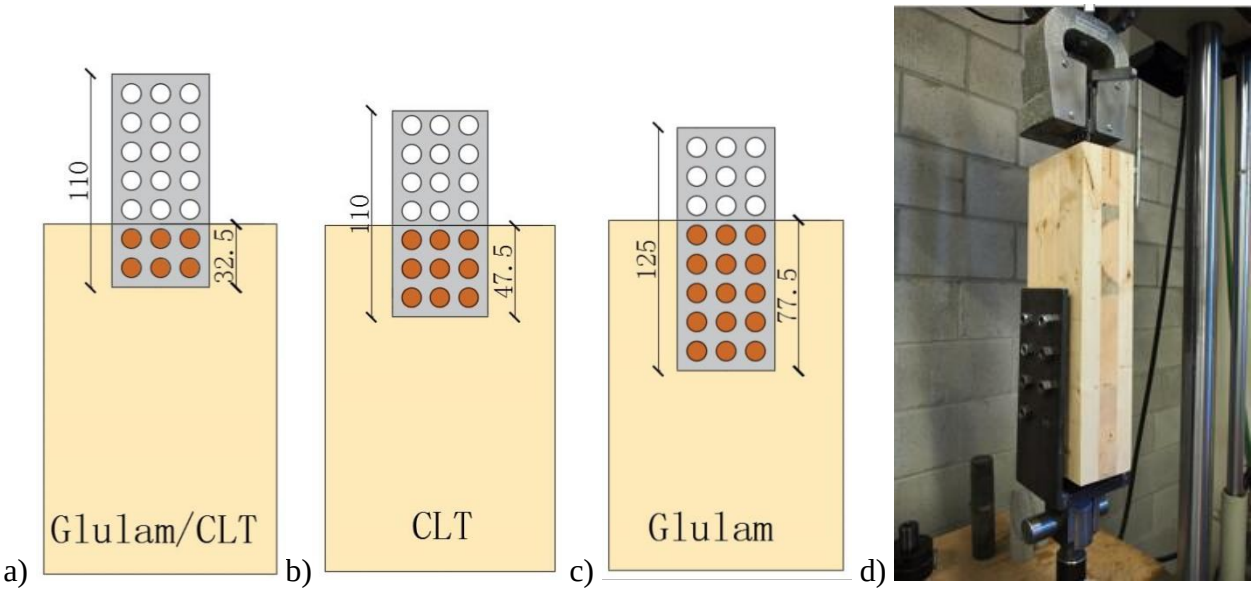

Figure 4.6 Material level test setup: a) Specimen configuration for Series 1-3a-c; b) Specimen configuration for Series 1-3d; c) Specimen configuration for Series 1-4; d) Test set-up for Series 1-3/4

Table 4.1 Series in material level tests

Series		#SL	#AD	Wood	Embedment direction.
1-1		2.0 ~ 3.3[1)]	0	-	-
1-2		4.0	0	-	-
1-3	a	4.0	6	Glulam	Parallel
	b	4.0	6	CLT	Perpendicular
	c	4.0	6	CLT	Parallel
	d	4.0	9	CLT	Perpendicular
1-4		3.4[1)]	15	Glulam	Parallel

Note: [1)] The number of SL is calculated based on the actual specimen geometry after cutting of the steel plates

From the recordings of load and displacement, the elastic stiffness, K_e, and ductility, μ, were calculated using Eq. 4.1 and Eq. 4.2, respectively, where F_y represents the yield force, D_y the yield displacement, F_{max} the maximum force, D_{max} the corresponding displacement; and D_u the ultimate displacement (when the force drops to 80% of its maximum).

Eq. 4.1
$$K_e = \frac{0.4F_{max} - 0.1F_{max}}{0.4D_{max} - 0.1D_{max}}$$

Eq. 4.2
$$\mu = \frac{D_u}{D_y}$$

4.6.3 Results

Table 4.2 summarizes the obtained results from the material level tests. In addition to the total values, the obtained yield force of one SL under tensile loading ($F_{y,SL,t}$), the maximum force of one SL steel link under tensile loading ($F_{max,SL,t}$), and stiffness of one SL under tensile loading ($K_{e,SL,t}$) are included to demonstrate the similarities between Series 1-1 and Series 1-4.

Table 4.2 Results from material level tests

Series	Replicate	# SL	# AD	F_y [kN]	F_{max} [kN]	K_e [kN/mm]	μ [-]	$F_{y,SL,t}$ [kN]	$F_{max,SL,t}$ [kN]	$K_{e,SL,t}$ [kN/mm]	$F_{max,AD}$ [kN]
S1-1	I	2	0	7.1	8.4	5.2	3.8	3.6	4.2	2.6	-
	II	2	0	7.4	9.0	5.5	4.0	3.7	4.5	3.2	-
	III	3.1	0	10.9	13.2	6.2	3.0	3.5	4.3	2.0	-
	IV	3.2	0	11.4	13.9	7.4	3.8	3.5	4.4	2.3	-
	V	3.3	0	11.6	14.1	7.6	3.5	3.5	4.3	2.3	-
	VI	3.3	0	11.7	14.6	7.5	4.0	3.6	4.4	2.3	-
S1-2	I	4	0	11.9	16.3	13.7	4.9	3.0	4.1	3.4	-
	II	4	0	11.0	16.4	13.1	4.7	2.7	4.1	3.3	-
	III	3.8	0	10.6	15.7	10.9	4.7	2.8	4.1	2.9	-
S1-3a	I	4	6	-	10.2	5.3	1.2	-	-	-	1.7
	II			-	10.4	8.4	1.1	-	-	-	1.7
S1-3b	I	4	6	-	10.2	2.9	1.1	-	-	-	1.7
	II			-	9.2	2.6	1.2	-	-	-	1.5
	III			-	8.3	3.6	1.1	-	-	-	1.4
S1-3c	I	4	6	-	13.2	3.3	1.2	-	-	-	2.2
	II			-	12.1	2.9	1.0	-	-	-	2.0
	III			-	13.1	4.1	1.1	-	-	-	2.2
S1-3d	I	4	9	-	15.0	2.5	1.0	-	-	-	1.7
	II			-	13.1	3.6	1.1	-	-	-	1.5
	III			-	15.2	4.6	1.3	-	-	-	1.7
S1-4	I	3.4	15	11.5	14.2	9.4	3.9	3.5	4.3	2.8	-
	II			12.5	16	9.0	4.2	3.6	4.6	2.6	-

Under quasi-static monotonic tensile loading, the failure of the perforated steel plates (Series 1-1) was yielding of the steel links between the holes, as shown in Figure 4.7a. The recorded load-displacement relationship is illustrated in Figure 4.7b. Under repeated cyclic loading (Series 1-2), the failure mode was similar to Series1-1; see Figure 4.7c. Figure 4.7d shows that the load-displacement followed a typical steel hysteresis. The hysteretic loops of the other two replicates were almost identical and are shown in Appendix A.1.

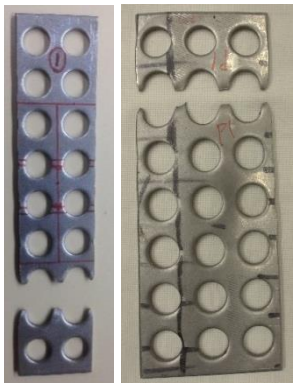

a)

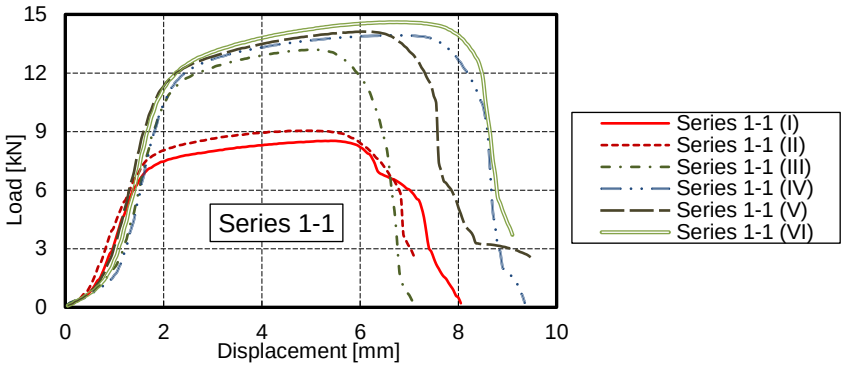

b)

c)

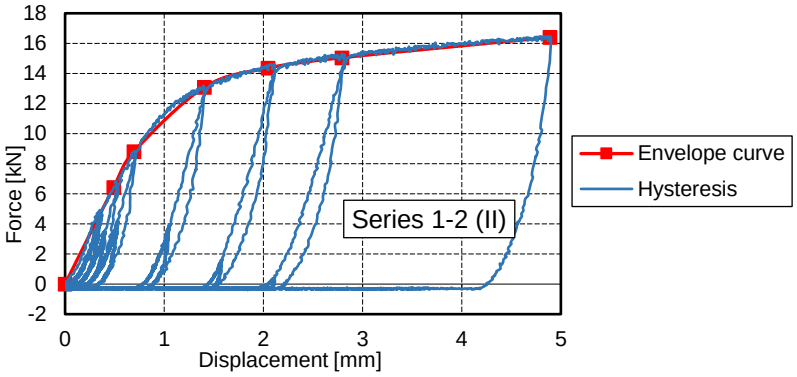

d)

e)

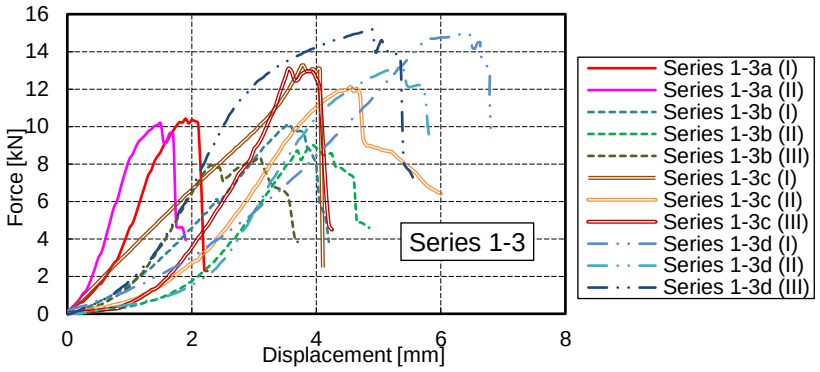

f)

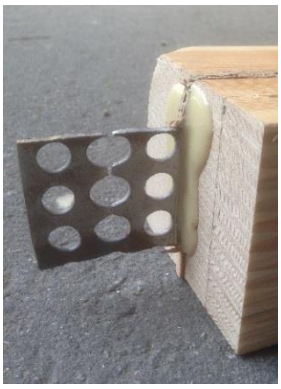

g)

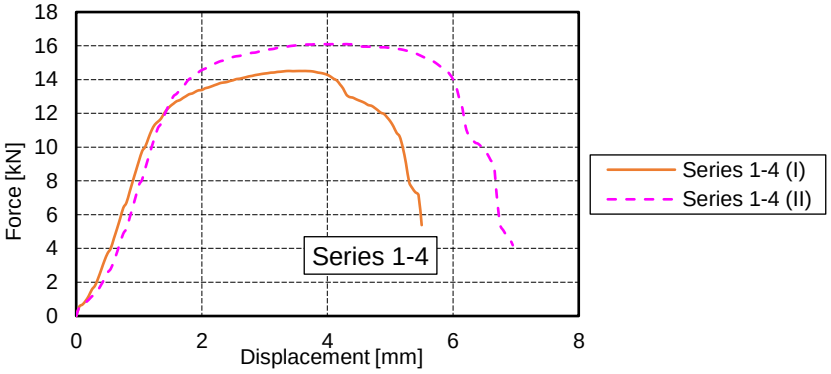

h)

Figure 4.7 Pictures of failed specimens (left) and load-displacement curves of the material level tests (right): Series 1-1 (a and b); Series 1-2 (c and d); Series 1-3 (e and f); Series 1-4 (g and h).

Figure 4.7e shows that the failure mode in Series 1-3 was brittle rupture of the adhesive bond with subsequent pull-out of the steel plate. The force-displacement curve shown in Figure 4.7f confirms the linear elastic behaviour and brittle failure independent of wood and embedment direction in CLT. The capacity depended entirely on the number of embedded adhesive dowels. Series 1-4 was designed to achieve ductile failure governed by the yielding of the steel links. The failure mode was rupture of the steel links, see Figure 4.7g, and the force-displacement curves were ductile, as shown in Figure 4.7h - similar to the tension tests in Series 1-1.

4.6.4 Discussion

The material level tests presented in the previous sections validated the HSK characteristics. In the tension tests on perforated steel plates (Series 1-1), the average yield stress, σ_y, and maximum stress, σ_{max}, for the six replicates were approximately 282 MPa and 345 MPa, respectively, which are appropriate for S275 steel. The yield force, F_y, and maximum force, F_{max}, depended on the number of embedded steel links. Knowing the yield and ultimate strength of the material, it is a straightforward task to cacalute the yield and maximum force for one SL under tensile loading, which were labeled $F_{y,SL,t}$ and $F_{max,SL,t}$, respectively. $F_{y,SL,t}$ and $F_{max,SL,t}$ were determined as 3.6 kN and 4.4 kN, respectively. The stiffness under tensile loading per SL, $K_{e,SL,t}$, was determined to average 2.4 kN/mm.

Series 1-2 tested the perforated steel plates under cyclic loading. Compared to the monotonic results, $F_{y,SL,t}$ and $F_{max,SL,t}$ were slightly lower with values of 2.8kN and 4.1 kN, respectively. This decrease was caused by low-cycle steel fatigue. The large and full shape of the obtained hysteresis loops demonstrated that the steel plate possesses good energy dissipation capacity.

The design capacity based on previous research was 1.2 kN/AD (Bathon et al., 2014). All test specimens in Series 1-3 failed in a brittle mode in the adhesive bond. The average $F_{max,AD}$ was 1.7 kN with slight differences between glulam and CLT. For Series 1-3b and 1-3d, the average $F_{max,AD}$ were similar at around 1.6 kN. The embedment direction in the CLT panel impacted capacity. For Series 1-3c the plates were inserted into the parallel layer of the CLT panel, and the $F_{max,AD}$ showed the highest observed value at 2.1 kN. All AD capacities were significantly higher than the expected capacity of 1.2 kN, allowing for a straightforward design for ductile SL failure.

Series 1-4 was designed to cause failure in the steel links, with 15 AD and 3.4 SL in the tensile loading direction and an expected yield force of approximately 12.2 kN, and expected 15.0 kN ultimate capacity. The tests confirmed that the desired steel failure mode can be obtained when the design AD capacity is larger than the SL capacity. In the tests, $F_{y,SL,t}$, $F_{max,SL,t}$ and $K_{e,SL,t}$ were 3.6 kN, 4.5 kN and 2.7 kN/mm, respectively, almost identical to the values obtained in the steel plate tension tests.

4.7 Component level test

4.7.1 Specimen specification

Since high-rise timber structures will likely rely on the solid nature of the mass-timber panels to provide fire-resistance to the structure, the component level tests used CLT panels. Two different lengths of the perforated steel plates were selected: 1) short plates which include 10 by 8 AD with 11 SL in one row, where the middle two rows are covered by the duct tape, as shown in Figure 4.8a; and 2) long plates which includes 22 by 7 AD with 23 SL in one row, with the one middle row covered by duct tape, as shown in Figure 4.8b.

The manufacturing of the component level specimens consisted of three steps: 1) a 4 mm wide slot was cut in the middle layer of the CLT panels. The slot was placed in the perpendicular to grain direction for the 3-ply panels and parallel to grain direction for the 5-ply panels. The depths of the slots varied based on the dimensions of the steel plates: 62.5 mm for the short plates and 55 mm for the long plates. 2) One half of the perforated plates were glued into the slot of one CLT panel, see Figure 4.8c-d. 3) After one day of curing, the exposed perforated steel plate was glued into the slot of the second CLT panel. To avoid any friction between the two CLT panels, first a layer duct tape and then a plastic separation layer was placed between the panels, as shown in Figure 4.8e. By doing so, any excess adhesive was prevented from bonding the CLT panels together.

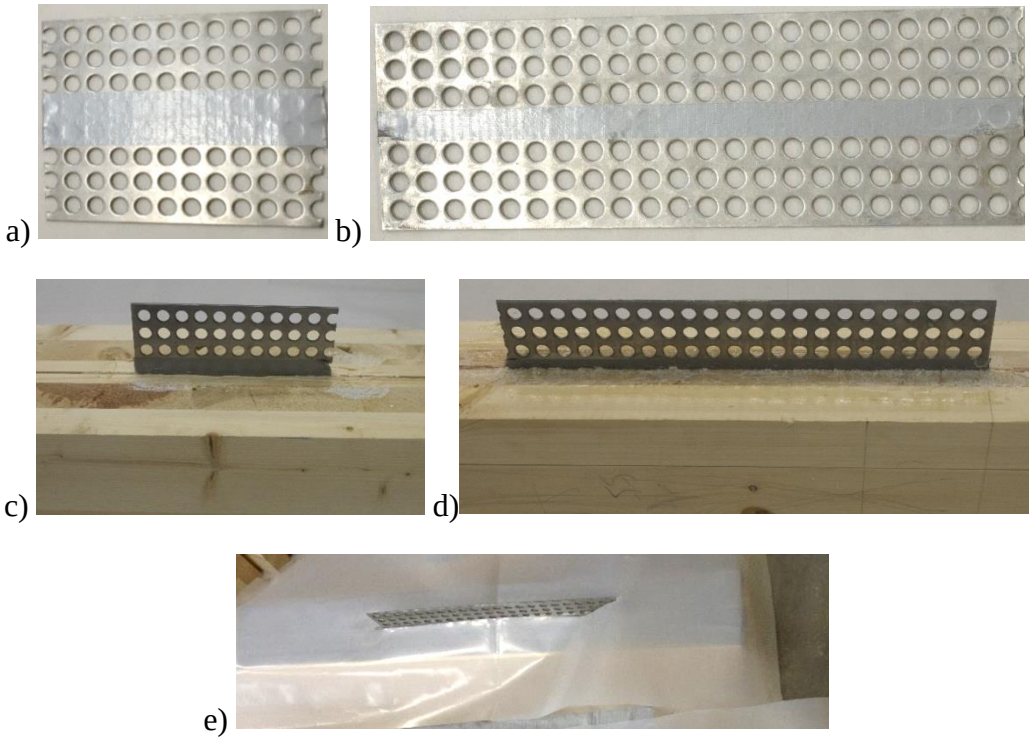

Figure 4.8 Configuration of perforated steel plate: a) Short plate; b) Long plate; c) Embedment of the short plate with two rows covered by duct tape; d) Embedment of the long plate with one row covered by duct tape; e) Duct tape and plastic sheet cover

4.7.2 Methodology for quasi-static monotonic shear tests

To investigate the in-plane shear resistance of the connection (aligning the resultant force of loading and support), the test specimens were rotated 14.5º, similar to the recommendations in EN 408 (CEN, 2012). The tests were performed under displacement-controlled loading with a rate of 2.0 mm/min utilizing a Baldwin® testing machine (400 kN capacity) located in the UBC Structures Lab. The loading for the tests was continued until the applied load dropped to 80% of the peak load. The applied load and the relative displacement between the CLT panels were recorded using LVDT's. A photo of the static test set up is shown in Figure 4.9. Two replicates for the four test series each were fabricated and subsequently tested, see Table 4.3.

Table 4.3 Static test series in component level

Series	Steel Plate dimension	No. of Rows Covered	Loading Direction	No. of replicates
2-1	Short (No. of SL:11)	2	Perpendicular (3-Ply)	2
2-2	Short (No. of SL:11)		Parallel (5-Ply)	
2-3	Long (No. of SL:23)	1	Perpendicular (3-Ply)	2
2-4	Long (No. of SL:23)		Parallel (5-Ply)	

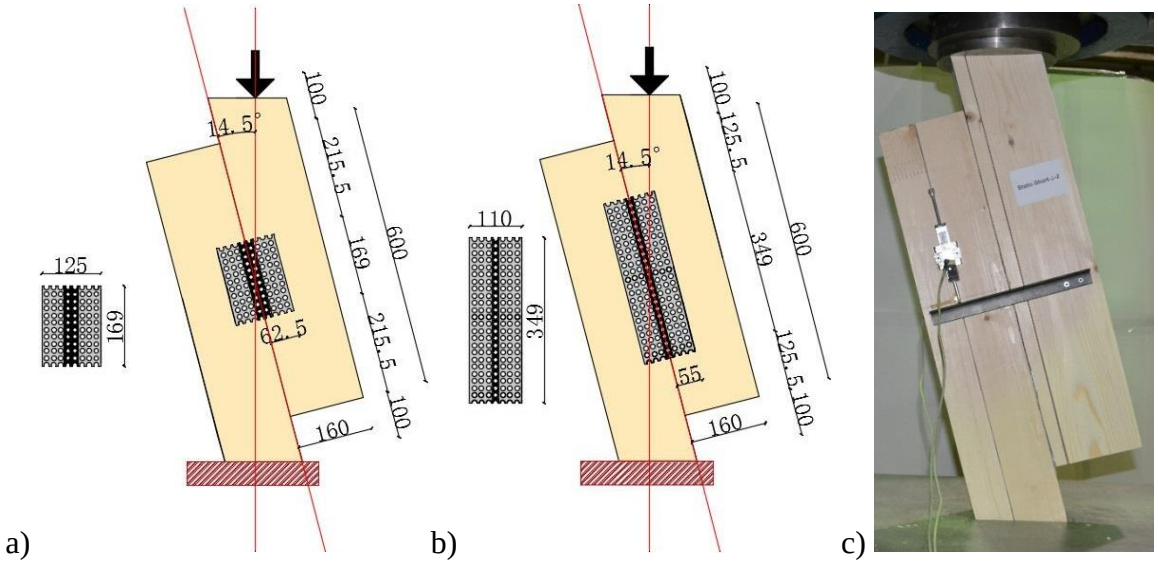

Figure 4.9 Static test setup: a) short plates; b) long plates; c) Photograph of a static test

4.7.3 Results for the quasi-static monotonic shear tests

Specimens with short steel plates where two rows of AD were covered by duct tape reached much larger displacements, reaching maximum values of approx. 30 mm; while the long plate specimens with one row of AD covered by duct tape reached only a 17 mm maximum displacement, see Figure 4.10. These displacements also include the movements of the embedded perforated steel plate.

a)  b) 

c) 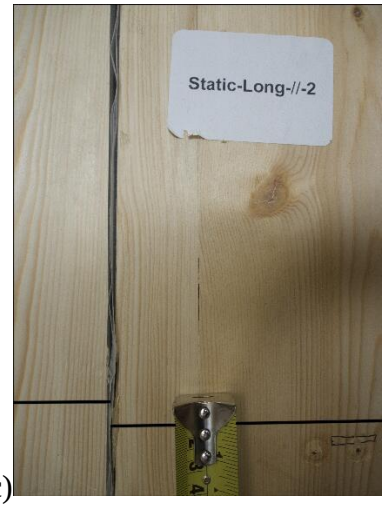

Figure 4.10 Movement between two CLT panels after static test: a) test specimen b) short perforated steel plate and c) long perforated steel plate

The relative load-displacement curves for all specimens (considering only the load-component parallel to the shear plane), are shown in Figure 4.11 This figure illustrates that the failure of the connections was ductile and was governed by the SL capacity. Table 4.4 summarizes the results, along with with $F_{y,SL,s}$, which represents the yield force for one SL under shear loading; $F_{max,SL,s}$, which represents the maximum force for one SL under shear loading; and $K_{e,SL,s}$ which represents the shear stiffness for one SL.

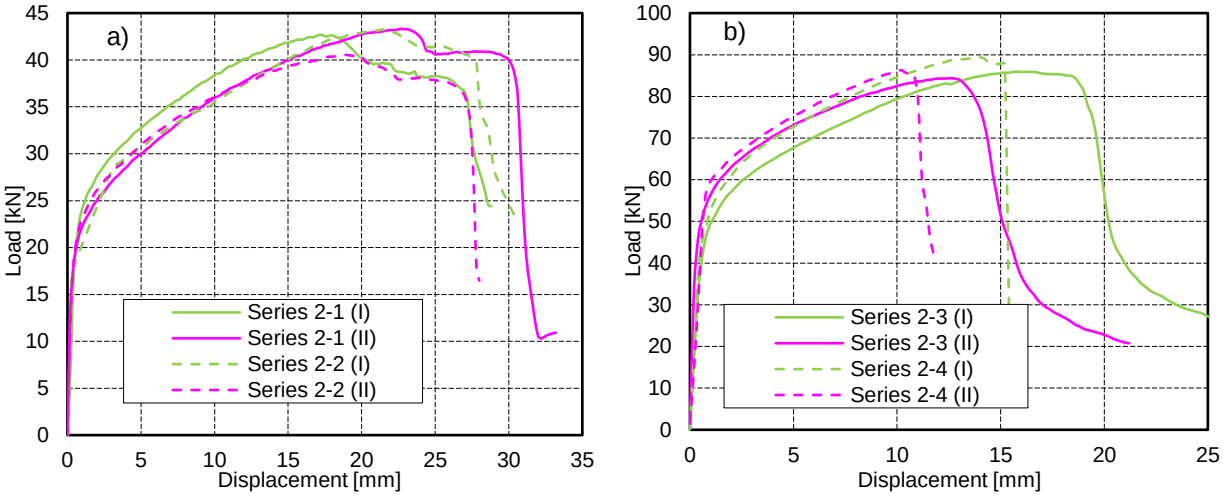

Figure 4.11 Load-displacement curve for specimens with a) short and b) long steel plates

Table 4.4 Results from static component level shear tests

Test series	F_y [kN]	D_y [mm]	F_{max} [kN]	D_{max} [mm]	D_u [mm]	K_e [kN/mm]	μ	$F_{y,SL,s}$ [kN]	$F_{max,SL,s}$ [kN]	$K_{e,SL.s}$ [kN/mm]
2-1	22.8	0.8	42.7	17.2	27.3	44.7	33.7	2.1	3.9	4.1
	22.2	0.9	43.3	22.7	29.8	42.1	32.0	2.1	3.9	3.8
2-2	24.0	1.0	43.3	21.4	28.1	48.9	29.6	2.2	3.9	4.4
	22.5	0.9	40.6	18.8	27.4	40.9	31.9	2.1	3.7	3.7
Average	23.1	0.9	42.5	20.0	28.1	44.2	31.8	2.1	3.9	4.0
2-3	50.2	1.1	86.0	15.8	19.7	84.5	18.1	2.2	3.7	3.7
	54.5	0.8	84.4	12.1	14.4	113.0	17.3	2.4	3.7	4.9
2-4	51.2	0.9	89.4	13.9	16.9	95.5	16.0	2.2	3.9	4.2
	54.9	0.7	86.3	10.2	11.2	81.4	15.8	2.4	3.8	3.5
Average	52.7	0.9	86.5	13.00	15.5	93.8	16.8	2.3	3.8	4.1

4.7.4 Discussion of the quasi-static monotonic shear test results

For the specimens with short steel plates with two rows of holes covered by duct tape (Series 2-1 and Series 2-2), the predicted SL capacity was 48.4 kN. For the specimens with long steel plates with one row of holes covered by duct tape (Series 2-3 and Series 2-4), the predicted SL capacity was 101 kN. The results presented in Table 4.4 demonstrate that the connection capacities can be

reliably predicted and that there was little to no difference between specimens with the mesh glued-in parallel to the grain of the wood (5-ply CLT) or perpendicular (3-ply CLT) as long as the AD capacity exceeded the SL capacity. In such situations, a ductile failure mechanism is achieved and the rigid adhesive bond between steel plate and CLT panels is independent of the grain orientation of the wood into which the steel plate is embedded.

The two different numbers of rows of holes that were covered by duct tape allowed for the assessment of its influence on the connection behaviour. The yield force, F_y, maximum force, F_{max}, and stiffness, K_e, from the specimens with long steel plates were almost twice the values for the specimens with short steel plates – this is closely correlated to the number of SL (23 for long plates and 11 for short plates). The values for the per SL ($F_{y,SL,s}$, $F_{max,SL,s}$ and $K_{e,SL}$) confirm this finding.

In the material level tests, the tensile yield force, $F_{y,SL,t}$, and maximum tensile force, $F_{max,SL,t}$, were determined as 3.6 kN and 4.4 kN, respectively. The expected shear yield force and maximum shear force can be calculated as 2.1 kN and 4.0 kN, respectively, based estimates by Deutschman et al. (1975) according to Eq. 4.3 and Eq. 4.4:

Eq. 4.3 $$F_{y(shear)} \approx 0.58 \times F_{y(tensile)}$$

Eq. 4.4 $$F_{max(shear)} \approx 0.9 \times F_{max(tensile)}$$

The obtained connection shear capacities per SL (2.2 kN and 3.8 kN for $F_{y,SL,t}$ and $F_{max,SL,t}$), respectively, were very close to these values and confirmed the predictability of the connection.

The maximum displacement and ductility showed a different trend, with values almost twice as high for the specimens with short steel plates. These parameters are not influenced by the length

of the steel plates (numbers of SL) but by the number of rows covered by duct tape. Figure 4.12 compares the failure mechanism and clearly shows that all displacement occurred in the rows of holes that were covered by duct tape. These holes and the adjacent SL can deform freely. While in the short plates two rows were free to deform (Figure 4.12a), only one row could deform in the long plates, (Figure 4.12b). The total displacement depends on the number of the free rows with the displacement of each row being very similar; therefore, the ductility and displacement capacity of the connection is proportional to the number of rows covered by duct tape.

a)  b) 

Figure 4.12 Failure mechanism: a) Two rows covered; b) One row covered

4.7.5 Methodology for reversed cyclic shear tests

As the hold-downs are to be applied in tall wood-based structure in high seismic zones, they should not only be strong enough to resist the uplift force required for wind design, but also exhibit high ductility and large energy dissipative capacity under seismic loading. The test specimens for the reversed cyclic tests were similar to the ones used in the quasi-static monotonic tests, only longer to accommodate drill holes for attaching steel brackets on both sides of the CLT panel (see Figure 4.13). Two replicates in four series were produced and subsequently tested with the same geometric configurations of the steel plates and rows covered by duct tape as in the monotonic tests.

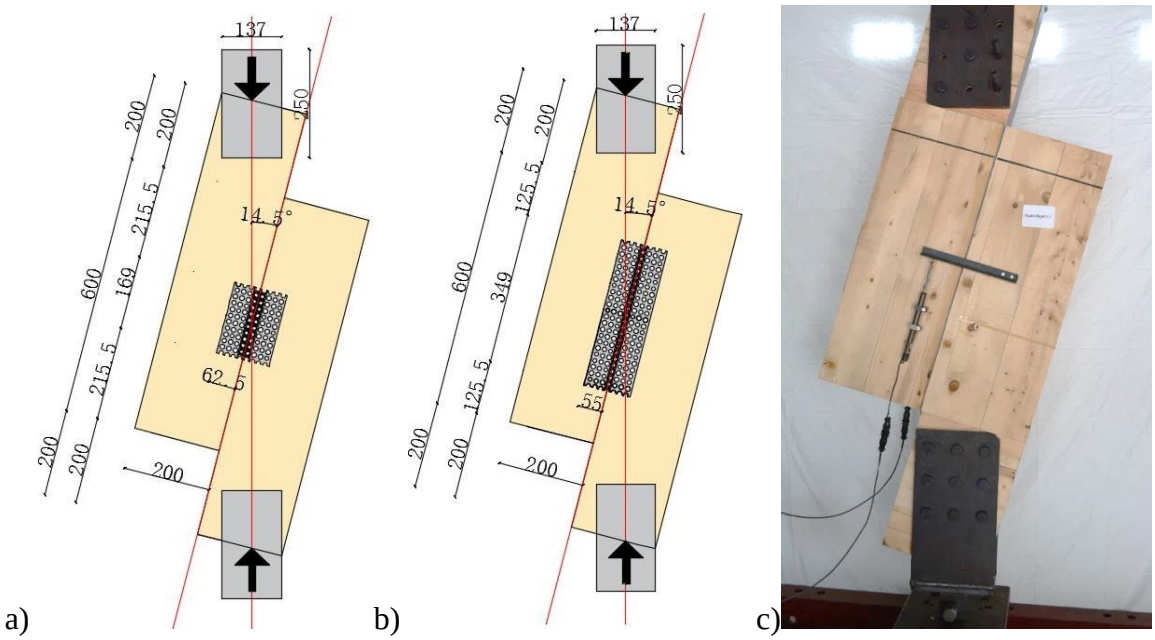

a) b) c)

Figure 4.13 Cyclic tests: a) Specimen sketch for short plates (Series 2-1 and Series 2-2); b) Specimen sketch for long plates (Series 2-3 and Series 2-4); c)Photograph of setup

The CUREE loading protocol (ASTM E2126-09, 2009) was applied with a target displacement set equal to the displacement of the monotonic test where the force dropped to 80% of its maximum value.. The tests were performed under displacement controlled loading at 1.0 mm/sec. The applied loads as well as the relative displacements between the CLT panels were recorded using two LVDT attached to the center parts of the panels. The tests were carried out utilizing a MTS-FlexTest® system (capacity of 250 kN) located in the Wood Mechanics Lab at UBC and stopped when the specimens failed.

4.7.6 Reversed cyclic shear test results

The load-displacement hysteresis curve for specimen Series 1-2 (I) is illustrated in Figure 4.14 together with the envelope curve and the average curve from the monotonic tests. Detailed results for all specimens are included in Appendix A.2. The hysteresis loop, which is representative of all the tests, is large and full, and typical for steel components under reversed cyclic loading.

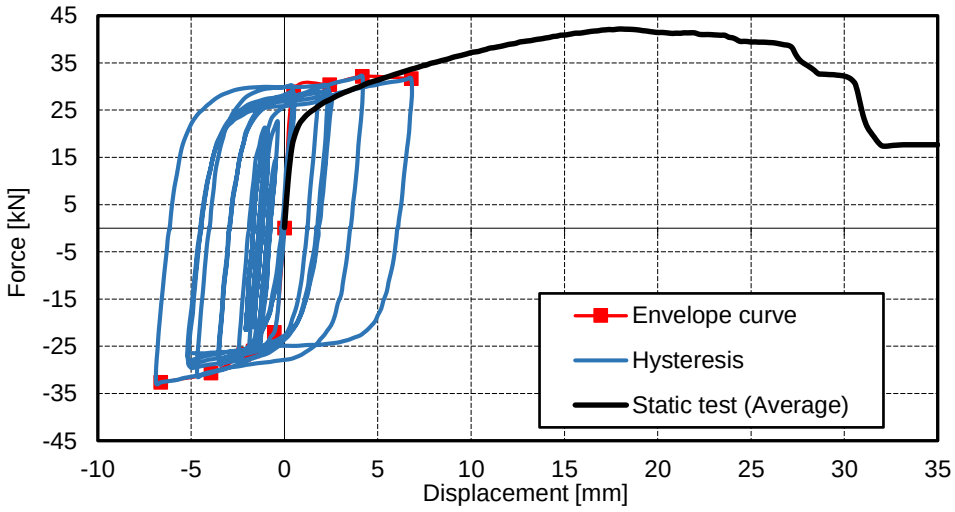

Figure 4.14 Hysteresis curve of specimen I from Series 2-1

Table 4.5 summarizes the cyclic test results for both the positive and negative envelopes. Energy dissipation (*ED)* was calculated as an indicator of seismic performance according to Eq. 4.5, where A_i represents the area within the hysteresis loop under each load cycle, and n is the total number of cycles:

Eq. 4.5

$$ED = \sum_{i=1}^{n} A_i$$

Table 4.5 Results for reversed cyclic component level tests

Test specimen	F_y [kN]	D_y [mm]	F_{max} [kN]	D_{max} [mm]	D_u [mm]	K_e [kN/mm]	μ	$F_{y,SL,s}$ [kN]	$F_{max,SL,s}$ [kN]	$K_{e,SL,s}$ [kN/mm]	ED [kNmm]
2-1 (I)	+28.8	+0.4	+32.1	+4.2	+6.8	+61.5	+17.0	+2.6	+2.9	+5.6	2851
	-22.2	-0.6	-32.6	-6.6	-6.6	-40.4	-11.0	-2.0	-3.0	-3.7	
2-1(II)	+21.5	+0.5	+34.6	+4.8	+7.6	+50.3	+15.2	+2.0	+3.1	+4.6	3399
	-19.2	-0.6	-32.7	-5.2	-7.8	-50.3	-13.0	-1.7	-3.0	-4.6	
2-2 (I)	+25.6	+0.5	+34.1	+4.8	+7.6	+50.1	+15.2	+2.3	+3.1	+4.6	3114
	-24.5	-0.7	-34.1	-6.4	-6.4	-34.8	-9.1	-2.2	-3.1	-3.2	
2-2(II)	+29.2	+0.7	+34.3	+4.8	+7.0	+40.4	+10.0	+2.7	+3.1	+3.7	2890
	-24.7	-0.8	-33.6	-7.0	-8.8	-33.5	-11.0	-2.3	-3.1	-3.1	
Average	+26.3	+0.5	+33.8	+4.7	+7.3	+50.6	+14.4	+2.4	+3.1	+4.6	3064
	-22.7	-0.7	-33.3	-6.3	-7.4	-39.8	-11.0	-2.1	-3.0	-3.6	
2-3 (I)	+49.8	+0.6	+86.9	+7.3	+7.3	+142.7	+13.4	+2.2	+3.8	+6.2	3967
	-60.0	-0.5	-73.6	-4.1	-4.1	-133.3	-9.1	-2.6	-3.2	-5.8	
2-3(II)	+58.1	+0.6	+81.2	+5.2	+5.2	+136.5	+9.5	+2.5	+3.5	+5.9	3266
	-47.3	-0.7	-74.9	-7.4	-7.4	-120.7	-10.6	-2.1	-3.3	-5.3	
2-4 (I)	+60.5	+0.7	+85.2	+4.8	+4.8	+143.3	+6.9	+2.6	+3.7	+6.2	3546
	-53.2	-0.7	-76.7	-6.5	-6.5	-156.0	-9.0	-2.3	-3.3	-6.8	
2-4(II)	+58.9	+0.7	+83.4	+4.6	+4.6	+133.5	+7.1	+2.5	+3.6	+5.8	3316
	-51.7	-0.7	-75.3	-6.4	-6.4	-120.7	-9.1	-2.3	-3.3	-5.2	
Average	+56.8	+0.6	+84.2	+5.5	+5.5	+139.0	+9.2	+2.5	+3.7	+6.0	3524
	-53.1	-0.6	-75.1	-6.1	-6.1	-132.7	-9.5	-2.3	-3.3	-5.8	

Note: + indicates the positive side and - indicates the negative side of the hysteresis loop

4.7.7 Discussion of the reversed cyclic shear test results

Table 4.5 demonstrate that, similar to the monotonic tests, there is little difference in the performance of the HSK connection when glued-in parallel or perpendicular to the grain if SL capacity governs. In this case, F_y, F_{max} and K_e depend entirely on the number of SL. The shear yield force, $F_{y,SL,s}$, under monotonic and cyclic loading are similar (2.2 kN and 2.3 kN, respectively), the shear capacity, $F_{max,SL,s}$, was reduced by 14% in the cyclic tests (3.3 kN vs. 3.8 kN) which was caused by low-cycle steel fatigue (Lefebvre and Ellyin, 1984).

In respect to ductility ratios, similar to the monotonic tests, specimens with two rows covered by duct tape (Series 2-1 and Series 2-2) reached higher values. The difference, however, was only 35% (12.7 vs. 9.3), and all values were significantly smaller than in the monotonic tests. This reduction in ductility under reversed cyclic loading was likely caused by the smaller maximum deformation due to low-cycle fatigue. A secondary explanation can be found in the test set up. To avoid eccentricity, the specimens were rotated by 14.5º, which causes a small force component to act perpendicular to the shear plane. In the monotonic tests, this component acted in compression only and could safely be ignored as friction between the two CLT panels was prevented by the plastic separation layer. In the reversed cyclic tests, however, additional tension loads to steel mesh caused the connection to separate. This effect can also be seen in the offset of the hysteresis loop, as seen in Figure 4.14.

Regarding the energy dissipation, the specimens with long steel plates (Series 2-3 and Series 2-4) reached larger values almost proportional to the plate lengths. The average energy dissipation per SL were 140 kNmm and 153 kNmm for short and long steel plates, respectively. Figure 4.15 shows that failure of the connection occurred in the SL similar to the monotonic tests.

a)  b) 

Figure 4.15 Failure Mechanism under reversed cyclic loading: a) short plates; b) long plates

4.8 Mid-scale tests

4.8.1 Specimen specification

In the component level tests, the influence of covering the steel mesh with duct tape, the number of SL and the HSK embedment direction were investigated. In the reversed cyclic tests, the tension load component in the chosen test setup led to asymmetric forces and offsets in the hysteresis loops. Therefore, mid-scale tests were conducted to validate the previous test results and gain a better understanding of the shear behaviour of the modified HSK connection.

Since the embedment with respect to the grain direction of the wood had no influence as long as the failure was governed by failure in the steel links, only 3-ply CLT panels were used, with all steel plates inserted into the perpendicular layer of the CLT panel. The manufacturing of the test specimens followed the same procedure as described in the component level tests. The dimensions for the specimens were 660 mm by 600 mm, and consisted of three CLT panels with two shear plates, see Figure 4.16a-c. For each specimen, two perforated steel plates were used to connect three CLT panels for a symmetric test configuration that allowed for two data sets (side A and side B) to be observed in every test. Three test series were fabricated, each of them with two replicates. The steel plate in Series 3-1 had 11 SL with 2 rows of covered duct tape, the steel plate for Series 3-2 had 23 SL with 1 row covered, and the steel plate for Series 3-3 had 23 steel links with 2 rows covered by duct tape. Table 4.6 summaries the relevant parameters.

Table 4.6 Test series in mid-scale level

Series	Steel Plate Dimension	No. of SL	No. of Rows Covered	Loading Direction	No. of replicates
3-1	125mm ×169mm	11	2	Perpendicular (3-Ply)	2
3-2	110mm ×349mm	23	1	Perpendicular (3-Ply)	2
3-3	125mm ×349mm	23	2	Perpendicular (3-Ply)	2

4.8.2 Methodology for mid-scale shear tests

The static tests were performed under displacement controlled loading at a rate of 2.0 mm/min, continued until the applied load dropped to 80% of peak load. The applied load and relative displacements were recorded. Four LVDT's were attached (two on each side of the test specimens) to capture the relative displacement between the two CLT panels. A photo of the static test set up is shown in Figure 4.16a. The test specimens in the reversed cyclic shear test were identical to those from the monotonic tests, other than the loading methods togther with the coresponding fixtures, a shown in Figure 4.16b. The reversed cyclic tests were performed under displacement controlled loading with at a rate of 1.0 mm/sec until failure. The CUREE basic loading protocol (ASTM E2126-09, 2009) was used for selecting the target displacements. All the tests were carried out utilizing a MTS-FlexTest® system (capacity of 250 kN) located in the Wood Mechanics Lab of UBC.

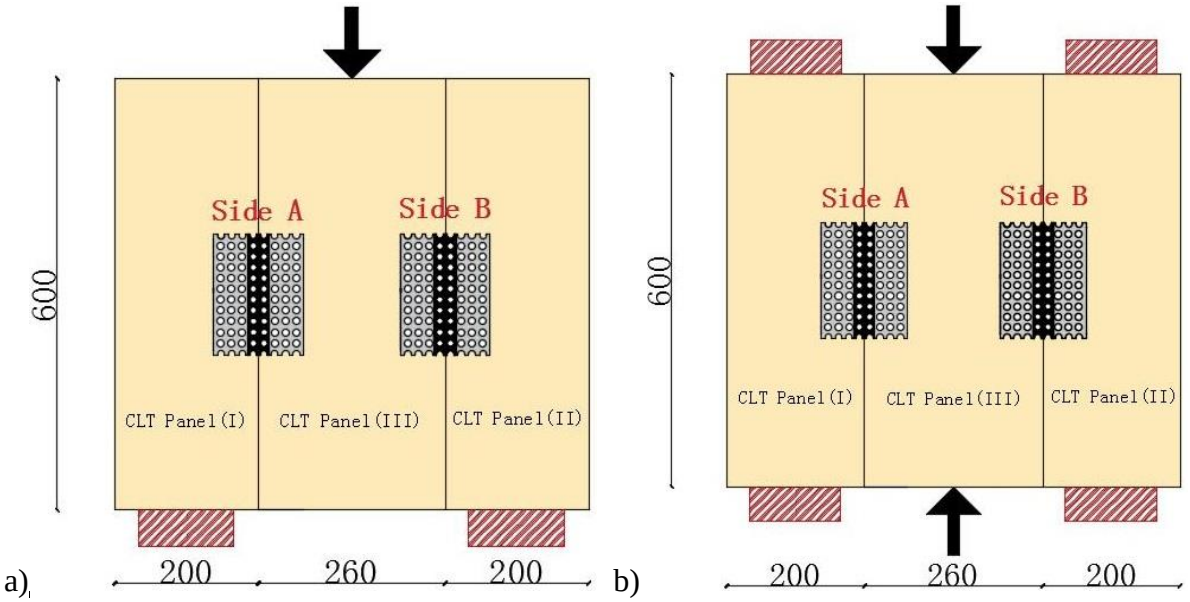

Figure 4.16 Mid-scale Test: a) Specimen sketch for static tests; b) Specimen sketch for cyclic tests

4.8.3 Results for the quasi-static monotonic shear tests

The relative load-displacement curves for all specimens are shown in Figure 4.17. Behaviour, of the connections was ductile with large deformations before failure, see Figure 4.17a. Similar to the component level tests, the specimens with two rows covered by duct tape (Series 3-1 and Series 3-3) exhibited much larger displacements, reaching approximately 26 mm; while for Series 3-2, where only one row was covered, only a 12 mm displacement was reached. There was some opening between panels at the bottom of the specimens observed during the tests. Table 4.7 summarizes the static test results for the mid-level tests.

Table 4.7 Mid-scale static shear test results

Series	Replicate	F_y [kN]	D_y [mm]	F_{max} [kN]	D_{max} [mm]	D_u [mm]	K_e [kN/mm]	μ [-]	$F_{y,SL,s}$ [kN]	$F_{max,SL,s}$ [kN]	$K_{e,SL.s}$ [kN/mm]
S3-1	(I) A	23.4	1.2	37.3	22.3	26.2	43.0	22.2	2.1	3.4	3.9
	(I) B	22.8	1.3	37.3	17.9	25.8	40.1	19.6	2.1	3.4	3.6
	(II) A	21.4	1.0	36.9	15.5	22.5	42.1	23.0	1.9	3.4	3.8
	(II) B	21.0	0.9	36.9	15.4	22.5	43.0	23.9	1.9	3.4	3.9
Average		22.1	1.1	37.1	17.8	24.2	42.0	22.2	2.0	3.4	3.8
S3-2	(I) A	52.8	0.8	78.9	10.4	12.2	100.1	14.6	2.3	3.4	4.4
	(I) B	48.8	1.0	78.9	10.4	10.9	97.7	11.3	2.1	3.4	4.2
	(II) A	49.1	1.0	78.6	9.7	11.7	87.9	11.7	2.1	3.4	3.8
	(II) B	47.4	0.9	78.6	8.3	8.9	92.9	9.5	2.1	3.4	4.0
Average		49.5	0.9	78.8	9.7	10.9	94.7	11.8	2.2	3.4	4.1
S3-3	(I) A	44.8	1.3	78.9	18.5	26.1	89.2	19.8	1.9	3.4	3.9
	(I) B	48.1	1.0	78.9	15.5	18.6	80.9	18.2	2.1	3.4	3.5
	(II) A	47.2	1.0	77.6	17.8	21.7	96.4	21.5	2.1	3.4	4.2
	(II) B	50.4	0.8	77.6	16.5	18.7	114.9	23.4	2.2	3.4	5.0
Average		47.6	1.0	78.2	17.1	21.3	95.3	20.7	2.1	3.4	4.1

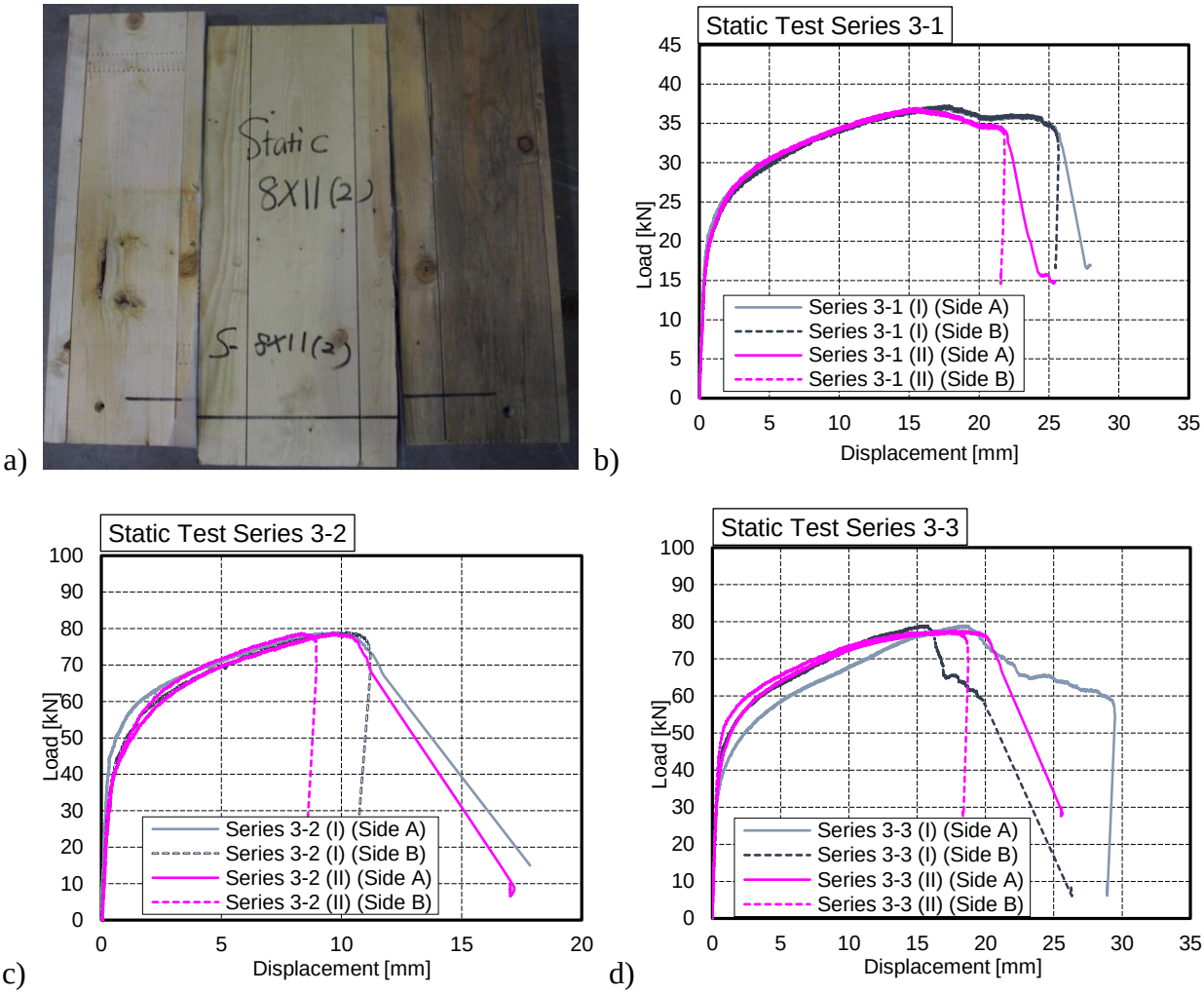

Figure 4.17 a) Series 3-3 after the monotonic loading; b) Force-displacement curve for Series 3-1; c) Force-displacement curve for Series 3-2; d) Force-displacement curve for Series 3-3

4.8.4 Discussion of the quasi-static monotonic shear test results

The results in Table 4.7 confirm the previously observed trends: yield force, F_y, capacity, F_{max}, and stiffness, K_e, are functions of the number of SL. This relationship is almost linear and the values per SL are almost constant. The values are also very similar to those obtained in the component level tests. A small decrease was observed, caused by the difference in test setup. The three-point bending loading in the mid-scale tests created a small tension force in the bottom of the specimens which reduced the force and stiffness capacity of the connection.

The yield displacement, D_y, was around 1.0 mm for all specimens, similar to the value in component level tests (D_y = 0.9 mm). The ultimate displacement, D_u, and ductility, μ, depend on the number of rows covered: for Series 3-1 and 3-3, which had two rows covered, displacement and ductility were almost twice those from Series 3-2, which had only one covered row. Ductility in the mid-scale tests were much lower than in the component level tests because of the change in test set-up. Nevertheless, the values still allow the connection to be classified as highly ductile. The number of rows covered permits designers to achieve high ductility levels. Figure 4.18a-c illustrates the failure mode for test Series 3-1, Series 3-2 and Series 3-3.

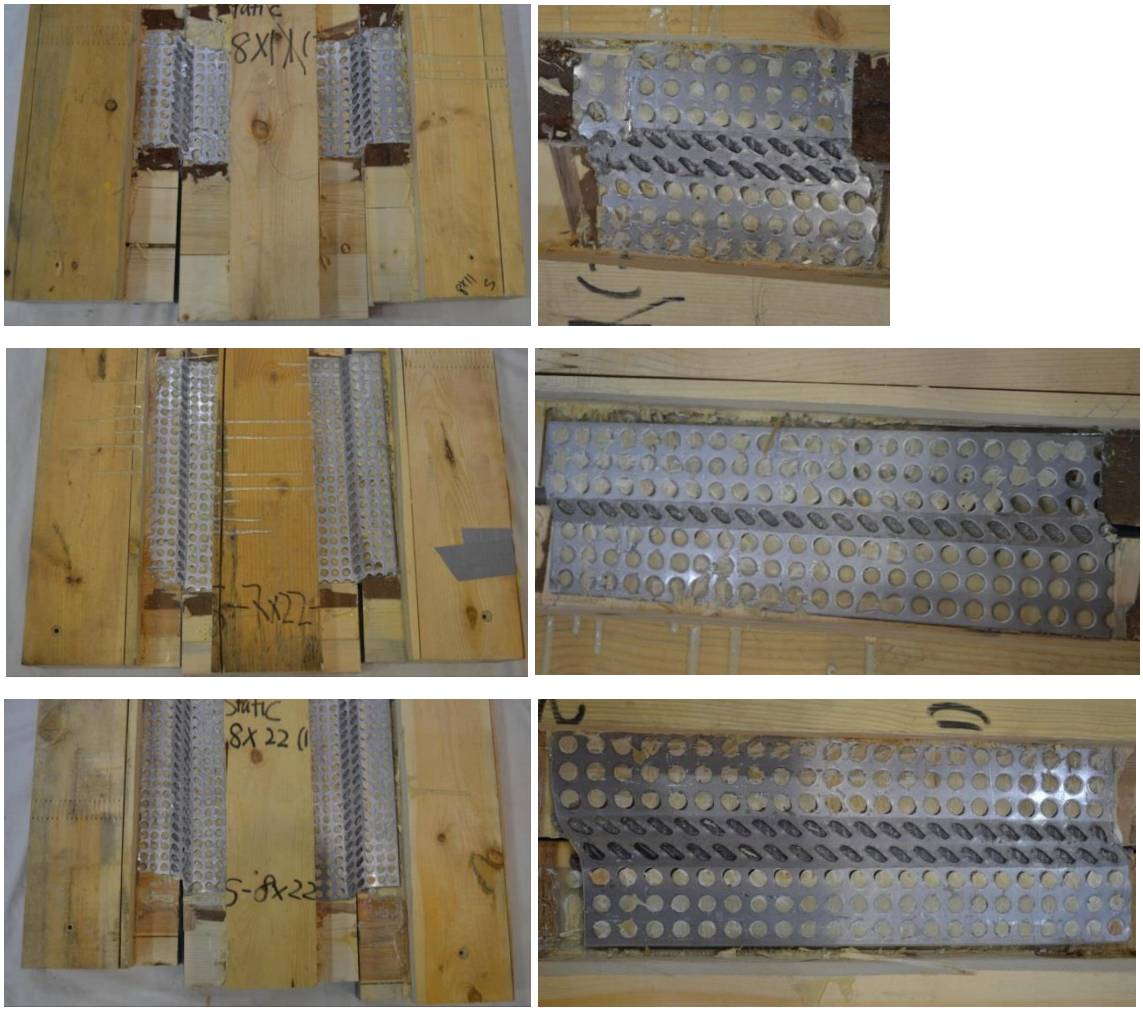

Figure 4.18 Failure mechanism under monotonic loading: a) Series 3-1; b) Series 3-2; c) Series 3-3

4.8.5 Reversed cyclic shear test results

The exemplarily Figure 4.19 shows the load-displacement hysteresis curve for specimen Series 3-1(I) for both Side A and Side B. All other results are presented in Appendix A.3. Similar to the loops obtained in the component level tests, all of the hysteretic loops here are large and full, with shapes typical for steel components. No offset was observed because of the symmetric loading. Additionally, the envelope curves and the average curves from the monotonic tests are included showing that the hysteresis loops are within the static curve.

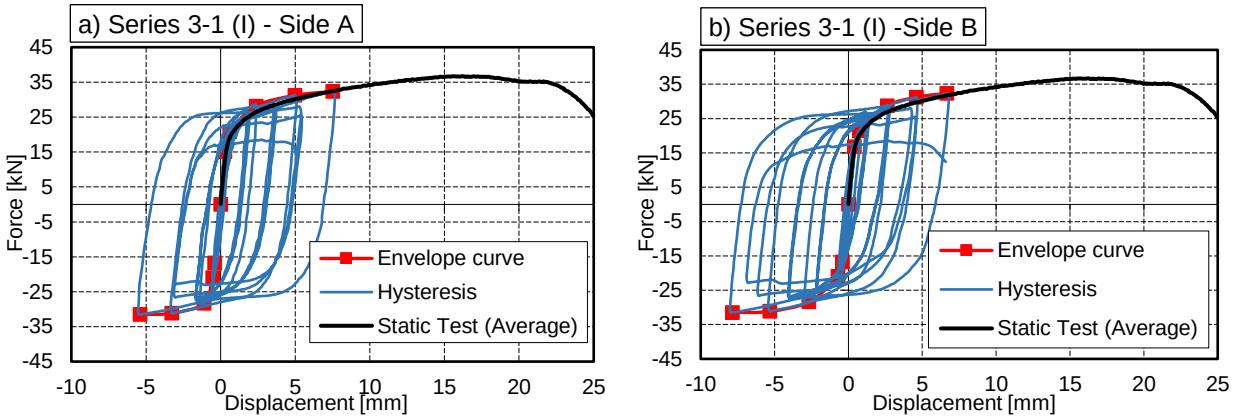

Figure 4.19 Hysteresis curve for specimen I Series 3-1 (I)-Side A; b) Series 3-1 (I)-Side B

4.8.6 Discussion of the reversed cyclic shear test results

The results summarized in Table 4.8 confirm that yield force, F_y, maximum force, F_{max}, and elastic stiffness, K_e, depend entirely on the number of SL. The yield force, capacity and stiffness per SL under monotonic and cyclic loading are similar with 2.1 kN vs. 2.0 kN for $F_{y,SL,s}$,; 3.1 kN vs. 3.4 kN for $F_{max,SL,s}$,; and 4.6 kN/mm vs. 4.0 kN/mm for $K_{e,SL,s}$, respectively. Comparing the results from the component and mid-scale level tests, the obtained values from the two setups are similar. The results from the mid-scale tests, however, are more constant between the positive and negative envelopes and the hysteresis loops show no offset due to the symmetric loading.

Table 4.8 Mid-scale cyclic shear test results

Series		F_y [kN]	D_y [mm]	F_{max} [kN]	D_{max} [mm]	D_u [mm]	K_e [kN/mm]	μ	$F_{y,SL,s}$ [kN]	$F_{max,SL,s}$ [kN]	$K_{e,SL,s}$ [kN/mm]	ED [kNmm]
S3-1 (I)	A	+20.1	+0.7	+32.4	+7.6	+7.6	+40.4	+11.7	+1.8	+2.9	+3.7	2250
		-21.7	-0.6	-31.5	-5.4	-5.4	-42.9	-9.0	-2.0	-2.9	-3.9	
	B	+19.5	+0.6	+32.3	+6.6	+6.6	+42.9	+11.0	+1.8	+2.9	+3.9	2677
		-19.5	-0.6	-31.5	-7.8	-7.8	-41.0	-13.0	-1.8	-2.9	-3.7	
S3-1 (II)	A	+20.7	+0.7	+31.1	+6.0	+6.0	+47.4	+8.6	+1.9	+2.8	+4.3	2486
		-20.6	-0.6	-31.5	-7.2	-7.2	-40.0	-12.0	-1.9	-2.9	-3.6	
	B	+20.4	+0.7	+31.1	+7.6	+7.6	+46.9	+10.9	+1.9	+2.8	+4.3	2635
		-20.5	-0.6	-31.5	-7.0	-7.0	-41.8	-11.7	-1.9	-2.9	-3.8	
Average		+20.2	+0.7	+31.7	+7.0	+7.0	+44.4	+10.5	+1.8	+2.9	+4.0	2512
		-20.6	-0.6	-31.5	-6.9	-6.9	-41.4	-11.4	-1.9	-2.9	-3.8	
S3-2 (I)	A	+45.0	+0.5	+75.5	+4.5	+4.5	+104.1	+8.9	+2.0	+3.3	+4.5	2306
		-52.2	-0.4	-70.7	-2.9	-2.9	-130.4	-7.3	-2.3	-3.1	-5.7	
	B	+44.0	+0.6	+74.9	+4.6	+4.6	+100.6	+7.7	+1.9	+3.3	+4.4	1795
		-53.2	-0.3	-71.0	-2.3	-2.3	-129.0	-7.4	-2.3	-3.1	-5.6	
Average		+44.5	+0.6	+75.2	+4.5	+4.5	+102.4	+8.3	+1.9	+3.3	+4.5	2051
		-52.7	-0.4	-70.8	-2.6	-2.6	-129.7	-7.3	-2.3	-3.1	-5.6	
S3-3 (I)	A	+45.1	+0.7	+75.8	+11.1	+11.1	+137.8	+15.9	+2.0	+3.3	+6.0	4065
		-48.3	-0.6	-63.1	-9.6	-9.6	-114.7	-16.0	-2.1	-2.7	-5.0	
	B	+47.3	+0.7	+75.9	+10.5	+10.5	+108.7	+15.0	+2.1	+3.3	+4.7	3865
		-47.8	-0.4	-63.3	-5.4	-5.4	-115.1	-13.6	-2.1	-2.8	-5.0	
S3-3 (II)	A	+47.6	+0.8	+73.8	+9.7	+9.7	+106.6	+12.2	+2.1	+3.2	+4.6	4342
		-50.0	-0.7	-71.8	-9.6	-9.6	-100.8	-13.7	-2.2	-3.1	-4.4	
	B	+44.8	+0.8	+73.8	+9.4	+9.4	+127.3	+12.5	+1.9	+3.2	+5.5	3921
		-47.1	-0.8	-71.7	-9.6	-9.6	-113.3	-11.4	-2.0	-3.1	-4.9	
Average		+46.2	+0.7	+74.8	+10.2	+10.2	+120.1	+13.9	+2.0	+3.3	+5.2	4048
		-48.3	-0.6	-67.5	-8.5	-8.5	-111.0	-13.6	-2.1	-2.9	-4.8	

Note: + indicates the positive side and - indicates the negative side of the hysteresis loop

For the ultimate displacement and ductility ratios, the specimens with two rows covered by duct tape reached higher values, similar to the results obtained in the monotonic tests. In the cyclic tests, however, the values were significantly lower and the difference was only 60% compared to the monotonic tests (12.4 vs. 7.8). This reduction in ductility under reversed cyclic loading was caused by low-cycle steel fatigue.

The failure modes are illustrated in *Figure 4.20*. For Series 3-1 and Series 3-3, with two rows of links covered, the displacement occurred in one row of SL together with some adjacent SL, see *Figure 4.20*a and *Figure 4.20*c. While in Series 3-2, only one row could deform freely, as shown in *Figure 4.20*b. With regard to energy dissipation, Series 3-3, which had two free rows, dissipated almost twice the energy as Series 3-2 (4048 kNmm vs. 2051 kNmm) . Comparing the series which have the same number of free rows but different numbers of steel links, energy dissipation for Series 3-3 (4048 kNmm) was only 60% larger than the energy dissipation measured for Series 3-1 (2512 kNmm).

Figure 4.20 Failure mechanism under reversed cyclic loading: a) Series 3-1; b) Series 3-2; c) Series 3-3

4.9 Full-scale HSK hold-down tests

4.9.1 Specimen configuration

After investigating the shear behaviour of the modified HSK connection, full-scale tests were conducted to investigate the performance of the system in a hold-down application. 7-ply CLT panels were used and cut to two dimensions 1200×600×239 mm (Series 4-1) and 2500×600×239 mm (Series 4-2). Two different lengths of perforated steel plates were selected with two rows of holes covered by duct tape: short plates containing 22 by 8 holes with 23 steel links in one row, and long plates containing 66 by 7 holes with 67 steel links in one row. Steel tubes (88.9×63.5×6.35 mm), steel side plates (88.9×19.05 mm) and 9.525 mm grade 8 bolts and nuts were used to clamp the HSK mesh. Four replicates for each test series were fabricated, two each for the quasi-static monotonic and reversed cyclic tests.

The preparation of the test specimens consisted of three steps: 1) cutting slots with the appropriate length into the CLT panel, see Figure 4.21a; 2) gluing the perforated steel plates into the CLT panel with two rows of covered by duct tape, see Figure 4.21b; 3) after two days when the adhesive was cured, connecting the exterior part of the perforated steel plate to the HSS steel tube with two steel side plates and bolts as shown in Figure 4.21c.

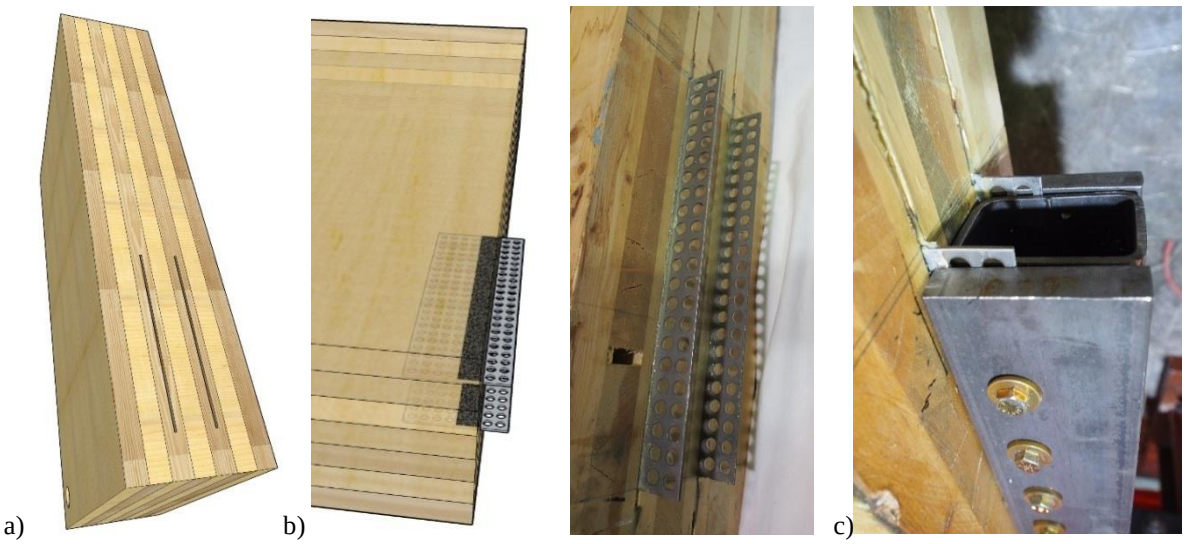

Figure 4.21 Preparation of test specimens: a) Cutting of the slots in CLT panels; b) Embedding of perforated steel plates; c) Clamping the perforated steel plate to steel profile

4.9.2 Methods

The tests were carried out under displacement-controlled loading utilizing a MTS actuator (with 445kN capacity) in the Structures Lab of UBC. One LVDT was attached to each side of the CLT panel to capture the uplifting displacement of the hold-down and a string-pot was used to measure the lateral movement of the CLT panel; Figure 4.22 illustrates the test set up for Series 4-1. Series 4-2 is shown in Appendix A.4. The monotonic tests were conducted with a constant loading rate of 8 mm/min. Based on the target displacement obtained, the loading protocols for the reversed cyclic tests were developed following the CUREE protocol (ASTM E2126-09. 2009). Based on the applied actuator force and the geometric properties of the CLT panes, the hold-down force can be calculated using Eq. 4.6:

Eq. 4.6

$$F_u = \frac{F_a \times D_{A-P}}{D_{H-P}}$$

Where F_u is the hold-down force, F_a is the applied load, $D_{A\text{-}P}$ is the distance from the actuator to the pin connection, and $D_{H\text{-}P}$ is the distance from the hold-down to the pin connection. Ductility, μ, and elastic stiffness, K_e, were calculated using Eq. 4.1 and Eq. 4.2.

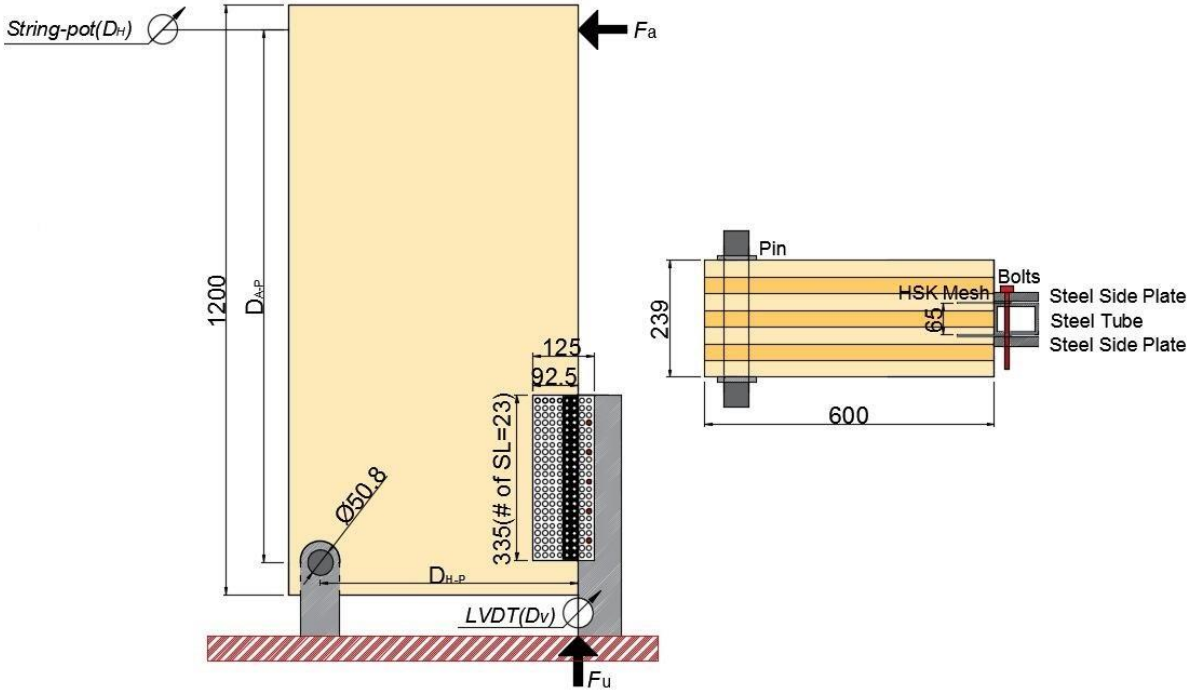

Figure 4.22 Test set up for full scale hold-down test Series 4-1

4.9.3 Results

The hold-down force (F_u) and the recorded uplifting displacement (D_v) were used to plot the force-displacement curves for both monotonic and cyclic tests, as shown in Figure 4.23. Table 4.9 summaries the results. However, one challenge that has not yet been sufficiently addressed remains: the HSK hold-down system does not exhibit any self-centring capability. The hysteresis loops do not return to zero displacement; after each cycle, a larger residual displacement remains. However, the system would be in a real structure with the weight of the structure pushing them down.

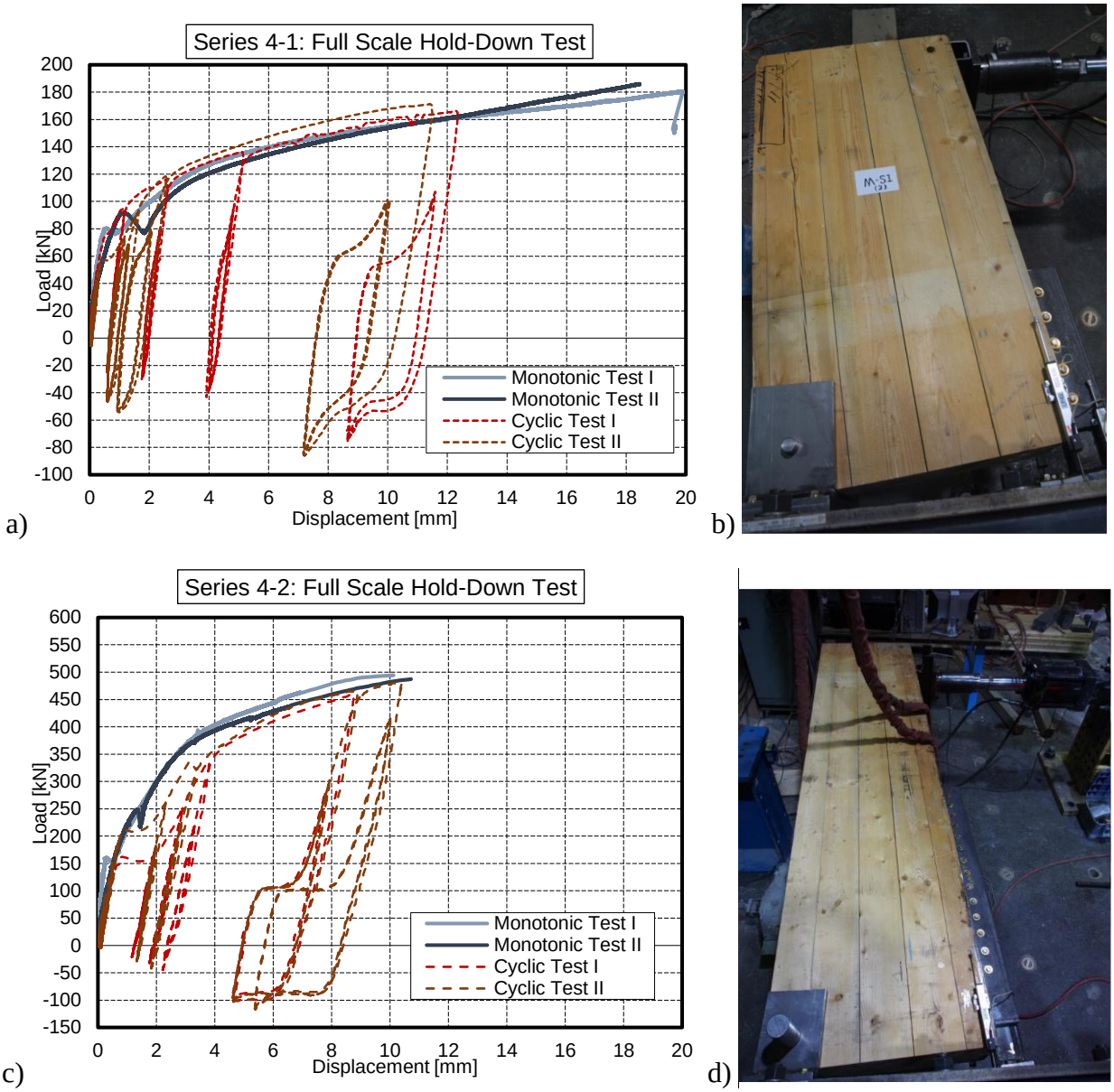

Figure 4.23 a) Force-displacement curves and b) test specimen after monotonic test for Series 4-1; c) Force-displacement curves and d) test specimen after monotonic test for Series 4-2

Table 4.9 Full scale hold-down test results

Series	Test	F_y [kN]	D_y [mm]	F_{max} [kN]	D_u [mm]	K_e [kN/mm]	μ [-]	$F_{y,SL}$ [kN]	$F_{max,SL}$ [kN]	$K_{e,SL}$ [kN/mm]
4-1	Monotonic I	98	1.5	180	19.8	151	13.1	2.1	3.9	3.3
	Monotonic II	102	1.7	186	18.5	109	10.9	2.2	4	2.4
	Cyclic I	98	1.3	167	12.3	159	9.7	2.1	3.6	3.5
	Cyclic II	91	1.4	172	11.5	134	8.1	2	3.7	2.9
4-2	Monotonic I	277	1.6	496	>10.1	448	>6.4	2.1	3.6	2
	Monotonic II	284	1.7	487	>10.7	266	>6.2	2.1	3.7	2.7
	Cyclic I	240	1.7	473	>10.3	240	>6.1	1.8	3.5	1.8
	Cyclic II	268	1.8	482	>10.4	395	>5.8	2	3.6	2.9

4.9.4 Discussion

The obtained results demonstrate that the modified HSK hold-downs achieve a high stiffness and reliably predictable capacity. In the monotonic tests, F_y and F_{max} are close to the expected values according to the material level and component level tests: 100 kN and 183 kN vs. 103 kN and 177 kN for Series 4-1, 280 kN and 492 kN vs. 300 kN and 516 kN for Series 4-2, respectively. Although the F_{max} of Series 4-2 didn't reach three times of that observed in Series 4-1, it is only 5% lower than the expected value. Average stiffness values were 356.8 kN/mm for Series 4-2 and 130 kN/mm for Series 4-1. With regard to the capacity per steel link, the averages for $F_{y,SL,s}$ and $F_{max,SL,s}$ were 2.2 kN and 3.85 kN, respectively; exactly the expected values, confirming the predictability of the hold-down. While there was higher variability in stiffness between replicates, the values are both large with the average being 130 kN/mm ($K_{e,SL}$ equal to 2.9 kN/mm) for Series 4-1 and 357 kN/mm ($K_{e,SL}$ equal to 2.4 kN/mm) for Series 4-2.

The maximum displacements for Series 4-2 were much smaller than Series 4-1, because the actuator reached its stroke limit. Failure occurred in the steel plate in the rows that were covered by duct tape. Specimens in Series 4-1 completely failed, the average ductility exceeded 10 and

confirmed the ductile behaviour of the hold-downs. For Series 4-2, the specimens didn't fail because of the actuator's stroke limit; therefore, the actual ductility was not determined.

The results from the reversed cyclic tests confirmed the findings from the monotonic tests. F_y and F_{max} for Series 4-1 and 4-2 reached on average 95% of the monotonic results. The difference can be explained by low-cycle steel fatigue. For the same reason, the displacements under cyclic loading were smaller, leading to smaller ductility ratios. For series 4-1, μ equaled 8.9 which was 6% lower than from the monotonic test.

The failure modes are shown Figure 4.24, illustrating the displacement between the two rows of holes which were covered by duct tape and that no plastic deformation occurred in SL where the holes where filled with adhesive. This failure mode demonstrated that yielding and plastification can be concentrated inside the CLT panel and the steel mesh can be effectively prevented from buckling. For Series 4-2, the displacement didn't research its maximum, as shown in Figure 4.24b, but there was some movement in the covered rows, which confirms that the maximum expected displacement is bigger than 10.4 mm and that μ should be bigger than 6.0.

a)  b) 

Figure 4.24 Failure mechanism after the test: a) Series 4-1; b) Series 4-2

4.10 Summary

In this chapter, a modified HSK hold-down system was developed and small-scale material, mid-scale shear, and full-scale hold-down tests were conducted. From these tests, the following main conclusions can be drawn:

1) From the material level tests, the basic structural characteristics of the HSK system were validated. Connection properties entirely depend on the number of steel links and the connections can reliably be designed to fail in a ductile mode with a given target yield force, capacity and stiffness based on the number of steel links.

2) Once a ductile steel failure mode is obtained, the connection properties are independent of the grain orientation of the wood into which the steel plates are embedded.

3) The two different setups used in the shear tests provided different advantages and disadvantages. Specimens rotated at 14.5^{o} with one shear plane are suitable for quasi-static monotonic tests because the resultant force of loading and support are aligned. The symmetric set-up using two shear planes is more appropriate for reversed cyclic tests as only a small tension force component is created. However, results from both setups were similar and allow for the studying of the connection.

4) Covering a certain number of rows of holes of the perforated steel plates inside the CLT panel with duct tape prevents these holes from being filled with adhesive. This approach allows for the ductile yielding and energy dissipation to be constrained inside the CLT panel which effectively prevents any risk of steel buckling.

5) The number of rows of free holes allows to design for a certain target displacement capacity, and as a consequence, a given target ductility.

5) The full-scale hold-down tests confirmed the behaviour of the modified HSK system. Test results indicate that capacity, stiffness and ductility can be controlled using the design parameters at hand: steel properties, number of adhesive dowels and steel links, as well as with the number of rows covered.

In conclusion, this research showed that the modified HSK connection can provide strong, stiff and ductile hold-downs with large energy dissipation capacity which are suitable for use in tall wood buildings.

Chapter 5: Ductility Factor Estimation for FFTT System [3]

5.1 Introduction

Current seismic design in North America, and in most of the world, is carried out in accordance with the force-based design approach. In force-based design, elastic forces are based on an initial elastic estimate of the building period combined with a design spectral acceleration for that period (Park, 1996). Design force levels are reduced from the elastic level by applying code-specified force-reduction factors. In the International Building Code (IBC, 2012) and FEMA P695 (FEMA, 2009), the response modification factor is defined as R; while in the NBCC (NRCC, 2010), it is set equal to $R_d \times R_o$ where R_d is the reduction factor for ductility, and R_o is an overstrength factor. R_d reflects the reduction in force seen in a structure responding in-elastically compared to the equivalent elastic structure, and is a function of the system ability to deform beyond yielding. R_o represents the system reserve strength which comes from factors such as member oversizing in design and strain hardening in the materials. The values for these two R factors for different types of -LLRS are presented in the NBCC 2010 (NRC, 2010). For timber-steel hybrid systems such as FFTT, however, these reduction factors are currently not yet available.

A recent study (Pei et al., 2013a) developed reduction factors for CLT structures and proposed that $R_d = 2$ and $R_o = 1.5$ were acceptable values. These values were also preliminarily assumed for the FFTT system in the Tall Wood Report (Green and Karsh, 2012) and in a study on the dynamic response of the FFTT system (Fairhurst et al., 2014). These reduction factors, however, were based

[3] A version of this chapter has been published in Journal of Structural Engineering. Zhang, X. , Fairhurst, M. , and Tannert, T. (2015). Ductility estimation for a novel timber–steel hybrid system. Journal of Structural Engineering. DOI: 10.1061/(ASCE)ST.1943-541X.0001296, E4015001.

upon a type of CLT structure that relies on yielding of its panel connectors to provide inelastic action. This assumption is not appropriate for the FFTT system, which is designed to rock at its base and primarily utilizes steel beams to yield and provide a ductile failure mechanism. Therefore, it is deemed necessary to develop seismic force reduction factors to allow the FFTT system to be efficiently designed.

5.2 Objective

The main objective of this work is to evaluate the nonlinear response of the FFTT system in order to provide a more reasonable estimate of the seismic ductility reduction factor R_d and verify this factor using an example of a 12-storey FFTT structure. Secondary objectives are to study the influence of selecting the steel-beams for the system according to two different approaches and the influence of two different approaches to match the seismic hazard level at the design location. To achieve these goals, a series of two-dimensional (2D) and three-dimensional (3D) numerical investigations were carried out. After obtaining the estimated ductility factor, the experimental test results of the connection descried in previous chapters will be used as a valuable input to investigate the seismic behaviour of the proposed novel timber-steel hybrid structure.

5.3 2D numerical investigation on FFTT system

5.3.1 Seismic design according to NBCC 2010

In the NBCC (NRC, 2010), the Equivalent Static Force Procure (ESFP) can be used to determine the seismic base shear and the distribution of the storey shear. In this method, an acceleration spectrum is used to determine the spectral acceleration at the fundamental elastic period of the structure. This acceleration is converted into a base shear force through multiplying by the weight of the structure, and then modified with several factors, including R_d, R_o, and an importance factor,

Higher mode effects are also taken into account by multiplying the design base shear with a period-based factor as specified in the NBCC (NRC, 2010). This resulting force is then distributed over the height of the structure to design the structural members. In the presented study, R_o was initially set to 1.5 (as suggested by Pei et al., 2013a) and then different values of R_d ranging from 1.5 to 6.0 were considered.

Based on a preliminary global 3D finite-element model that investigated the seismic response of the FFTT system (Fairhurst et al., 2014), the periods for the FFTT system with different building heights were obtained (Table 5.1). The research reported in this chapter focuses exclusively on the more flexible building direction of Option 1 of the FFTT system. Four different building heights (3 storeys, 6 storeys, 9 storeys, and 12 storeys) were considered.

Table 5.1 Periods for four building prototypes of FFTT system Option 1

No. of Storeys	Period from FEM (s)	Period from Building Code (s)	Spectral Acceleration (g)
3	0.49	0.44	0.64
6	0.90	0.74	0.39
9	1.34	1.01	0.28
12	1.90	1.25	0.19

The building location was taken as Vancouver, British Columbia, a moderately high seismic zone, and the location proposed for the FFTT system in the original report (Green and Karsh, 2012). The 5% damped, 2% in 50-year design spectrum as provided in the NBCC (NRC, 2010) was used to determine spectral accelerations. The importance factor was taken as the default 1.0 (normal importance). The periods obtained from the building code were calculated based on the equation for steel moment frames as this approach is believed to best approximate the dynamic properties of the FFTT system. According to NBCC requirements (NRC, 2010), the period used for the

design should not be greater than 2 times the code determined period. Based on this requirement, the final periods used in the ESFP are same as the model periods shown in Column 2 of Table 5.1.

All models were simplified in order to streamline the design process and expedite the analyses. According to the dynamic analyses of the global 3D model, the first mode shape of FFTT Option 1 is the deflection in the east-west direction, where the more flexible LLRS is the core wall system highlighted in Figure 5.1a. For design and analysis, only half of the symmetric LLRS in this direction was developed; specifically only two CLT walls with one linking steel beam was modelled, as shown in Figure 5.1b.

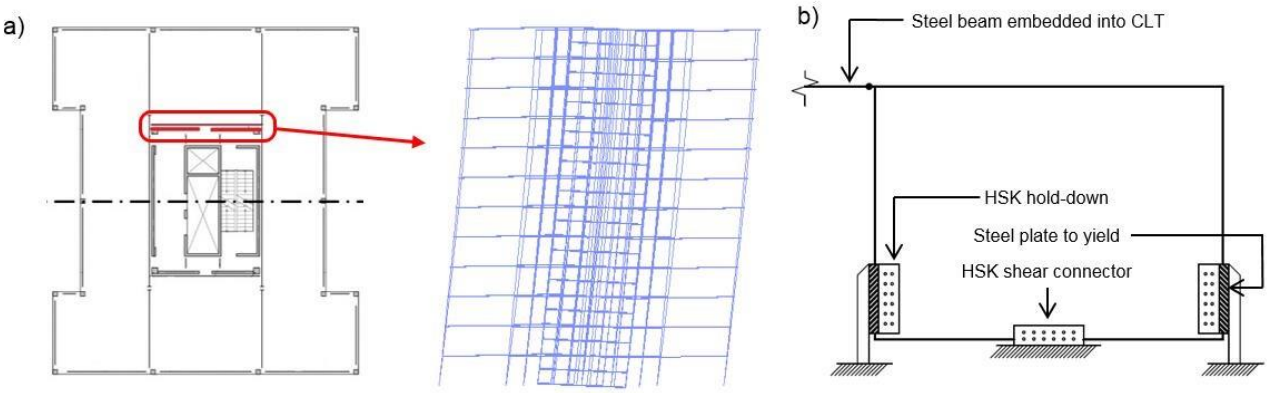

Figure 5.1 a) Floor layout for FFTT system, Option 1; b) First mode shape; c) Portion of the system considered for modelling

Based on the design details from the Tall Wood Report (Green and Karsh, 2012), specifically the expected design dead load of 4.0 kPa for each floor, the seismic weight was calculated. Half of the seismic weight of 887 kN per floor was applied to the CLT walls (756 kN at the roof level) since only one out of the two symmetric walls in the considered direction was modelled. The base shear demands (absolute values, V_{base}, and the percentage of building weight, %W) calculated according to NBCC (NRC, 2010) for the different R_d factors are listed in Table 5.2.

Table 5.2 Base shear demands for four building prototypes

R_d	3-Storey		6-Storey		9-Storey		12-Storey	
	V_{base} (kN)	%W	V_{base} (kN)	% W	V_{base} (kN)	% W	V_{base} (kN)	% W
1.5	720	28.5	905	17.4	962	12.2	869	8.3
2.0	540	21.3	678	13.1	721	9.2	652	6.2
2.5	432	17.1	543	10.5	577	7.3	522	5.0
3.0	360	14.2	452	8.7	481	6.1	435	4.1
3.5	308	12.2	388	7.5	412	5.2	373	3.5
4.0	270	10.7	339	6.5	361	4.6	326	3.1
4.5	240	9.5	302	5.8	321	4.1	290	2.8
5.0	216	8.5	271	5.2	289	3.7	261	2.5
5.5	196	7.7	247	4.8	262	3.3	237	2.3
6.0	180	7.1	226	4.4	240	3.1	217	2.1

5.3.2 Steel beam selection

Based on the strong-column/weak-beam capacity design methodology, the FFTT system relies primarily on well-defined steel beam plastic hinges to yield and dissipate the seismic energy. Therefore, in this study, the interconnecting steel beams were considered to be the main mechanism providing ductility for seismic demands.

To determine the appropriate steel beam cross sections was an important step for this study. Based on the shear forces, different designs corresponding to different R_d factors result in different required steel beam sections. Considering the plastic hinges, the yield moment of the suitable steel beam should be slightly bigger than its bending moment under the specified design lateral load, but not too large so as not to yield before the wood breaks. Based on this principle, a number of 2D models were generated in SAP2000 (CSI, 2002). Using these models, Class-I wide flange sections from the Canadian Steel Design Handbook (CSA, 2010) were chosen to resist the moment demands developed from the base shear distributed over the height of the structure, reduced by

each trial R_d factor. Figure 5.2 shows the steel beam bending moment diagrams of four building height models with R_d = 4.0.

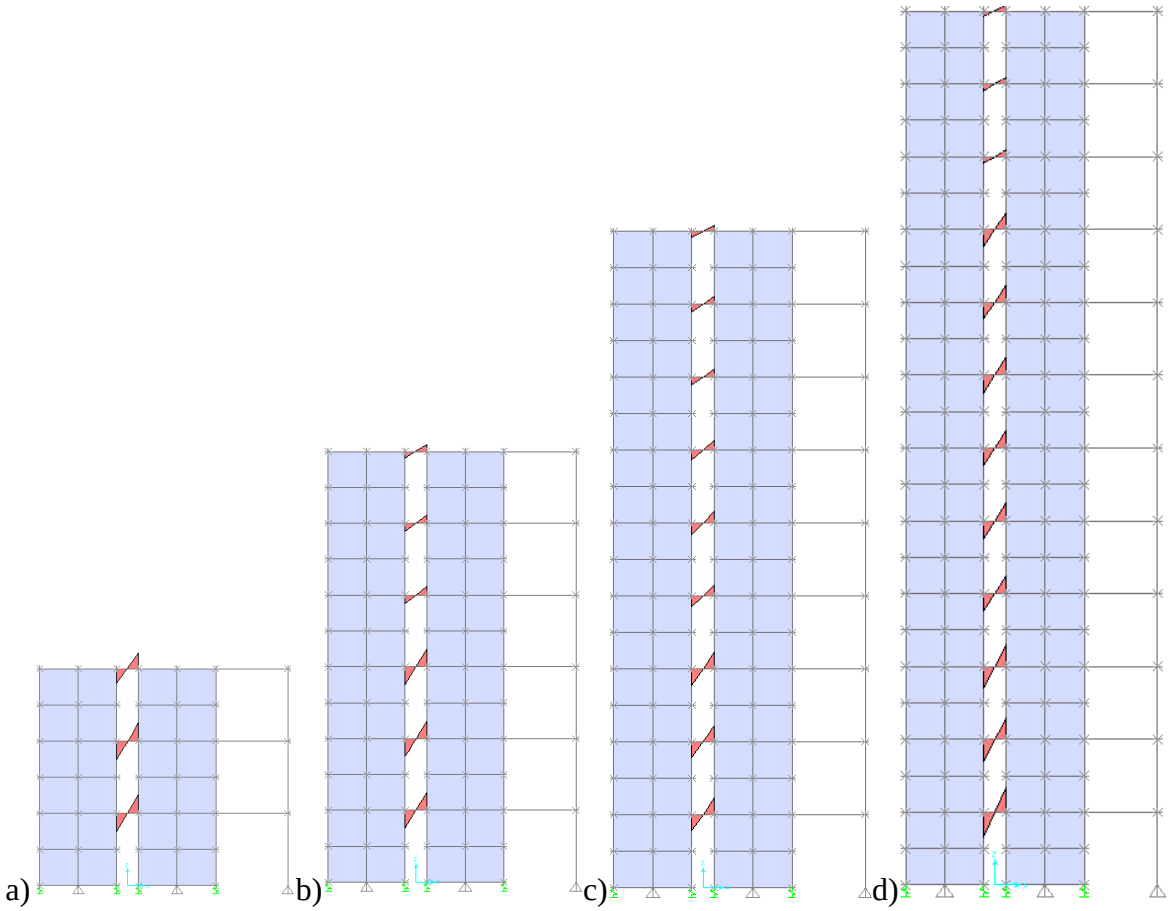

Figure 5.2 SAP2000 models for steel beam selection: a) 3-storey; b) 6-storey; c) 9-storey; d)12-storey

When selecting the suitable steel beam section, two methods were taken into account. First, each storey level was designed using a different steel beam cross section based on the individual storey moment demands, subsequently referred to as method DSB (derived from different steel beams). This selection results in steel beams that match the demands well. Secondly, the steel beam sections were kept constant over three storeys, subsequently referred to as method SSB (derived from same steel beams). This method represents a more practical procedure although many of the storeys will be slightly overdesigned.

Table 5.3 provides an example of the steel beam selection for the 9 storey FFTT system designed with R_d = 4.0. For all the other prototype buildings, steel beam section tables are given in Appendix B. Figure 5.3 gives an example of how to select the beam section in SAP.

Table 5.3 Steel beam selection for the 9 storey FFTT system designed with R_d = 4.0

Storey	DSB			SSB		
	Steel Cross Section	Yield Moment (kNm)	Required Moment (kNm)	Steel Cross Section	Yield Moment (kNm)	Required Moment (kNm)
1	W250×28	105.9	88.9	W250×28	105.9	90.1
2	W310×24	96.6	82.7	W250×28	105.9	82.3
3	W250×25	91.8	73.5	W250×28	105.9	84.6
4	W250×22	78.3	66.8	W250×22	78.3	60.5
5	W250×22	78.3	65.3	W250×22	78.3	62.5
6	W250×22	78.3	63.8	W250×22	78.3	63.2
7	W200×22	66.9	51.2	W130×24	48.0	36.4
8	W130×24	48.0	27.9	W130×24	48.0	34.9
9	W150×18	41.4	24.6	W130×24	48.0	28.4

5.3.3 2D OpenSees modeling

After the steel beam cross sections had been determined, 2D finite element models were developed using the OpenSees framework (McKenna et al., 2000). Figure 5.4 provides a sketch of the models. In this study, and in accordance with the original design proposal for the FFTT system, the majority of the ductility is provided by yielding of the linking steel beams which can only be activated when the panels are allowed to rock. Therefore all the models are pinned in the middle of CLT walls at the base to allow the desired failure mechanism to form.

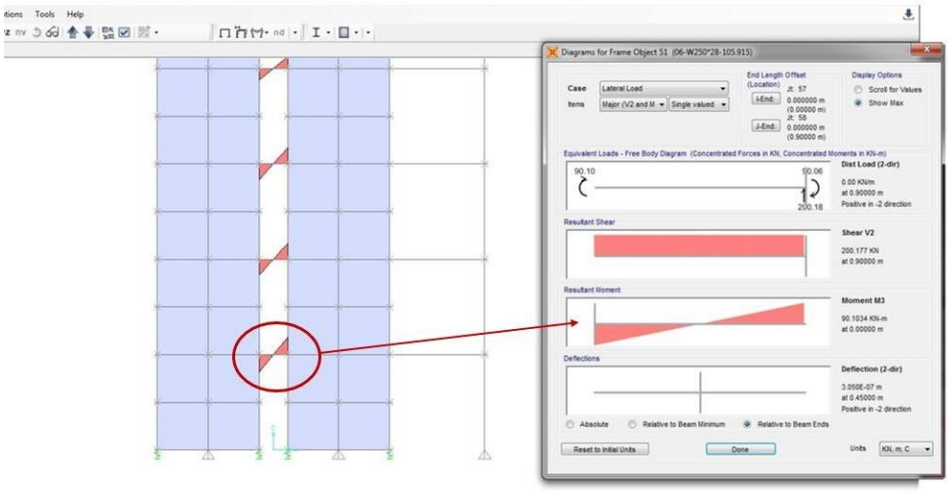

Figure 5.3 Example of beam selection in SAP for the first storey in 9-storey FFTT with R_d*=4.0 (SSB)*

In practice, this behavior can be facilitated with a stiff shear connector placed at the midpoint of the panels. For example, the Holz-Stahl- Komposit (HSK) system is suggested as it has already been proved to be very stiff and have a high strength in Chapter 4, as illustrated in Figure 5.1b. As a possible hold-down solution, the HSK hold-downs would be designed to yield in shear, before any premature wood failure could occur, providing a ductile yielding mechanism with a stable and symmetric hysteretic response. The CLT panels would be allowed to rock about their midpoint, thus allowing the hold-downs to yield in both directions. The hold-downs contribute to the energy dissipation of the system, but play an inferior role in the conceptual design of FFTT system compared to the CLT wall-steel beam connections (Green and Karsh, 2012). In this case, the HSK hold-downs were modeled as springs at both sides of the shear walls; the nonlinear properties of the hold-downs were modeled with an elastic perfectly plastic material with stiffness and yield force values according to published test results (Bathon et al., 2014).

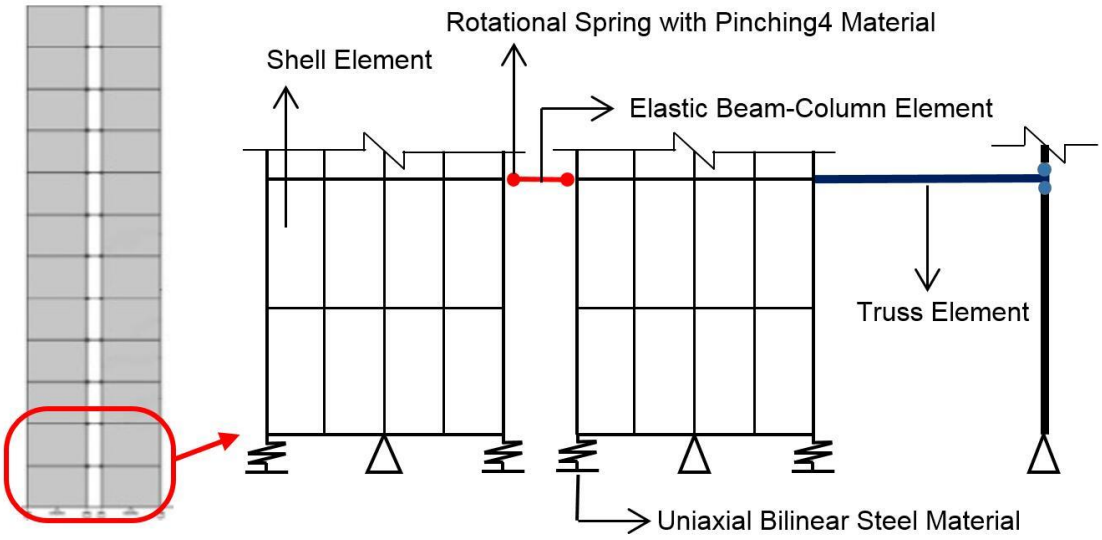

Figure 5.4 Schematic of 2D OpenSees model for the FFTT system

In each structure, the steel beams were modeled with elastic beam elements connected by zero length elements which serve as rotational springs to represent the structure's nonlinear behavior. The results from monotonic and cyclic tests on a variety of beam sections with varying cross sections and embedment lengths and depths (Bhat, 2013) allowed calibrating the hysteretic response of these rotational springs.

Based on the test result in Chapter 3, the hysteresis loop of series S5 were chosen first, as shown in Figure 5.5. Although it is the hollow rectangular beam, it showed good ductility and energy dissipation. In order to simulate the behaviour, the test setup and CUREE loading protocol was modelled in OpenSees. The Pinching4 material in OpenSees (Lowes et al., 2003) was utilized to calibrate the moment-rotation relationship of the hinges. Figure 5.6 illustrates a good fit between experimental results and numerical calibration indicating that this material model sufficiently captures the behaviour observed in the tests including steel yielding, limited localized wood crushing, and energy dissipation. An analysis of the dissipated energy showed an acceptable

difference. The selected Pinching4 material model reflects the ductile yielding of the steel beams as well as the small localized wood crushing that was observed in previous experimental investigation.

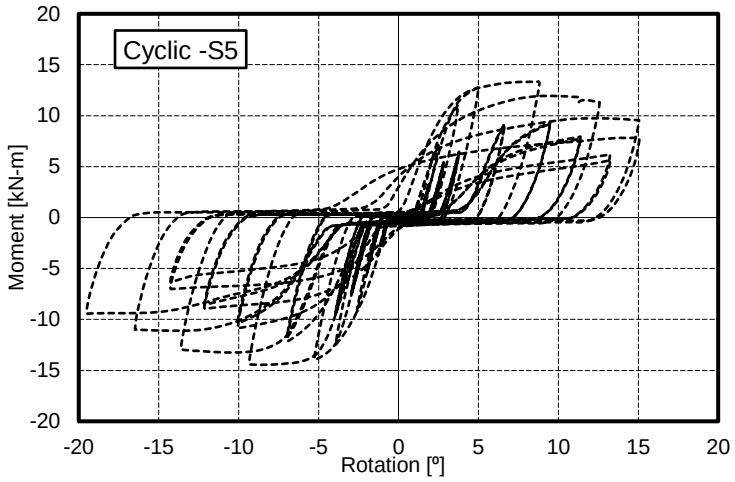

Figure 5.5 Hysteresis loop for HSS steel beam-CLT wall connection (S5)

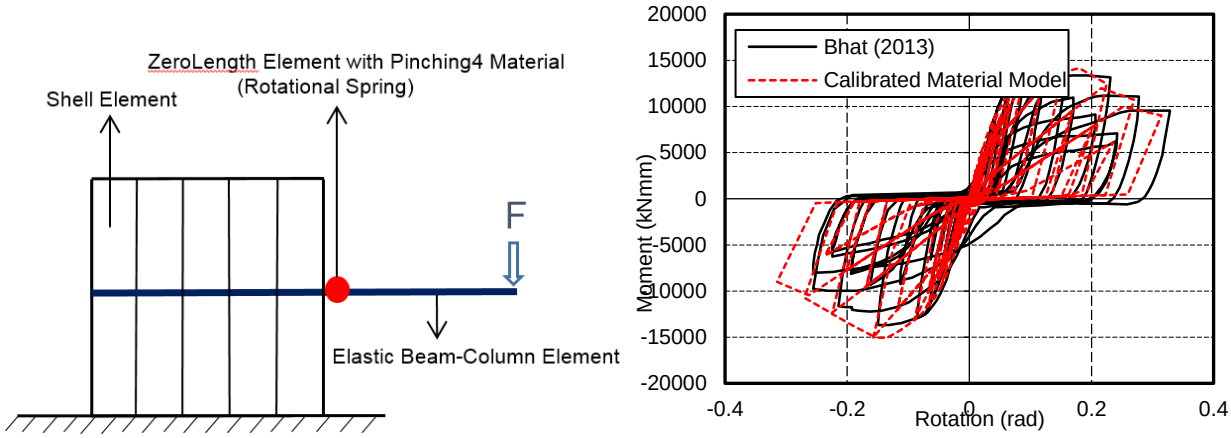

Figure 5.6 Calibration of steel beam CLT panel connection (S5) with OpenSees hinge

As it is not possible to experimentally test connections with all the selected beam cross sections, several assumptions were made to extend the test results to predict the response from other steel sections with a similar connection detail. First, the rotation at each change in stiffness of the backbone curve was assumed to be constant for each steel section, then the ratio of the each subsequent moment along the

moment-rotation curve to the initial yield moment was assumed to be constant. And finally the hysteretic behavior and strength degradation properties of each model were taken as identical.

These assumptions are summarized and illustrated in Figure 5.7, where My*, M1*, M2*, and M3* represent the parameters of the material model that was utilized to calibrate the hysteretic response of the hinge in Bhat's test (Bhat, 2013); and My, M1, M2, and M3 represent the assumed parameters for the rotational spring of other selected steel beams. For any steel beam that was selected, the My*, M1*, M2*, and M3* are known variables, then M1, M2, and M3 can be obtained from Eq. 5.1.

Eq. 5.1

$$\frac{M1}{My}=\frac{M1^*}{My^*} \quad \frac{M2}{My}=\frac{M2^*}{My^*} \quad \frac{M3}{My}=\frac{M3^*}{My^*}$$

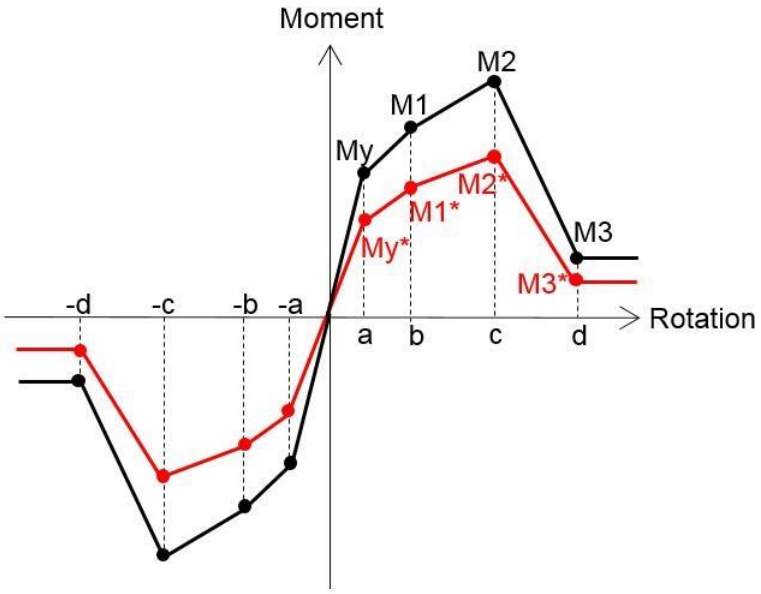

Figure 5.7 Typical moment-rotation curve of a steel beam-CLT panel plastic hinge

According to these assumptions, all backbone curves of the rotational springs corresponding to different steel beams were obtained and used as input for the model.

Leaning columns (P-Delta Columns) with additional gravity loads were linked to the structures by truss elements to simulate the P-Delta effect due to additional gravity loads not modelled directly on the CLT walls. In order to represent an aggregate effect of all the gravity glulam columns, the leaning columns were considered to be rigid and modeled as elastic beam-column elements. The leaning columns were connected to the beam-column joint by zeroLength rotational spring elements with very small stiffness values so that the columns do not attract significant moments. Rigid truss elements were used to link the frame and leaning columns and transfer the P-Delta effects. The shear walls and the leaning column were pinned at the base. The pins were required to allow the desired failure mechanism to form.

The CLT walls were considered to be elastic as the timber crushing was captured in the material model used for the beam concentrated plastic hinges. The ShellMITC4 element (Dvorkin and Bathe, 1984) which can resist both in-plane and out-of-plane deflections together with an elastic orthotropic material model was utilized to represent the elastic timber shear walls with orthotropic properties.

The orthotropic stiffness properties of the CLT walls were determined by the method called "*k* method" (Blass, 2004) in the CLT handbook (Gagnon and Pirvu, 2011). This method can be used to calculate the effective bending stiffness of a CLT panel given its layer geometry and material properties based on the loading configuration. Table 5.4 shows the orthotropic stiffness used for modeling, where E_0 represents the elastic modulus parallel to the grain of the timber laminations.

The strength parameters correspond to the material used in tests (Bhat, 2013) and are summarized in Table 5.5. Since CLT panels can only be constructed with a limited height, a maximum feasible length of a panel would be about four storeys (3m for each storey and 12m total height;Green and

Karsh, 2012), modeling one continuous panel over the height of a high-rise building would be inappropriate. In this case, connections between CLT panels were considered for every four storeys. The material properties of the connection are assumed elastic in tension and rigid in compression. Vertical connections within the four storeys are assumed to be rigid as they would most likely be provided through rigid, capacity designed shear connectors; thus, rocking between panels would not be expected. Although the nonlinear behavior of the CLT walls was not explicitly modeled, local crushing at the steel beam interface was considered as it was included in the material model used to simulate the wall-beam interface which was calibrated to physical test results.

Table 5.4 Orthotropic stiffness values used for modelling

Loading		Effective Stiffness	Composite factor
Perpendicular to Plane Loading	Bending Parallel	$E_0 \cdot k_1$	k_1=0.930
In-Plane Loading	Bending Parallel	$E_0 \cdot k_3$	k_3=0.675
	Bending Perpendicular	$E_0 \cdot k_4$	k_4=0.377

Table 5.5 Timber member summary

Member	Material	Section	Compression Strength (MPa)	Tensile Strength (MPa)	Shear Strength (MPa)
Glulam Beam	D. Fir 16c-E	264x484mm	30.2	20.4	2.0
Glulam Column	D. Fir 20f-EX	418x418mm	30.2	20.4	2.0
CLT Wall	D. Fir	204mm (6 layers)	11.5	5.5	1.5

5.3.4 Ground motion selection and scaling

In nonlinear dynamic analyses, the predicted structural response can be sensitive to the characteristics of the individual ground motions used as input; therefore, several analyses are

required using different ground motion records to achieve a reliable estimate of the mean structural response. In addition to finding suitable ground motions that match the hazard at a building site, a design acceleration response spectrum must also be defined. In the NBCC (NRC, 2010), the design response spectrum is taken as the 5% damped uniform hazard spectrum (UHS) with a 2% in 50 year probability of exceedance.

In the research, the appropriate hazard for Vancouver, British Columbia, was chosen based on NBCC (NRC, 2010) values. The default values for Site Class C with 5% critical damping were utilized. The 22 far-field earthquake ground motions considered in FEMA P-695 (FEMA, 2009) were selected as the record set, seeTable 5.6. Two commonly used methods were adopted for modifying the records to match the seismic hazard level at the design location: (1) linear scaling of the individual records to the design response spectrum over the period range of the model, and (2) spectrally matching the ground motions to the design acceleration spectrum over the period range of the model. These two hazard matching methods were chosen to gain insight into the effect of how ground motion modification could impact the results. The linearly scaled records are highly variable away from this period range; therefore they are predicted to produce more scattered results. The spectrally matched motions agree well with the specified design spectrum at and around the period range of the structure; however, it has been theorized that the smooth spectrum may lower the demand on the structures (Atkinson and Macais, 2009).

Table 5.6 Ground Motion record set from FEMA P695

ID No.	Earthquake			Recording Station	
	Magnitude	Year	Name	Name	Owner
1	7.4	1990	Manjil,Iran	Abbar	BHRC
2	7.5	1999	Kocaeli,Turkey	Arcelik	KOERI
3	6.5	1976	Friuli,Italy	Tolmezzo	--
4	6.5	1987	Superstition Hills	El Centro Imp. Co.	CDMG
5	7.1	1999	Duzce,Turkey	Bolu	ERD
6	6.5	1987	Superstition Hills	Poe Road (temp)	USGS
7	6.9	1989	Loma Prieta	Capitola	CDMG
8	7.6	1999	Chi-Chi,Taiwan	CHY101	CWB
9	7.3	1992	Landers	Coolwater	SCE
10	7.5	1999	Kocaeli,Turkey	Duzce	ERD
11	6.9	1989	Loma Prieta	Gilroy Array #3	CDMG
12	6.5	1979	Imperial Valley	Delta	UNAMUCSD
13	6.5	1979	Imperial Valley	El Centro Array #11	USGS
14	7.1	1999	Hector Mine	Hector	SCSN
15	6.7	1994	Northridge	Canyon Country-WLC	USC
16	6.7	1994	Northridge	Beverly Hills - Mulhol	USC
17	6.9	1995	Kobe,Japan	Nishi-Akashi	CUE
18	6.6	1971	San Fernando	LA-Hollywood Stor	CDMG
19	7.0	1992	Cape Mendocino	Rio Dell Overpass	CDMG
20	6.9	1995	Kobe,Japan	Shin-Osaka	CUE
21	7.6	1999	Chi-Chi,Taiwan	TCU045	CWB
22	7.3	1992	Landers	Yermo Fire Station	CDMG

A period range of 0.2T-1.5T, where T is the fundamental period of the elastic structure was chosen for scaling and matching. This range is commonly used to capture the response of a structure over its entire range of periods; 0.2T is assumed to reflect the period range of significant higher modes, while 1.5T is assumed to capture the period of the structure once it softens post-yielding. To accomplish the spectral matching, the motions were modified in the time domain through the wavelet algorithm proposed by Abrahamson (1992) and Hancock et al. (2006) using the

SeismoMatch software package (Seismosoft, 2013). Figure 5.8 illustrates the different scaled response spectra of the ground motions compared to the NBCC design spectrum for four building prototypes. For each model designed to a trial R_d factor, a suite of nonlinear dynamic analyses were conducted to assess the variability in the response of the model. Based on this variability, an appropriate R_d factor was determined in order to provide acceptable performance with a high degree of confidence.

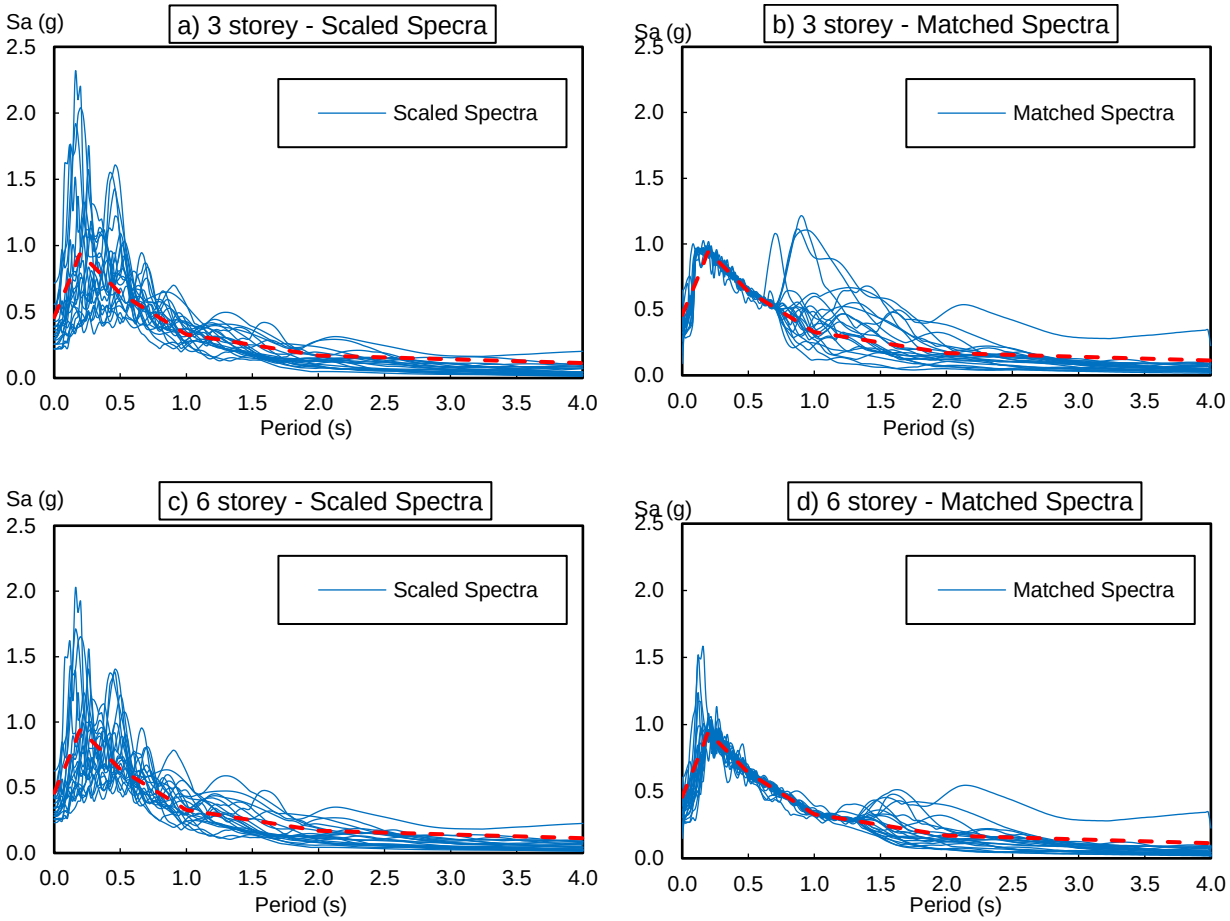

Figure 5.8 Spectra for ground motions: a) 3-storey model using linear scaling; b) 3-storey model using spectral matching; c) 6-storey model using linear scaling; d) 6-storey model using spectral matching;

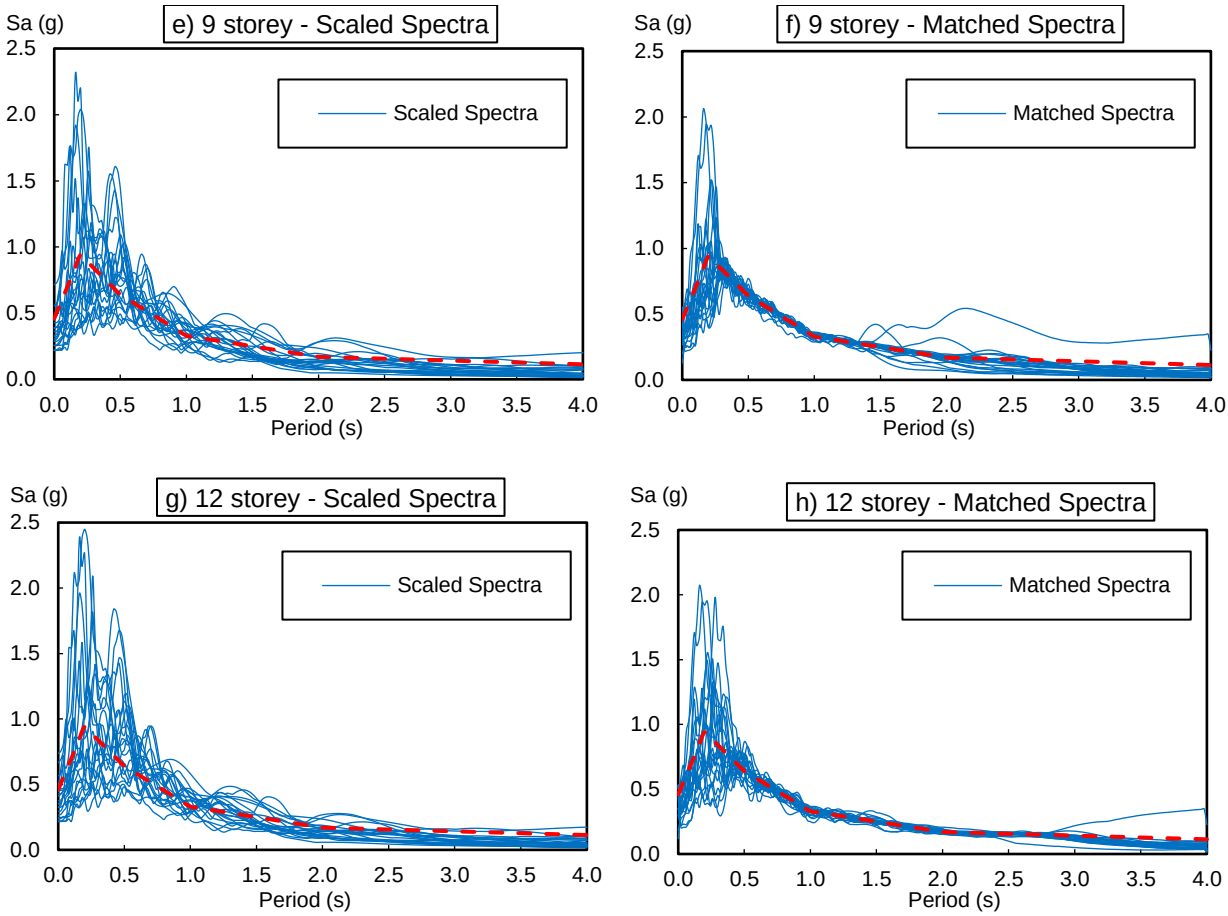

Figure 5.8 continued: e) 9-storey model using linear scaling; f) 9-storey model using spectral matching; g) 12-storey model using linear scaling; h) 12-storey model using spectral matching

5.3.5 Two-dimensional nonlinear time-history analysis results

In the nonlinear time history analysis, 20 sets of models (10 sets of models with different R_d factors ranging from 1.5 to 6.0 in steps of 0.5 for both the DSB and SSB beam section methods) were developed for the four building heights. A total of 80 models were analyzed for two suites of the scaled 22 acceleration time history records (linear scaling and spectral matching). The absolute maximum interstorey drift observed in each model for each analysis was recorded and rank-ordered.

In NBCC (NRC, 2010), the largest interstorey deflection at any level is limited to 0.025 h_S, where h_S is the storey height (equivalent to 2.5% interstorey drift). Therefore, if a design is capable of limiting the maximum interstorey drift to this performance for the majority of the 22 earthquake records, the R_d factor used in that design can be regarded as appropriate. Herein, a probability of drift non-exceedance of 90% was considered, meaning that a minimum of 90% of the motions must meet the interstorey drift requirements for the trial R_d factor to be acceptable.

The empirical cumulative distribution functions (CDFs) of the maximum interstorey drifts for different R_d factors and the two steel beam selection methods (DSB and SSB) under the two ground motion suites are presented in Figure 5.9 for the 3-storey building; Figure 5.10 for 6 storey building; Figure 5.11 for 9 storey building; and Figure 5.12 for 12 storey building. Based on the CDFs of interstorey drifts it can be seen the all R_d values that satisfy the performance expectations (2.5% drift with 90% probability of non-exceedance) within all the beam selection and time-history scaling methods.

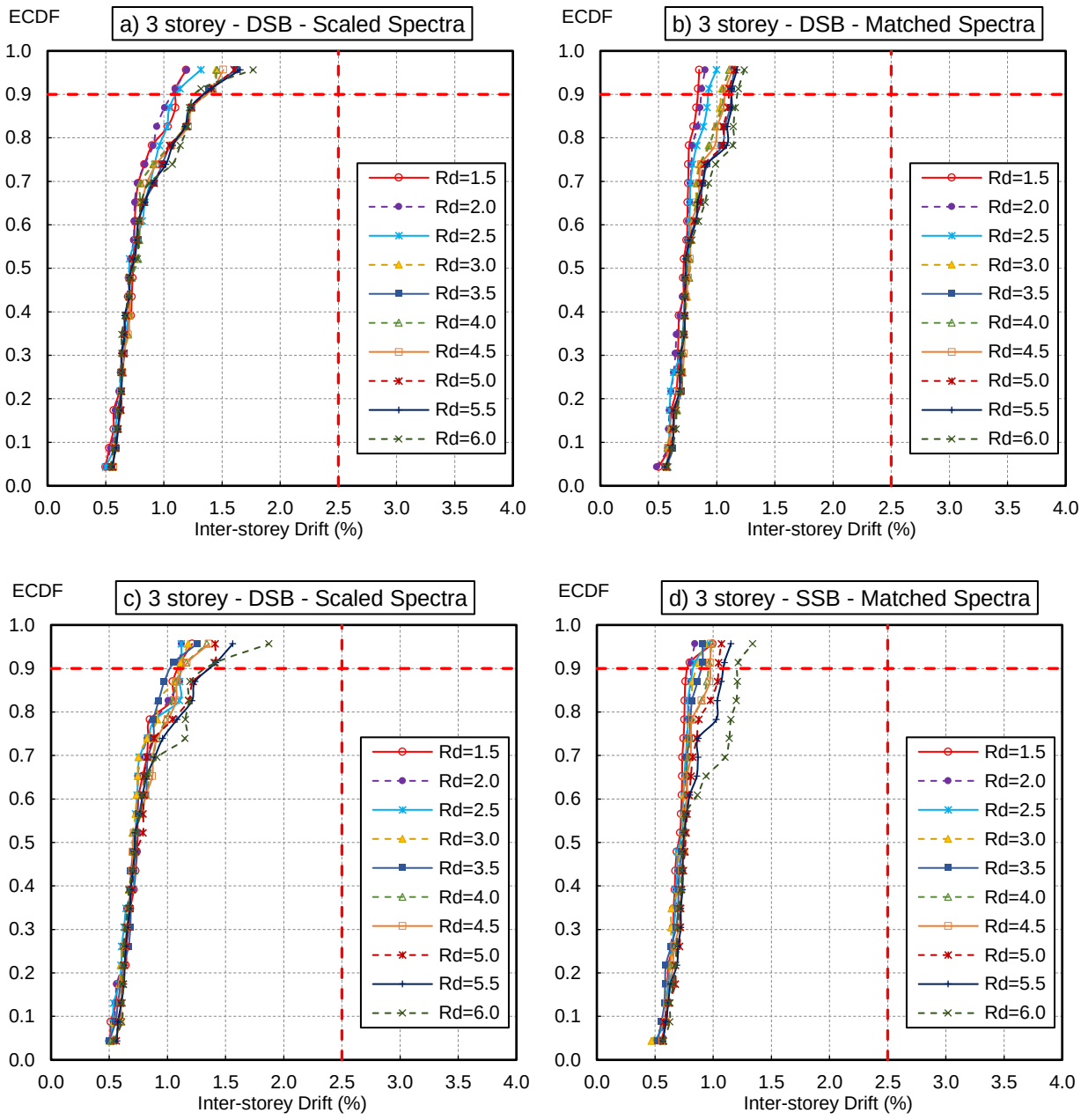

Figure 5.9 Cumulative distribution functions of maximum interstorey drift for 3-storey building: a) DSB steel beam selection method and scaled response spectra; b) SSB steel beam selection method and scaled response spectra; c) DSB steel beam selection method and matched response spectra; d) SSB steel beam selection method and matched response spectra

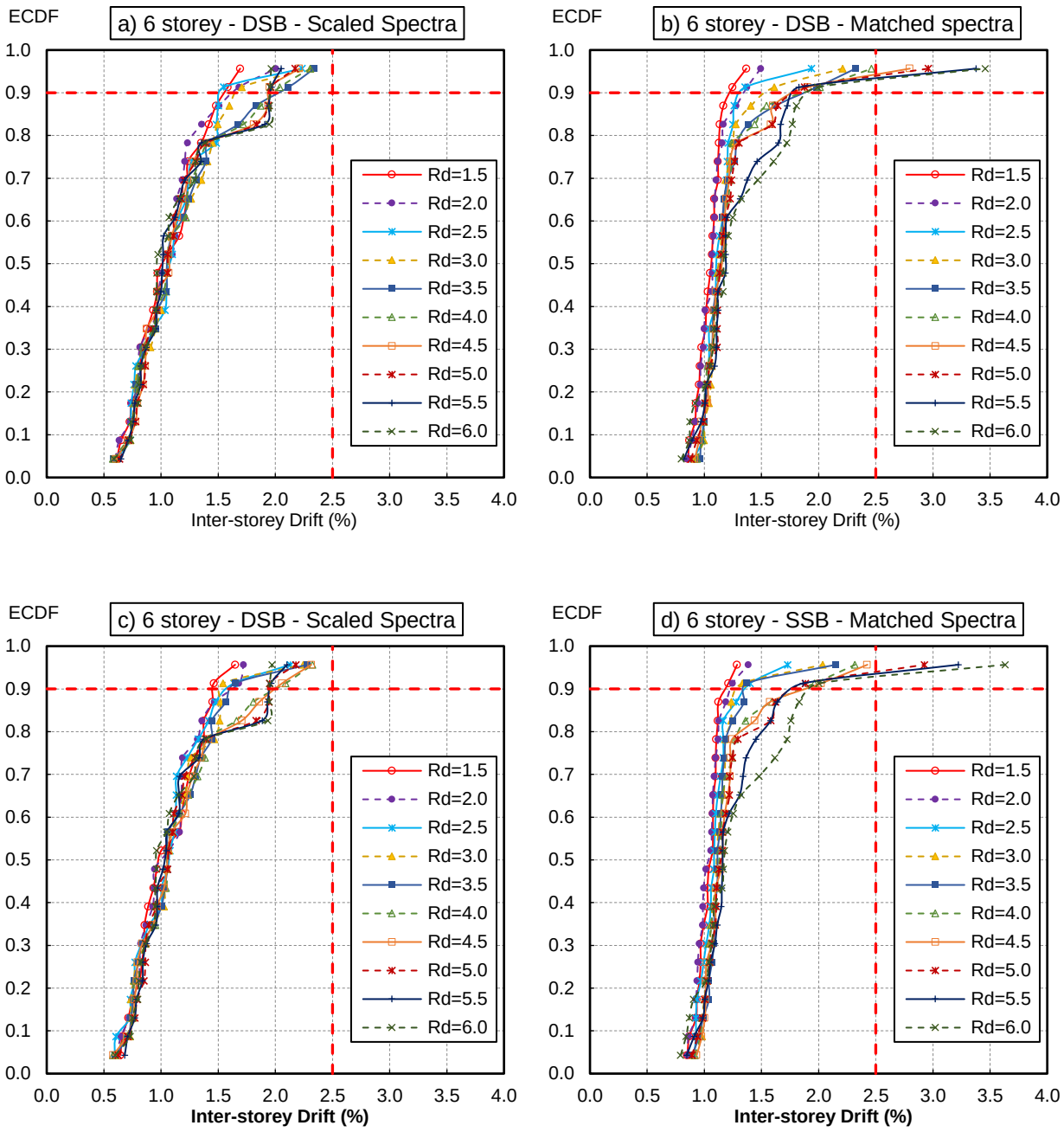

Figure 5.10 Cumulative distribution functions of maximum interstorey drift for 6-storey building: a) DSB steel beam selection method and scaled response spectra; b) SSB steel beam selection method and scaled response spectra; c) DSB steel beam selection method and matched response spectra; d) SSB steel beam selection method and matched response spectra

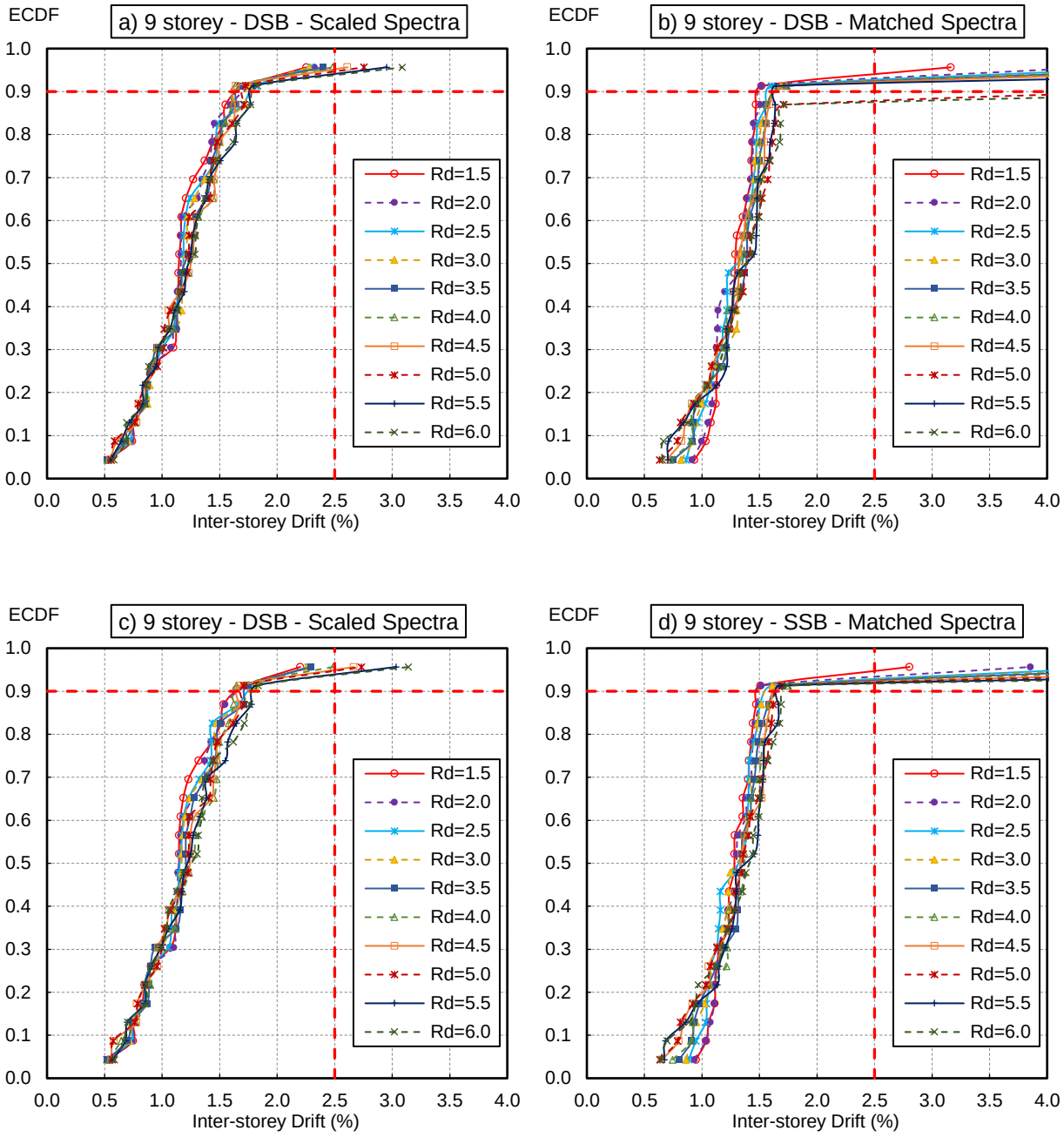

Figure 5.11 Cumulative distribution functions of maximum interstorey drift for 9-storey building: a) DSB steel beam selection method and scaled response spectra; b) SSB steel beam selection method and scaled response spectra; c) DSB steel beam selection method and matched response spectra; d) SSB steel beam selection method and matched response spectra

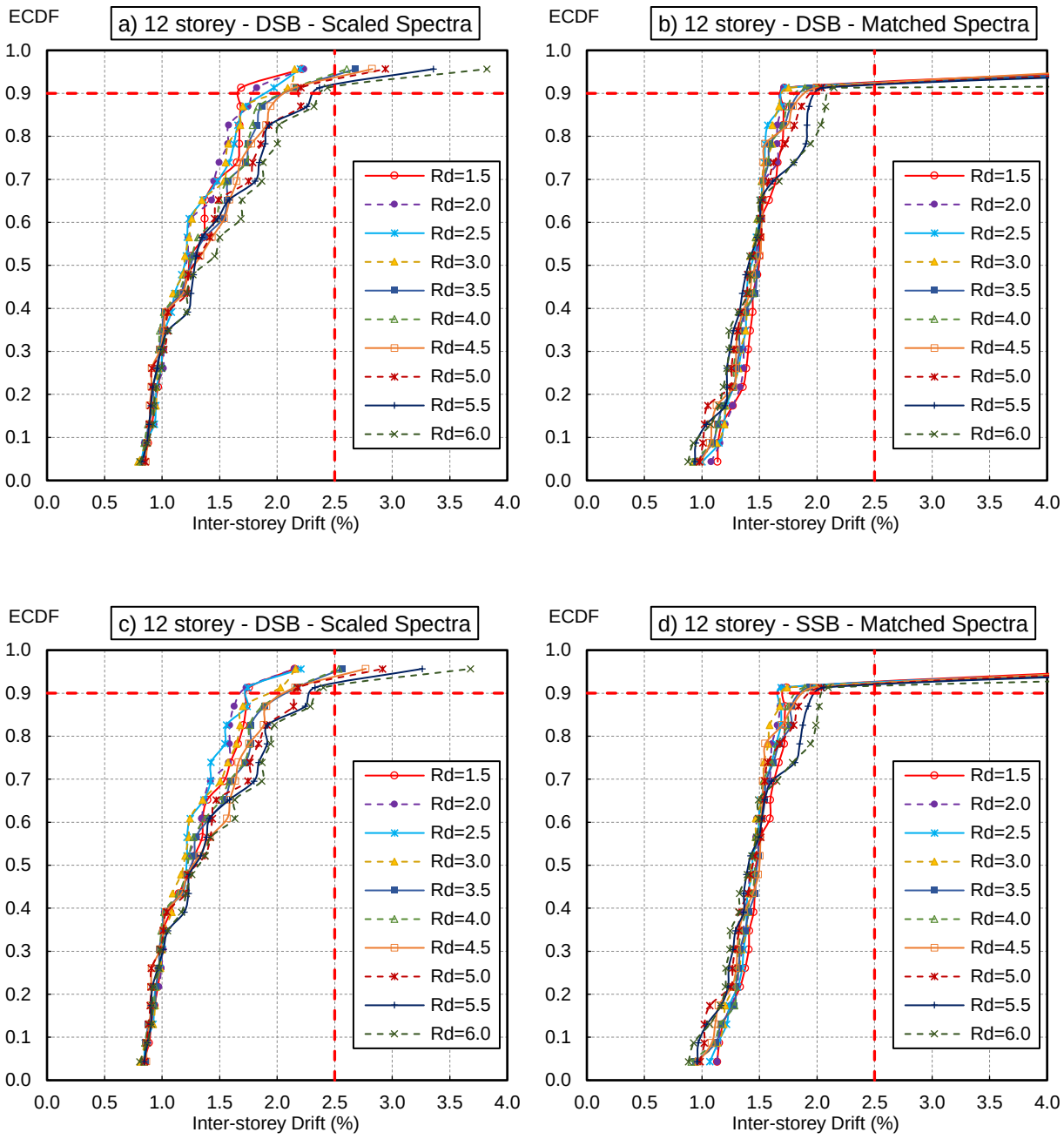

Figure 5.12 Cumulative distribution functions of maximum interstorey drift for 12-storey building: a) DSB steel beam selection method and scaled response spectra; b) SSB steel beam selection method and scaled response spectra; c) DSB steel beam selection method and matched response spectra; d) SSB steel beam selection method and matched response spectra

Figure 5.9 to Figure 5.12 illustrat the results for the SSB and DSB steel beam selection methods along with both record modifying approaches. All investigated R_d factors met the design requirements. However, for timber-steel hybrid systems, no higher ductility factor can be recommended than that applied for a ductile moment-resisting steel frame. Therefore an R_d factor of 5.0 is proposed as an acceptable conservative measure for Option 1 of the FFTT system designed up to 12 storeys. This value, seemingly high for a timber-based system, is reasonable since in the FFTT system, the steel beams are designed to yield. Assuming that most of the ductility comes from the steel beams, the ductility factor should be similar to that of ductile moment-resisting frames steel structures as defined in the NBCC (NRC, 2010). In NBCC (NRC 2010), the R_d of this type of structure is also equal to 5.0.

For the analyses using the DSB steel beam selection method and the second scaling methods, they showed very similar results indicating that neither the record scaling method nor the steel beam selection method have any significant impact on the results. Especially for beam section method, where the cumulative distribution functions of maximum interstorey drift curve are almost the same for DSB and SSB.

One important aspect to be considered is that for tall wood structures is that wind loads may govern the lateral design, and the actual design may be different than that assumed for these analyses. Nevertheless, the simplified models presented in this paper provide valuable input about the potential R_d factors that can be applied for the FFTT system. The subsequent investigation for the 12-storey FFTT system using a 3D global finite-element model is used to verify the suitability of the proposed R_d factor.

5.4 3D numerical investigation of FFTT system

5.4.1 Numerical model

In order to verify proposed reduction factors, a more sophisticated nonlinear 3D model was developed using the OpenSees framework. The model was for a 12-storey building with the floor plan according to Option 1 of the FFTT system (Figure 5.1). The interior core walls were modeled with shell elements using an elastic orthotropic material, similar to the 2D models in the previous section. The gravity-resisting glulam perimeter frame was modeled with elastic beam-column elements and pinned between connecting elements.

The concentrated plasticity steel beam and material models developed for the 2D models were utilized. Base connections were modeled similarly to the 2D models and slabs were not explicitly modeled but accounted for through rigid diaphragm constraints at each storey.

The section properties used for the timber members are listed in Table 5.5. Material properties were based on the Canadian Wood Design Manual (CSA-O86, 2010). The stress state in all timber members was recorded throughout all analyses to ensure crushing did not occur in the elastically modeled members. Rayleigh damping (5%) was considered for the model. The appropriate load combined from NBCC (NRC, 2010) was 1.0DL + 0.5LL + 0.25SL, where DL is the dead load, LL is the live load, and SL is the snow load which also considers rain. Gravity loads are summarized in Table 5.7. The steel beams in the structure were designed using the ESFP with an R_dR_o = 7.5 (R_d = 5.0). The location of the structure was taken as Vancouver, British Columbia, and the design spectrum considered was the same NBCC Vancouver 2% in 50-year spectrum considered in for the 2D design and analyses. Base on the obtained results from 2D analysis, it is known that the beam selection method doesn't have a significant influence on the seismic behavior of the FFTT

system. In this case, the steel beam used in 3D model were selected based on SSB method as it is a more practical method for real construction. The resulting design steel sections are listed inTable 5.8.

Table 5.7 Design gravity loads

Load	Floors	Roof
Dead	4.0 kpa (+ perimeter walls)	3.0 kpa
Live	1.9 kpa	1.8 kpa
Snow	-	1.8 kpa
Rain	-	0.2 kpa

Table 5.8 Steel section summary

Storeys	Section	Yielding Moment (kNm)
1-3	W310x28	121.1
4-6	W200x31	103.2
7-9	W250x25	91.8
10-12	W150x18	41.4

5.4.2 Ground motion selection and scaling

The same 22 FEMA P-695 (FEMA, 2009) far-field record set as used to analyze the 2D models was also considered for the analyses of the 3D models. As a first method to make the records compatible with the Vancouver spectrum, the geometric means (geomeans) of the ground motions were linearly scaled with a constant scaling factor to match the Vancouver spectrum between periods of 0.2T to 1.5T on average (where T is the fundamental period of the model). As a second modification method, the motions were spectrally matched in both directions to the Vancouver spectrum for the same period range. Figure 5.13 shows the spectral values of the ground motion suite obtained using these two common record modification methods.

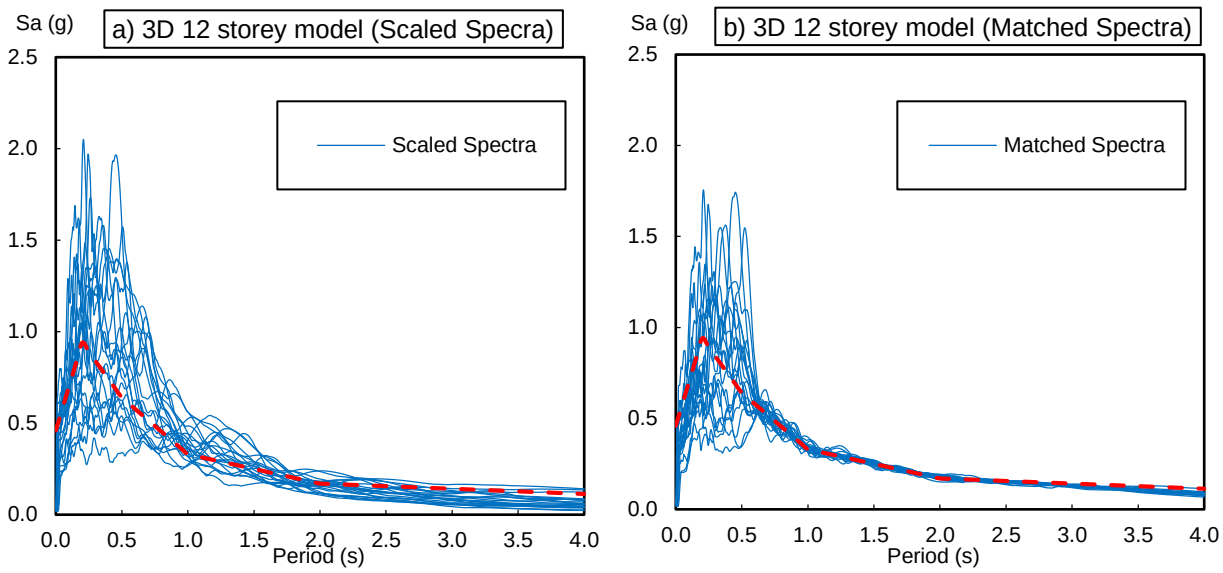

Figure 5.13 Spectral accelerations: a) linearly scaled motions; b) spectrally matched motions for the 12-storey 3D model

5.4.3 Three dimensional nonlinear time-history analysis results

The two suites of scaled bidirectional motions were applied to the model in both of its primary directions (Direction 1: East-West; Direction 2: North-South). Figure 5.14 presents the interstorey drift results. The mean and 90th percentile results from the maximum response observed from the 22 motions are presented, along with the minimum and maximum values to give insight into the range of results. The maximum response was observed when the primary component of the motions was applied in Direction 2 (North-South) of the models, and the mean of the suite of results was approximately 1.25% drift. The 90th percentile drift was approximately 1.5%, which is reasonable and expected given that the reduction factors were chosen to give 90% or greater probability of non-exceedance at 2.5% drift. However, the extreme events result in larger interstorey drifts. Although the maximum observed values are quite extreme, mean results are typically used in design and the maximum values are only included to show the range of the results. Additionally the interstorey drift was relatively constant over the height of the structures, meaning

that the core walls were almost rigid and rocked at their base, distributing damage over the height of the building, rather than concentrating it at certain storeys. Once again, the results were insensitive to the type of record modification method used.

As a further performance criterion, the plastic beam rotations and maximum accelerations were computed. The plastic rotation limit in the steel beams was set to 0.05 rad in order to achieve life safety performance based on a similar methodology as employed in ASCE/SEI 41-13 (ASCE, 2014), in which life safety is defined at the plastic rotation (total rotation minus elastic) where strength degradation in the hinge begins. The plastic rotations are illustrated in Figure 5.15 show that the mean results, which are typically used for design and assessment, meet this rotational limit. The extreme events results in larger plastic rotations. These extreme rotations, however, do not necessarily affect the life safety of the structure. Large beam plastic rotations only decrease the stiffness and coupling of the beams, making the structure more flexible, potentially allowing for larger interstorey drifts.

Finally, Figure 5.16 illustrates the accelerations observed at each storey. Accelerations peaked at the base and near the top of the structures, but were within reasonable limits to maintain nonstructural integrity throughout the structures. The results were insensitive to the type of record modification method used.

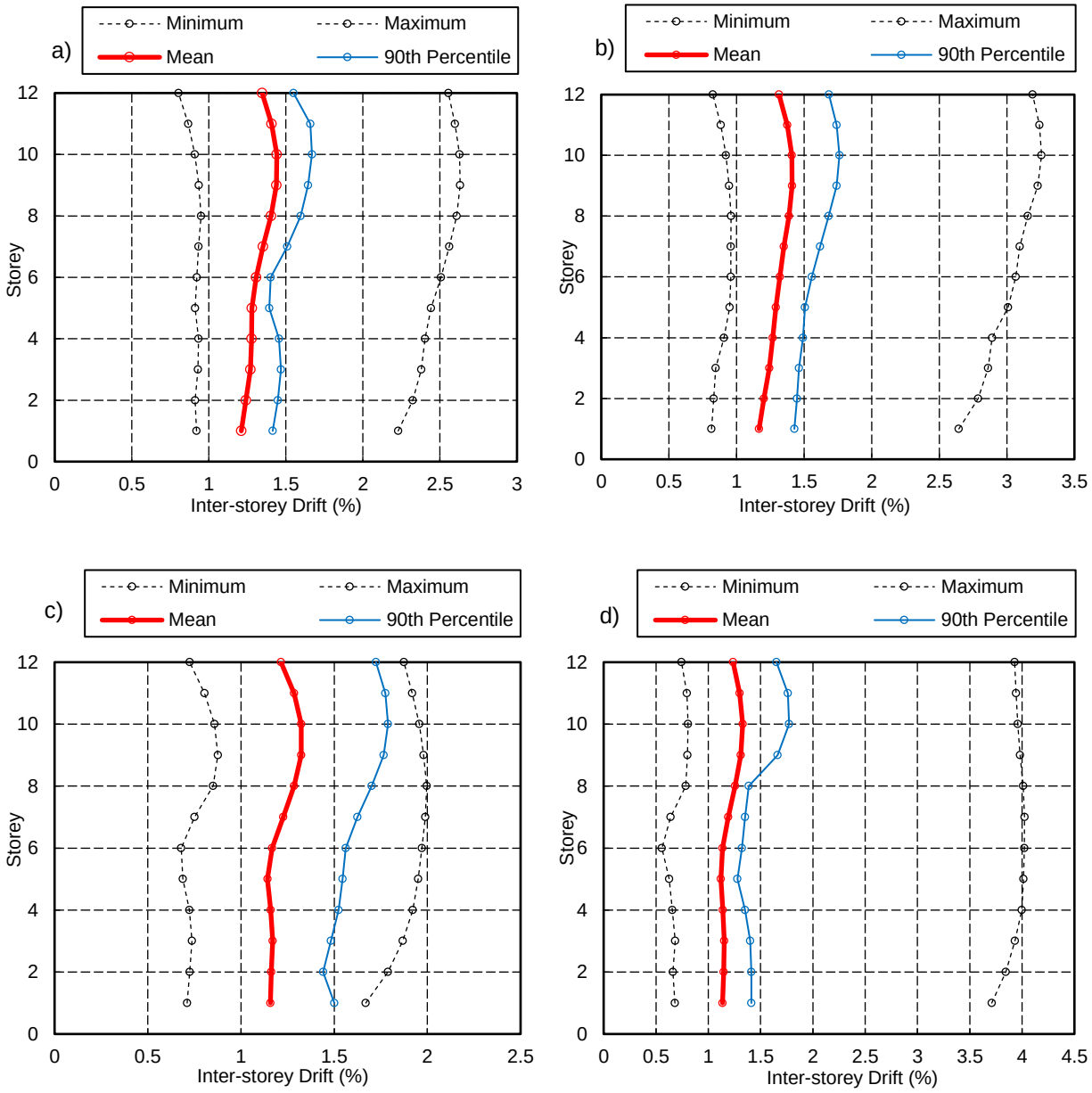

Figure 5.14 Interstorey drift results from 3D model with a) spectrally matched motions with the primary component applied in direction 1; b) spectrally matched motions with the primary component applied in direction 2; c) linearly scaled motions with the primary component applied in direction 1; d) linearly scaled motions with the primary component applied in direction 2

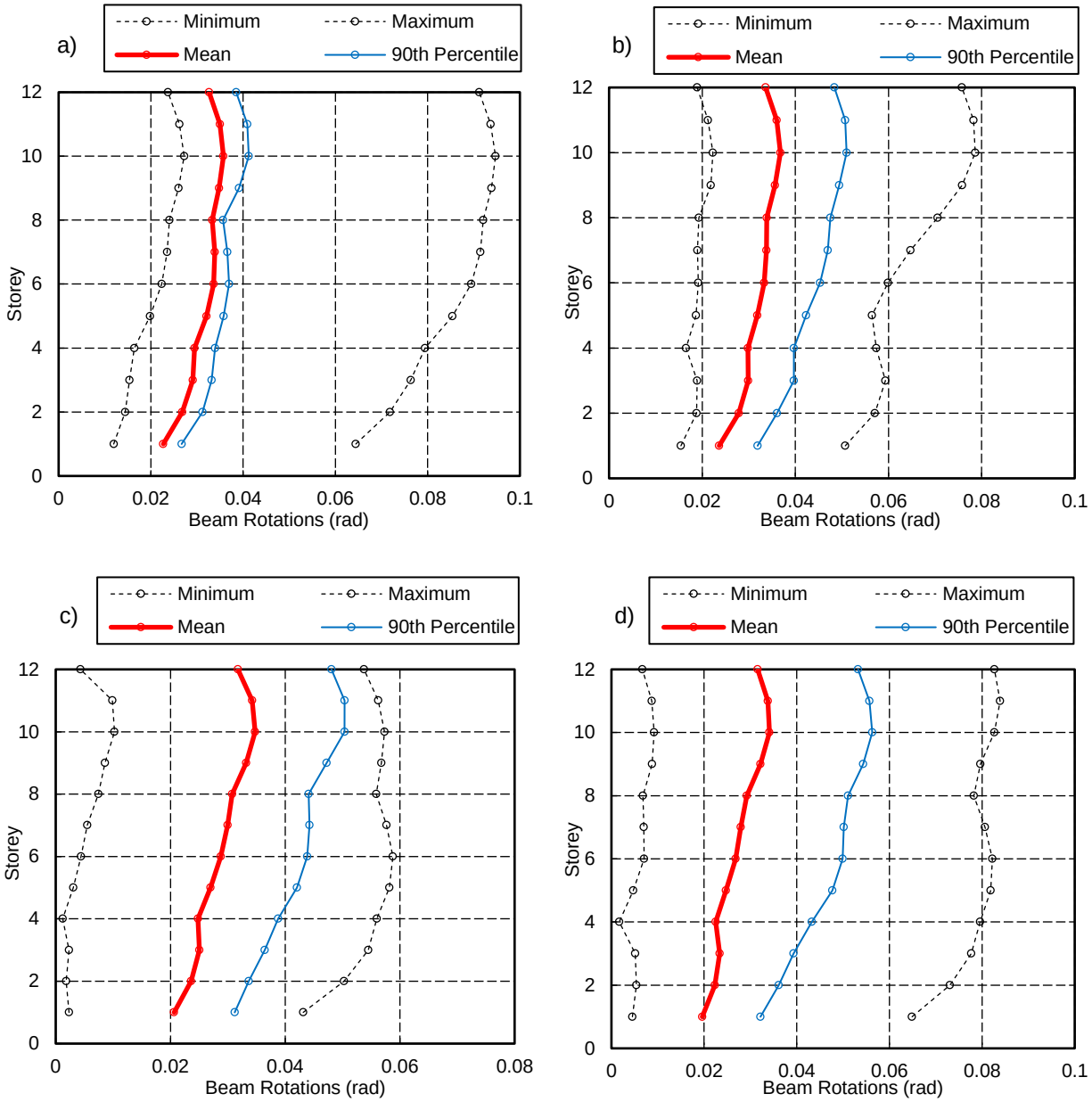

Figure 5.15 Steel beam rotations from 3D model with a) spectrally matched motions with the primary component applied in direction 1; b) spectrally matched motions with the primary component applied in direction 2; c) linearly scaled motions with the primary component applied in direction 1; d) linearly scaled motions with the primary component applied in direction 2

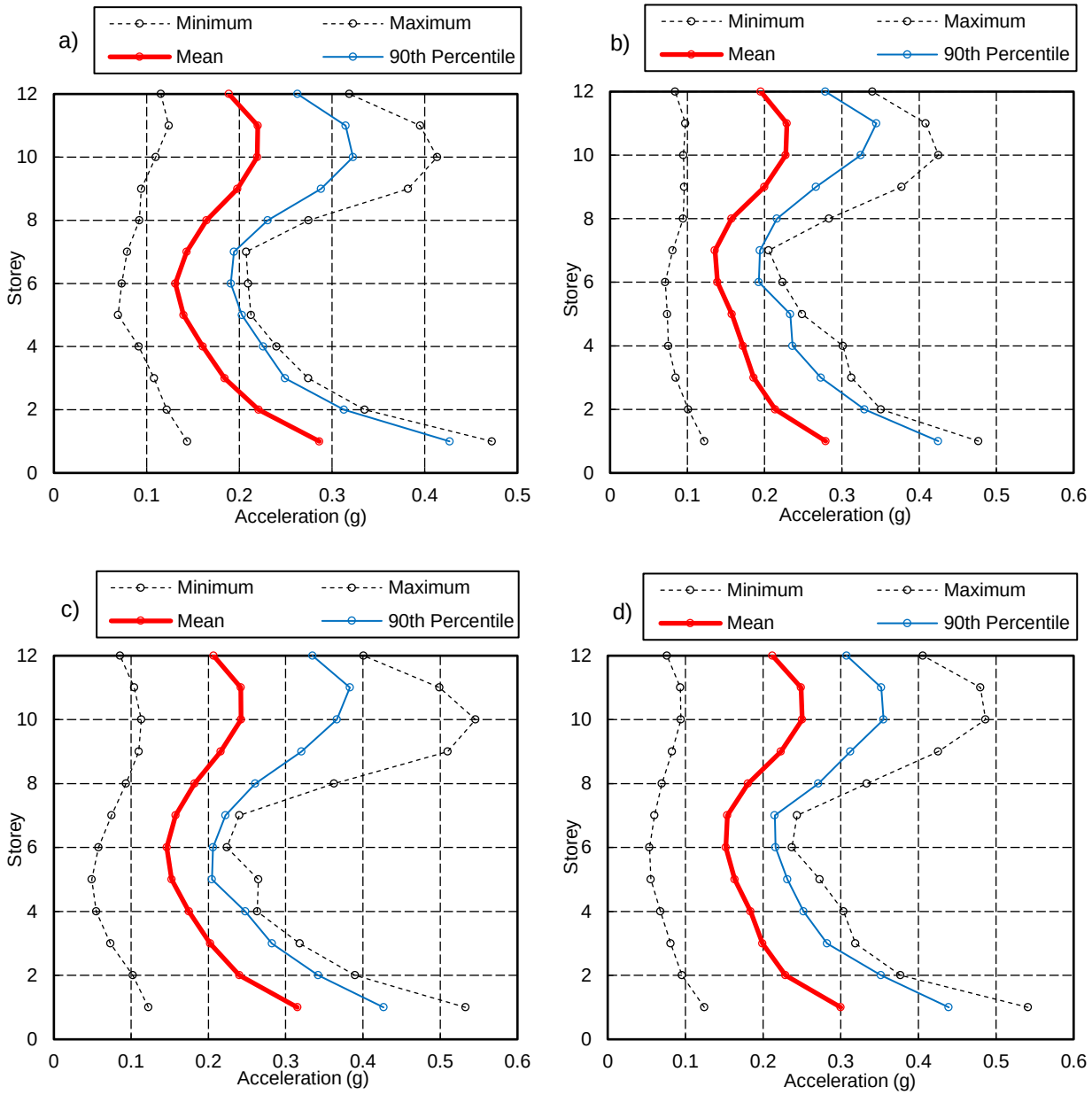

Figure 5.16 Storey accelerations from 3D model with a) spectrally matched motions with the primary component applied in direction 1; b) spectrally matched motions with the primary component applied in direction 2; c) linearly scaled motions with the primary component applied in direction 1; d) linearly scaled motions with the primary component applied in direction 2

5.5 Summary

This Chapter discussed a methodology to determine R_d factors for simplified nonlinear models for structural systems. An example of Option 1 of the FFTT system, a novel timber-steel hybrid system proposed for buildings up to 12 storeys tall (Green and Karsh, 2012), was used to illustrate this methodology. The presented approach can be generalized for other structural systems.

Two different approaches to determine the steel beam cross sections were studied, as follows: (1) varying steel beams at each floor level, and (2) varying steel beams after every third story. Nonlinear dynamic analyses were conducted on both 2D and 3D models. The 2D models were analyzed with 22 unidirectional ground motion records, while the 3D model was subjected to a suite of 22 bidirectional motions. In each case, the records were modified to match the target design spectrum using two commonly used modification methods: (1) linear scaling, and (2) spectral matching. From the results presented in this chapter, the following main conclusions can be drawn:

1) Based on nonlinear dynamic analysis of 80 2D numerical models, a ductility-related seismic reduction factor $R_d = 5$ is recommended, on a preliminary basis, for Option 1 of the FFTT system. This reduction factor yields acceptable mean and 90^{th} percentile interstorey drifts, regardless of the ground motion modification method considered.

2) The subsequent 3D numerical investigation of a 12 story building, based on FFTT Option 1, supported the suitability of the estimated R_d factor equal to 5, as both the mean and 90^{th} percentile interstorey drifts were well below the 2.5% limit.

3) Using an R_d factor equal to 5.0, the mean steel beam plastic rotations also met the life safety performance criterion for a flexural deformation-controlled beam. Compared to pure mass-timber

buildings that may be limited by an R_d factor equal to 2.0, the FFTT system benefits significantly from the ductile behavior of the interconnecting steel members.

4) The selection of the steel beam cross sections has little impact on the building period, and consequently, the more practical SSB method (with identical cross sections over 3 storeys) is recommended. The results were insensitive to the ground motion modification method utilized.

Chapter 6: Reliability Analysis for FFTT system [4]

6.1 Introduction

Reliability analyses are of great importance in performance-based seismic structural design as there are inherent uncertainties in both the actions (earthquakes) and the reactions (properties of the structural systems). As mentioned in section 2.4, most of the current seismic reliability research are mainly related on steel and reinforced concrete structures and to some extent, the light frame middle/low-rise structure. For mass timber tall wood-based high-rise buildings, seismic reliability study is still a novel filed. Reliability analyses form the basis of "Performance-Based Design Guidelines" (FEMA, 1997) and allow for quality control procedures in the design process. Using reliability-based procedures, novel structural systems, such as the FFTT system, that are not covered by building codes can be designed to be as "safe" as other systems that are explicitly referred to in building codes.

FFTT system, as an example of novel timber steel hybrid structure, it is important to assess the seismic reliability to evaluate the influence of the structural input variables of interest for future performance-based design of this timber-steel hybrid system.

6.2 Objective

For any novel structure, there are a variety of uncertainties that should be considered when conducting analyses. The same holds true for the FFTT system. Accordingly, it is difficult to find simple and appropriate equations to represent the data using a response surface method. A

[4] A version of this chapter has been submitted to Engineering Structures. Zhang, X., Shahnewaz M. and Tannert, T. (2017). Seismic Reliability Analyses of Timber-Steel-Hybrid System. (Under Review)

convenient way to do this is to only consider one characteristic structural mass and stiffness along with ground motion and error uncertainty (Li et al., 2011b, Lam et al., 2015). Based on the methods from Li et al. (2011b) and Lam et al. (2015), an increase in the number of considered random variables will lead to more items and higher orders in the function which makes it much more complicated and increases the difficulties when preparing the performance function during the reliability analysis. In this chapter, I extend the application of the method by Li et al. (2011b) to determine response surface database with polynomial functions by considering more uncertainties and simplifying the equations. Two methods are used and compared to process the simplification, one is Analysis of Variance (ANOVA) with stepwise selection method, another is genetic algorithm (GA). Aleatory uncertainty is accounted for in the record-to-record variability in the large suite of ground motions selected and their intensity, and epistemic uncertainty is captured through variability in the structural properties.

The primary objective of this study is to utilize response surface and Second Order Reliability Methods (SORM) to estimate the seismic reliability index, β, of the FFTT system, as example of timber-steel hybrid structure. The secondary objective is to compare the simplification of the ANOVA and GA methods.

6.3 Response surface database

6.3.1 Numerical models of FFTT system

The finite element models developed for the nonlinear dynamic analyses in this chapter are similar to the numerical models previously developed in OpenSees to study Option 1 of the FFTT system under seismic loads, as described in Chapter 5. As there are various uncertainties that must be taken into account when conducting a reliability study, it was necessary to use more

computationally efficient models. Accordingly, in lieu of a grid of 2D shell elements to model the CLT walls, as was used in the models presented in Chapter 5, more efficient TwoNodeLink elements were used. These elements were modeled as three linear springs to provide equivalent axial, shear and bending stiffness to the shell elements. Figure 6.1 shows the schematic sketch of the simplified 2D model for one story of the FFTT system.

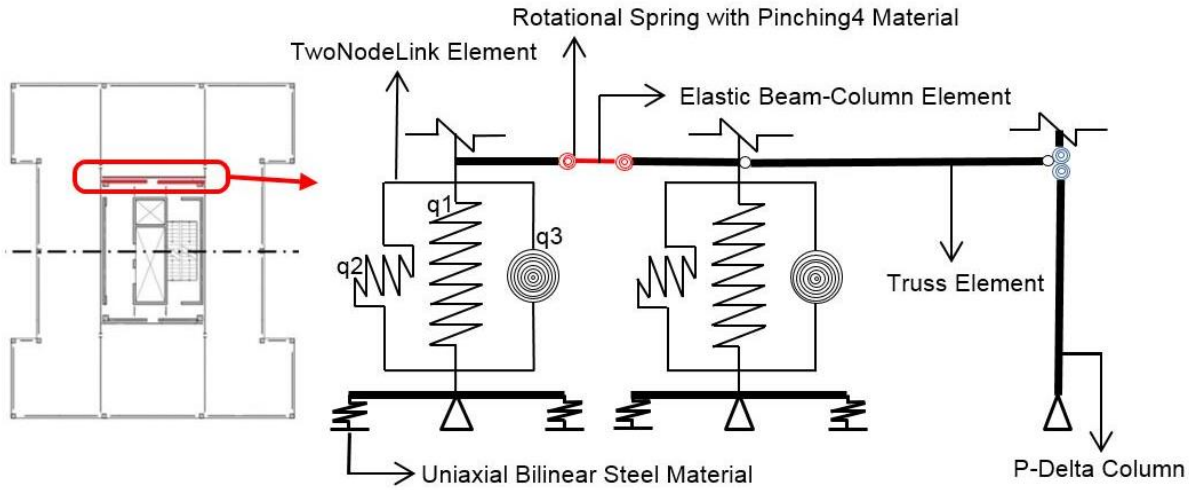

Figure 6.1 Schematic sketch of the simplified 2D OpenSees model for 1 storey of an FFTT building

6.3.2 Uncertainties for consideration

In seismic reliability analyses, uncertainty can be characterized as either 'aleatory' (stems from natural randomness and cannot be reduced) or 'epistemic' (stems from a fundamental lack of knowledge and can be reduced) (Kiureghian and Ditlevsen, 2009). In this study, aleatory uncertainty is accounted for in the record-to-record variability in the large suite of ground motions selected and their intensity. Epistemic uncertainty is captured through modeling variability in the structural properties such as weight and connection properties.

In order to achieve a reliable record-to-record variability estimation, the 22 far-field earthquake ground motions considered in FEMA P-695 (FEMA, 2009) were selected as the ground motion record set and the intensity measure (IM) is represented by the average spectral acceleration over the period range of the models. Because the FFTT system was first proposed for Vancouver, BC, the 5% damped 2% in 50 year spectrum for Vancouver was chosen as the target spectrum to represent the seismic hazard.

First, all 22 individual far-field records are linearly scaled to the Vancouver design response spectrum over the period range of the models. Then these ground motion records are further scaled to multiple intensity levels (25, 50, 75, 100, 125, 150, 175, 200, 225 and 250% of the target spectrum). A period range from $0.2T_{low}$ to $1.5T_{high}$ was chosen, where T_{low} is the lowest fundamental period and T_{high} is the largest fundamental period of all of the models based on selected weight (mass) and hold-down stiffness level. Although the ductility factor, R_d, for the FFTT Option 1 was recommend equal to 5.0 based on the ductility study in Chapter 5, the seismic reliability study presented herein considers three FFTT prototypes with different ductility design factors (R_d=3.0, 4.0 and 5.0) in order to investigate the effect of variations of the R_d factor. The scale range is different for different ductility factor, Figure 6.2 gives an example of the scaled response spectra of the 22 records for a 12-story FFTT system building designed with a ductility factor R_d = 3.0.

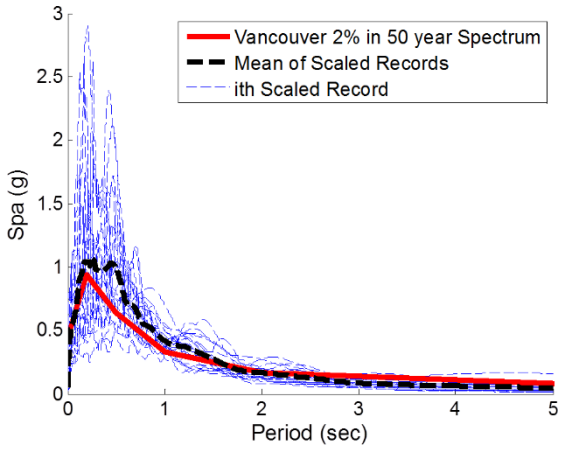

Figure 6.2 Scaled response spectra for a 12-storey FFTT system with a ductility factor equal to 3.0

As a hold-down solution for the FFTT system, the Holz-Stahl-Komposit-System (HSK-System)™ is chosen based on the study in Chapter 4. To model this as a random variable, four hold-down stiffness levels (2.0，4.0，6.0，8.0×10^5 kN/m) are considered in this study. Three structural weight levels (3.0, 4.0, 5.0 kN/m^2) were taken into account - the calculated mass of the structure is approximately 4.0 kN/m^2. The resulting period ranges (0.416 ~ 4.807s for R_d=3, 0.417 ~ 4.882s for R_d=4 and 0.420 ~ 4.965s for R_d=5) can be used to cover both the elastic and inelastic range of the structures.

Aside from the IM, building weight, and hold-down stiffness, the uncertainty caused by the bearing connection between steel beams and CLT panels is also taken into account. The steel beams are related to the system ductility factor as they are designed to yield and absorb seismic energy. Chapter 5 demonstrated that a properly-calibrated concentrated rotational spring model located at the beam-wall interface can efficiently capture the complete nonlinear behavior of the connection detail including steel yielding and timber crushing, as well as cyclic and in-cycle strength and stiffness degradation. Figure 5.6 illustrates the material model for this connection.

To investigate the influence of the connection properties for the structural reliability, the fitted parameters are considered to be mean values from the test results, as shown in Figure 6.3. In Figure 6.3 the black piecewise linear curve represents the backbone curve and the stiffness, *k*, which are obtained from the test calibration model. The coefficient of variation of *k* is assumed to be 0.2 from a similar study on wood shear walls (Ceccotti and Foschi, 1998). In this case, three different stiffness scale levels (80%, 100%, 120%) were selected to represent the uncertainty of connection stiffness. The red line in Figure 6.3 presents the variation of the stiffness in the bearing connection.

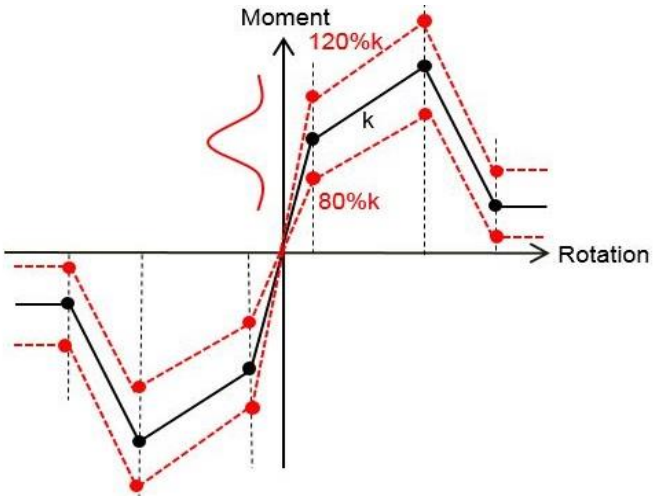

Figure 6.3 Piecewise linear hysteresis backbone curve

For the 12 storey design Option 1 of the FFTT system, buildings designed assuming three different R_d factors (R_d =3.0, 4.0 and 5.0) are studied. For each individual design, the 22 ground motion suite with 10 different intensity levels, three structural weight levels, four hold-down stiffness levels and three connection stiffness levels were considered. A simplifying assumption is made that the peak interstorey drift corresponds to the damage in the FFTT system. In order to obtain the seismic response database, a total of 23,760 nonlinear dynamic analyses were run.

6.4 Optimized polynomial function

Table 6-1 shows the complete range of random variables that were considered in the database. Polynomial functions are required to define both μ_Δ and σ_Δ in order to include interstorey drift as a random variable in the reliability analysis. By doing so, the record-to-record uncertainty of the ground motions is captured in the structural system. A Genetic Algorithm (GA) was used to fit the μ_Δ and σ_Δ of the peak interstorey drift over the domain of the five random variables i.e., IM (x_1), structural weight (x_2), hold-down stiffness (x_3), capping point of the connection hysteresis loop (x_4), and R_d (x_5).

Table 6.1 Range of random variables for 12-storey FFTT system

Random Variables	Min	Max	Mean	SD
R_d (x_5)	3	5	5	0.5
IM (x_1: *%*)	25	225	137.5	71.84
Weight(x_2: *kN/m*^{2})	3.0	5.0	4.0	0.82
Hold-down Stiffness (x_3: *kN/m*)	200000	800000	500000	223710
Connection Stiffness Scale Factor (x_4: *%*)	80	120	100	16.34

In the seismic response database, it is possible to obtain the mean, μ_Δ and standard deviation, σ_Δ of the peak interstorey drift response over the 22 ground motions for each combination of defined variables. Herein, there are 360 sets of μ_Δ and σ_Δ for each ductility design values leading to 1,080 sets in total. For brevity, Table 6.2 provides a partial set of these statistical data of the peak inter-story drift form the 12 storey building.

Table 6.2 Partial set of statistical data of the peak inter-story drift from the 12-storey FFTT model

R_d (x_5)	IM (x_1)	Weight (x_2)	Hold-down Stiffness (x_3)	Connection Stiffness Scale Factor (x_4)	μ_Δ	σ_Δ
	(%)	(kN/m^2)	(kN/m)	(%)	(mm)	(mm)
3	25	4.0	200000	80	12.04	2.87
3	50	5.0	800000	100	23.67	5.42
3	75	4.0	400000	120	33.41	7.71
3	100	5.0	200000	80	49.90	14.15
3	125	3.0	600000	100	44.49	10.42
3	150	4.0	400000	120	61.48	15.15
3	175	3.0	800000	100	59.74	14.76
3	200	4.0	400000	80	82.09	26.29
3	225	5.0	800000	120	92.36	24.72
3	250	3.0	200000	80	99.41	30.11
4	25	4.0	400000	100	12.40	3.20
4	50	5.0	800000	120	23.63	5.42
4	75	3.0	600000	80	29.86	6.59
4	100	4.0	400000	100	42.34	9.31
4	125	5.0	200000	120	60.62	16.80
4	150	3.0	800000	80	51.70	12.62
4	175	4.0	600000	100	70.78	20.26
4	200	5.0	400000	120	86.72	21.88
4	225	3.0	200000	100	90.92	27.71
4	250	4.0	800000	120	96.86	25.44
5	25	3.0	400000	100	12.01	3.45
5	50	5.0	400000	80	24.76	5.75
5	75	3.0	200000	120	32.52	8.56
5	100	5.0	600000	100	44.82	10.24
5	125	4.0	800000	80	50.25	13.19
5	150	3.0	400000	100	55.61	13.45
5	175	4.0	200000	80	78.79	27.41
5	200	5.0	400000	120	89.41	24.26
5	225	3.0	800000	100	80.04	23.36
5	250	5.0	400000	120	111.04	28.55

6.4.1 Polynomial function development using Stepwise Analysis of Variance

This section utilizes Analysis of Variance (ANOVA) for developing the polynomial functions of the mean and standard deviation, μ_{Δ} and σ_{Δ}, of the peak interstorey drift. ANOVA consists of calculations that provide information about levels of variability within a regression model and form a basis for tests of significance (Runger and Montgomery, 2010).

Before involving ANOVA in response surface procedures, a regression to fit the obtained response surface data is performed. Usually, an i^{th} order multivariate polynomial function is used as a potential regression model to fit the data base. All the possible combinations of the random variables will be considered as the components of the regression and all the coefficients of the equation can be obtained by minimizing the square errors between the actual response data and the fitted response surface. However, the higher the order and the more random variables, the more of the components will be exist in the multivariate polynomial function, and that will result in the increased complexity of the reliability analysis. In this case, the stepwise testing methods of multivariate analysis of variance can be used to simplify the equation based on the principle variables (Dempster, 1963).

Based on the stepwise ANOVA methods, the polynomial equations for μ_{Δ} and σ_{Δ} of the peak inter-storey drift over the five random variables can be developed. The database used in the stepwise ANOVA process consisted of 1,080 sets of μ_{Δ} and σ_{Δ} for each different ductility design value.

First, a second order multivariate polynomial regression was used to fit the obtained response surface database. Eq. 6.1 and Eq. 6.2 show the fitting polynomial functions with all possible components and the coefficients in the equations which were obtained by minimizing the square errors between the actual response data and the fitted response surface.

Eq. 6.1

$$\mu_{\Delta} = 3.7 + 27.2x_1 + 2.6x_2 - 1.5e^{-5}x_3 + 4.2x_4 - 2.1x_5 + x_1(3.4x_2 - 6.0e^{-6}x_3 - 3.6x_4 + 1.1x_5) + x_2(1.2e^{-6}x_3 - 0.9x_4 + 0.3x_5) + x_3(8.2e^{-7}x_4 - 5.0e^{-7}x_5) - 1.5x_4x_5 + 0.1x_1^2 - 0.4x_2^2 + 1.1e^{-11}x_3^2 + 3.9x_4^2 + 0.3x_5^2$$

Eq. 6.2

$$\sigma_{\Delta} = -8.8 + 6.9x_1 + 6.1x_2 - 6.7e^{-6}x_3 - 1.2x_4 - 0.1x_5 + x_1(0.7x_2 - 1.7e^{-6}x_3 - 1.7x_4 + 0.5x_5) + x_2(-1.4e^{-7}x_3 - 0.1x_4 - 6.4e^{-3}x_5) + x_3(1.5e^{-6}x_4 - 4.0e^{-7}x_5) - 0.8x_4x_5 + 0.8x_1^2 - 0.7x_2^2 + 5.5e^{-12}x_3^2 + 2.2x_4^2 + 0.1x_5^2$$

Although the F-value for these two equations are 22346.33 and 1302.47, respectively, which imply the fitting modes are significant, the model terms are not all needed and the regressions can be simplified by stepwise ANOVA methods. This procedure iteratively constructs a sequence of regression models by adding or removing variables at each step. The criterion for adding or removing a variable at any step is expressed in terms of a partial F-test. After the selection based on the significant level, all the remaining variables in the selected regression model should have P-value < 0.05 which means they have the highest correlation with the response variable (Runger and Montgomery, 2010). Eq. 6.3 and Eq. 6.4 present the much simpler fitted regressions by using stepwise selecting method with α-in value and α-out value both equal 0.05.

Eq. 6.3

$$\mu_{\Delta,ANOVA} = -0.6 + 27.5x_1 + 2.6x_2 - 1.4e^{-5}x_3 + 12.4x_4 - 2.1x_5 + x_1(3.4x_2 - 6.0e^{-6}x_3 - 3.6x_4 + 1.1x_5) + x_2(1.2e^{-6}x_3 - 0.9x_4 + 0.3x_5) - x_5(5.0e^{-7}x_3 + 1.5x_5) - 0.4x_2^2 + 1.1e^{-11}x_3^2 + 0.3x_5^2$$

Eq. 6.4

$$\sigma_{\Delta,ANOVA} = -12.1 + 6.9x_1 + 5.9x_2 - 7.3e^{-6}x_3 + 3.6x_4 + 0.6x_5 + x_1(0.7x_2 - 1.7e^{-6}x_3 - 1.7x_4 + 0.5x_5) - 0.8x_4x_5 + 0.8x_1^2 - 0.7x_2^2 + 5.5e^{-12}x_3^2$$

Comparing Eq. 6.3 with Eq. 6.1, the terms of x_3x_4, x_1^2, and x_4^2 were selected out as these three parameters are not significant, given the other variables. Comparing Eq. 6.4 with Eq. 6.2, the terms of x_2x_3, x_2x_4, x_2x_5, x_3x_4, x_3x_5, x_4^2, x_5^2 were selected out as these seven parameters are not significant, given the other variables. Table 6.3 illustrates the stepwise ANOVA results for the response surface reduced quadratic models for mean of the interstorey drift, μ_Δ, (Eq. 6.3) and standard deviation of the interstorey drift, σ_Δ, (Eq. 6.4). It can see that these two fitted models are significant and there is only a 0.01% chance that a Model F-Value this large could occur due to noise. At the same time, Values of "Prob > F" for all the considered terms in these two equations are less than 0.05, which indicates all model terms are significant, given the other variables. The goodness of fit, R^2 of the $\mu_{\Delta,\text{ANOVA}}$ and $\sigma_{\Delta,\text{ANOVA}}$ models was found 0.99 and 0.96, respectively, which indicates that the stepwise ANOVA models predicted analytical data with a high level of accuracy. Comparison of the predicted and calculated μ_Δ and σ_Δ database is shown in Figure 6.4. As the 5D response surface of the obtained polynomial functions is difficult to illustrate, Figure 6.5 gives an example of a 3D response surfaces of μ_Δ and σ_Δ obtained from stepwise ANOVA method for the 12-storey FFTT building with a fixed hold-down stiffness, connection stiffness scale factor, and ductility factor (x_3 = 600,000 kN/m; x_4 = 100%; x_5 = 4.0 kN/m^2).

Table 6.3 Stepwise ANOVA for response surface reduced quadratic models

Eq.6.3					*Eq. 6.4*				
Source	Sum of Squares	DF	Mean Square	p-value Prob. > F	Source	Sum of Squares	DF	Mean Square	p-value Prob. > F
Model	867748.6	17	51044.0	< 0.0001	Model	71269.3	13	5482.3	< 0.0001
x_1	678568.8	1	678568.8	< 0.0001	x_1	55241.8	1	55241.8	< 0.0001
x_2	14162.2	1	14162.2	< 0.0001	x_2	887.0	1	887.0	< 0.0001
x_3	1134.7	1	1134.7	< 0.0001	x_3	230.1	1	230.1	< 0.0001
x_4	123.7	1	123.7	< 0.0001	x_4	100.7	1	100.7	< 0.0001
x_5	316.2	1	316.2	< 0.0001	x_5	220.7	1	220.7	< 0.0001
x_1x_2	4354.0	1	4354.0	< 0.0001	x_1x_2	158.7	1	158.7	< 0.0001
x_1x_3	1013.1	1	1013.1	< 0.0001	x_1x_3	83.3	1	83.3	< 0.0001
x_1x_4	189.1	1	189.1	< 0.0001	x_1x_4	43.7	1	43.7	< 0.0001
x_1x_5	423.7	1	423.7	< 0.0001	x_1x_5	95.8	1	95.8	< 0.0001
x_2x_3	50.0	1	50.0	< 0.0001	x_4x_5	11.3	1	11.3	0.0419
x_2x_4	15.5	1	15.5	0.0048	x_1^2	134.7	1	134.7	< 0.0001
x_2x_5	31.2	1	31.2	< 0.0001	x_2^2	123.0	1	123.0	< 0.0001
x_3x_5	8.9	1	8.9	0.0323	x_3^2	52.1	1	52.1	< 0.0001
x_4x_5	42.4	1	42.4	< 0.0001	Residual	2913.2	1066	2.7	
x_2^2	39.3	1	39.3	< 0.0001					
x_3^2	208.4	1	208.4	< 0.0001					
x_5^2	16.1	1	16.1	0.004					
Residual	2065.3	1062	1.9						

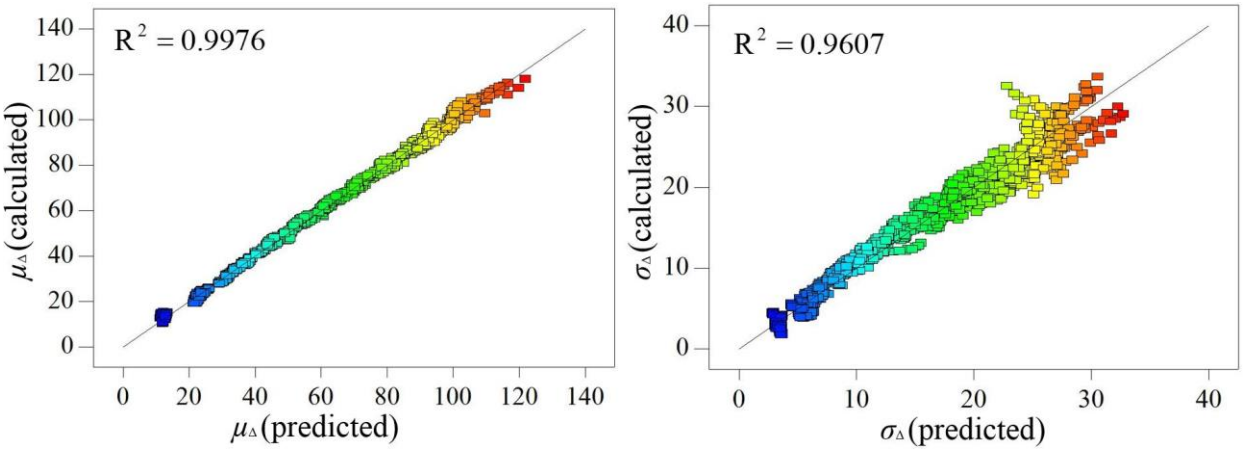

Figure 6.4 Calculated versus predicted models for μ_Δ and σ_Δ from stepwise ANOVA method

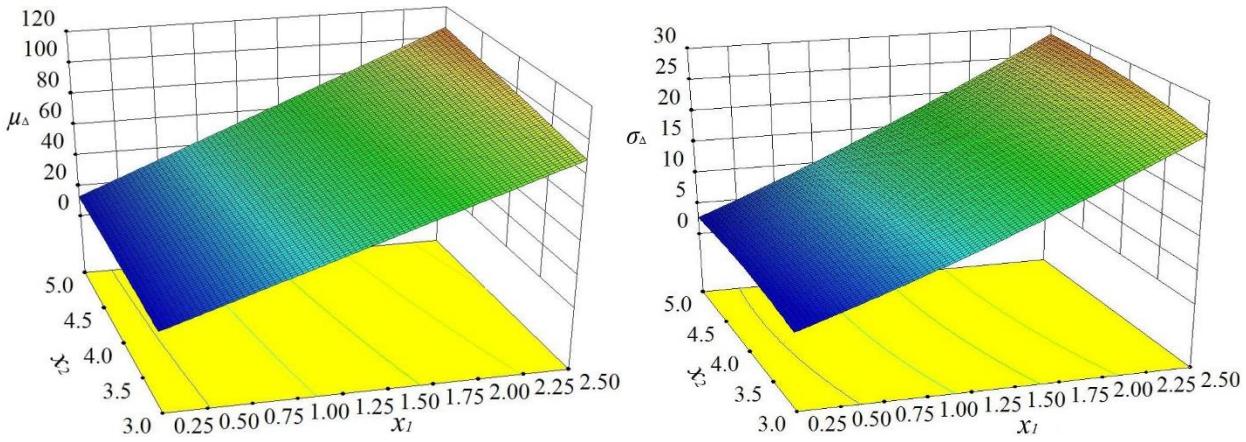

Figure 6.5 3D response surface of μ_Δ *and* σ_Δ *obtained from stepwise ANOVA method for the 12-storey FFTT building with fixed* x_3, x_4, *and* x_5

The regression models only give approximations of the predicted mean μ_Δ and standard deviation σ_Δ. The response surface fitting errors in should be taken into account to adjust the mean μ_Δ and standard deviation σ_Δ ,as shown in Eq. 6.5 and Eq. 6.6:

Eq. 6.5 $$\bar{\mu}_\Delta = \mu_\Delta(1-\varepsilon_{\mu_\Delta})$$

Eq. 6.6 $$\bar{\sigma}_\Delta = \sigma_\Delta(1-\varepsilon_{\sigma_\Delta})$$

where, ε_{μ_Δ} and $\varepsilon_{\sigma_\Delta}$ are random variables representing the response surface fitting errors and assume to follow a normal distribution. The errors of the generic i^{th} combination of the random variables can be calculated are calculated (Li et al., 2011b) by Eq. 6.7 and Eq. 6.8.

Eq. 6.7 $$\varepsilon^i_{\mu_\Delta} = \frac{\mu^i_{\Delta(predicted)} - \mu^i_{\Delta(calculated)}}{\mu^i_{\Delta(predicted)}}$$

Eq. 6.8 $$\varepsilon^i_{\sigma_\Delta} = \frac{\sigma^i_{\Delta(predicted)} - \sigma^i_{\Delta(calculated)}}{\sigma^i_{\Delta(predicted)}}$$

The mean and standard deviation of the overall fitting errors, ε_{μ_Δ} and $\varepsilon_{\sigma_\Delta}$, respectively, can be obtained when all combinations are considered. Therefore, ε_{μ_Δ} and $\varepsilon_{\sigma_\Delta}$ are considered as additional random variables of x_6 and x_7, respectively. After considering the fitting errors, the adjusted mean polynomial functions can be rewritten as Eq. 6.9 and Eq. 6.10:

Eq. 6.9

$$\bar{\mu}_{\Delta,ANOVA} = [-0.6 + 27.5x_1 + 2.6x_2 - 1.4e^{-5}x_3 + 12.4x_4 - 2.1x_5 + x_1(3.4x_2 - 6.0e^{-6}x_3 - 3.6x_4 + 1.1x_5) + x_2(1.2e^{-6}x_3 - 0.9x_4 + 0.3x_5) - x_5(5.0e^{-7}x_3 + 1.5x_5) - 0.4x_2^2 + 1.1e^{-11}x_3^2 + 0.3x_5^2] \times (1 - x_6)$$

Eq. 6.10

$$\bar{\sigma}_{\Delta,ANOVA} = [-12.1 + 6.9x_1 + 5.9x_2 - 7.3e^{-6}x_3 + 3.6x_4 + 0.6x_5 + x_1(0.7x_2 - 1.7e^{-6}x_3 - 1.7x_4 + 0.5x_5) - 0.8x_4x_5 + 0.8x_1^2 - 0.7x_2^2 + 5.5e^{-12}x_3^2] \times (1 - x_7)$$

For the mean of the peak inter-storey drift database (μ_Δ), the mean of and standard deviation of x_6 (ε_{μ_Δ}), was found as 0.025 and 0.030, respectively. Similarly, the standard deviation of the peak inter-storey drift database (σ_Δ), mean of and standard deviation of x_7 ($\varepsilon_{\sigma_\Delta}$), was found as 0.104 and 0.128, respectively. Error mean μ_Δ and standard deviation σ_Δ will be used in the limited state function when considering the error as a random variable.

6.4.2 Polynomial function development using GA method

The GA technique emulates the biological process of the survival of the fittest using three major processes: selection or reproduction, crossover, and mutation, using a population of possible solutions (Goldberg, 1989). In a regression method, a simple form of the relationship among independent and dependent variables is assumed. Then the parameters of the model are determined such that it best fits the data. This is one of the limitations of classical regression methods where

the polynomial function in the analysis is fixed. GA methods can overcome this limitation by searching for the best form of the functional relationship within the optimization process in addition to model parameters (Jeon et al., 2014). GA can "learn" to improve its prediction based on the experiences that it gained from previous steps (Mjolsness and DeCoste, 2001). GA has been widely used to predict various physical models for the experimental and analytical database. Shahnewaz and Alam (2014) developed improved shear equations based on GA where they incorporated statistical analysis to optimize analytical models. Later, they also utilized GA based optimized models for reliability analysis (Shahnewaz et al., 2015). Their GA models had a high level of accuracy which ensures higher structural safety.

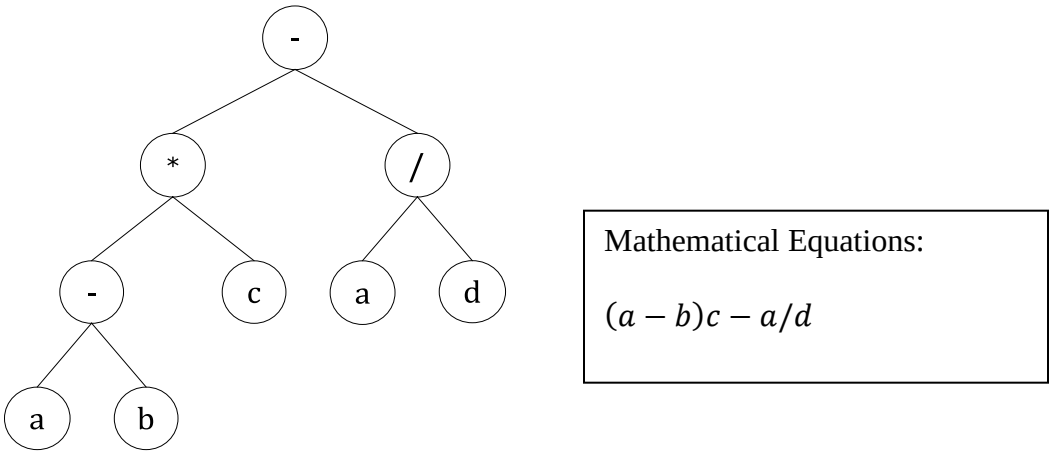

Figure 6.6: Equation tree for GA and corresponding equation

The computer implementation of a GA is hierarchical and its objective is to find a solution within the population by searching for the most fit one. By searching, it makes the problem approach a near global optimum solution. The creation of the initial population is a random search defined by the problem to be solved. A GA program has elements from terminal and functional sets that are called the nodes (Ashour et al., 2003). The terminal nodes (see Figure 6.6) consists of variables such as a, b, c, and the functional set consists of mathematical operators e.g. (+, -, *, /, *exp*, *sqrt*,

log). These operators are used to generate the polynomial functions. To find the best possible solution, GA go through the following steps: a) generate an initial population and terminals of the problem, b) run each program in the population and the solution is selected on the basis of the assigned fitness functions, c) a new population is created by three basic genetic operators: reproduction, crossover and mutation (Shahnewaz et al., 2015).

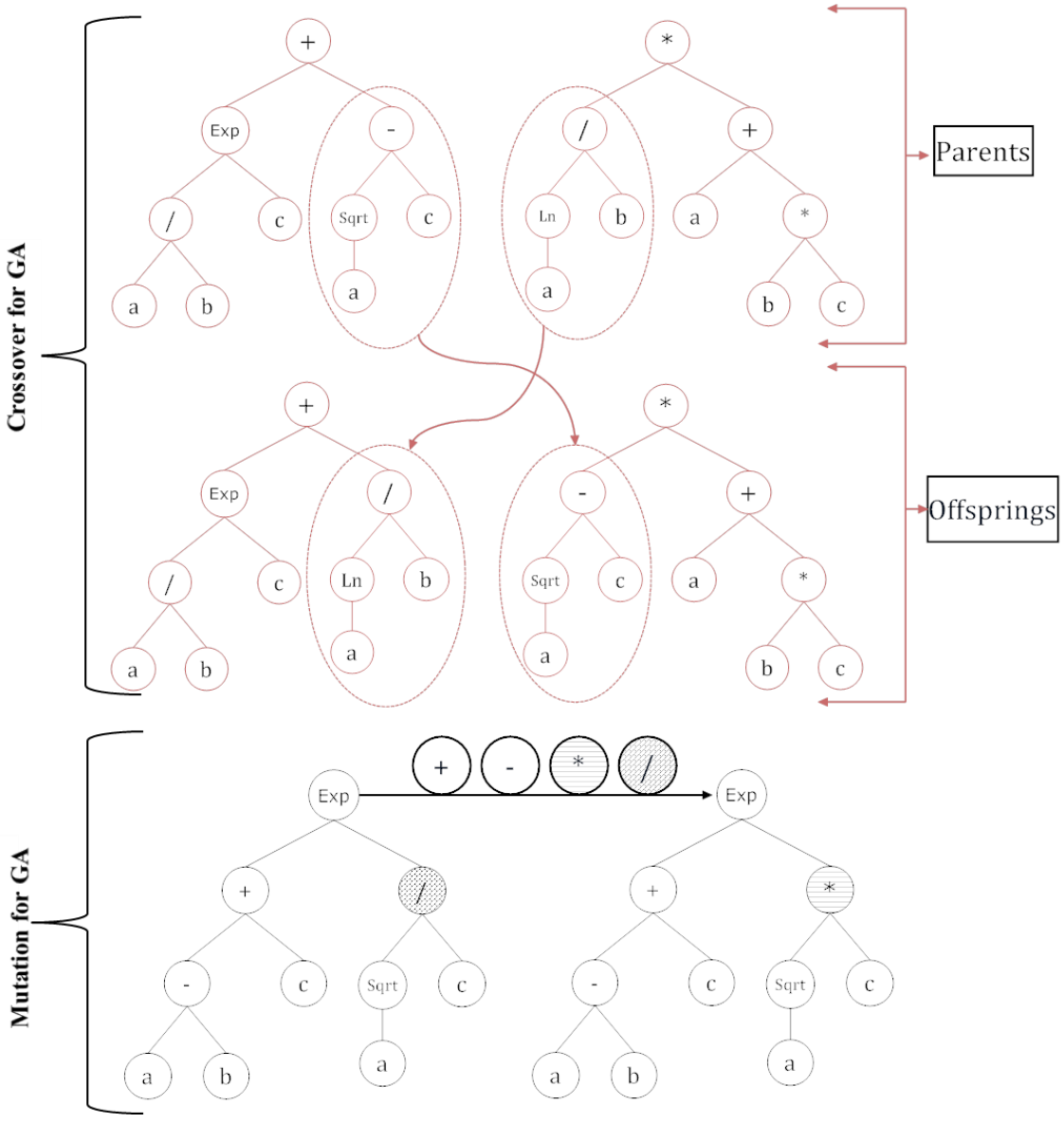

Figure 6.7: Crossover (top) and mutation (bottom) for GA

At first, the fittest individuals are selected in the population for reproduction. In this process, the best solutions are passed to the new population and the worst fitted ones are killed and the populations are filled with the surviving trees (Figure 6.7). The second process, crossover, is the exchange of genetic material between two parents to produce offspring (Figure 6.7). The swapping is done randomly to improve the fitness of the offspring. After crossover is performed, the third process of mutation is done randomly to the offspring adjusting their chromosome. These processes are repeated until the performance of the specimens does not improve significantly. For selecting an expression tree, GA executes a tournament selection procedure that establishes the selection on the basis of the fitness of the solution. For this purposes, GA uses a fitness function. The fitness function checks the accuracy of the expression tree to develop the polynomial function with the experimental or the numerical data.

The GA technique was implemented to develop polynomial equations for μ_Δ and σ_Δ over the domain of the five random variables. In developing the GA equations, the physical relation among the input and output variables was also considered. However, the relationship among all the input variables (x_1 to x_5) and output variables (μ_Δ and σ_Δ) do not have a clear trend due to complex nature of the problem (see Figure 6.8). Figure 6.8 shows the mean value plot for μ_Δ and σ_Δ with respect to x_1 to x_5. It is observed that input variables x_1 and x_2 contributed positively and x_3 contributed negatively to μ_Δ and σ_Δ. On the contrary, no clear trend was found for both x_4 and x_5.

Half of the data was selected randomly from the database and used to develop the GA equation, while the rest of the data was used for the validation purposes. The absolute error metric was used as a fitness function to search for a solution in the GA process. The mathematical operators {+,

$-, *, /, \sqrt{x}\ x^a\}$ were considered for the program runs. The fitness function can be described with the following equation:

Eq. 6.11

$$f_i = \frac{1}{N}\sum_{N=1}^{N}\left|y - f(x)\right|$$

Where, *f(x)* is the GA predicted value over N points and *y* is the experimental or analytical results.

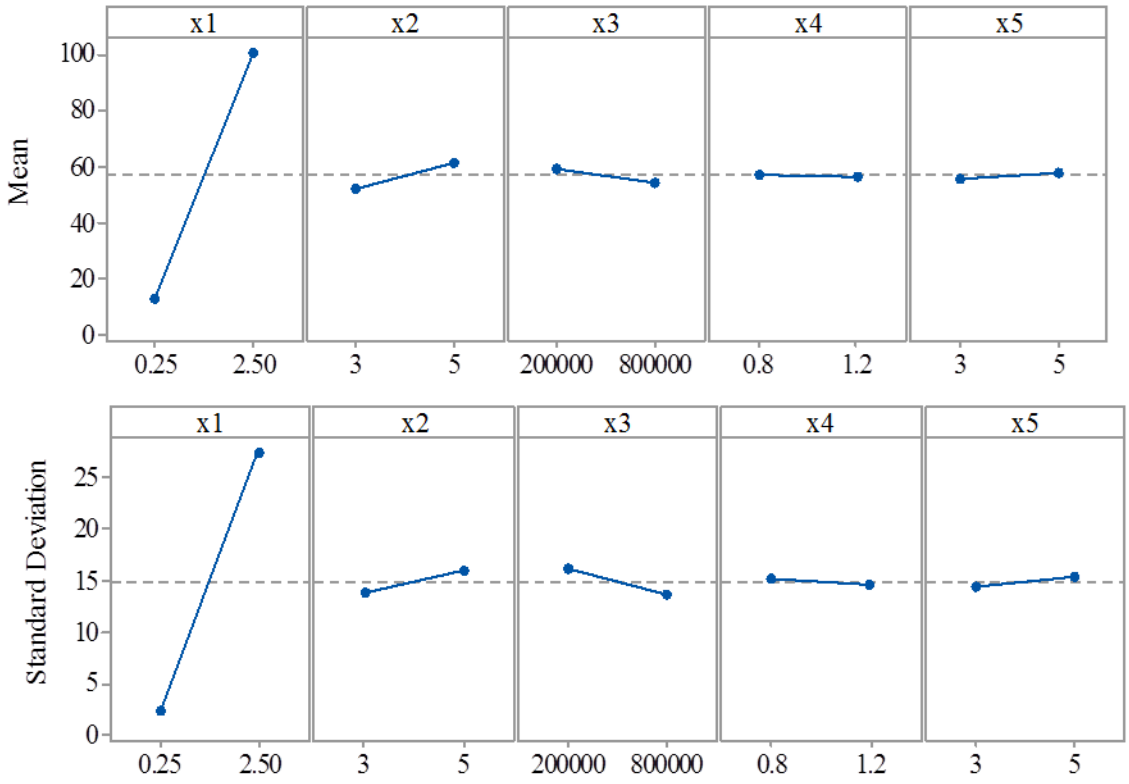

Figure 6.8 Mean (top) and standard deviation (bottom) of the peak interstorey drift versus the random variables

The GA process to establish the polynomial functions for μ_Δ and σ_Δ was run using the Eureqa program developed by Schmidt and Lipson (2009). The best fit polynomial functions for interstorey drift is given as Eq. 6.12 and Eq. 6.13:

Eq. 6.12 $\mu_{\Delta,GA} = 8.44 + x_1\left(26.11 + 3.45x_2 - 6.94e^{-6}x_3 - 1.69x_4 + x_5\right) - 1.14e^{-5}x_3\left(1 - e^{-6}x_3\right) - 0.67x_5$

Eq. 6.13 $\sigma_{\Delta,GA} = 3.32 + x_1\left(1.28 + 1.44x_1 + x_2 - 2.57e^{-6}x_3 + 0.78x_5\right) - 0.49x_4x_5$

Figure 6.9 shows the comparison of calculated vs predicted μ_Δ and σ_Δ from the validation database. The goodness of fit, R^2 of the $\mu_{\Delta,GA}$ and $\sigma_{\Delta,GA}$ models was found 0.99 and 0.96, respectively.

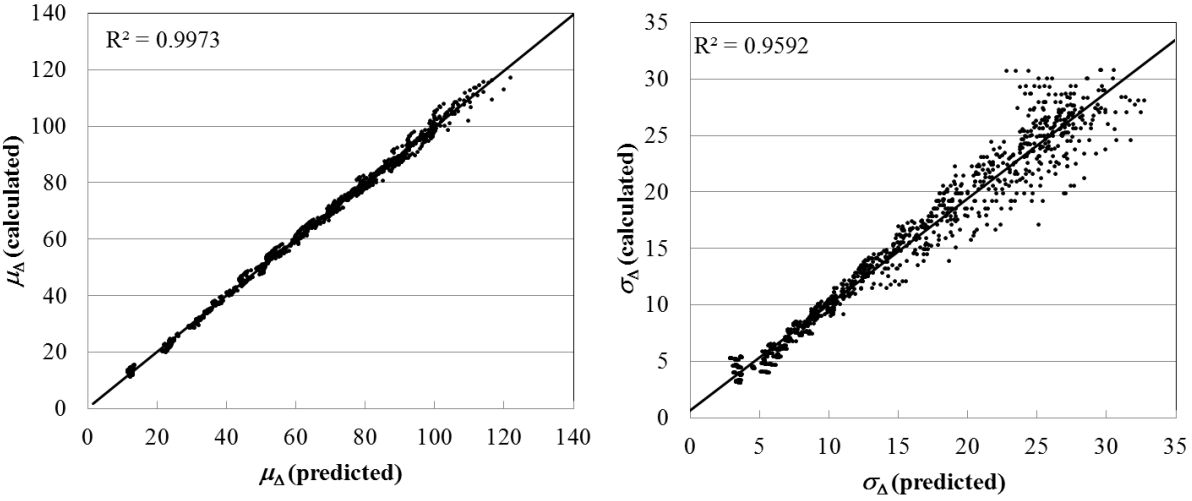

Figure 6.9 Calculated versus predicted models for μ_Δ and σ_Δ from GA method

After obtaining the fitted regression based on the GA method, the last step in developing the polynomial function, similar to stepwise ANOVA, is taking into account the response surface fitting errors ε_{μ_Δ} and $\varepsilon_{\sigma_\Delta}$ as random variables x_6 and x_7, respectively. The adjusted polynomial function for mean (Eq. 6.12) and standard deviation (Eq. 6.13) can be rewritten as Eq. 6.14 and *Eq. 6.15:*

Eq. 6.14

$$\bar{\mu}_{\Delta,GA} = [8.44 + x_1\left(26.11 + 3.45x_2 - 6.94e^{-6}x_3 - 1.69x_4 + x_5\right) - 1.14e^{-5}x_3\left(1 - e^{-6}x_3\right) - 0.67x_5] \times (1 - x_6)$$

Eq. 6.15

$$\bar{\sigma}_{\Delta,\mathrm{GA}} = [3.32 + x_1\left(1.28 + 1.44x_1 + x_2 - 2.57e^{-6}x_3 + 0.78x_5\right) - 0.49x_4x_5] \times (1 - x_7)$$

For the mean of the peak inter-storey drift database (μ_Δ), the mean and standard deviation of x_6 (ε_{μ_Δ}), was found as 0.025 and 0.027, respectively. Similarly, the standard deviation of the peak inter-storey drift database (σ_Δ), mean of and standard deviation of x_7 ($\varepsilon_{\sigma_\Delta}$), were found to be 0.090 and 0.086, respectively.

6.5 Reliability analysis

Reliability methods have been established to take into account the uncertainties involved in the analysis of an engineering problem. Generally, the failure (i.e. an undesired or unsafe state of the structure) is defined in terms of a limit-state function: g(X), by the set F = {X : g(X)<0}. Z = g(X) is called the limit-state surface, which separates the failure domain from the safe domain (Der Kiureghian, 2005).

6.5.1 Limit-state function

In structural safety community, the primary objective of reliability analyses is to quantify risks by computing the failure probability, denoted P_f. The reliability problem, i.e. computing P_f, has two components: i) random variables that describe the uncertainty and ii) a limit-state function that defines failure. The limit-state function g(X) can be expressed as the difference between the resistance: R(X), and the demand on the system: S(X). For example, g(X) =R(X) – S(X). The failure probability, P_f, is determined as:

Eq.6.16

$$P_f = P[\mathrm{g(X)} \le 0] = \int_{g(X)\le 0} f_X(X)\, d_{x_1} d_{x_2} \cdots d_{x_n} = \Phi(-\beta)$$

where, β is the reliability index of the system. Solving Eq.6.16 analytically is usually not possible; therefore, approximate reliability methods have been developed such as the First-Order Reliability Method (FORM), Second-Order Reliability Method (SORM) and Importance Sampling (IS) (Der Kiureghian, 2005). For FORM and IS, the linearization of the limit-state function may lead to inaccuracies when the limit-state function is highly nonlinear. In such cases, SORM is more appropriate to approximate the limit-state function by second-order Taylor series by employing a hyper-paraboloid to approximate the limit-state function instead of a hyper-plane.

In performance-based seismic design, the extent of structural damage can be related to performance in seismic events and design methodologies to mitigate future losses can be developed. When conducting the reliability analysis of the FFTT system, performance - as a predictor of total structural damage - can be defined by structural peak interstorey drift. Based on this assumption, the limit-state function of the seismic response of FFTT system can be described by Eq. 6.17 in the response surface method:

Eq. 6.17 $$G = \delta - \Delta(Gms, IM, M, K_1, K_2, \mathrm{R}_d, \varepsilon_{\mu_\Delta}, \varepsilon_{\sigma_\Delta})$$

Where δ is the interstorey drift capacity of the building and Δ is the peak inter-story drift demand, which includes the record-to record variability of ground motions, *Gms*, which is represented by μ_Δ and σ_Δ over the 22 selected ground motions; the intensity measurement, *IM*; structural weight (mass), *M*; hold-down stiffness, K_1; CLT wall-steel beam connection stiffness, K_2; ductility design factor, R_d; and the response surface fitting errors ($\varepsilon_{\mu_\Delta}, \varepsilon_{\sigma_\Delta}$).

Although Eq. 6.17 is a simple limit function to express the seismic response, there is no close form solution where drift demand is a function of 8 random variables. To calculate the reliability index

β using reliability methods, a limit state function is required that can be transformed into a standard normal space with an explicit function symmetric around the origin. Then the design point which is the closest point from the origin, can be calculated. Herein, using the assumption that the peak inter-storey drift follows a lognormal distribution (Li et al., 2011b), Eq. 6.17 is transformed:

Eq. 6.18
$$G = \delta - \Delta = \zeta H - \frac{\bar{\mu}_{\Delta}}{\sqrt{1+\bar{\upsilon}_{\Delta}^2}} \exp(R_N \sqrt{\ln(1+\bar{\upsilon}_{\Delta}^2)})$$

Where the interstorey drift capacity, δ, is equal to the drift ratio limit, ζ, multiplied by the storey height H; $\bar{\mu}_{\Delta}$ is the mean of the peak interstorey drift demand with consideration of the fitting error; $\bar{\upsilon}_{\Delta}$ is the coefficient of variation ($\bar{\sigma}_{\Delta} / \bar{\mu}_{\Delta}$); R_N is the standard normal variate, $R_N = (0,1)$; and adjusted $\bar{\mu}_{\Delta}$ and $\bar{\sigma}_{\Delta}$ for the FFTT system with different ductility designs can be given by Eq. 6.9 and Eq. 6.10 from the stepwise ANOVA method, or Eq. 6.14 and *Eq. 6.15* from GA method.

6.5.2 Reliability results

Once the explicit limit-state function, Eq. 6.18, and the probability distributions for the considered variables are obtained, the reliability index, β, can be estimated by the Second-Order Reliability Method (SORM). Herein, the *Rt* software was used to conduct the reliability index calculation (Mahsuli and Haukaas, 2013). Three different performance expectations are considered: 1.5% interstorey drift limit for Immediate Occupancy (IO); 2.5% interstorey drift limit for Life Safety (LS) and 5% interstorey drift limit for Collapse Prevention (CP) (Pei et al., 2013a, Lam et al., 2015).

For the 12 storey FFTT systems designed with different ductility factors, the ground motion intensity measure (x_1) is assumed to follow a lognormal distribution, with a mean value equal 100%

of the target design spectrum and the COV of the design spectrum is 0.24 which is calculated from Geological Survey of Canada (GSC) Open File 7576 (Halchuk et al., 2014); The seismic weight (x_2) and the hold-down stiffness (x_3) are both assumed to follow a lognormal distribution with COV of 0.1; The scale factor of CLT wall-steel beam connection stiffness (x_4) is assumed to follow a lognormal distribution, with a mean value equal to the 100% of test results and COV of 0.2 (Ceccotti and Foschi, 1998); The ductility factor R_d (x_5) is assumed to follow a normal distribution with the COV of 0.1; The response surface fitting errors $\mathcal{E}_{\mu\Delta}$ and $\mathcal{E}_{\sigma\Delta}$ are assumed to follow a normal distribution and represented as x_6 and x_7 respectively. For GA method, the mean and the standard deviation for $\mathcal{E}_{\mu\Delta}$ are 0.025 and 0.027, respectively; the mean and the standard deviation for $\mathcal{E}_{\sigma\Delta}$ are 0.09 and 0.086, respectively. For the stepwise ANOVA method, the mean and the standard deviation for $\mathcal{E}_{\mu\Delta}$ are 0.025 and 0.030, respectively; the mean and the standard deviation for $\mathcal{E}_{\sigma\Delta}$ are 0.104 and 0.128, respectively.

Table 6.4 shows the influence of the system ductility designs for the SORM reliability index under different performance objectives with the mean of weight equal 4.0 kN/m^2, mean hold-down stiffness equal to 600,000 kN/m, and mean wall-beam connection stiffness scale factor equal to 100% of the test results. 4.0 kN/m^2 is the designed structural weight according to tall wood report (Green and Karsh, 2012), 600,000 kN/m is chosen based on HSK hold-down design. Figure 6.10 shows the variation trend of the reliability index for the FFTT system when varying the mean value of the ductility design factor R_d under the GA and stepwise ANOVA methods.

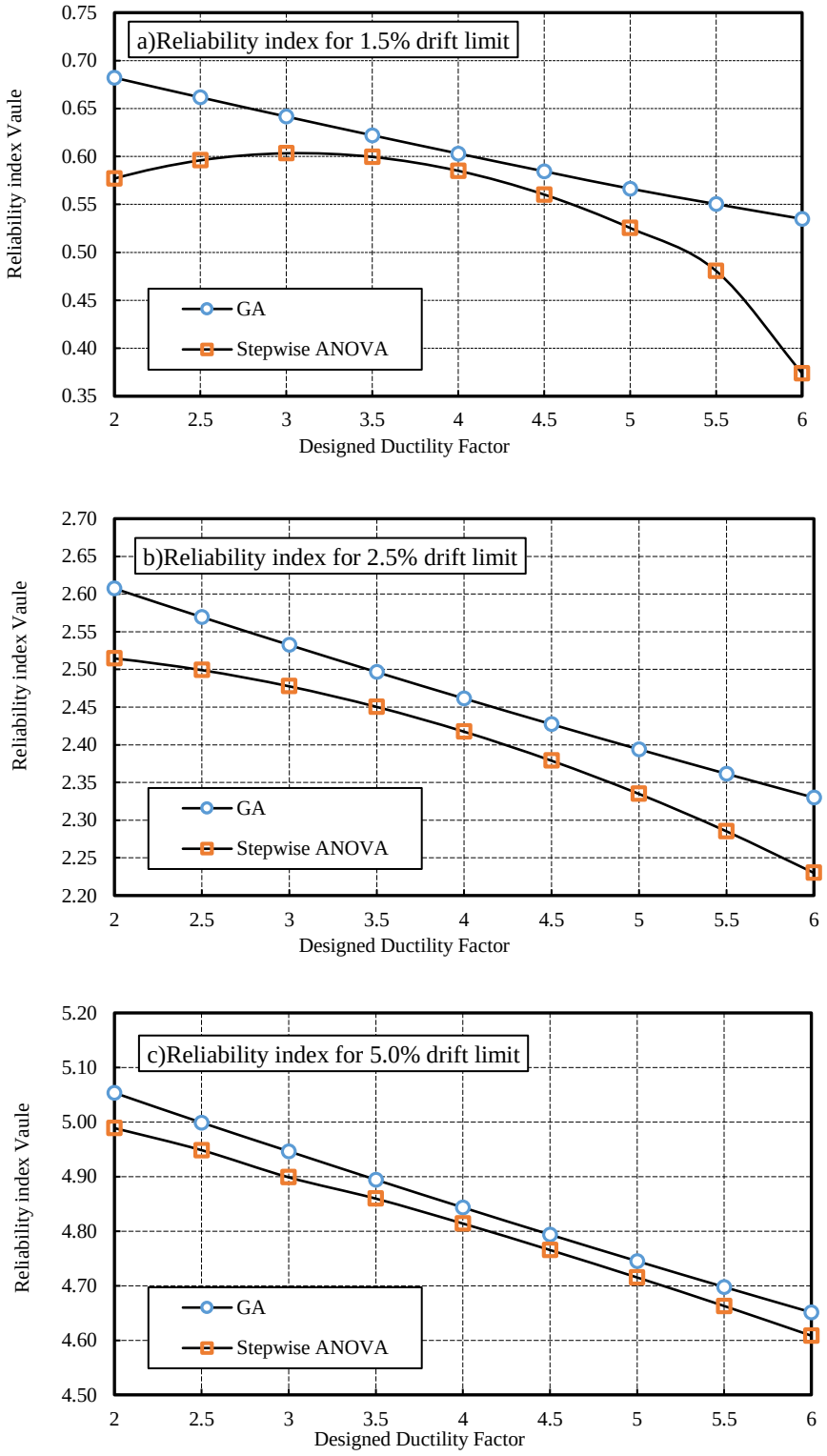

Figure 6.10 : Influence of R_d for 12 storey FFTT system reliability index with GA and stepwise ANOVA methods for different performance objectives: a) 1.5% drift limit; b) 2.5% drift limit; c) 5% drift limit

Table 6.4 Reliability index with three ductility designs for three performance objectives

SORM Reliability Index β						
R_d	1.5% drift limit		2.5% drift limit		5% drift limit	
	GA	Stepwise ANOVA	GA	Stepwise ANOVA	GA	Stepwise ANOVA
1.5	0.70	0.55	2.65	2.52	5.11	5.03
2	0.68	0.58	2.61	2.51	5.05	4.99
2.5	0.66	0.60	2.57	2.50	5.00	4.95
3	0.64	0.60	2.53	2.48	4.95	4.90
3.5	0.62	0.60	2.50	2.45	4.89	4.86
4	0.60	0.59	2.46	2.42	4.84	4.81
4.5	0.58	0.56	2.43	2.38	4.79	4.77
5	0.57	0.53	2.39	2.33	4.75	4.72
5.5	0.55	0.48	2.36	2.29	4.70	4.66
6	0.53	0.37	2.33	2.23	4.65	4.61

Aside from the ductility factor, the effects of weight and stiffness for the reliability index of FFTT system are also studied. Figure 6.11 to Figure 6.13 show the effects of structural weight, hold-down stiffness, and CLT wall-steel beam connection stiffness, respectively, on the reliability index of the FFTT model with R_d = 5 for the 2.5% inter-story drift limit objective. For brevity, only the results for $R_d = 5$ are given; for the designs using other ductility factors in other performance expectations, similar trends were observed.

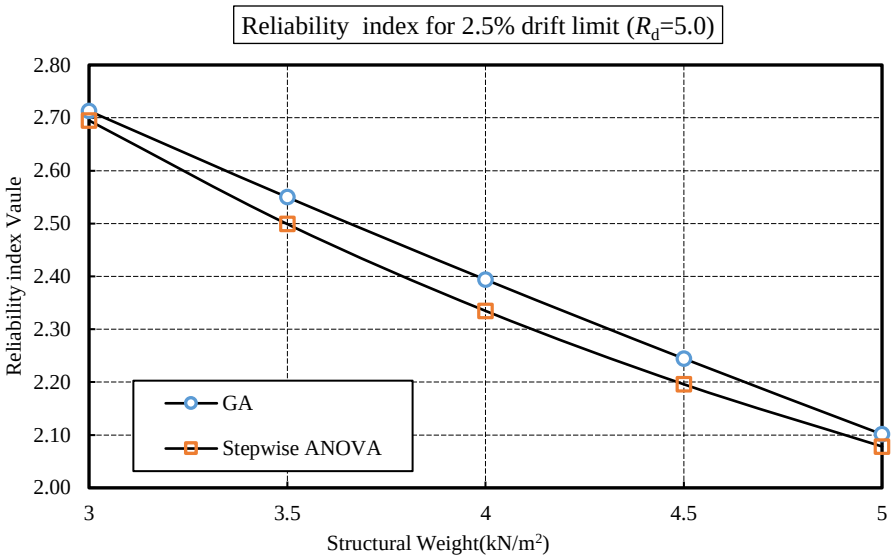

Figure 6.11 The influence of structural weight on the reliability index for the FFTT system design under the 2.5% drift limit objective (mean of x_3=600000 kN/m, mean of x_4=100% of the test stiffness, mean of x_5=5.0)

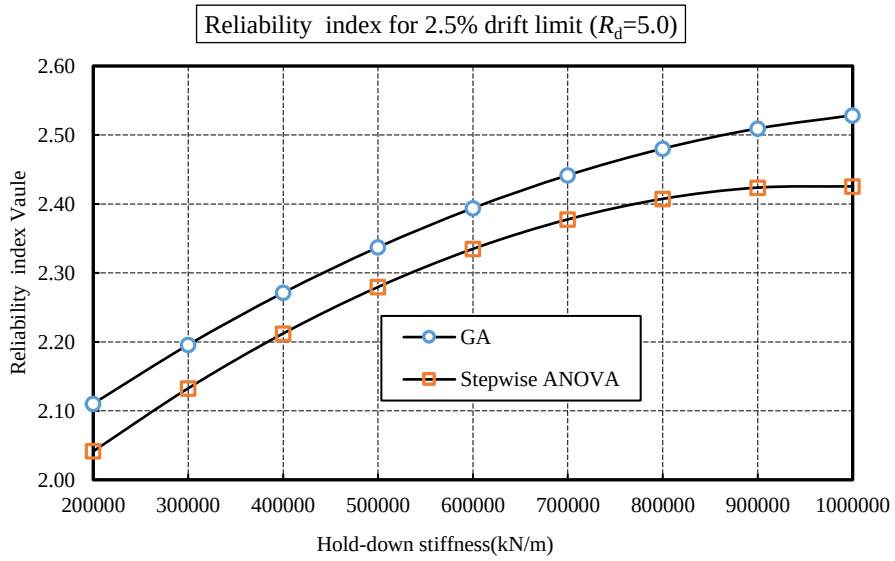

Figure 6.12 The influence of hold-down stiffness on the reliability index for the FFTT system design under the 2.5% drift limit objective (mean of x_2=4.0 kN/m^2, mean of x_4=100% of the test stiffness, mean of x_5=5.0)

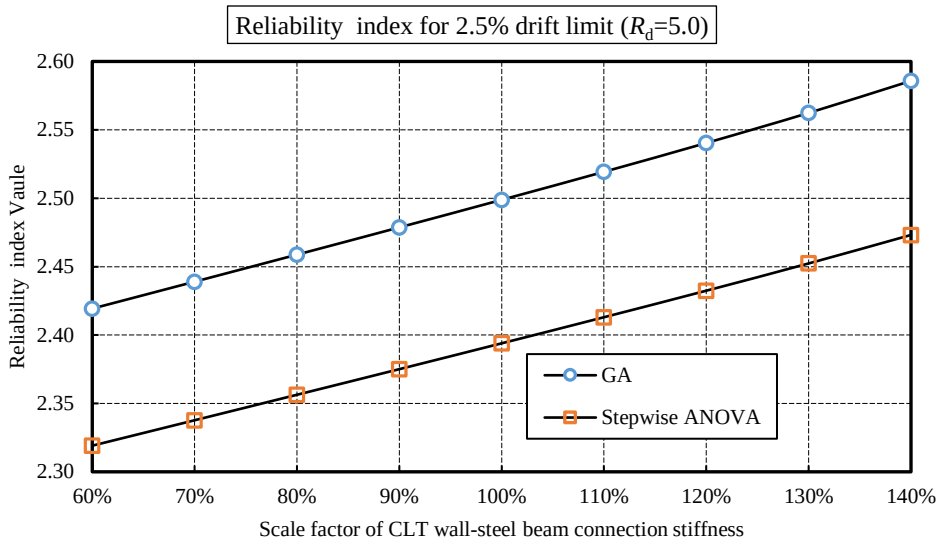

Figure 6.13 The influence of CLT wall-steel beam stiffness on the reliability index for the FFTT system design under the 2.5% drift limit objective (mean of x_2=4.0 kN/m^2, mean of x_3=600000 kN/m, mean of x_5=5.0)

Under the assumption that the mean of the ground motion level is 100% of the NBCC 2010 Vancouver design spectrum with a coefficient of variation of 0.24, the mean structural weight, hold-down stiffness and CLT wall-steel beam connection stiffness have some influence on the reliability index. However, when changing this assumption, a much more significant difference was observed.

Figure 6.14 shows the effect of choosing a different COV of the ground motion design spectrum on the reliability of FFTT system with R_d = 5. A small change of this value has a big effect on the reliability of the FFTT system for both the GA and stepwise ANOVA methods. A higher COV leads to a significantly higher probability of failure.

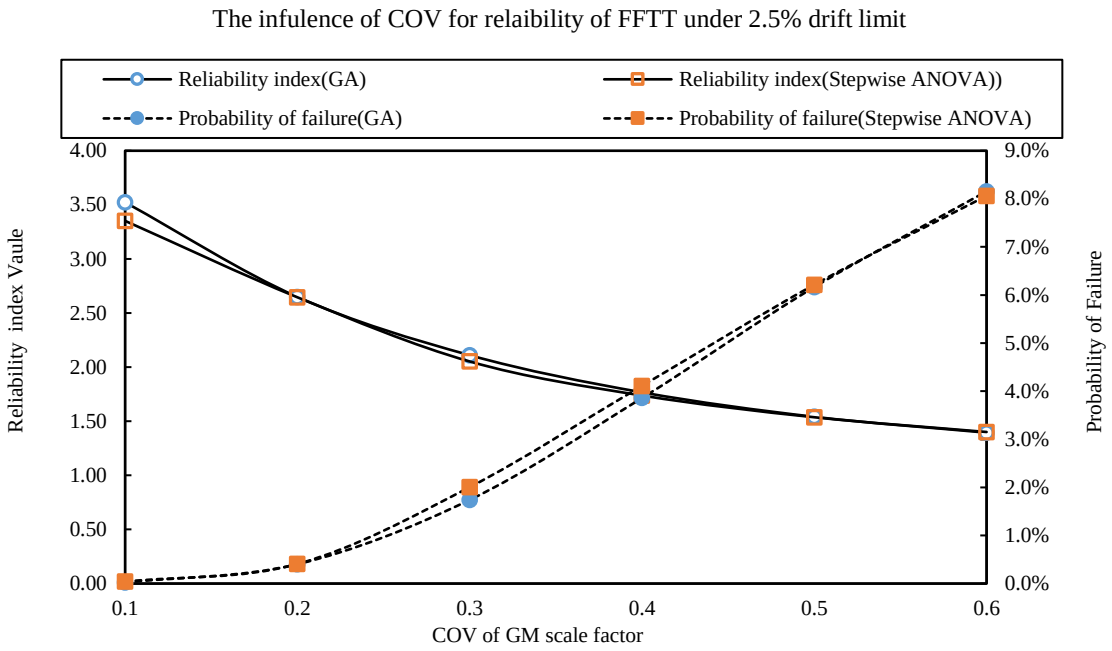

Figure 6.14 The influence of coefficient of variation of the ground motion scale factor on the reliability of the FFTT system design with R_d=5 under the 2.5% drift limit objective (mean of x_2=4.0 kN/m^2, mean of x_3=600000 kN/m, mean of x_4=100% of the test stiffness)

6.6 Discussion

From Table 6.4, it can be observed that based on the GA method, given the structural mass, hold-down stiffness, wall-beam connection stiffness and seismic hazard assumption, the increase in the design ductility value leads to a decrease of the reliability index for all performance criteria. When the design ductility factor increased by 0.5, the β decreased by 1.0% ~ 3.1% with respect to each performance objective. Figure 6.10 also confirmed this trend and showed there is an almost linear trend between the ductility design value and the reliability index for the analysis based on GA method. This phenomenon is explainable. In the NBCC2010, the ductility factor is used when conducting the equivalent static force design procedure. With the increase in the ductility design factor, the design base shear force decreases; as a consequence, the structure can be designed to

be softer, which will lead a larger inter-story drift response during the seismic events compared to the structures designed with lower R_d values. Therefore, as R_d is increased, the probability of failure under a given performance objective will increase, which will result in the decrease of the reliability index. While for the results from the stepwise ANOVA method, this obvious downward trend can only be found in the 5.0% drift limit performance objective. The lower the drift limit, the less the design ductility value effects the reliability index. For the 1.5% drift limit performance criteria, only the ductility values from 3.0 to 5.0 show this downward trend. This is because, for the stepwise ANOVA method, the polynomial functions are predicted completely based on the response surface database by minimizing the square errors between the actual response data and the fitted response surface, without considering any physical meanings of the mode terms. The database was only developed for R_d equal to 3.0, 4.0, and 5.0. In this case, when conducting the reliability index analysis, the downward trend can be observed for the ductility values from 3.0 to 5.0, while when the R_d exceeds the data range from the original database, uncertainties and errors may exist, especially for the performance criteria that has a large failure probability.

The results in Figure 6.11 imply that, for this FFTT system designed with certain ductility reduction values (for example, $R_d = 5.0$), with a given design stiffness and seismic assumption, the increase in the applied structural weight will lead a significant decrease in the reliability index for both the GA and stepwise ANOVA methods. The reliability index differences between the GA and stepwise ANOVA methods are relatively small: only 1.7%.

The results in Figure 6.12 and Figure 6.13 indicate that, with a given R_d value, structural weight and ground motion intensity assumption, both the hold-down stiffness and wall-beam connection stiffness have a positive influence on the reliability index. When varying the mean of the hold-down stiffness, the reliability indices obtained from the GA method are relatively close to stepwise

ANOVA method, with GA method results only 3.0% higher. When varying the scale factor of the CLT wall-steel beam connection stiffness, the results from the GA method are around 4.2% larger than the stepwise ANOVA method.

The results in Figure 6.14 show that when changing the seismic assumption (the COV of the design spectrum), a much more significant difference on the reliability of the FFTT system was observed for both the GA and stepwise ANOVA methods. The higher of the COV of the design spectrum value, the higher the probability of larger seismic loads, and the higher the probability of failure for the designed structure. The seismic input is the most important variable which effects the structural response compared to the other variables discussed in this chapter.

Unlike Figure 6.10, the results shown in Figure 6.11 to Figure 6.14 have almost the same variation tendency for the GA and stepwise ANOVA methods. In Figure 6.11, the structural weight parameter: x_2, varies from 3.0 to 5.0 kN/m^2, which is within the original database. In this case, the trends between the ANOVA and GA methods are consistant. In Figure 6.12 and Figure 6.14, although partial parameters (hold-down stiffness, x_3; scale factor of CLT wall-steel beam connection stiffness, x_4; and COV of GM scale factor, x_1) exceed the range of the original database, the trend in the stepwise ANOVA method are similar to the GA method. Accordingly, it can be observed that the reliability analyses combined with the stepwise ANOVA method may give inaccurate results if the study parameter exceeds the range of the original database. However, this is not always the case: it depends on how the multivariate polynomial function was developed as the regression only relies on the database instead of considering the physical meaning of each mode terms. In this case, the reliability analysis based on the stepwise ANOVA method may exist with large amounts of uncertainly and error compared to the GA method.

6.7 Summary

This chapter presented seismic reliability analyses of the FFTT system as an example of a novel timber-steel hybrid structural system. Two optimized response surface methods, including a Genetic Algorithm and a stepwise Analysis of Variance method were considered. These two optimized Response Surface Methods together with the Second-Order Reliability Method were used to derive polynomial functions and to estimate the structural reliability. Seven different uncertainties were considered including ground motion level, structural weight, hold-down stiffness, beam-wall connection stiffness, design ductility factor, error mean, and error standard deviation. The influence of these random variables can be summarized as follows:

(1) The reliability indices, β, obtained from the two methods are slightly different. Although using the stepwise selecting method in ANOVA can simplify the fitted regression to some extent, the GA method still produced a much simpler expression for the response surface polynomial function. At the same time, the obtained reliability indicates based on the GA method were much more accurate when compared to the stepwise ANOVA method, as each mode term in the regression has a physical meaning.

(2) For the reliability analysis of the FFTT system, the ductility design value shows a negative influence on the reliability of this 12 story structure: with the increase of the R_d value, the β decreases. Structural weight has a negative influence on the reliability of FFTT system for both GA and stepwise methods: β increased with a decrease in the weight. For both hold-down stiffness and CLT wall-steel beam connection stiffness, a positive influence on the reliability of FFTT system: β , was observed.

(3) The variability of the ground motions has the most significant influence on the reliability of FFTT system compared to all the other design variables. The higher the COV of the ground motion design spectrum, the higher probability of failure will be observed.

In Chapter 4, the ductility factor R_d equal to 5.0 was recommend for the FFTT Option 1. This result was obtained using the design values from the Tall Wood report (Green and Karsh, 2012) without any uncertainty consideration (the structural weight is 4.0 kN/m^2, hold-down stiffness is 600000 kN/m, the wall-beam connection stiffness is the 100% of the test results and all the selected 22 ground motion were scaled exactly to Vancouver design spectrum based on NBCC2010). After considering all these design values as random variables and using the largest COV of Vancouver design spectrum (0.24), the FFTT system designed with R_d = 5.0 is still acceptable as its probability of non-exceedance under the 1.5% drift limit objective is larger than 70% and the probability of non-exceedance under the 2.5% drift limit objective is larger than 99%.

To summarize: by using the GA and stepwise ANOVA methods, the study presented in this chapter indicated that the GA method gives more accurate results when conducting the response surface method together with the reliability analysis. It also confirmed that FFTT is a reliable system. The comparison procedure presented here showed that the GA response surface method is a very useful tool to evaluate the seismic performance of novel systems, not only because all terms in the polynomial function had physical meanings, but also more random variables can be taken into account without adding to the complexity of the response polynomial function. This is very important when conducting research on a novel structure. The reason for this is that for a system which has not yet been constructed, there are many uncertainties that should be accounted for in order to achieve a safe and reliable system.

Chapter 7: Feasibility Study of FFTT System and Design Guidance

7.1 Introduction

The FFTT system is a unique structural concept that effectively balloon-frames mass-timber panels to create tall buildings. The structural design is based on the "strong column/weak beam" principle where embedded steel beams are designed to yield and plasticize, (without leading to total collapse) before the CLT shearwalls, and the other structural components, reach their capacity. By forming plastic hinges, the ductility of the structure increases, and large lateral displacements can be accommodated.

Chapter 5 and Chapter 6 analyzed the global behaviour of the FFTT system based on this design principle. In the numerical models, the CLT wall to steel beam connections were considered as energy dissipating hinges, the hold-downs were modelled using elastic perfectly plastic properties, and the shear keys in the middle of the CLT panels were modelled as pins to allow the rocking motion of the panels. The results showed that 1) the maximum inter-storey drifts were within the 2.5% limit when using a ductility value of R_d = 5.0, and 2) the structures designed with R_d = 5.0 can achieve a 99% probability of non-exceedance of the 2.5% drift limit.

In practice, however, designing the pin connection would pose a challenge. The HSK shear connector could be applied in the middle of the CLT panel, as shown in Figure 5.1b. The modified HSK hold-down could be used to resist the uplifting load, designed as secondary failure mechanism to absorb seismic energy after all steel beams reach their inelastic range. The remainder of the structure is capacity designed.

7.2 Objective

The objective of this study is to investigate if the strong column/weak beam failure mechanism can be achieved for the balloon-framed FFTT system by checking the yielding prioritization for the dissipative connections: first the CLT wall-steel beam connections starting from the upper floor levels, and then the modified HSK hold-downs.

7.3 Feasibility investigation

7.3.1 Modeling

In order to investigate the feasibility of the FFTT system, the Option 1 (12 storey) building was modeled using the material properties as determined in Chapter 3 and Chapter 4. The models were similar to 2D OpenSees models developed in Section 5.3.3; Figure 7.1 illustrates the schematic of the revised model. Unlike the assumptions for the 2D model in Chapter 5, the pin connection of the CLT wall was replaced by the HSK shear connector, which is a more realistic assumption according to the Tall Wood Report (Green and Karsh, 2012).

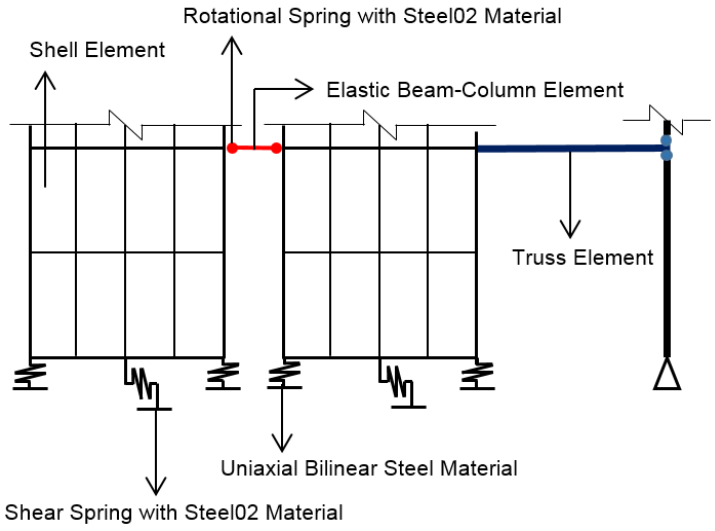

Figure 7.1 Schematic of revised 2D OpenSees model for the FFTT system

The properties of the shear connection were calibrated based on the mid-scale test results from Series 3-1 in Chapter 4, as shown in Figure 7.3. The required shear capacity is 261kN (see Table 5.2). The CLT wall-steel beam rotational connections were modeled with wide flanged steel beams (series S7 in Chapter 3) instead of the HSS hollow section steel beams (series S5 in Chapter 3), as shown in Figure 7.3.

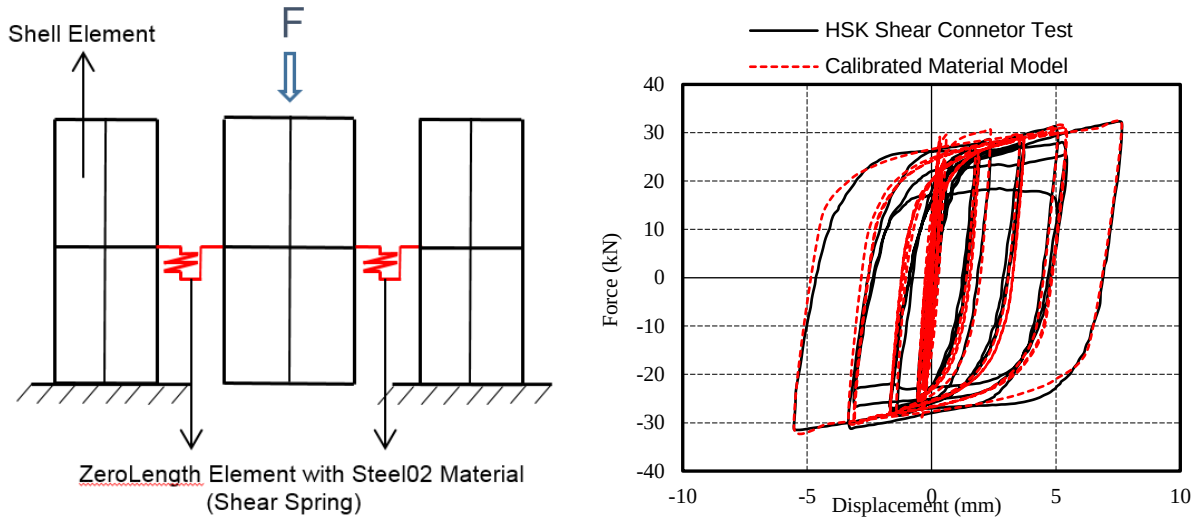

Figure 7.2 Calibration of modified HSK shear connection (S3-1) with OpenSees hinge

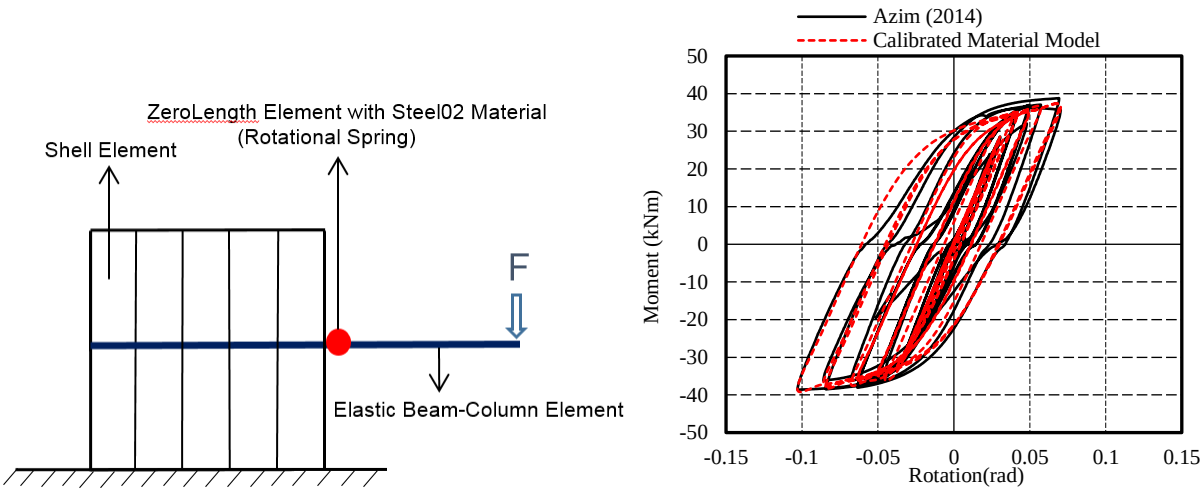

Figure 7.3 Calibration of steel beam CLT panel connection (S7) with OpenSees hinge

As the HSK modified hold-downs were designed as the secondary failure mechanism for the system, the material properties for this connection were considered elastic perfectly plastic. The yielding force of the hold-down is 2,076 kN, obtained from the elastic SAP models in Chapter 5. Based on the this force, the stiffness of the hold-down can be calculated as 2,633 kN/mm according to the full scale hold-down test results in Chapter 4 ($F_{y,SL}$ = 2.1 kN; $k_{e,SL}$ = 2.6 kN/mm). R_d and R_o were considered as 5.0 and 1.5, respectively, similar to the values from the studies in Chapter 5 and Chapter 6 for the 12 storey Option 1 FFTT system. In the nonlinear time history analysis, 22 far-field earthquake ground motions were selected from FEMA P695 (FEMA 2009) as the record set and were scaled linearly to the design response spectrum over the period range of the model.

7.3.2 Results and discussion

Figure 7.4 illustrates the cumulative distribution function for the maximum interstorey drift of the 12 storey FFTT model for the selected individual ground motions. Table 7.1 shows the drift for each storey and Figure 7.5 summaries the cumulative distribution functions of interstorey drift. The results show that all the interstorey drifts are within NBCC drift limit (2.5% drift with 90% probability of non-exceedance). The CDFs of interstorey drifts also satisfy the 2.5% performance expectations. These results confirm the ductility study from Chapter 5 and that, when using R_d = 5.0, the FFTT system's interstorey drift performance meets code requirements.

Table 7.1Interstorey drift results for 22 ground motions

GM No.	1	2	3	4	5	6	7	8	9	10	11
Interstorey Drift (%)	1.55	2.39	0.85	1.10	0.85	1.13	0.91	1.77	0.86	0.81	1.38
GM No.	12	13	14	15	16	17	18	19	20	21	22
Interstorey Drift (%)	1.30	1.30	0.83	1.11	0.70	0.77	1.30	0.79	1.71	0.98	1.17

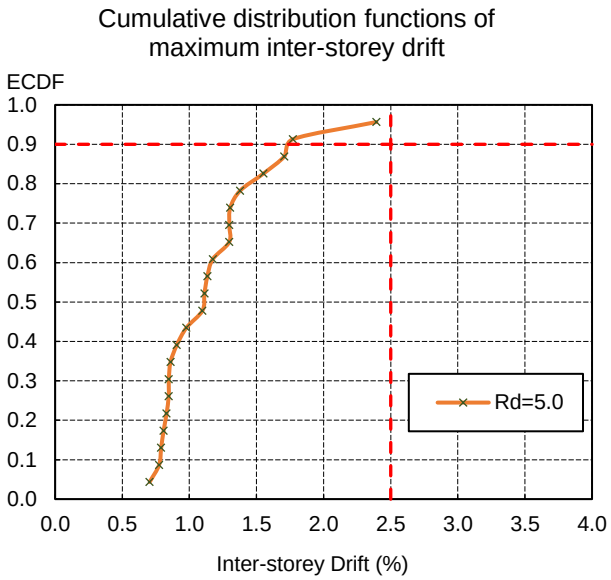

Figure 7.4 Cumulative distribution function of interstorey drift for individual 22 GMs

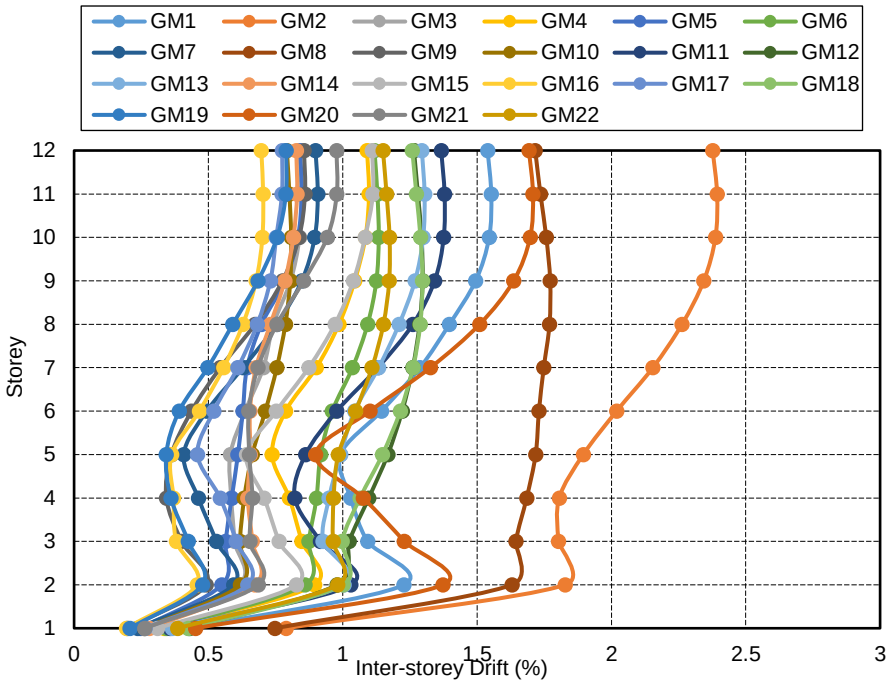

Figure 7.5 Interstorey drift for each storey under the 22 GMs

To investigate the strong column/weak beam approach of the FFTT system, the dynamic behaviour of the CLT wall-steel beam rotational hinges and the HSK hold-down connections were evaluated. As an example of the force-displacement curves for these two connections under 22 GMs, the dynamic behaviours under GM NO.11 are shown in Figure 7.6 and Figure 7.7. From Figure 7.7, it can be observed that the hold-downs remained elastic and the inelastic behaviour was concentrated in the rotational hinges representing the CLT wall-steel beam connections, as shown in Figure 7.6. This structure will yield and dissipate seismic energy before the hold-downs reach their inelastic range. The results demonstrate that the hold-downs can be considered as a secondary failure mechanism after all CLT wall-steel beam connections reach their yielding rotation. The remainder of the structure can be capacity-designed.

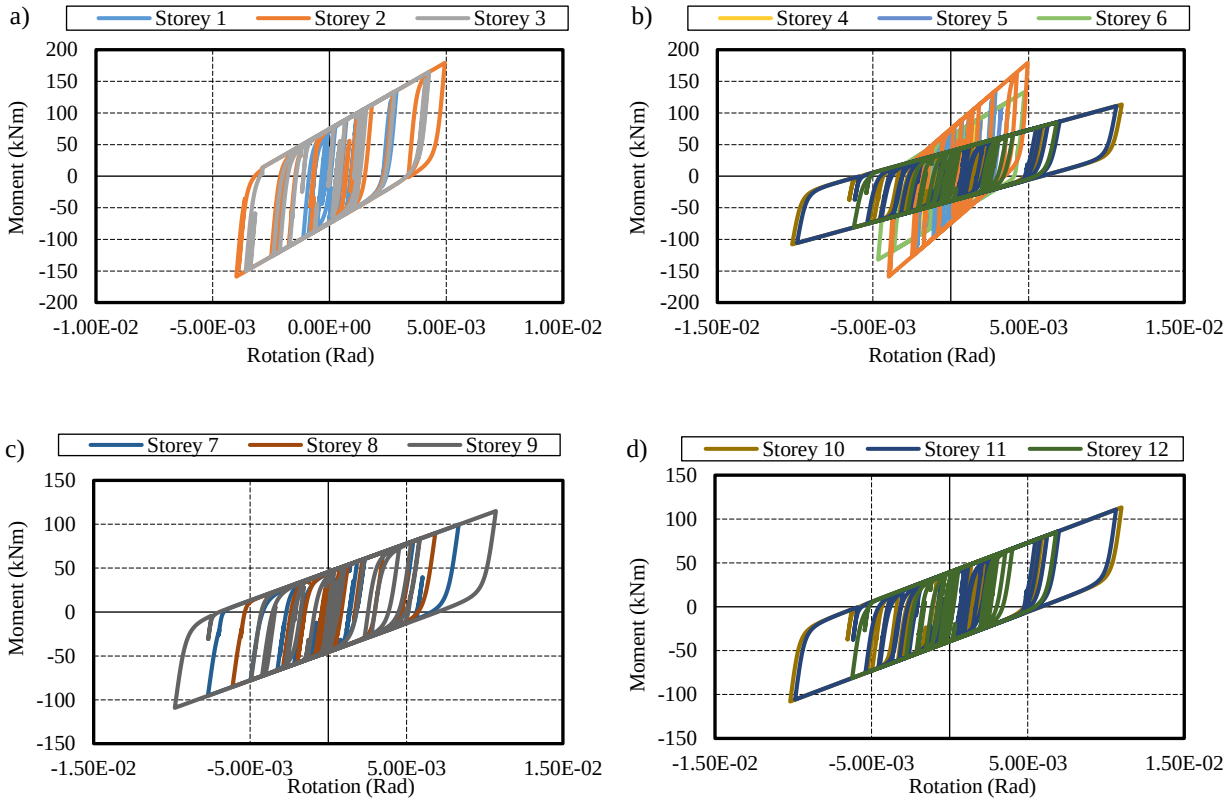

Figure 7.6 Moment-rotation curve for wall-beam connections under GM No. 11

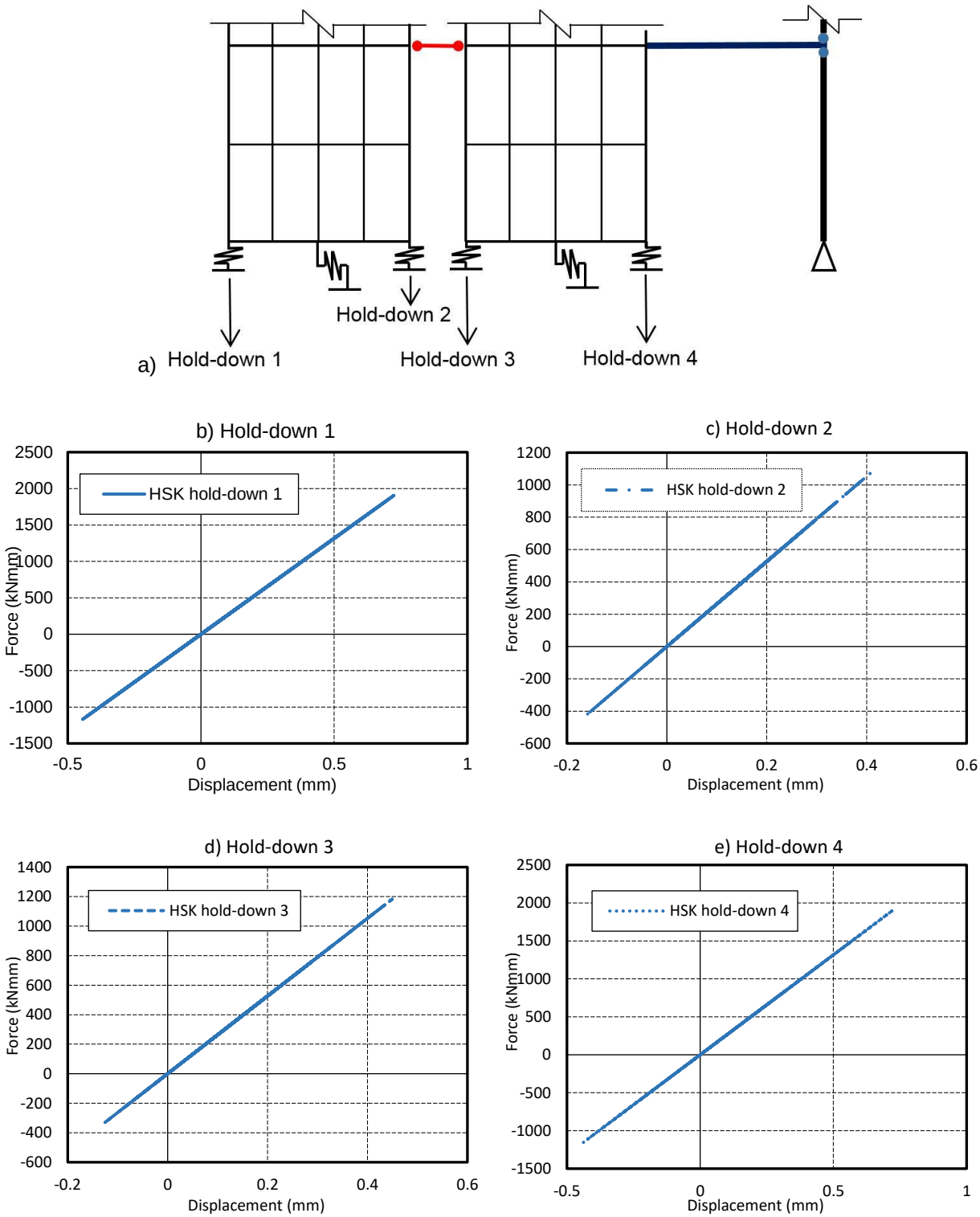

Figure 7.7 Force-displacement curve for the hold-downs under GM No. 11: a) sketch of the hold-down location; b) hold-down 1; c) hold-down 2; d) hold-down 3; e) hold-down 4

7.4 Design guidance

The study presented in this chapter confirms the feasibility of achieving the desired failure mechanism of the FFTT system when using the component properties as determined in Chapters 3 and 4. The CLT wall-steel beam connections and HSK shear connector and hold-downs can be applied in a building using the FFTT system.

Additional design guidance, however, needs to be given. For the CLT wall-steel beam connections, both HSS hollow and wide flange steel beam sections can provide good energy dissipation. For actual buildings, the cross sections can be determined based on the load requirements; for the wide flanged sections, steel side plates and bearing plates need to be added. The HSK shear connections and hold-downs can be safely designed, knowing the force requirements. For the example of a 12 storey FFTT Option 1 building, designed for the Vancouver 2010 uniform hazard spectrum, the base shear and uplift requirements are V_{shear} = 261 kN and F_{uplift} = 2,076 kN. The required number of steel links for the HSK shear connector and hold-downs, according to the results from Chapter 4, are then 125 and 989, respectively. Subsequently, the number of steel plates and their lengths and widths can be designed. Figure 7.8 illustrates an example for the HSK shear connector consisting of three steel plates with 42 SL per plate for a shear connection. Figure 7.9a shows the design example for the modified HSK hold-down and Figure 7.9b the shear connector and hold-down for a 12 storey Option 1 building.

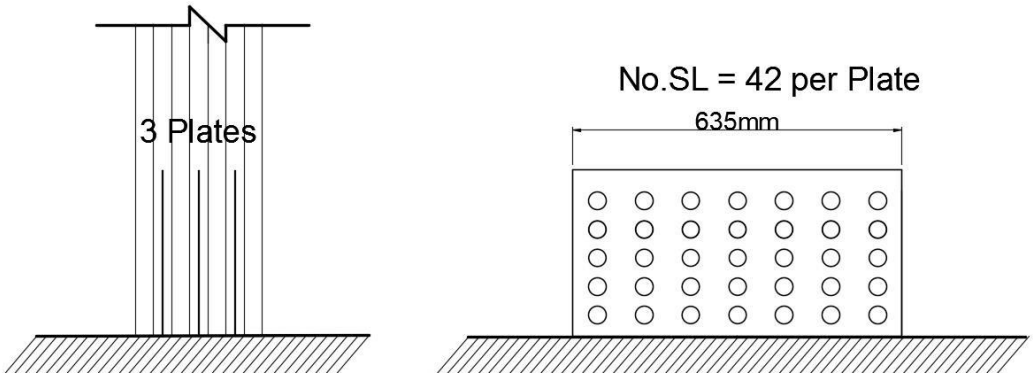

Figure 7.8 Design of HSK shear connector

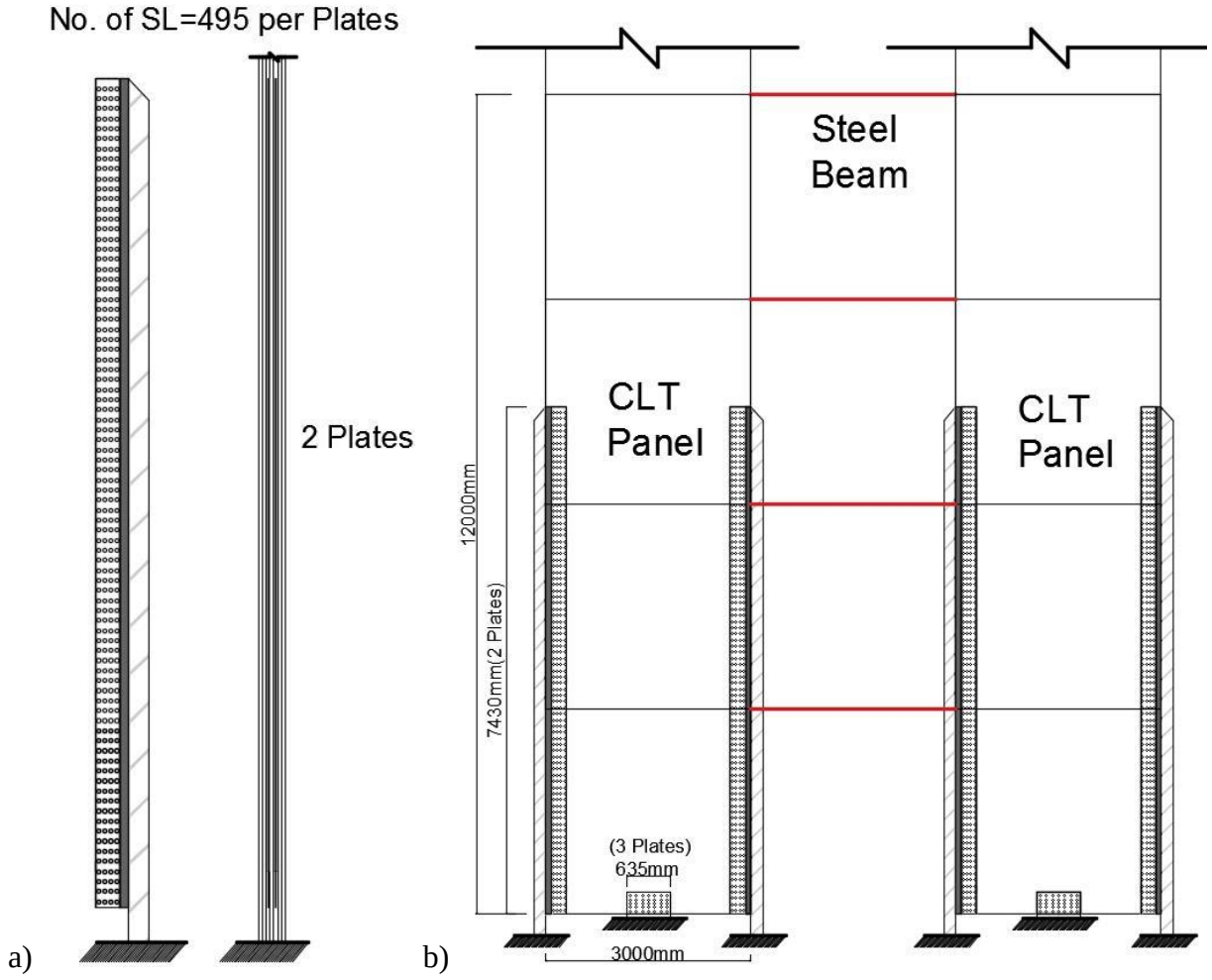

Figure 7.9 a) Design of HSK hold-down connector; b) HSK system design in the FFTT system

Chapter 8: Conclusions

8.1 Summary

Tall wood buildings are one strategy for societies to reduce their carbon footprint while addressing pressures on land resources. Timber-steel hybrid systems utilizing timber as one main construction material, but also taking advantage of the ductility that steel provides are a viable option. The FFTT system is one proposal for a hybrid system using mass-timber panels as shear walls and floor slabs connected with steel header beams. This research investigated the structural feasibility of FFTT system on the component and system levels using experimental and numerical methods.

The performance of the LLRS of a structure depends on the main components and the key connections between them. In the case of the FFTT system, the key connections consist of the joints between the embedded steel beams and the mass-timber panels which facilitate the desired strong-column/weak-beam failure mechanism and the hold-downs that provide overturning resistance while at the same time allowing the timber panels to rock to facilitate the desired failure mechanism.

The performance of different configurations of the CLT wall-steel beam connections under quasi-static monotonic and reversed cyclic loading were analysed, considering the effects of the chosen beam profile as well as beam embedment length and embedment depth. The results showed that both the wide flange and HSS hollow section steel beams can provide the desired failure mechanism. Wide flange sections achieved higher capacity; HSS sections, however, provided higher ductility and were not prone to out-of-plane buckling. Additional elements like steel side and bearing plates helped avoiding excessive crushing of the wood.

To resist the uplifting forces caused by large lateral loads, anchorage with high a capacity is required for tall wood buildings. A high capacity hold-down, based on a modified HSK system, was designed and investigated in material level tests, component level shear tests, as well as full-scale tests. The results showed that a stiff and ductile connection with good energy dissipation can be achieved using the modified HSK system hold-down.

A system-level numerical analysis of the FFTT system was conducted to estimate the ductility factor: R_d. Based on extensive parameter variations, including the influence of selecting the steel-beams according to two different approaches and two different approaches to match the seismic hazard level at the design location, using a factor R_d = 5.0 to design the FFTT system met the building code requirements regarding inter-storey drift. The applied procedure provides a framework for future work on developing seismic force reduction factors for other novel systems.

A subsequent reliability analysis considered uncertainties such as ground motion level, weight (mass), connection stiffness, and system ductility factor. Two response surface methods, which included Genetic Algorithms and Analyses of Variance method, were applied and combined with the Second-Order Reliability Method to develop polynomial functions and conduct reliability-based seismic analyses. The results showed that considering all design values as random variables, and using the Vancouver 2010 design spectrum, the FFTT system designed with R_d = 5.0 can achieve a 99% probability of non-exceedance of the 2.5% drift limit.

The feasibility analysis applied the ductility factor R_d = 5.0 and the obtained experimental results to an Option 1 12-storey FFTT building. The results confirmed that the ‘strong column/weak beam” failure mechanism can be achieved through yielding of the dissipative CLT wall-steel beam connections before the non-dissipative HSK hold-downs.

8.2 Main contributions

1) The analysis of the experimental investigation of the wall-beam connection provides design guidance for the key connection of the FFTT system. These results are an important step towards the practical application of the FFTT system as they prove that appropriate connection layouts can lead to the desired ductile failure mode.

2) The modified HSK hold-down provides a solution to one of the key structural challenges of tall and light structures: a hold-down that is strong and stiff enough to resist overturning forces, while, at the same time, provides the desired failure mechanism. This modified HSK hold-down and the shear connector can be applied to other mass timber-based structural systems which require a high-capacity and ductile behavior.

3) The R_d factor estimation provides important guidance for the practical design, and ultimately, the application, of the FFTT system. The study also provides guidance for future work on developing seismic force reduction factors for other novel structural systems.

4) The seismic reliability analyses compared two response surface methods which includes stepwise ANOVA and GA method, together with Second Order Reliability Method to estimate the structural reliability considering a wide range of random variables.

5) The feasibility investigation confirmed the possibility of achieving the "strong column/weak beam" failure mechanism in the FFTT system and provided design guidance for the modified HSK shear and hold-down connections.

8.3 Limitations and future research

The research presented here gives an overview of a timber-steel hybrid system by investigating the seismic behavior of FFTT system from the component level and system level. However, there are the limitations in this work and additional research is needed to address the practical implementation of FFTT system. These future studies, outside the scope of this research, include:

1) In this thesis, only the two key connections (CLT wall-steel beam connection and the modified HSK hold-down connection) in the FFTT system were experimentally studied. These two connections were tested separately and the obtained performance provided important input for the analysis of the whole system. However, to establish the system level behaviour of the FFTT system, full-scale wall tests which include the CLT wall-steel beam connections together with the hold-down connections are needed. These tests should involve the key design parameters such as shear capacity of the wall, ultimate drift, strength and stiffness degradation under cyclic loads, and the seismic behaviour investigation under a full scale shake table test. The desired strong column/weak beam failure mechanism should be confirmed based on this experimental approach.

2) Aside from these two studied connections, other connections need to be designed and investigated for an actual building. Examples include the CLT diaphragm-wall connections, glulam beam-column connections, panel-panel connections, and so on. More importantly, the connection between glulam columns in the adjacent storeys needs to be well designed. As an essential component in the gravity system of the building, the shrinkage in the wood members should be controlled. A successfully application for this type of connection in the UBC's Brock Commons (AOAI, 2016) can be considered as a reference. The design and the study on the

capacity and dynamic behavior for these connections are of great importance for a timber based high-rise building.

3) In the structural numerical modeling, the CLT panels were modeled as elastic and the strength properties did not account for post yield inelastic behavior. In a further study, a more accurate finite element numerical model with nonlinear timber properties can be developed that might better simulate the behaviour of the system. Other mass-timber products like laminated veneer lumber, which is stronger than CLT, should also be considered.

4) This thesis mainly considered the seismic performance of the FFTT system and only scratched the surface of analyses that need to be performed in order to assess the feasibility of the novel FFTT hybrid system. Before it is constructed in reality, many more studies need to be conducted. For example: the building physics performance, e.g. fire resistance, durability and acoustic properties; the practical aspects building logistics, and cost analyses.

Bibliography

Abrahamsen R. B. and Malo K. A. (2014). Structural design and assembly of the “TREET” - a 14-storey timber residential building in Norway. World Conference on Timber Engineering. Quebec, Canada.

Abrahamson N. A. (1992). Non-Stationary Spectral Matching. Seismological Research Letters, 63(1), 30.

Action Ostry Architects Inc. (AOAI) (2016). Brock Commons Phase 1. Retrieved Nov. 10, 2016, from:*https://raic.org/sites/default/files/civicrm/persist/contribute/files/bulletin/2016/march/brock_eng.pdf.*

Allen E. E. and Iano J. (2004). Fundamentals of building construction, materials and methods, 4th Ed., Wiley, New York.

APA - The Engineered Wood Association. (2010). A Guide to Engineered Wood Products. Form C800.

American Wood Council (AWC) (2015). Designing for Earthquakes. Retrieved Sep. 15. 2016, from:*http://www.awc.org/pdf/education/des/ReThinkMag-DES411A1-DesigningForEarthquakes-150901.pdf.*

ANSI/APA PRG 320 (2011). APA - The Engineered Wood Association. Standard for Performance-Rated Cross Laminated Timber. Tacoma, USA.

Atkinson G. M. and Macias M. (2009). Predicted Ground Motions for Great Interface Earthquakes in the Cascadia Subduction Zone. Bulletin of the Seismological Society of America, 99(3), 1552-1578.

Audenaert A., De Cleyn S. H. and Vankerckhove B. (2008). Economic Analysis of Passive Houses and Low-energy Houses Compared with Standard Houses. Energy Policy, 36, 47-55.

Schreyer A. (2012). How tall can we build in wood? Retrieved Sep.10, 2016, from: https://alexschreyer.net/engineering/how-tall-can-we-build-in-wood/.

ASCE (2014). Seismic Evaluation and Retrofit of Existing Buildings. American Society of Civil Engineer/ Structural Engineering Institute (SEI) 41-13, Reston, Virginia.

ASCE (2010). Minimum design loads for buildings and other structures. American Society of Civil Engineers/Structural Engineering Institute (SEI) 7-10, Reston, Virginia.

Ashour A. F., Alvarez L. F., and Toropov V. V. (2003). Empirical modelling of shear strength of RC deep beams by genetic programming. Computers and Structures, 81(5), 331-338.

Assakkaf I. (2002). Introduction to structural steel design. Lecture Note. Retrieved Oct. 2, 2016, from: *http://www.assakkaf.com/courses/ence355/lectures/part2/chapter1.pdf.*

ASTM E2126-09. (2009). Standard Test Methods for Cyclic (Reversed) Load Test for Shear Resistance of Walls for Buildings. American Society for Testing and Materials.

Azim M.R. (2014). Numerical and experimental investigations of connection for the timber-steel hybrid system. MASc thesis, University of British Columbia, Vancouver, Canada.

Badescu V. and Sicre B. (2003). Renewable Energy for Passive House Heating Part 1. Building Description. Energy and Buildings, 35, 1077-1084.

Bathon L., Bletz-Mühldorfer O., Schmidt J. and Diehl F. (2014). Fatigue Design of Adhesive Connections Using Perforated Steel Plates. World Conference for Timber Engineering. Quebec, CA.

Beaucher S. (2015). District 03 Le plus haut multirésidentiel en bois de l'est du continent, CÉCOBOIS. Québec, Canada, pp. 1-8.

Birch A. (2011). A technical look at Bridport House's timber structure. Retrieved Oct. 11, 2016, from:*http://www.bdonline.co.uk/a-technical-look-at-bridport-houses-timber-structure/5020465.article.*

Bhat P. (2013). Experimental Investigation of Connection for the FFTT, a Timber-Steel Hybrid System. MASc Thesis, University of British Columbia, Canada.

Bhat P., Azim R., Popovski P. and Tannert, T. (2014) Experimental and numerical investigation of novel steel-timber-hybrid system. World Conference on Timber Engineering (WCTE 2014), Quebec City, Canada.

Blass H. J. and Fellmoser P. (2004). Design of Solid Wood Panels with Cross Layers. In 8th World Conference on Timber Engineering.

BS EN 10025 (1993). Specification for Hot Rolled Products of Non-alloy Structural Steels and Their Technical Delivery Conditions. British Standards Institution, London.

Buchanan A., Östman B.and Frangi A. (2014). Fire resistance of timber structures. National Institute of Standards and Technology, Gaithersburg.

Buchanan A. H. (2001). Structural design for fire safety. Vol. 273. New York, Wiley.

Building Code of British Columbia (BCBC). (2012). Office of Housing and Construction Standards. National Research Council Canada, Victoria, BC, CA.

Build up energy solutions for better buildings (BUESBB), (2013) LifeCycle Tower One Building. Retrieved Sep. 22, 2016, from: *http://www.buildup.eu/cases/37881*.

Bugge A. (1953). Norwegian stave churches, Oslo: Dreyers Forlag.

Campbell F.C. (2008) Elements of metallurgy and engineering alloys. ASM International, Materials Park, OH.

Canadian Wood Council (2012). Innovating with Wood: A Case Study Showcasing Four Demonstration Projects. Retrieved Nov. 22, 2016, from: *http://www.cecobois.com/publications_documents/publications-casestudy-Four-demonstration-Case-Study_May_30.pdf*

Canadian Wood Council (2010). Wood Design Manual. Ottawa, Canada.

CAN/CGSB 51.34-M86. (1996). Vapour Barrier, Polyethylene Sheet for Use in Building Construction. Canadian General Standards Board, Gatineau, Canada K1A 1G6.

Ceccotti A., Lauriola M., Pinna M. and Sandhaas, C. (2006). SOFIE Project -Cyclic Tests on Cross-Laminated Wooden Panels. Wood Conference on Timber Engineering (pp. 1-8). Portland, USA: WCTE Proceedings.

Ceccotti A., Sandhaas C., and Yasumura M. (2010). "Seismic behavior of multistory cross-laminated timber buildings." Rep. Prepared for the Convention of Society of Wood Science and Technology, Geneva.

Ceccotti A., and Foschi R. O. (1998). Reliability assessment of wood shear walls under earthquake excitation. Proc. 3rd International Conference on Computational Structural Mechanics, Thera-Santorini, Greece.

CECOBOIS (2013). Toujours plus haut. Québec, Canada, 5(1), pp. 1- 12.

Cheung K.C. (2000). Multi-Story Wood-Frame Construction. Retrieved May 23, 2016, from: *http://www.icomos.org/iiwc/seismic/Cheung-K.pdf*

Cree GmbH (2010). LifeCycle Tower research project.

CSA S-16. (2009). Design of Steel Structures. Ottawa: Canadian Standards Association.

CSA-O86. (2014). Engineering Design in Wood. Ottawa: Canadian Standards Association.

CSA-O177. (2015) Qualification Code for Manufacturers of Structural Glued-laminated Timber. Fifth edition, Mississauga, Ont., Canadian Standards Association.

CSI, S. V. 8 (2002). Integrated Finite Element Analysis and Design of Structures Basic Analysis Reference Manual. Berkeley, California (USA): Computers and Structures Inc.

Dempster A. P. (1963). Stepwise multivariate analysis of variance based on principal variables. International Biometric society. Vol. 19, No. 3, 478-490. DOI: 10.2307/2527936.

Der Kiureghian A. (2005). “First- and second-order reliability methods.” Engineering Design Reliability Handbook, E. Nikolaidis, D. M. Ghiocel, and S. Singhal, eds.,CRC Press.

Deutschman A.D., Michels W.A. and Wilson C.E. (1975). Machinery's Handbook 27th edition. Machine design Theory and Practice. Prentice Hall.

Dickof C., Stiemer S., Tesfamariam S. and Wu D. (2012). Wood-steel Hybrid Seismic Force Resisting Systems: Seismic Ductility. World Conference for Timber Engineering, (pp. 104 - 111). Auckland, New Zealand.

Dickof C. (2013). CLT Infill Panels In Steel Moment Resisting Frames As A Hybrid Seismic Force Resisting System. MASc Thesis, University of British Columbia, Vancouver, Canada.

Dvorkin E. N. and Bathe K. J. (1984). A Continuum Mechanics Based Four-Node Shell Element for General Non-Linear Analysis. Engineering computations, 1(1), 77-88.

Dymiotis C., Kappos A. J. and Chryssanthopoulos M. K. (1999). Seismic reliability of RC frames with uncertain drift and member capacity. Journal of Structural Engineering, 125(9), 1038-1047.

European Committee for Standardization. (2004). Eurocode 5: Design of timber structures. Part 1-1: General - Common rules and rules for buildings. EN 1995-1-1. Brussels: CEN.

EN 408 (2012). Timber structures - Structural timber and glued laminated timber - Determination of some physical and mechanical properties. European Standard, European Committee for Standardization.

Fazio M. W., Moffett M. and Wodehouse L. (2003). A World History of Architecture. McGraw-Hill Professional. p. 201. ISBN 978-0-07-141751-8.

Fairhurst M. (2014). Dynamic Analysis of the FFTT System. MASc Thesis, University of British Columbia, Vancouver, Canada.

Fairhurst M., Zhang X. and Tannert T. (2014). Nonlinear Dynamic Analysis of a Novel Timber-Steel Hybrid System. World Conference on Timber Engineering 2014, Quebec City, Canada.

FEMA (1997). NEHRP guidelines for the seismic rehabilitation of buildings. Report No. FEMA P-273. Federal Emergency Management Agency, Washington, D.C.

FEMA (2006). Next-Generation Performance-Based Seismic Design Guidelines. Report No. FEMA P-445. Federal Emergency Management Agency, Washington, D.C.

FEMA (2009). Recommended Methodology for Quantification of Buildings System Performance and Response Parameters, Report No. FEMA P-695, Prepared by Applied Technology Council, prepared for the Federal Emergency Management Agency, Washington, D.C.

FEMA (2011). Quantification of Building System Performance and Response Factors - Component Equivalency Methodology, FEMA P-795, Prepared by Applied Technology Council, prepared for the Federal Emergency Management Agency, Washington, D.C.

Filiatrault A. and Folz B., (2002). Performance-based seismic design of wood framed buildings. Journal of Structural Engineering, 128(1), pp.39-47.

Fragiacomo M., Dujic B., and Sustersic I. (2011). "Elastic and ductile design of multi-storey crosslam massive wooden buildings under seismic actions." Engineering Structure, 33(11), 3043-3053.

Gagnon S., and Pirvu C. (eds.) (2011). Cross Laminated Timber (CLT) handbook, FPInnovations, Vancouver, Canada.

Gagnon S., and Rivest S. (2010). A Case Study of A 6-storey Hybrid Wood-concrete Office Building in Quebec City, Canada.1st International Conference on Structure and Architecture. Guimaraes, Portugal.

Gavric I., Fragiacomo M., and Ceccotti A. (2014). "Cyclic behaviour of typical metal connectors for cross-laminated (CLT) structures." Material Structure, in press.

Gerard R. (2014) A Short History of Tall Wood Buildings. Retrieved Nov.6, 2016, from: *http://doggerel.arup.com/a-short-history-of-tall-wood-buildings/.*

Goldberg D. (1989). Genetic Algorithms in search, optimization and machine learning. Addison-Welsley 1989; Reading, MA.

Gosselin A., Lehoux N., Cimon Y., and Blanchet P. (2015). Main Motivations and Barriers for Using Wood as a Structural Building Material - A Case Study. 11th International Industrial Engineering Conference - CIGI2015.Quebec, Canada.

Gonzales E., Tannert T., and Vallee T. (2016). The impact of defects on the capacity of timber joints with glued-in rods. International Journal of Adhesion and Adhesives, 65, 33-40.

Green M., and Karsh J. E. (2012). Tall wood -The case for tall wood buildings, Wood Enterprise Coalition, Vancouver, Canada.

Grosse M. (2005). Zur numerischen Simulation des physikalisch nichtlinearen Kurzzeittragverhaltens von Nadelholz am Beispiel von Holz-Beton-Verbundkonstruktionen (In German). Dissertation, Bauhaus-Universität Weimar.

Halchuk S., Allen T.I., Adams J. and Rogers G.C. (2014). Fifth Generation Seismic Hazard Model Input Files as Proposed to Produce Values for the 2015 National Building Code of Canada; Geological Survey of Canada, Open File 7576. DOI:10.4095/293907.

Hausegger G. (2013). Aussichtsturm Pyramidenkogel Kärnten (In German). pro: Holz. Retrieved Oct.15, 2016, from: *http://www.proholz.at/kommunalbauten/aussichtsturm-pyramidenkogel-kaernten/*.

Handbook of Steel Construction (2010). Canadian Institution of Steel Construction. 10th Edition. Markham, Canada.

Harms B., Prass G. and Schröder C. (2012). Timber Tower - er ist gebaut. The eighteenth international conference on wooden structures. Garmisch-Partenkirchen, Germany.

Hancock J., Watson-Lamprey J., Abrahamson N. A., Bommer J. J., Markatis A., McCoyth E. and Mendis, R. (2006). An Improved Method of Matching Response Spectra of Recorded

Earthquake Ground Motion Using Wavelets. Journal of Earthquake Engineering, 10(S1), 67-89.

Haukaas T. (2008). Unified reliability and design optimization for earthquake engineering. Probabilistic Engineering Mechanics, 23,471-481.

Hirschmann B. (2011). Ein Beitrag zur Bestimmung der Scheibenschubfestigkeit von Brettsperrholz. Master thesis, Institute of Timber Engineering and Wood Technology, Graz University of Technology (In German).

Holland M.A. (2001). Perry Brothers: more than a household name. Journal of the Royal Historical Society of Queensland, Vol. 17, No. 9: 385-405.

Hungarian Midleks (2016). Construction Timber. Retrieved from: *http://www.hungarian-midleks.com/*.

IBC (International Building Code). (2012). International code council. Washington, DC.

Jöbstl R A, Bogensperger T. and Schickhofer G. (2008). In-plane shear strength of cross laminated timber. CIBW18/41-12-3, St. Andrews, Canada.

Jeon J. S., Shafieezadeh A. and DesRoches R. (2014). Statistical models for shear strength of RC beam-column joints using machine-learning techniques. Earthquake Engineering & Structural Dynamics, 43(14), 2075-2095.

Karacabeyli E. and Lum C. (eds.) (2014). Technical Guide for the Design and Construction of Tall Wood Buildings in Canada. FPInnovations Special Publication SP-55E. Canada.

Karacabeyli E. and Popovski M. (2003). Design for earthquake engineering. In: Thelandersson S & Larsen H.J. (eds). Timber Engineering. Wiley, Chichester.

Karsh E. and Gafner B. (2012). The Flying Stairs at the University of British Columbia's Earth Sciences Building. The eighteenth international conference on wooden structure. Garmisch-Partenkirchen, Germany.

Khatibinia M., Fadaee M. J., Salajegheh J. and Salajegheh E. (2013). Seismic reliability assessment of RC structures including soil–structure interaction using wavelet weighted least squares support vector machine. Reliability Engineering & System Safety, 110, 22-33.

Khorasani Y. (2011). Feasibility Study of Hybrid Wood Steel Structures. MASc Thesis, University of British Columbia, Vancouver, Canada.

Kim, J. H. and Rosowsky, D. V. (2005). Fragility analysis for performance-based seismic design of engineered wood shearwalls. Journal of structural engineering, 131(11), 1764-1773.

Kiureghian A. D., and Ditlevsen O. (2009). Aleatory or Epistemic? Does it Matter?. Structural Safety, 31(2), 105-112.

KLH, (2015) Stadthaus, Murray Grove. Retrieved Oct. 10, 2016, from: *http://www.klhuk.com/portfolio/residential/stadthaus-murray-grove.aspx.*

Koo K. (2013). A Study on Historical Tall Wood Buildings in Toronto and Vancouver. Canadian Forest Service Final Report.

Koshihara M., Isode H. and Yusa S. (2005). The Design and Installation of a Five-Story New Timber Building in Japan. Summary of Technical Papers of Annual Meeting of Architectural Institute of Japan, C-1, pp. 201-206.

Kretschmann D. E. (2010). “Mechanical Properties of wood.” Wood handbook: Wood as an engineering material, General Technical Report FPL-TR 113, U.S. Department of Agriculture, Forest Service, Forest Products Laboratory, Madison, WI.

Kulak G.L. and Grondin G.Y. (2011). Limit States Design in Structural Steel, 9th edition, Canadian Institute of Steel Construction, Ontario, Canada. ISBN 978-088811-157-9.

Lackner M. and Vodicka M. (2013). The World’s Tallest Wooden Observatorion Tower. Design for Durability. Advanced Materials Research. Vol. 778, pp. 1028-1033. DOI: 10.4028/www.scientific.net/AMR.778.1028.

Lam F., He M. and Yao C. (2008).Example of traditional tall timber buildings in China: the Yingxian Pagoda. Structural Engineering International, 2, pp. 126-129.

Lam F., Li, Z. He, M. and Li, M. (2015). Comparison of Two Reliability Assessment Methods for the Seismic Performance of Timber-Steel Hybrid Structures. 12th International Conference on Applications of Statistics and Probability in Civil Engineering, ICASP12,Vancouver, Canada.

Land Lease, (2015) Exploring the world's tallest timber apartment. Retrieved Sep. 8, 2016, from: *http://www.forteliving.com.au*.

Lefebvre D. and Ellyin, F. (1984). Cyclic response and inelastic strain energy in low cyclic fatigue. International Journal of Fatigue. 6(1): 9-15. DOI: 10.1016/0142-1123(84)90003-3.

López-Almansa F., Segués E., and Cantalapiedra, I.R. (2014). A new steel framing system for seismic protection of timber platform frame buildings. Implementation with hysteretic energy dissipators. Earthquake Engineering & Structural Dynamics. 44(8).PP 1181-1202.

Lowes L. N., Mitra N. and Altoontash, A. (2003). A beam-column joint model for simulating the earthquake response of reinforced concrete frames. Prepared for the Pacific Earthquake Engineering Research Center, College of Engineering, University of California, Berkley, CA.

Li M., Lam F., Foschi R. O., Nakajima S. and Nakagawa, T. (2011a). Seismic Performance of Post and Beam Timber Buildings I: Model Development and Verification. Journal of Wood Science, 58(1), 20–30.

Li M., Lam F., Foschi R. O., Nakajima S. and Nakagawa T. (2011b). Seismic Performance of Post-and-Beam Timber Buildings II: Reliability Evaluations. Journal of Wood Science, 58(2), 135–143.

Li M., Lam F. and Li Y. (2014). Evaluating rolling shear strength properties of cross laminated timber by torsional shear tests and bending tests. The World Conference on Timber Engineering, WCTE 2004, Quebec City, Canada.

Lin K. C., Lin C. C. J., Chen J. Y. and Chang H. Y. (2010). Seismic reliability of steel framed buildings. Structural safety, 32(3), 174-182.

Mahsuli M., and Haukaas T. (2013). Computer Program for Multimodel Reliability and Optimization Analysis. Journal of Computing in Civil Engineering, 27(1), 87-98.

McKenna F., Fenves G. L., Scott M. H., and Jeremic B. (2000). Open System for Earthquake Engineering Simulation (OpenSees). Pacific Earthquake Engineering Research Center, University of California, Berkeley, CA.

Miodek A. (2002). Corrosion protection of steel structures. Ochrona Przed Korozja 7: 183-187.

Mjolsness E. and DeCoste D. (2001). Machine learning for science: state of the art and future prospects. Science, 293(5537), 2051-2055.

Moore M. (2000). Scotia Place-12 Story Apartment Building A Case Study of High-rise Construction Using Wood and Steel. New Zealand. Timber Design Journal, 10(1), 5-12.

Mohammad M., Gagnon S., Douglas B. K., and Podesto L. (2012). Introduction to cross-laminated timber. Wood Design Focus, 22 (2), 3-12.

NRC (2010). National Building Code of Canada 2010. Canadian Commission on Building and Fire Code, National Research Council of Canada, Ottawa, Canada.

Origine Écocondos de la Pointe-aux-Lièvres. (2015). Projet. Retrieved Oct.22, 2016, from: *http://condosorigine.com/projet/*.

Papadrakakis M., Tsompanakis Y., Lagaros N. D. and Fragiadakis, M. (2004). Reliability based optimization of steel frames under seismic loading conditions using evolutionary computation. Journal of Theoretical and Applied Mechanics, 42(3), 585-608.

Park R. (1996). A Static Force-based Procedure for the Seismic Assessment of Existing Reinforced Concrete Moment Resisting Frames. Proceedings NZ National Conference on Earthquake Engineering, New Plymouth.

Pei S., Popovski M. and van de Lindt J.W. (2012). Seismic Design of A Multi-Story Cross Laminated Timber Building Based On Component Level Testing. Proceedings of the 12th World Conference on Timber Engineering, Auckland, New Zealand.

Pei S., Popovski M., and van de Lindt, J. W. (2013a). "Analytical study on seismic force modification factors for cross-laminated timber building for NBCC." Canadian Journal of Civil Engineering. 40(9), 887-896.

Pei S., Popovski M. and van de Lindt, J.W. (2013b). Approximate R-factor for Cross Laminated Timber Walls in Multi-storey Buildings. Paper accepted for publication in ASCE Journal of Architectural Engineering.

Popovski M., Schneider J., and Schweinsteiger M. (2010). "Lateral load resistance of cross-laminated wood panels." World Conference on Timber Engineering. Trentino, Italy.

Popovski M., Karacabeyli E. and Ceccotti, A. (2011). Seismic Performance of Cross-Laminated Timber Buildings - Chapter 4. CLT Handbook - Cross-Laminated Timber, FPInnovations Special Publication SP-528E Canadian Edition Edited by S. Gagnon and Ciprian Pirvu.

Poirier E., Moudgil M., Fallahi A., Staub-French S. and Tannert T. (2016) Design and Construction of a 53 Meter Tall Timber Building at The University Of British Columbia. World Conference on Timber Engineering, Vienna, Austria.

Professner H. and Mathis C. (2012). LifeCycle Tower - high-rise buildings in timber. ASCE Structures Congress. Chicago, Illinois, USA.

Priestley M.J.N. (1993). Myths and Fallacies in Earthquake Engineering - Conflicts Between Design and Reality, Bulletin of the New Zealand National Society for Earthquake Engineering, 26 (3), 329-341.

Priestley M.J.N. (2002). Direct Displacement-Based Design of Precast/ Prestressed Concrete Buildings. PCI Journal.

Pyramidenkogel (2013). Kärnten Pyramidenkogel. Retrieved Oct. 21, 2016, from: *http://www.pyramidenkogel.info/*.

Rosowsky, D. V. (2002). Reliability-based seismic design of wood shear walls. Journal of structural Engineering, 128(11), 1439-1453.

Rosowsky, D. V. and Ellingwood, B. R. (2002). Performance-based engineering of wood frame housing: Fragility analysis methodology. Journal of Structural Engineering, 128(1), 32-38.

Runger G. C. and Montgomery D. C. (2010). Applied Statistics and Probability for Engineers, 5th edition, John Wiley & Sons, Inc.

Schmidt M. and Lipson, H. (2009). Distilling free-form natural laws from experimental data. Science, 324(5923), 81-85.

Serrano E. (2009). Limnologen - Experiences from an 8 - storey timber building. Växjö, Sweden, pp. 1-12.

Seismosoft (2013). SeismoMatch v2.1 - A Computer Program for Spectrum Matching of Earthquake Records. Retrieved from: *http://www.seismosoft.com*.

Simpson Strong-Tie Company Inc. (SSTCI) (2015). Strong-Rod™ Systems RTUD Ratcheting Take-Up Device. Retrieved Nov.23, 2016, from: *https://www.strongtie.com*.

SOM. (2013). Tall Timber Research Project. Skidmore, Owings & Merrill. Chicago, II.

Storaenso (2015). Via Cenni. Retrieved Oct. 22, 2016, from: *http://buildingandliving.storaenso.com/-news/rethinkarticles/viacenni*.

Stiemer S. F. (2012). Position Paper on Hybrid (Timber / Steel) Structures. Vancouver, Canada.

Structurlam. (2012). Cross Laminated Timber Design Guide-Version 7. Vancouver, BC.

Shahnewaz M., and Alam M. S. (2014). Improved shear equations for steel fiber-reinforced concrete deep and slender beams. ACI Structural Journal, 111 (4), 851-860.

Shahnewaz M., Machial R., Alam M. S. and Rteil A. (2015). Optimized shear design equation for slender concrete beams reinforced with FRP bars and stirrups using Genetic Algorithm and reliability analysis. In Press, Engineering Structures.

Shi S. and Walker J. (2006). Wood-based composites: plywood and veneer-based products. J.C.F. Walker (Ed.), Primary wood processing principles and practice (2nd ed.), pp. 391-392.

Shinozuka M., Feng M. Q., Kim H. K., and Kim S. H. (2000a). Nonlinear static procedure for fragility curve development. Journal of Engineering Mechanics, 126(12), 1287-1295.

Schneider J. (2015). Conventional and novel timber steel hybrid connections: testing, performance and assessment. PhD thesis, University of British Columbia, Vancouver, Canada.

Schneider J., Zhang X., Tannert T., Popovski M., Karacabeyli E., Stiemer S.F., Tesfamariam S. (2014). Novel Steel Tube Connection for Hybird System. World Conference for Timber Engineering. Quebec, CA.

Takei T., Hamajima M. and Kamba N. (1997). Fourier transform infrared spectroscopic analysis of the degradation of structural lumber in Horyu-ji temple. Mokuzai Gakkaishi, 43 (3), pp. 285-294 (in Japanese).

UBC News (2016). Structure of UBC's tall wood building now complete. Retrieved Nov. 3, 2016, from: *http://news.ubc.ca/2016/09/15/structure-of-ubcs-tall-wood-building-now-complete/*.

Van de Lindt J., and Walz M. A. (2003). Development and Application of Wood Shear Wall Reliability Model. Journal of Structural Engineering, 129(3), 405–413.

Van de Lindt, J.W. (2005). Damage-based seismic reliability concept for woodframe structures. Journal of structural engineering 131(4), 668-675.

Van de Lindt, J. W., Pei, S. and Liu, H. (2008). Performance-based seismic design of wood frame buildings using a probabilistic system identification concept. Journal of structural engineering 134(2), 240-247.

Wang, Y., Rosowsky, D. V. and Pang, W. (2010). Performance-based procedure for direct displacement design of engineered wood-frame structures. Journal of structural engineering, 136(8), 978-988.

Wood Solutions design and build (2013). Forte an innovative CLT apartment building. Retrieved Nov.11, 2016, from: *https://www.woodsolutions.com.au/Inspiration-CaseStudy/forte-living*.

Yin Y.-J., and Li Y. (2011). Probabilistic Loss Assessment of Light-frame Wood Construction Subjected to Combined Seismic and Snow Loads. Engineering Structures, Elsevier Ltd, 33(2), 380–390.

Yun S.Y., Hamburger R.O., Cornell C.A. and Foutch D.A. (2002). Seismic performance evaluation for steel moment frames. Journal of Structural Engineering, 128(4), pp.534-545.

Zangerl M., Tahan N. (2013). LCT ONE, Wood Design & Building. Retrieved Oct.28, 2016, from: *http://wooddesign.dgtlpub.com/2013/2013-02-28/pdf/LCT_ONE.pdf.*

Appendices

Appendix A Experimental tests results

A.1 Hysteresis loops for series 1-2

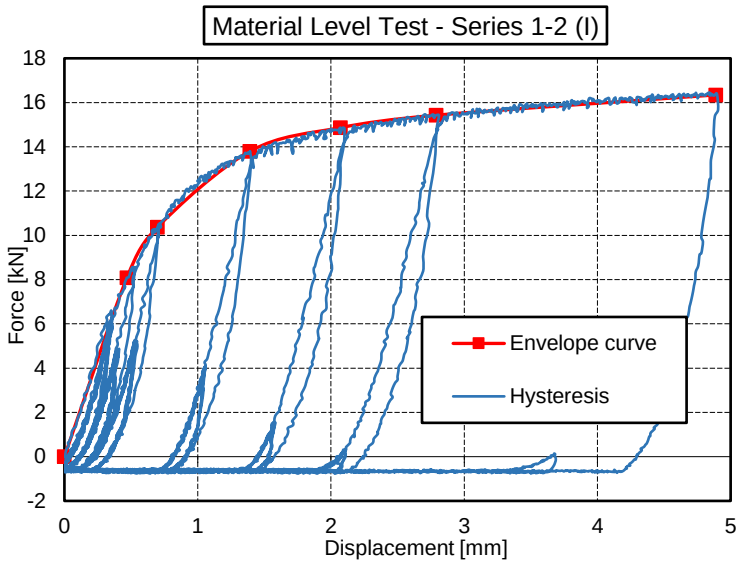

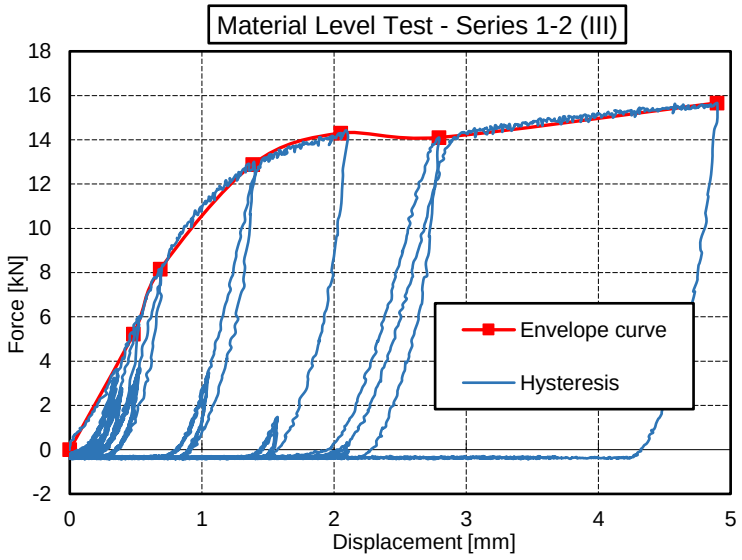

A.2 Hysteresis loops for Component level tests

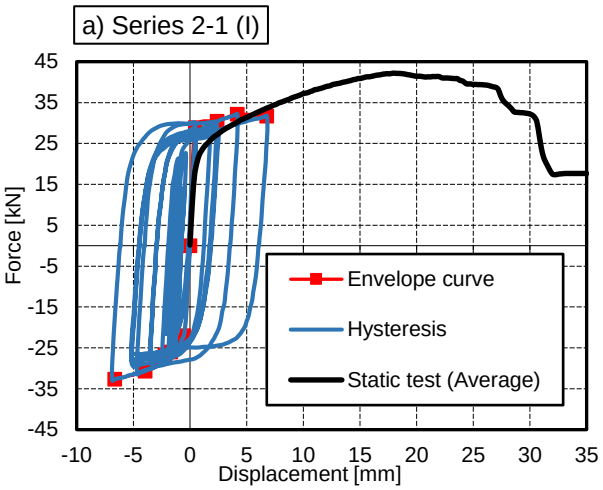

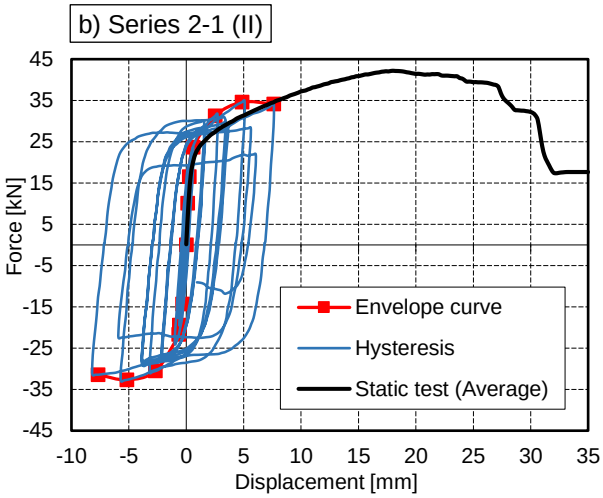

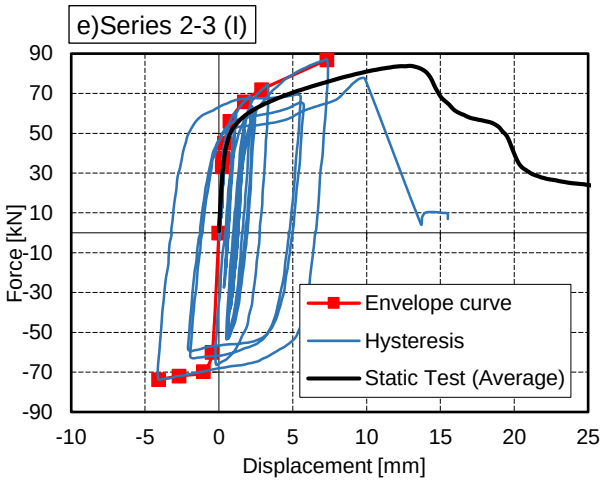

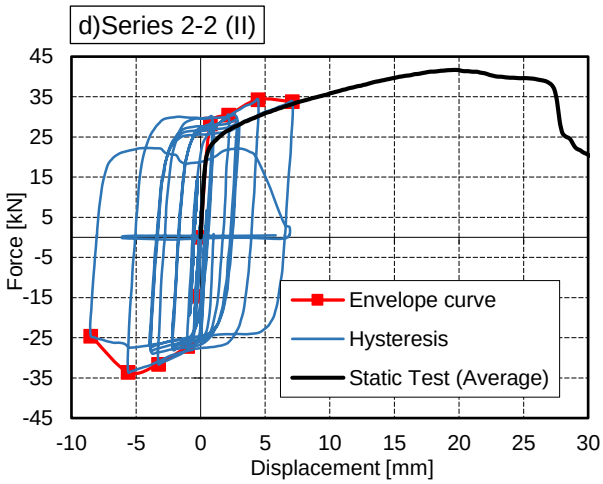

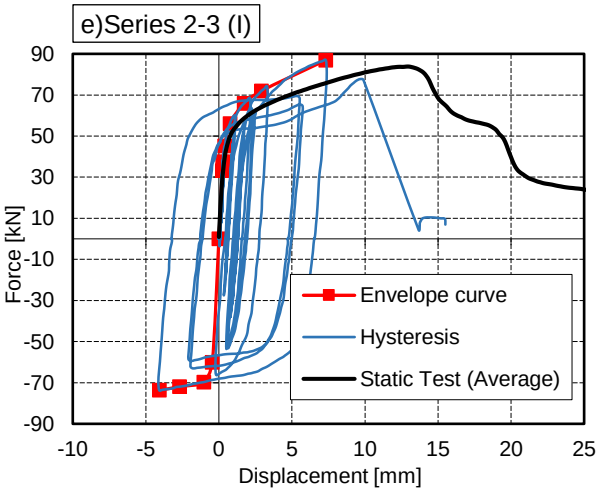

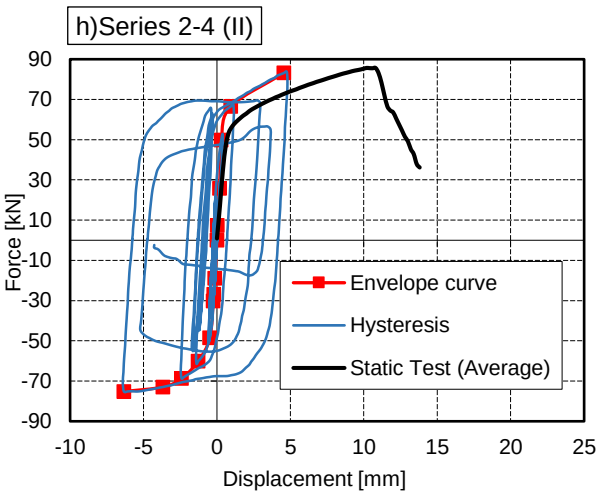

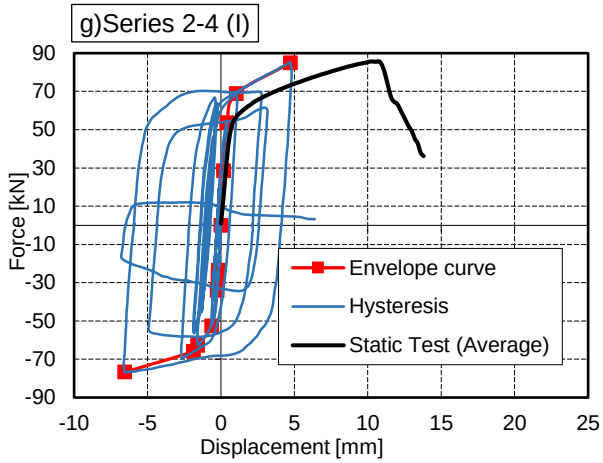
g)Series 2-4 (I)
Force [kN]
Displacement [mm]
Envelope curve
Hysteresis
Static Test (Average)

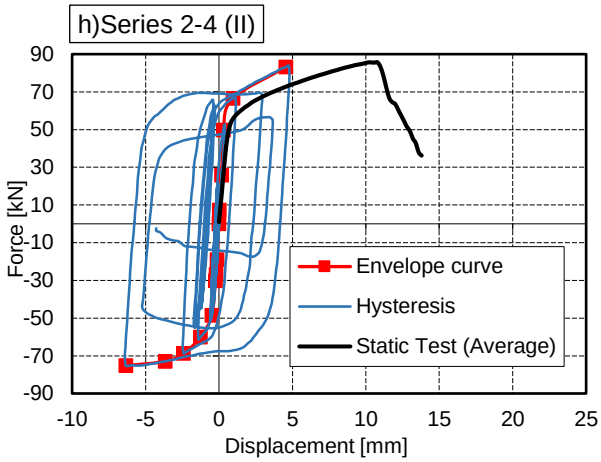
h)Series 2-4 (II)
Force [kN]
Displacement [mm]
Envelope curve
Hysteresis
Static Test (Average)

A.3 Hysteresis loops for Mid-scale tests

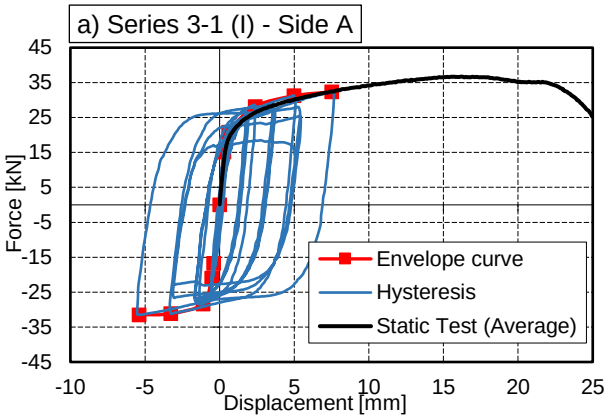

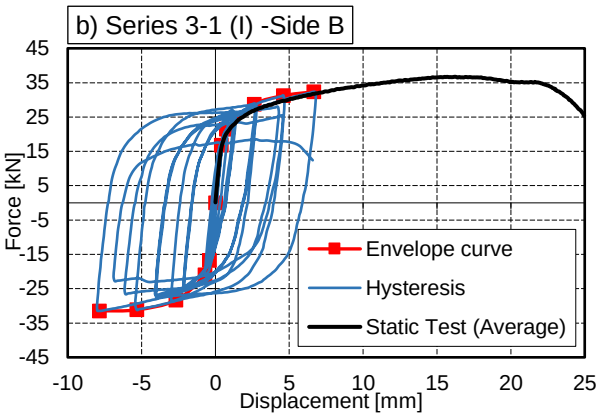

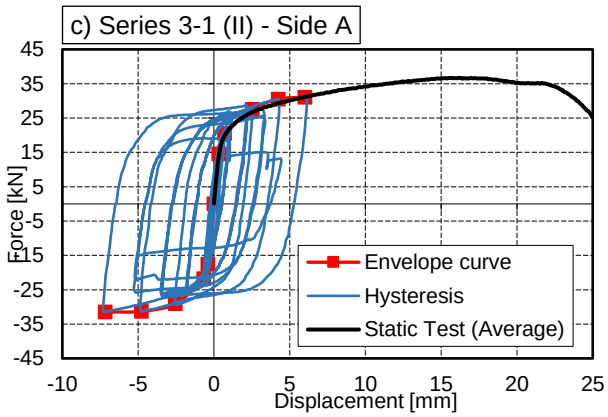

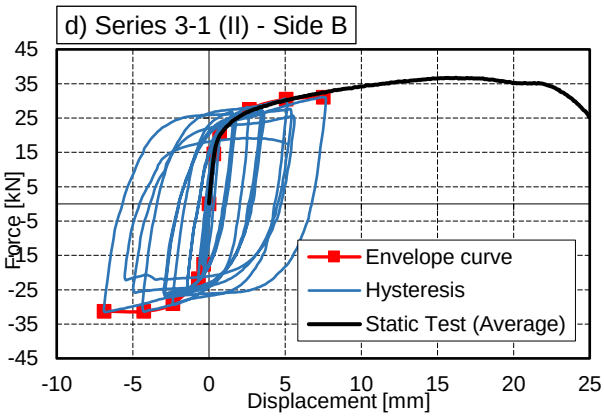

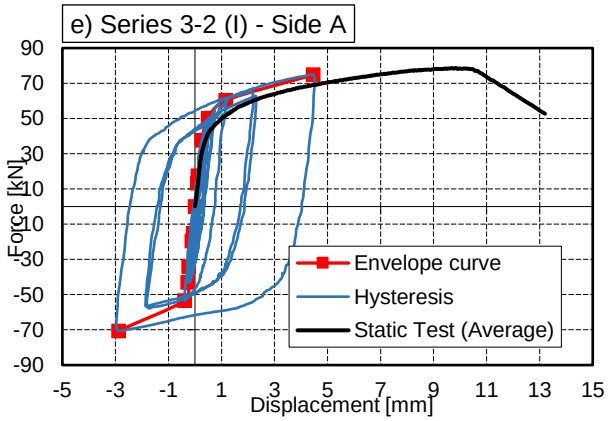

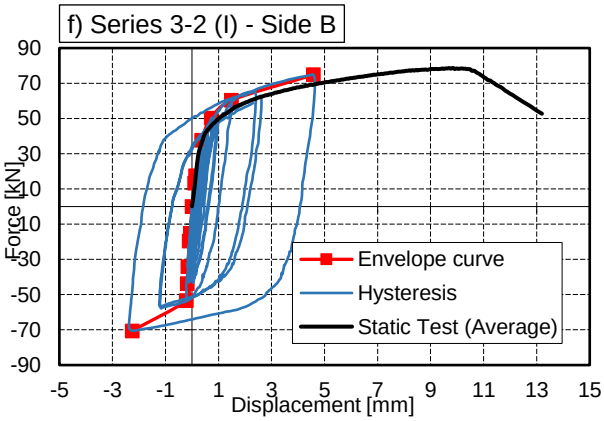

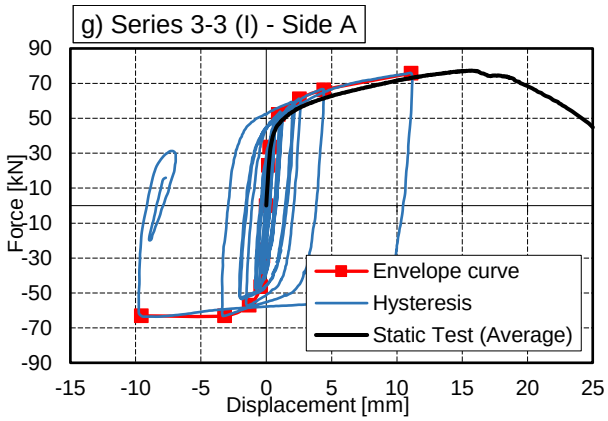
g) Series 3-3 (I) - Side A
Force [kN]
Displacement [mm]
Envelope curve
Hysteresis
Static Test (Average)

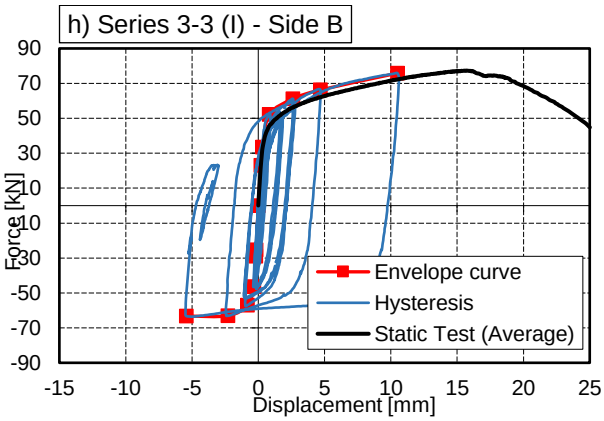
h) Series 3-3 (I) - Side B
Force [kN]
Displacement [mm]
Envelope curve
Hysteresis
Static Test (Average)

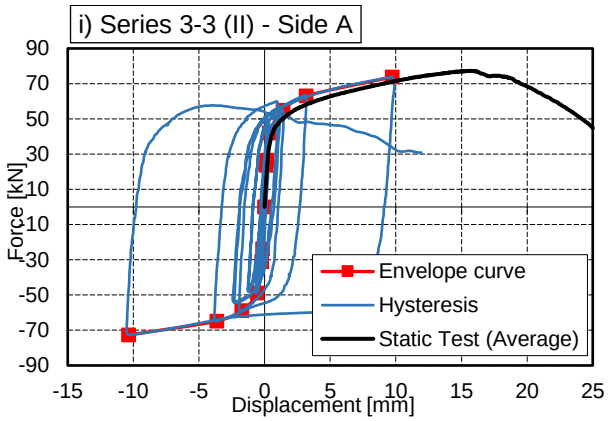
i) Series 3-3 (II) - Side A
Force [kN]
Displacement [mm]
Envelope curve
Hysteresis
Static Test (Average)

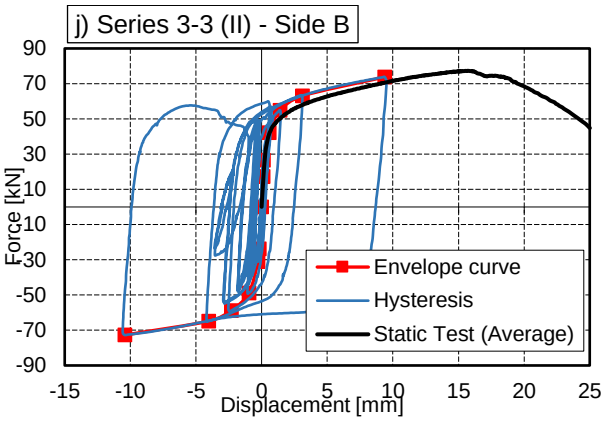
j) Series 3-3 (II) - Side B
Force [kN]
Displacement [mm]
Envelope curve
Hysteresis
Static Test (Average)

A.4 The test set up for full scale hold-down test series 4-2

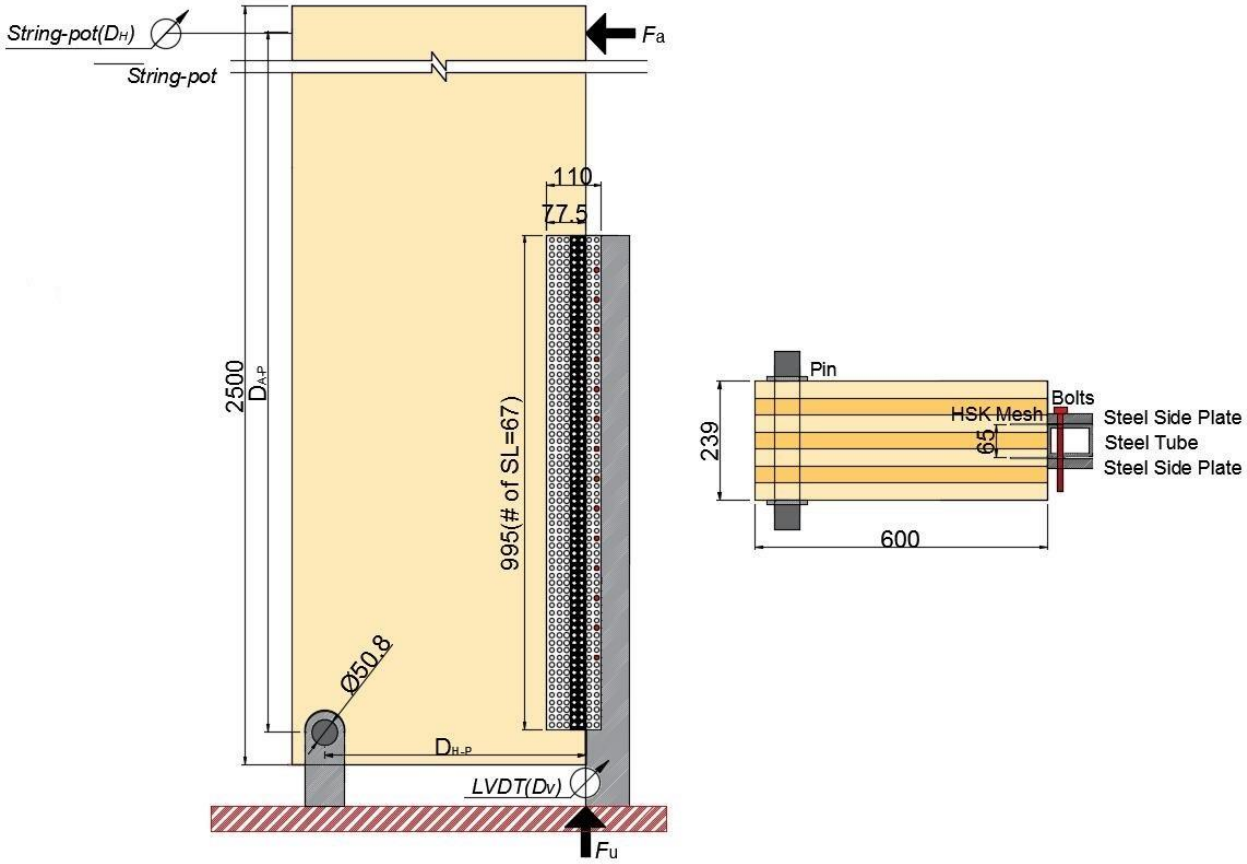

Appendix B Steel beam selection table

Appendix B presents the selection of the steel beam cross sections for the 3-storey, 6-storey, 9-storey and 12-storey FFTT system Option 1 designed with different R_d factors.

B.1 Steel beam selection for 3-storey FFTT system Option 1 with different R_d

Table B1- Steel beam selection for 3-storey (R_d=1.5)

Storey	DSB		SSB	
	Steel Cross Section	Yield Moment (kNm)	Steel Cross Section	Yield Moment (kNm)
1	W200×42	137.7	W310×28	121.1
2	W150×37	94.5	W310×28	121.1
3	W150×24	58.0	W310×28	121.1

Table B2- Steel beam selection for 3-storey (R_d=2.0)

Storey	DSB		SSB	
	Steel Cross Section	Yield Moment (kNm)	Steel Cross Section	Yield Moment (kNm)
1	W250×28	105.9	W150×37	94.5
2	W250×22	78.3	W150×37	94.5
3	W150×18	41.4	W150×37	94.5

Table B3 - Steel beam selection for 3-storey (R_d=2.5)

Storey	DSB		SSB	
	Steel Cross Section	Yield Moment (kNm)	Steel Cross Section	Yield Moment (kNm)
1	W250×22	78.3	W250×22	78.3
2	W150×24	58.0	W250×22	78.3
3	W150×18	41.4	W250×22	78.3

Table B4- Steel beam selection for 3-storey (R_d=3.0)

Storey	DSB		SSB	
	Steel Cross Section	Yield Moment (kNm)	Steel Cross Section	Yield Moment (kNm)
1	W200×22	66.9	W200×22	66.9
2	W150×18	41.4	W200×22	66.9
3	W100×19	31.0	W200×22	66.9

Table B5- Steel beam selection for 3-storey (R_d=3.5)

Storey	DSB		SSB	
	Steel Cross Section	Yield Moment (kNm)	Steel Cross Section	Yield Moment (kNm)
1	W130×24	48.0	W130×28	58.0
2	W100×19	31.0	W130×28	58.0
3	W100×19	31.0	W130×28	58.0

Table B6- Steel beam selection for 3-storey (R_d=4.0)

Storey	DSB		SSB	
	Steel Cross Section	Yield Moment (kNm)	Steel Cross Section	Yield Moment (kNm)
1	W130×24	48.0	W130×24	48.0
2	W100×19	31.0	W130×24	48.0
3	W100×19	31.0	W130×24	48.0

Table B7- Steel beam selection for 3-storey (R_d=4.5)

Storey	DSB		SSB	
	Steel Cross Section	Yield Moment (kNm)	Steel Cross Section	Yield Moment (kNm)
1	W150×18	41.4	W150×18	41.4
2	W100×19	31.0	W150×18	41.4
3	W100×19	31.0	W150×18	41.4

Table B8- Steel beam selection for 3-storey (R_d=5.0)

Storey	DSB		SSB	
	Steel Cross Section	Yield Moment (kNm)	Steel Cross Section	Yield Moment (kNm)
1	W130×24	48.0	W150×18	41.4
2	W100×19	31.0	W150×18	41.4
3	W100×19	31.0	W150×18	41.4

Table B9- Steel beam selection for 3-storey (R_d=5.5)

Storey	DSB		SSB	
	Steel Cross Section	Yield Moment (kNm)	Steel Cross Section	Yield Moment (kNm)
1	W150×18	41.4	W100×19	31.0
2	W100×19	31.0	W100×19	31.0
3	W100×19	31.0	W100×19	31.0

Table B10- Steel beam selection for 3-storey (R_d=6.0)

Storey	DSB		SSB	
	Steel Cross Section	Yield Moment (kNm)	Steel Cross Section	Yield Moment (kNm)
1	W150×18	41.4	W100×19	31.0
2	W100×19	31.0	W100×19	31.0
3	W100×19	31.0	W100×19	31.0

B.2 Steel beam selection for 6-storey FFTT system Option 1 with different R_d

Table B11- Steel beam selection for 6-storey (R_d=1.5)

Storey	DSB		SSB	
	Steel Cross Section	Yield Moment (kNm)	Steel Cross Section	Yield Moment (kNm)
1	W310×45	218.7	W310×45	218.7
2	W250×45	184.2	W310×45	218.7
3	W360×33	163.5	W310×45	218.7
4	W200×42	137.7	W310×28	121.1
5	W200×31	103.2	W310×28	121.1
6	W200×22	66.9	W310×28	121.1

Table B12- Steel beam selection for 6-storey (R_d=2.0)

Storey	DSB		SSB	
	Steel Cross Section	Yield Moment (kNm)	Steel Cross Section	Yield Moment (kNm)
1	W360×33	163.5	W360×33	163.5
2	W310×33	143.2	W360×33	163.5
3	W310×28	121.1	W360×33	163.5
4	W310×24	96.6	W310×24	96.6
5	W310×24	96.6	W310×24	96.6
6	W130×24	47.7	W310×24	96.6

Table B13- Steel beam selection for 6-storey (R_d=2.5)

Storey	DSB		SSB	
	Steel Cross Section	Yield Moment (kNm)	Steel Cross Section	Yield Moment (kNm)
1	W310×33	143.2	W310×28	121.1
2	W250×28	105.9	W310×28	121.1
3	W310×24	96.6	W310×28	121.1
4	W250×25	91.8	W250×22	78.3
5	W200×22	66.9	W250×22	78.3
6	W150×18	41.4	W250×22	78.3

Table B14- Steel beam selection for 6-storey (R_d=3.0)

Storey	DSB		SSB	
	Steel Cross Section	Yield Moment (kNm)	Steel Cross Section	Yield Moment (kNm)
1	W310×28	121.1	W250×28	105.9
2	W310×24	96.6	W250×28	105.9
3	W250×22	78.3	W250×28	105.9
4	W200×22	66.9	W200×22	66.9
5	W150×24	58.0	W200×22	66.9
6	W150×18	41.4	W200×22	66.9

Table B15- Steel beam selection for 6-storey (R_d=3.5)

Storey	DSB		SSB	
	Steel Cross Section	Yield Moment (kNm)	Steel Cross Section	Yield Moment (kNm)
1	W310×24	96.6	W250×25	91.77
2	W310×24	96.6	W250×25	91.77
3	W200×22	66.93	W250×25	91.77
4	W150×24	57.96	W200×22	66.93
5	W130×24	47.955	W200×22	66.93
6	W150×18	41.4	W200×22	66.93

Table B16- Steel beam selection for 6-storey (R_d=4.0)

Storey	DSB		SSB	
	Steel Cross Section	Yield Moment (kNm)	Steel Cross Section	Yield Moment (kNm)
1	W250×22	78.3	W250×22	78.3
2	W250×22	78.3	W250×22	78.3
3	W200×22	66.9	W250×22	78.3
4	W150×24	58.0	W150×24	58.0
5	W130×24	48.0	W150×24	58.0
6	W150×18	41.4	W150×24	58.0

Table B17- Steel beam selection for 6-storey (R_d=4.5)

Storey	DSB		SSB	
	Steel Cross Section	Yield Moment (kNm)	Steel Cross Section	Yield Moment (kNm)
1	W200×22	66.9	W250×22	78.3
2	W200×22	66.9	W250×22	78.3
3	W150×24	58.0	W250×22	78.3
4	W130×24	48.0	W130×24	48.0
5	W150×18	41.4	W130×24	48.0
6	W100×19	31.0	W130×24	48.0

Table B18- Steel beam selection for 6-storey (R_d=5.0)

Storey	DSB		SSB	
	Steel Cross Section	Yield Moment (kNm)	Steel Cross Section	Yield Moment (kNm)
1	W200×22	66.9	W150×24	58.0
2	W200×22	66.9	W150×24	58.0
3	W130×24	48.0	W150×24	58.0
4	W150×18	41.4	W150×18	41.4
5	W150×18	41.4	W150×18	41.4
6	W100×19	31.0	W150×18	41.4

Table B19- Steel beam selection for 6-storey (R_d=5.5)

Storey	DSB		SSB	
	Steel Cross Section	Yield Moment (kNm)	Steel Cross Section	Yield Moment (kNm)
1	W130×24	48.0	W130×24	48.0
2	W130×24	48.0	W130×24	48.0
3	W150×18	41.4	W130×24	48.0
4	W150×18	41.4	W150×18	41.4
5	W150×18	41.4	W150×18	41.4
6	W100×19	31.0	W150×18	41.4

Table B20- Steel beam selection for 6-storey (R_d=6.0)

Storey	DSB		SSB	
	Steel Cross Section	Yield Moment (kNm)	Steel Cross Section	Yield Moment (kNm)
1	W130×24	48.0	W150×18	41.4
2	W150×18	41.4	W150×18	41.4
3	W150×18	41.4	W150×18	41.4
4	W100×19	31.0	W100×19	31.0
5	W100×19	31.0	W100×19	31.0
6	W100×19	31.0	W100×19	31.0

B.3 Steel beam selection for 9-storey FFTT system Option 1 with different R_d

Table B21- Steel beam selection for 9-storey (R_d=1.5)

Storey	DSB		SSB	
	Steel Cross Section	Yield Moment (kNm)	Steel Cross Section	Yield Moment (kNm)
1	W360×51	274.6	W360×51	274.6
2	W250×58	239.1	W360×51	274.6
3	W360×39	200.1	W360×51	274.6
4	W250×45	184.2	W360×33	163.5
5	W250×39	158.4	W360×33	163.5
6	W250×39	158.4	W360×33	163.5
7	W200×42	137.7	W310×28	121.1
8	W310×28	121.1	W310×28	121.1
9	W200×22	66.9	W310×28	121.1

Table B22- Steel beam selection for 9-storey (R_d=2.0)

Storey	DSB		SSB	
	Steel Cross Section	Yield Moment (kNm)	Steel Cross Section	Yield Moment (kNm)
1	W360×39	200.1	W360×39	200.1
2	W360×33	163.5	W360×39	200.1
3	W310×33	143.2	W360×39	200.1
4	W310×33	143.2	W310×33	143.2
5	W200×42	137.7	W310×33	143.2
6	W200×42	137.7	W310×33	143.2
7	W310×28	121.1	W250×28	105.9
8	W250×28	105.9	W250×28	105.9
9	W130×28	58.0	W250×28	105.9

Table B23- Steel beam selection for 9-storey (R_d=2.5)

Storey	DSB		SSB	
	Steel Cross Section	Yield Moment (kNm)	Steel Cross Section	Yield Moment (kNm)
1	W250×39	158.4	W250×39	158.4
2	W310×33	143.2	W250×39	158.4
3	W310×28	121.1	W250×39	158.4
4	W310×28	121.1	W250×28	105.9
5	W250×28	105.9	W250×28	105.9
6	W250×28	105.9	W250×28	105.9
7	W310×24	96.6	W310×24	96.6
8	W250×22	78.3	W310×24	96.6
9	W130×24	48.0	W310×24	96.6

Table B24- Steel beam selection for 9-storey (R_d=3.0)

Storey	DSB		SSB	
	Steel Cross Section	Yield Moment (kNm)	Steel Cross Section	Yield Moment (kNm)
1	W310×33	143.2	W310×33	143.2
2	W310×28	121.1	W310×33	143.2
3	W310×28	121.1	W310×33	143.2
4	W310×24	96.6	W310×24	96.6
5	W310×24	96.6	W310×24	96.6
6	W250×25	91.8	W310×24	96.6
7	W250×22	78.3	W250×22	78.3
8	W250×22	78.3	W250×22	78.3
9	W150×18	41.4	W250×22	78.3

Table B25- Steel beam selection for 9-storey (R_d=3.5)

Storey	DSB		SSB	
	Steel Cross Section	Yield Moment (kNm)	Steel Cross Section	Yield Moment (kNm)
1	W310×28	121.1	W310×28	121.1
2	W310×24	96.6	W310×28	121.1
3	W310×24	96.6	W310×28	121.1
4	W250×25	91.8	W250×25	91.8
5	W250×25	91.8	W250×25	91.8
6	W250×22	78.3	W250×25	91.8
7	W200×22	66.9	W200×22	66.9
8	W200×22	66.9	W200×22	66.9
9	W150×18	41.4	W200×22	66.9

Table B26- Steel beam selection for 9-storey (R_d=4.0)

Storey	DSB		SSB	
	Steel Cross Section	Yield Moment (kNm)	Steel Cross Section	Yield Moment (kNm)
1	W250×28	105.9	W250×28	105.9
2	W310×24	96.6	W250×28	105.9
3	W250×25	91.8	W250×28	105.9
4	W250×22	78.3	W250×22	78.3
5	W250×22	78.3	W250×22	78.3
6	W250×22	78.3	W250×22	78.3
7	W200×22	66.9	W130×24	48.0
8	W130×24	48.0	W130×24	48.0
9	W150×18	41.4	W130×24	48.0

Table B27- Steel beam selection for 9-storey (R_d=4.5)

Storey	DSB		SSB	
	Steel Cross Section	Yield Moment (kNm)	Steel Cross Section	Yield Moment (kNm)
1	W310×24	96.6	W250×22	78.3
2	W250×22	78.3	W250×22	78.3
3	W250×22	78.3	W250×22	78.3
4	W200×22	66.9	W200×22	66.9
5	W200×22	66.9	W200×22	66.9
6	W200×22	66.9	W200×22	66.9
7	W130×28	58.0	W150×18	41.4
8	W130×24	48.0	W150×18	41.4
9	W100×19	31.0	W150×18	41.4

Table B28- Steel beam selection for 9-storey (R_d=5.0)

Storey	DSB		SSB	
	Steel Cross Section	Yield Moment (kNm)	Steel Cross Section	Yield Moment (kNm)
1	W250×22	78.3	W250×22	78.3
2	W250×22	78.3	W250×22	78.3
3	W200×22	66.9	W250×22	78.3
4	W200×22	66.9	W150×24	58.0
5	W200×22	66.9	W150×24	58.0
6	W150×24	58.0	W150×24	58.0
7	W150×18	41.4	W150×18	41.4
8	W150×18	41.4	W150×18	41.4
9	W100×19	31.0	W150×18	41.4

Table B29- Steel beam selection for 9-storey (R_d=5.5)

Storey	DSB		SSB	
	Steel Cross Section	Yield Moment (kNm)	Steel Cross Section	Yield Moment (kNm)
1	W200×22	66.9	W150×24	58.0
2	W200×22	66.9	W150×24	58.0
3	W150×24	58.0	W150×24	58.0
4	W150×24	58.0	W130×24	48.0
5	W130×24	48.0	W130×24	48.0
6	W130×24	48.0	W130×24	48.0
7	W150×18	41.4	W100×19	31.0
8	W100×19	31.0	W100×19	31.0
9	W100×19	31.0	W100×19	31.0

Table B30- Steel beam selection for 9-storey (R_d=6.0)

Storey	DSB		SSB	
	Steel Cross Section	Yield Moment (kNm)	Steel Cross Section	Yield Moment (kNm)
1	W150×24	58.0	W130×24	48.0
2	W150×24	58.0	W130×24	48.0
3	W130×24	48.0	W130×24	48.0
4	W130×24	48.0	W150×18	41.4
5	W150×18	41.4	W150×18	41.4
6	W150×18	41.4	W150×18	41.4
7	W100×19	31.0	W100×19	31.0
8	W100×19	31.0	W100×19	31.0
9	W100×19	31.0	W100×19	31.0

B.4 Steel beam selection for 12-storey FFTT system Option 1 with different R_d

Table B31- Steel beam selection for 12-storey (R_d=1.5)

Storey	DSB		SSB	
	Steel Cross Section	Yield Moment (kNm)	Steel Cross Section	Yield Moment (kNm)
1	W360×51	274.6	W360×51	274.6
2	W250×58	239.1	W360×51	274.6
3	W360×39	200.1	W360×51	274.6
4	W360×39	200.1	W250×45	184.2
5	W250×45	184.2	W250×45	184.2
6	W250×45	184.2	W250×45	184.2
7	W360×33	163.5	W360×33	163.5
8	W250×39	158.4	W360×33	163.5
9	W200×42	137.7	W360×33	163.5
10	W310×28	121.1	W310×28	121.1
11	W310×24	96.6	W310×28	121.1
12	W150×24	58.0	W310×28	121.1

Table B32- Steel beam selection for 12-storey (R_d=2.0)

Storey	DSB		SSB	
	Steel Cross Section	Yield Moment (kNm)	Steel Cross Section	Yield Moment (kNm)
1	W360×39	200.1	W360×39	200.1
2	W360×33	163.5	W360×39	200.1
3	W360×33	163.5	W360×39	200.1
4	W310×33	143.2	W310×33	143.2
5	W200×42	137.7	W310×33	143.2
6	W200×42	137.7	W310×33	143.2
7	W310×28	121.1	W310×28	121.1
8	W250×28	105.9	W310×28	121.1
9	W310×24	96.6	W310×28	121.1
10	W310×24	96.6	W310×24	96.6
11	W250×22	78.3	W310×24	96.6
12	W130×24	48.0	W310×24	96.6

Table B33- Steel beam selection for 12-storey (R_d=2.5)

Storey	DSB		SSB	
	Steel Cross Section	Yield Moment (kNm)	Steel Cross Section	Yield Moment (kNm)
1	W360×33	163.5	W360×33	163.5
2	W310×33	143.2	W360×33	163.5
3	W310×33	143.2	W360×33	163.5
4	W310×28	121.1	W310×28	121.1
5	W310×28	121.1	W310×28	121.1
6	W250×28	105.9	W310×28	121.1
7	W250×28	105.9	W250×28	105.9
8	W310×24	96.6	W250×28	105.9
9	W310×24	96.6	W250×28	105.9
10	W250×22	78.3	W250×22	78.3
11	W250×22	78.3	W250×22	78.3
12	W150×18	41.4	W250×22	78.3

Table B34- Steel beam selection for 12-storey (R_d=3.0)

Storey	DSB		SSB	
	Steel Cross Section	Yield Moment (kNm)	Steel Cross Section	Yield Moment (kNm)
1	W310×33	143.2	W310×33	143.2
2	W310×28	121.1	W310×33	143.2
3	W310×28	121.1	W310×33	143.2
4	W310×28	121.1	W250×28	105.9
5	W250×28	105.9	W250×28	105.9
6	W250×28	105.9	W250×28	105.9
7	W310×24	96.6	W310×24	96.6
8	W250×25	91.8	W310×24	96.6
9	W250×22	78.3	W310×24	96.6
10	W250×22	78.3	W200×22	66.9
11	W200×22	66.9	W200×22	66.9
12	W150×24	58.0	W200×22	66.9

Table B35- Steel beam selection for 12-storey (R_d=3.5)

Storey	DSB		SSB	
	Steel Cross Section	Yield Moment (kNm)	Steel Cross Section	Yield Moment (kNm)
1	W250×28	105.9	W250×28	105.9
2	W310×24	96.6	W250×28	105.9
3	W310×24	96.6	W250×28	105.9
4	W250×25	91.8	W250×25	91.8
5	W250×22	78.3	W250×25	91.8
6	W250×22	78.3	W250×25	91.8
7	W200×22	66.9	W200×22	66.9
8	W200×22	66.9	W200×22	66.9
9	W150×24	58.0	W200×22	66.9
10	W150×24	58.0	W130×24	48.0
11	W130×24	48.0	W130×24	48.0
12	W150×18	41.4	W130×24	48.0

Table B36- Steel beam selection for 12-storey (R_d=4.0)

Storey	DSB		SSB	
	Steel Cross Section	Yield Moment (kNm)	Steel Cross Section	Yield Moment (kNm)
1	W310×24	96.6	W310×24	96.6
2	W310×24	96.6	W310×24	96.6
3	W250×25	91.8	W310×24	96.6
4	W250×25	91.8	W250×25	91.8
5	W250×22	78.3	W250×25	91.8
6	W250×22	78.3	W250×25	91.8
7	W250×22	78.3	W250×22	78.3
8	W200×22	66.9	W250×22	78.3
9	W200×22	66.9	W250×22	78.3
10	W150×24	58.0	W130×24	48.0
11	W150×24	58.0	W130×24	48.0
12	W130×24	48.0	W130×24	48.0

Table B37- Steel beam selection for 12-storey (R_d=4.5)

Storey	DSB		SSB	
	Steel Cross Section	Yield Moment (kNm)	Steel Cross Section	Yield Moment (kNm)
1	W250×25	91.8	W250×25	91.8
2	W250×25	91.8	W250×25	91.8
3	W250×22	78.3	W250×25	91.8
4	W250×22	78.3	W250×22	78.3
5	W250×22	78.3	W250×22	78.3
6	W200×22	66.9	W250×22	78.3
7	W200×22	66.9	W200×22	66.9
8	W150×24	58.0	W200×22	66.9
9	W150×24	58.0	W200×22	66.9
10	W130×24	48.0	W150×18	41.4
11	W150×18	41.4	W150×18	41.4
12	W150×18	41.4	W150×18	41.4

Table B38- Steel beam selection for 12-storey (R_d=5.0)

Storey	DSB		SSB	
	Steel Cross Section	Yield Moment (kNm)	Steel Cross Section	Yield Moment (kNm)
1	W250×22	78.3	W250×22	78.3
2	W250×22	78.3	W250×22	78.3
3	W200×22	66.9	W250×22	78.3
4	W200×22	66.9	W200×22	66.9
5	W200×22	66.9	W200×22	66.9
6	W150×24	58.0	W200×22	66.9
7	W150×24	58.0	W130×24	48.0
8	W130×24	48.0	W130×24	48.0
9	W130×24	48.0	W130×24	48.0
10	W150×18	41.4	W150×18	41.4
11	W150×18	41.4	W150×18	41.4
12	W100×19	31.0	W150×18	41.4

Table B39- Steel beam selection for 12-storey (R_d=5.5)

Storey	DSB		SSB	
	Steel Cross Section	Yield Moment (kNm)	Steel Cross Section	Yield Moment (kNm)
1	W200×22	66.9	W200×22	66.9
2	W200×22	66.9	W200×22	66.9
3	W150×24	58.0	W200×22	66.9
4	W150×24	58.0	W150×24	58.0
5	W150×24	58.0	W150×24	58.0
6	W130×24	48.0	W150×24	58.0
7	W130×24	48.0	W130×24	48.0
8	W150×18	41.4	W130×24	48.0
9	W150×18	41.4	W130×24	48.0
10	W150×18	41.4	W100×19	31.0
11	W100×19	31.0	W100×19	31.0
12	W100×19	31.0	W100×19	31.0

Table B40- Steel beam selection for 12-storey (R_d=6.0)

Storey	DSB		SSB	
	Steel Cross Section	Yield Moment (kNm)	Steel Cross Section	Yield Moment (kNm)
1	W150×24	58.0	W150×24	58.0
2	W150×24	58.0	W150×24	58.0
3	W150×24	58.0	W150×24	58.0
4	W130×24	48.0	W130×24	48.0
5	W130×24	48.0	W130×24	48.0
6	W150×18	41.4	W130×24	48.0
7	W150×18	41.4	W150×18	41.4
8	W150×18	41.4	W150×18	41.4
9	W100×19	31.0	W150×18	41.4
10	W100×19	31.0	W100×19	31.0
11	W100×19	31.0	W100×19	31.0
12	W100×19	31.0	W100×19	31.0